



# Development of grain boundaries and phase boundaries in WCCo cemented carbides

Maxime Pellan

## ► To cite this version:

Maxime Pellan. Development of grain boundaries and phase boundaries in WCCo cemented carbides. Materials. Université Grenoble Alpes, 2015. English. NNT : 2015GREAI121 . tel-01319087

**HAL Id: tel-01319087**

**<https://theses.hal.science/tel-01319087>**

Submitted on 20 May 2016

**HAL** is a multi-disciplinary open access archive for the deposit and dissemination of scientific research documents, whether they are published or not. The documents may come from teaching and research institutions in France or abroad, or from public or private research centers.

L'archive ouverte pluridisciplinaire **HAL**, est destinée au dépôt et à la diffusion de documents scientifiques de niveau recherche, publiés ou non, émanant des établissements d'enseignement et de recherche français ou étrangers, des laboratoires publics ou privés.

# UNIVERSITÉ GRENOBLE ALPES

## THÈSE

Pour obtenir le grade de

### DOCTEUR DE L'UNIVERSITÉ GRENOBLE ALPES

Spécialité : **Science et Génie des Matériaux**

*Arrêté ministériel : 7 août 2006*

préparée au sein du

**Laboratoire de Science et Ingénierie des Matériaux et Procédés**  
dans l'École Doctorale « **Matériaux et Génie des Procédés** »

présentée et soutenue publiquement  
par

**Maxime PELLAN**

le 10 décembre 2015

## DEVELOPPEMENT DES JOINTS DE GRAIN ET DES JOINTS DE PHASE DANS LES CARBURES CEMENTES WC-Co

Thèse dirigée par **Jean-Michel MISSIAEN**  
et codirigée par **Sabine LAY**

Devant le jury composé de :

**Mr François VALDIVIESO**

Président

**Mr Hans-Olof ANDREN**

Rapporteur

**Mr Lionel GERMAIN**

Rapporteur

**Mr Jean-Michel MISSIAEN**

Membre

**Mme Sabine LAY**

Membre

**Mme Susanne NORGRÉN**

Membre

**Mr Tomas PERSSON**

Invité



---

# Acknowledgments

The finalization of a thesis work is a long and demanding commitment. Obviously, this work would not have been conducted with the same quality and in such an enjoyable atmosphere without the qualities and the involvement of a lot of people. In consequence, I owe them a worthy acknowledgment.

In the first place I want to warmly thank the director and co-director of my thesis, Jean-Michel and Sabine. First, for their high professionalism, their scientific value and their pedagogical supervision which are solid and necessary bases to build on such a project. But also for the warm and constructive working atmosphere they contributed to establish in our team. The confidence and the autonomy they credited me with were essential in building a dynamic and lively relationship in which each party actively engages the other in an ongoing exchange of ideas. The numerous discussions we had on fundamental issues for the project (or even on details sometimes!) might have been long, but they always took place in a helpful atmosphere and came out on a general agreement. Last, I very appreciated their unlimited commitment during the manuscript reviewing process. For all these reasons I am very grateful for the pleasure I took working with them during the three past years.

In a second time I want to really thank our Swedish partners, for their support, their enthusiasm, and for the pertinence of their scientific criticisms. Beyond the professional relationship, I am particularly grateful to Susanne, Tomas and Ernesto for their warm welcome during my travels in Sweden and for the share of their Swedish culture. Thanks to them I keep excellent memories of this international collaboration. I also have to thank (and apologized to!) people at Sandvik Vestberga laboratory who had to accommodate with the long periods during which I monopolized the SEM department for my analyses.

I also want to thank Chalmers' partners for their involvement in the project and their scientific contributions: the open-mindedness and the scientific quality of our joined meetings were particularly beneficial to my work.

---

Special mention to the several PhD Students (friends!) involved in this project with whom I spend very nice time in Stockholm, Goteborg or during different conferences. I especially thank my friend Amine for the moments spent in Mexico!

I don't forget to thank warmly all the people working in the TOP research group, for the numerous coffee brakes we shared and which were good opportunities to taste their sense of humour. I particularly thank Fabienne and Sylvie for their patience, dealing with my administrative in-efficiency.

Last but not least, I want to thank and congratulate PhD student colleagues sharing my office: JP, Adrien, Julien and Matthieu. It was not always easy to support my hyperactivity and bad jokes! Anyway, I spent really great time in this office and this is thanks to them. Not forgetting Leslie and Simon of course! Good luck to all of those among them who have not finished yet!

---

The work presented in this manuscript was carried out at the SIMaP laboratory, part of the Grenoble Institute of Technology (France). It was financially and technically supported by Sandvik Mining (Sweden), Sandvik Coromant (Sweden) and Seco Tools (Sweden) companies.

---

---

# Table of Content

<b>Introduction .....</b>	<b>9</b>
<b>Chapter I Bibliography .....</b>	<b>13</b>
<b>I.A Presentation of cemented carbides.....</b>	<b>13</b>
I.A.1 Thermodynamic description of W-C-Co system.....	13
I.A.2 Crystalline structures .....	15
<i>I.A.2.i Introduction to crystallography.....</i>	<i>15</i>
<i>I.A.2.ii Crystal Structures in WC-Co system.....</i>	<i>17</i>
<b>I.B Grain growth in cemented carbides.....</b>	<b>21</b>
I.B.1 Grain growth mechanisms .....	21
I.B.2 Influence of Carbon content .....	27
I.B.3 Influence of Cobalt content .....	31
I.B.4 Influence of initial grain size distribution.....	33
<b>I.C Grain boundary in WC-Co system .....</b>	<b>37</b>
I.C.1 Grain boundary denomination and characterization.....	37
I.C.2 Technics for grain boundary study .....	38
I.C.3 CSL approach for description of grain boundaries.....	39
I.C.4 Grain boundary energy .....	41
<i>I.C.4.i Experimental results.....</i>	<i>41</i>
<i>I.C.4.ii DFT calculations.....</i>	<i>41</i>
<i>I.C.4.iii Infiltration and segregation in WC boundaries .....</i>	<i>42</i>
I.C.5 The formation of WC grain boundaries in WC-Co .....	42
I.C.6 Distribution of WC grain boundary character in WC-Co.....	44

---

<b>I.D Contiguity .....</b>	<b>53</b>
I.D.1 Definition.....	53
I.D.2 Equilibrium VS Geometry approach .....	53
I.D.3 Influence of composition .....	54
I.D.4 Modelling contiguity .....	56
<b>I.E Grain shape .....</b>	<b>61</b>
 <b>Chapter II Experimental details .....</b>	 <b>65</b>
<b>II.A Sample preparation .....</b>	<b>65</b>
II.A.1 Compositions .....	65
II.A.2 Elaboration .....	69
<i>II.A.2.i WC-Co samples.....</i>	<i>69</i>
<i>II.A.2.ii WC-Cu sample .....</i>	<i>70</i>
II.A.3 Cross-sections preparation .....	70
<b>II.B EBSD method .....</b>	<b>71</b>
II.B.1 Experimental parameters.....	71
II.B.2 Data cleaning and post processing .....	72
II.B.3 Influence of resolution on measurements.....	74
<b>II.C Focused Ion Beam microscopy .....</b>	<b>77</b>
II.C.1 Experimental parameters.....	78
II.C.2 Post-processing.....	78
<b>II.D Image Analysis and microstructure characterization .....</b>	<b>80</b>
II.D.1 Basics of stereological methods .....	80
II.D.2 Distribution of grain size and 3D reconstruction .....	83
<i>II.D.2.i Reconstruction of 3D grain size distribution.....</i>	<i>85</i>
II.D.3 Measuring contiguity .....	87



---

II.D.4 Grain boundary characterization .....	90
<i>II.D.4.i Part I: collection of orientation data (Aphelion™)</i> .....	90
<i>II.D.4.ii Part II: treatment of orientation data (MatLab®)</i> .....	98
II.D.5 WC/Co phase boundary identification .....	105
II.D.6 3D image analysis .....	107
 <b>Chapter III Influence of carbon and cobalt content on grain growth and carbide grain shape .....</b>	<b>109</b>
<b>III.A Evolution of grain shape .....</b>	<b>109</b>
III.A.1 2D analysis of grain shape .....	109
III.A.2 FIB analysis .....	111
<b>III.B 3D equivalent diameter distributions .....</b>	<b>115</b>
<b>III.C Evolution of mean grain size .....</b>	<b>119</b>
<b>III.D Abnormal grain growth .....</b>	<b>121</b>
 <b>Chapter IV Influence of C and Co on the interface development .....</b>	<b>125</b>
<b>IV.A Evolution of contiguity .....</b>	<b>125</b>
IV.A.1 Measurements results .....	125
IV.A.2 Influence of composition .....	126
IV.A.3 Fitting of experimental values .....	126
IV.A.4 Comparison with literature value .....	127
<b>IV.B Phase boundaries distribution .....</b>	<b>130</b>
IV.B.1 Influence of composition on grain boundary development .....	130
<i>IV.B.1.i Evolution of the number of grain boundaries .....</i>	<i>130</i>
<i>IV.B.1.ii Evolution of the grain boundaries surface area .....</i>	<i>131</i>
IV.B.2 Evolution of grain boundary type population .....	133

---

IV.B.2.i Distribution of rotation axes .....	133
IV.B.2.ii Rotation angles .....	138
IV.B.2.iii Discussion about the origin of the special boundaries.....	146
IV.B.2.iv Grain boundary planes .....	147
IV.B.3 WC/Co phase boundaries .....	153
 <b>Chapter V Discussion: development of grain and phase boundaries in cemented carbides</b> .....	<b>157</b>
<b>V.A Grain boundary formation.....</b>	<b>157</b>
V.A.1 Scenario for grain boundary formation.....	159
V.A.2 Particular analysis of special boundary formation.....	161
<b>V.B Grain boundary and phase boundary migration .....</b>	<b>164</b>
V.B.1 Phase boundary and grain boundary migration.....	165
V.B.2 Modelling the role of grain boundaries and phase boundaries on grain growth.....	169
V.B.2.i Kinetic approach .....	169
V.B.2.ii Energetic approach: influence of grain boundary pinning.....	171
 <b>Conclusion.....</b>	<b>177</b>
 <b>References.....</b>	<b>183</b>
<b>Appendix .....</b>	<b>189</b>
<b>Appendix 1: Principles of EBSD method .....</b>	<b>191</b>
<b>Appendix 2: Basics of image analysis .....</b>	<b>195</b>
<b>Appendix 3: Migration pressure for grain growth in systems containing phase boundaries and grain boundaries .....</b>	<b>201</b>
<b>Appendix 4: Calculation of the dragging force .....</b>	<b>203</b>

---

---

---

# Introduction

The development of composite materials made from tungsten carbide (WC) and cobalt (Co) commenced in the late 1920's, and the first commercially available cemented carbide tool was presented during the 1927 Leipzig spring fair. The so called WIDIA alloy (acronym for Wie Diamand, literally “like diamond”) represented a major breakthrough in tool engineering thanks to its exceptional hardness and wear resistance. If, at first, only small amounts of WIDIA were produced, cemented carbide production never stopped developing and is nowadays a flourishing industry. Thanks to the wide range of mechanical properties cemented carbide can cover, they are used in various applications, such as metal machining, drilling or mining.

For a material, hardness (resistance to compressive load) and toughness (ability to plastically deform without fracturing) are two competing properties. The singularity of cemented carbides results from the balance between the high mechanical properties of tungsten carbide (very hard but brittle) and the toughness of cobalt. Cemented carbides are obtained by classical powder metallurgy process: WC and Co powder are mixed, pressed in a desired shape and sintered (often in liquid phase, between 1380°C and 1500°C). During sintering, WC crystals development and rearrangement leads to the creation of a continuous skeleton that will ensure the mechanical resistance of the sintered part.

Nonetheless, mechanical properties of cemented carbides are strongly linked to the microstructure. For example limiting the growth of WC grains during sintering increases the hardness of the final product. At the opposite, the uncontrolled growth of a few crystals at the expenses of the others (“abnormal growth”) is detrimental for mechanical properties. In another hand, bonds between WC crystals are expected to play an important role in the mechanical behavior of the material. Hence relationships between microstructural parameters (such as mean grain size, grain size distribution, mean free path in the binder, binder fraction...) and mechanical properties (strength, hardness, fracture toughness) have been widely studied and are well documented. However, in the aim of predicting mechanical properties, a full understanding of

---

the microstructure development as a function of composition and process conditions is still necessary.

In ternary W-C-Co cemented carbides, the two parameters of composition are cobalt content (binder content) and carbon content in the binder. In the literature, the effect of cobalt content on grain growth has been partially investigated but no clear tendency has been established yet. As well, although an influence of carbon content on carbide shape and grain growth has been demonstrated, effect of this parameter on contacts organization has never been investigated yet. Last, despite the unquestionable influence of grain boundaries on the properties, no results are found on the influence of composition on the character of WC/WC grain boundaries and WC/Co phase boundaries in the microstructure.

Considering issues outlined above, this study focuses on the understanding of composition effect on grain growth, on the development of grain and phase boundaries and on the resulting boundary character distribution, with the effort to separate cobalt content and carbon content influences. The aim is also to shed light on the mechanisms of grain boundary and phase boundary formation and development, which accompany sintering and grain growth. The investigated cobalt range is chosen to vary from 10 vol% (close to industrial compositions) up to 50 vol% in order to cover a wide range for a general understanding of mechanisms. The effect of carbon content is also studied. For sample characterization a large place is given to Electron Backscattered Diffraction and image analysis methods, with the development of dedicated methods for quantifying the distribution of boundary types.

The first chapter aims at giving the necessary background for a good understanding of the issues approached in this study. A first part is dedicated to the description of thermodynamic and crystallographic aspects of the W-C-Co system. Then, the main results found in the literature on the microstructure development in cemented carbides are presented, with the effort to put them into perspective with the objectives of our study. Especially grain growth, evolution of the grain boundary population and development of grain boundaries in cemented carbides are broached.

In a second part, materials of the study and experimental methods are presented. The composition of the samples and the processing operations are detailed. Acquisition parameters and data treatment in EBSD are specified in order to be aware of the advantages and limitations of the

---

technique. Various microstructure analysis methods based on image analysis and implemented for the study are explained. A program based on EBSD data and dedicated to grain boundary character analysis was developed especially for this work and is described in this part.

The third chapter approaches the influence of cobalt and carbon content on grain growth and grain shape. Grain shape was investigated by the mean of 2D shape factors estimated on EBSD images. In complement, Focus Ion Beam characterization and reconstruction of 3D volumes of some samples allowed to qualitatively observe grain shape, and confirm 2D measurements. Grain size was evaluated by reconstruction of the 3D equivalent diameter from 2D measurements, with the Saltykov method. Evolution of the average grain size and of the grain size distribution is discussed.

The fourth chapter focuses on the influence of cobalt and carbon content on the interface developments. It regroups different aspects, commencing with the evolution of contiguity, which is the fractional area of grain boundaries per grain. An empirical model for contiguity variation with cobalt content is proposed, and the method for contiguity measurement, based on EBSD image analysis, is compared with the classical methods in the literature. A second major aspect is the characterization of grain boundary character distribution. The evolution of the distribution with composition is investigated. Finally, the evolution of the fraction of grain boundary and phase boundary presenting a remarkable plane is presented.

In a last chapter, two main issues are put into perspective with the main results obtained through the study. On one hand, the mechanism of formation of grain boundaries and phase boundaries is discussed. A scenario, describing how the population of grain boundaries evolves through the sintering process is proposed. Two approaches, mechanical and energetic, are considered to foresee the limit grain boundary fraction the system can reach for the special grain boundaries formed in the initial stage. On the other hand, grain boundary and phase boundary migration mechanisms are discussed, and their correlation is investigated. Finally, the specific role of grain boundaries on grain growth is discussed, and the observed influence of the contiguity is explained with support of a model taking into account the influence of grain boundary pinning on the kinetics of interface migration and on mechanical equilibrium in the system.

---



# Chapter I Bibliography

## I.A Presentation of cemented carbides

Industrial cemented carbides are two-phase alloys. The presence of a third phase considerably affects mechanical properties. Thus, a correct understanding of the W-C-Co phase diagram is necessary to properly control cemented carbides production. The following part is not an exhaustive analysis of W-C-Co ternary diagram but aims at presenting its most important aspects concerning the present study. Crystallographic notions and description of WC crystal are also approached in this part.

### I.A.1 Thermodynamic description of W-C-Co system

Several isothermal sections can be found in the literature, either based on the Calphad calculation method or on experimental measurements. The notions considered here are illustrated with isothermal sections plotted by Åkesson [1], which are considered to be in good agreement with experimental measurements. First section (Figure 1a) is plotted at a temperature of 1200°C, temperature at which every phase is in the solid state. The second one (Figure 1b) is plotted at a temperature of 1450°C, at which the binder phase is liquid.

According to Figure 1 WC is in equilibrium with Co in a narrow region of composition, and {WC-Co} domain width varies with temperature and binder content. At given temperature and cobalt content, C/W ratio determines the present phases. Carbon excess leads to the crystallization of graphite ( $C_g$ ), and places the system in a three-phase domain: {WC- $\beta$ - $C_g$ } in the solid state or {WC-liquid- $C_g$ } at higher temperatures ( $\beta$  phase refers to the cobalt rich solid solution). At the opposite, carbon default leads to the crystallization of cubic carbides, placing the system in another three-phase domain: {WC- $\beta$ - $M_{12}C$ } at low temperatures, {WC- $\beta$ - $M_6C$ } in solid

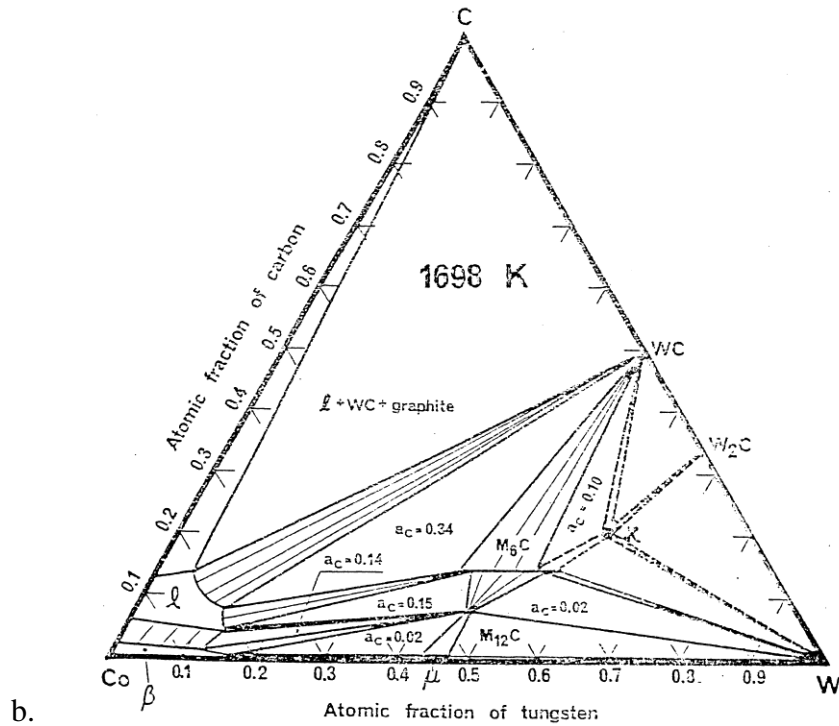
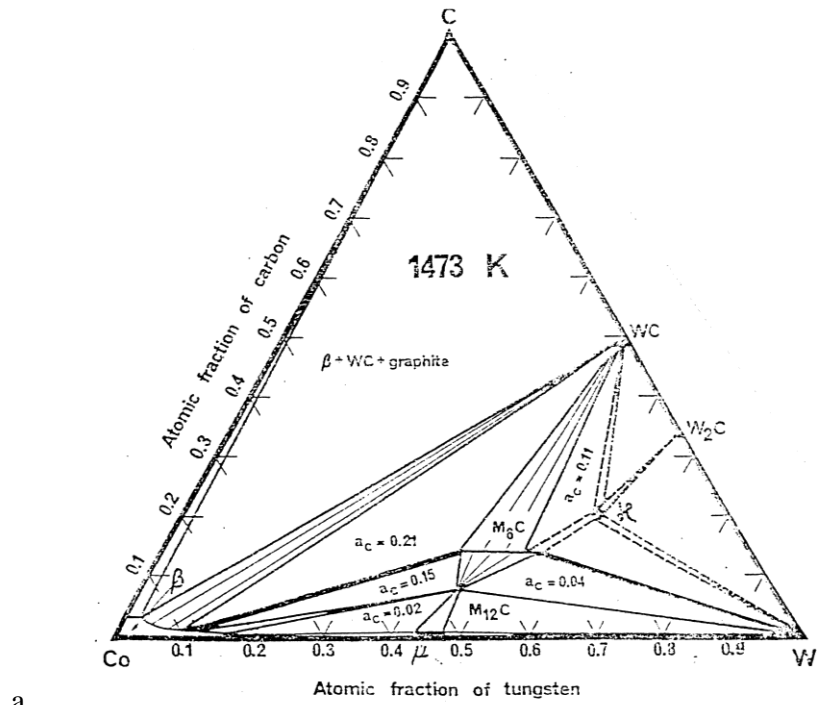


Figure 1: Isothermal section at  $T = 1200^\circ\text{C}$  (a) and  $T = 1450^\circ\text{C}$  (b) of W-C-Co ternary system [1].  $\beta$  phase refers to a cobalt rich solid solution, and  $M_xC$  to a metallic carbide.

state but for temperatures above 1151°C, or {WC-liquid-M<sub>6</sub>C} at higher temperatures. M<sub>6</sub>C (resp. M<sub>12</sub>C) is also referred to as η phase (resp. η' phase): this is the denomination that is used in this study. Melting temperature of the binder decreases with C content. Calculations by Kruse et al. [2] estimate l+WC+β+C<sub>g</sub> and l+WC+β+η equilibrium temperatures to be respectively 1298°C and 1368°C. Melting temperature of the binder is comprised between those two values.

Solubility of WC in cobalt is high, very depending upon temperature, and decreases with carbon content (2.18 at% in C-rich binder at 1200°C, when it is only 0.92 at% in W-rich binder, if we assume that the element with the smaller solubility limits WC solubility [3]). According to Rautala and Norton measurements [4], WC solubility reaches a maximum of 10 at% at 1320°C in β phase, and increases up to 24 at% in the liquid. Guillermet [5] calculations indicate that maximum solubility would rather be 7 at% at 1315°C in β, and 20 at% in the liquid. At ambient temperature, tungsten solubility has been reported to be 3.5 wt% [6]. At the opposite, solubility of cobalt in WC is very small and can be neglected ([7], [8]).

These observations on thermodynamic properties in {WC-Co} system underline the fundamental importance of adjusting C/W ratio during the elaboration process to control the microstructure.

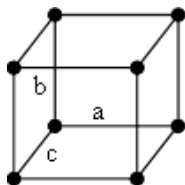
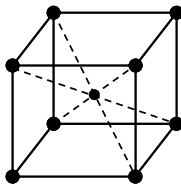
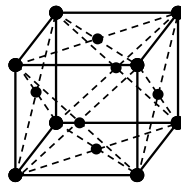
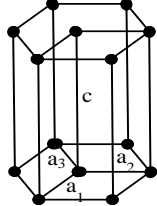




## I.A.2 Crystalline structures

### I.A.2.i Introduction to crystallography

Organization of the matter in a material can be characterized with its “ordering level”, varying from *amorphous* to *crystalline*. In an amorphous material, atoms organization does not show any specific arrangement. At the opposite, in crystalline material atoms are ordered and form a periodic pattern that infinitely repeats in three dimensions. This pattern is called the *crystal structure*. An intermediate level exists and is called *polycrystalline* state: atoms are ordered but at a smaller scale, the lattice is no longer completely continuous. A polycrystalline material is composed of many *grains* (groups of ordered atoms, also referred to as *crystallites*) of various sizes and orientations. Interfaces where crystals of different orientations meet are called grain boundaries.

In order to understand the behavior of crystals, it is necessary to describe the crystal structure. It consists in elementary atomic patterns, repeated all along the three directions of the space, by translation along the vectors of a space-lattice. Considering this characteristic, only fourteen different space-lattices exist. Unit cells of the most common space-lattices are presented in Table 1. Eventually, to describe the place of atoms in a unit cell, a system of axes, called *crystal system* is used. In crystallography seven systems are used to describe all space-lattices (examples in Figure 2). Finally, the positioning of atomic patterns in unit cells of the space-lattice makes possible the description of any crystal structure.

**Table 1: Most common space lattices with corresponding crystal systems and examples.**

Space lattice	Simple Cubic	Body-centered Cubic	Face-centered Cubic	Simple Hexagonal
Unit cell				
Crystal system	Three axes at right angle (all equal). $a = b = c$ $\alpha = \beta = \gamma = 90^\circ$			3 axes are coplanar at $120^\circ$ ; last axis is at $90^\circ$ . $a_1 = a_2 = a_3 \neq c$
Example	 Pyrite crystal	 Petzite crystal	 NaCl crystal	 Red beryllium crystal

For crystallographic consideration it is often necessary to denominate a particular plane. Miller indices ( $hkl$ ) are universally used for this purpose. They are based on the intercept of a plane with the crystal system: a ( $hkl$ ) plane cuts the  $X$  axis (resp.  $Y$  or  $Z$ ) at a coordinate  $1/h$  (resp.  $1/k$  or  $1/l$ ) with respect to the basis vectors of the unit cell. Among the advantage of this notation is that in a cubic space-lattice equivalent planes have similar indices, so are easily identifiable (for example plan (132) and (123) are equivalents). However, this is no longer true in hexagonal system.

For this reason another system, called Miller-Bravais system ( $hkil$ ), can be used. Rules to establish those indices are the same as the ones specified above excepted that four axes (Table 1)  $a_1$   $a_2$   $a_3$  and  $c$  are now considered. The third index is always completely determined by the first two:

$$i = -(h + k)$$

In the Miller-Bravais system crystallographic directions are also expressed in the four axes system. Their indices ( $uvtw$ ) correspond to the coordinates of the vector in the four axes system, with the condition:

$$t = -(u + v)$$

For conciseness of the notation, negative indices  $-h$  are noted  $\bar{h}$ .

With this notations equivalent planes or directions correspond to circular permutations of the first three indices and sign opposition. For example  $[1\bar{2}10]$ ,  $[11\bar{2}0]$  and  $[2\bar{1}\bar{1}0]$  planes are equivalent, which is not obvious with Miller notation ( $[0\bar{1}0]$ ,  $[110]$  and  $[100]$ ).

#### I.A.2.ii Crystal Structures in WC-Co system

WC has a non-centrosymmetric hexagonal space lattice with W atoms at the position (0,0,0) and C atoms at the position (2/3, 1/3, 1/2) (Figure 2). Lattice constants give a ratio  $c/a = 0.976$ , very close to 1, which will be of main interest in WC/WC grain boundaries formation. The densest planes in this structure are (0001) (referred to as basal plane) and  $(10\bar{1}0)$  (referred to as prismatic

plane). In alloys sintered with Co, WC grains shape is close to triangular prisms with basal and prismatic planes as habit planes.

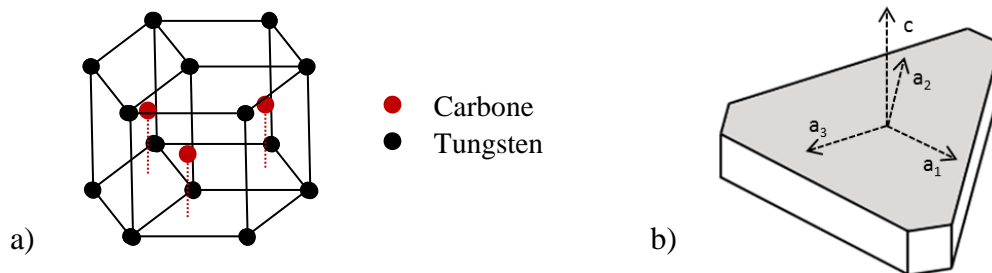


Figure 2: Unit Cell of WC crystal structure (a) and identification of prismatic (white) and basal (grey) planes (b).

WC structure possesses several symmetries: a 6-fold rotation-inversion axis around  $[0001]$ , and two mirror reflections through  $(1\bar{2}10)$  and  $(0001)$  planes (Figure 3). Figure 4 represents the stereographic projection of axes of the WC hexagonal structure on the equatorial plan  $(0001)$ . The whole sphere can be reconstructed from the trihedron  $[2\bar{1}\bar{1}0]/[10\bar{1}0]/[0001]$  (fundamental trihedron) thanks to the symmetries described above.

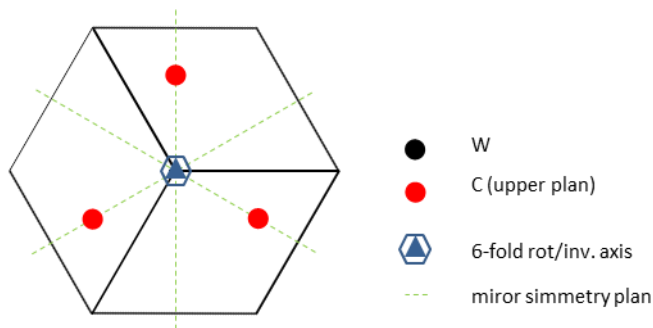


Figure 3: Representation of symmetries in WC hexagonal structure.

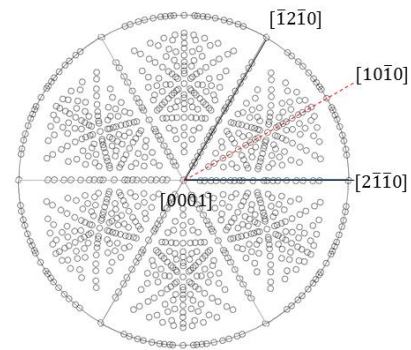


Figure 4: Stereographic representation of directions in the hexagonal system.  $[10\bar{1}0]/[2\bar{1}\bar{1}0]/[0001]$  correspond to the fundamental trihedron.

Co exists in two allotropic forms: the first one, stable at temperatures below  $422\pm 5^\circ\text{C}$  [1] crystallizes in hexagonal system. The second ( $\beta$ ) crystallizes in face centered cubic system, and

is stable at higher temperatures. In practice, cubic cobalt is found even at low temperature in WC-Co alloys, thanks to both stabilization of cubic structure due to W and C dissolution in cobalt and mechanical stress resulting from different thermal dilatation coefficients between cobalt and carbide [9].

$\eta$  phase composition depends on temperature, and changes from  $\text{Co}_2\text{W}_4\text{C}$  at low temperatures to  $\text{Co}_3\text{W}_3\text{C}$  at high temperatures. At the opposite,  $\eta'$  phase has a composition  $\text{Co}_6\text{W}_6\text{C}$  which undergoes very little change with temperature.

Table 2 and 3 summarized the characteristics of the different phases.

**Table 2: Crystallographic structure of phases present in WC-Co system.**

Phase	Space lattice	Space group	Lattice constant (nm)	Atom position
WC	hexagonal	P-6m2	$a = 0.2906$ $c = 0.2836$	W (0,0,0) C ( $\frac{1}{3}, \frac{2}{3}, \frac{1}{3}$ )
Co	hexagonal	P63/mmc	$a = 0.2507$ $c = 0.4069$	Co ( $\frac{1}{3}, \frac{2}{3}, \frac{1}{4}$ )
	cubic, face centered	Fm-3m	$a = 0.3544$	Co (0,0,0)
$\eta$ ( $\text{Co}_2\text{W}_4\text{C}$ )	cubic	Fd-3m	$a = 1.1210$	W (0,0,0) W ( $0.43, \frac{1}{8}, \frac{1}{8}$ ) Co (0.20,0.20,0.20) C ( $\frac{1}{2}, \frac{1}{2}, \frac{1}{2}$ )
$\eta$ ( $\text{Co}_3\text{W}_3\text{C}$ )	cubic	Fd-3m	$a = 1.1116$	W ( $0.43, \frac{1}{8}, \frac{1}{8}$ ) Co (0,0,0) Co (0.20,0.20,0.20) C ( $\frac{1}{2}, \frac{1}{2}, \frac{1}{2}$ )
$\eta'$ ( $\text{Co}_6\text{W}_6\text{C}$ )	cubic	Fd-3m	$a = 1.0900$	W ( $0.43, \frac{1}{8}, \frac{1}{8}$ ) Co (0,0,0) Co (0.20, 0.20, 0.20) C ( $\frac{3}{8}, \frac{3}{8}, \frac{3}{8}$ )

**Table 3: Molar Volume and molar mass of phases present in WC-Co system at ambient temperature.**

	Molar Volume (cm <sup>3</sup> /mol)	Molar Mass (g/mol)	Atomic Number
WC	6.24	97.93	40
W	9.53	183.84	74
C(graphite)	5.31	12	6
Co (pure)	6.7	58.93	27
η	7.18	105.76	~ [44.1 - 50.8]
η'	7.50	112.97	~ 47



## I.B Grain growth in cemented carbides.

It is established that mechanical properties of WC-Co cemented carbides, as hardness, bending strength, or toughness for example, are critically depending on grain size [10]. Therefore, controlling grain growth during the sintering process is of major interest. In the aim of a better understanding of grain growth, different classical mechanisms that have already been mentioned in the literature are described here. Several studies have linked those mechanisms to experimental measurements, trying to determine the predominant one. The influence of cobalt content or C/W ratio in binder has also been investigated, just as initial grain size distribution of the initial WC powder. Main results are reported here.

### I.B.1 Grain growth mechanisms

The so-called Ostwald ripening process is often assumed as the main mechanism of grain growth. It consists in the dissolution of the smallest grains, followed by diffusion of solute species (W and C) and a re-precipitation on bigger grains. This process is capillary-driven and spontaneous because of the need for the system to reduce its total interface energy. The limiting stage can be the solute diffusion in the liquid, or the reaction of dissolution/precipitation at the phase boundary. The classical LSW theory (exposed independently by Lifshitz and Slyozov[11], and Wagner [12]) describes the Ostwald ripening kinetics of a population of spherical particles. In the case where diffusion is the limiting process, cubic law is obtained for the variation of the average diameter of the spheres:

$$D^3 - D_0^3 = K_d t \quad (1.1)$$

In the case of surface reaction as the limiting process, kinetics is described with a parabolic law:

$$D^2 - D_0^2 = K_r t \quad (1.2)$$

Measurements of grain size evolution with sintering time by Shin and Matsubara [13] (Figure 5.a), or Coster and Chermant [14] (Figure 5.b) are in favour of a cubic law which would mean a

mechanism limited by diffusion. But this mechanism would imply a diminution of the growth rate with binder content increase (increasing diffusion length), which is not consistent with experimental observation ([13], [14], see next part: Influence of Cobalt content).

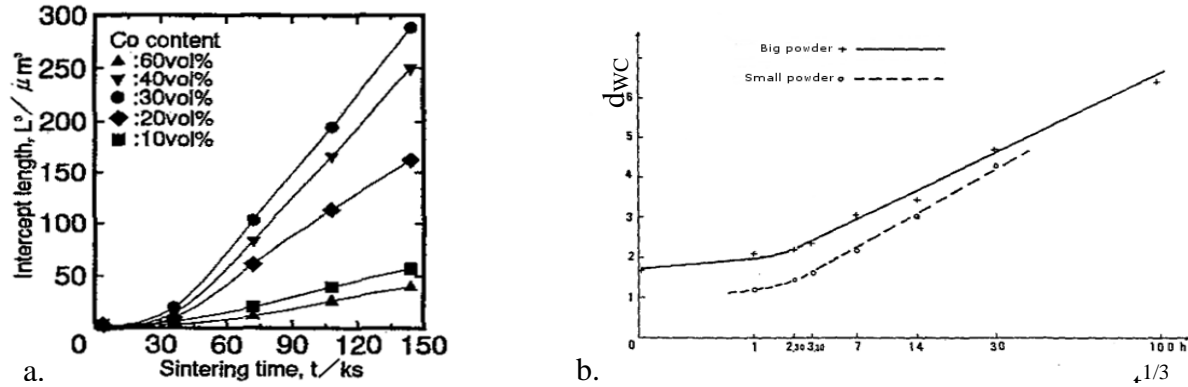
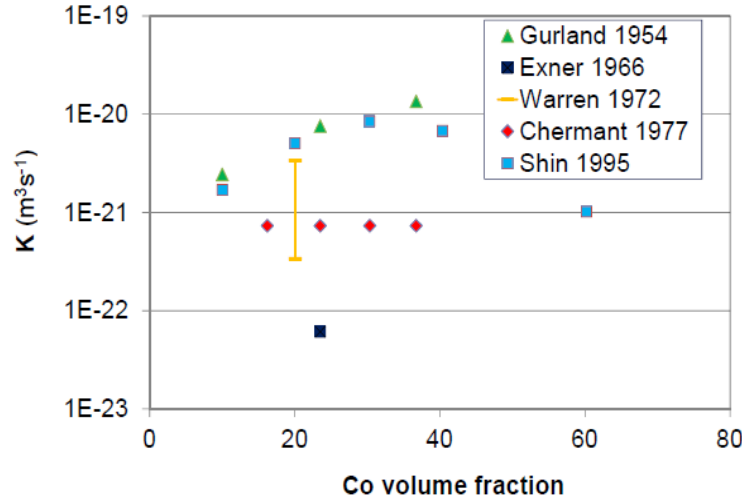


Figure 5: a) Variation of intercept length in WC with sintering time, by Shin and Matsubara [13]. b) Evolution of the 2D equivalent diameter of WC grains with time, measured by Coster and Chermant [14], for two sizes of initial powder. In both cases (a and b) the curve follows a cubic law, excepted at the short time.

Additionally, the kinetic constant  $K$  has been measured by different authors (Figure 6) and appears to be significantly lower than the theoretical value calculated by Warren and Waldron [15] for diffusion controlled growth ( $1-2 \times 10^{-18} m^3.s^{-1}$ ). Last, LSW theory is based on the hypothesis of spherical particles completely surrounded by the liquid phase: it is not the case in cemented carbide, where carbide grains are faceted and present numerous contacts or grain boundaries with neighbours. Therefore, simple Ostwald ripening theory is not sufficient to explain grain growth in cemented carbides.



**Figure 6: Variation of the kinetic constant  $K$  of grain growth (Cf. Equation [1.1]) [16].**

LSW theory predicts an evolution towards a stationary particle size distribution ([11], [12]). Although this kind of distribution is often observed in practice, LSW theory cannot explain the occurrence of abnormal grain growth. In some particular conditions bigger grains grow faster, leading to a bimodal grain size distribution. Park et al. [17] explain it by the fact that precipitation would not be uniform on the WC planar facets, as assumed in the LSW diffusion-limited model, but limited by a 2D-nucleation process. This way, growth rate would not be linearly dependent on the driving force created by the grain size distribution, but would increase abruptly above a critical driving force (Figure 7). Considering that defects are preferential sites for nucleation, the presence of a small number of grains with defects would enhance abnormal grain growth, as compared to the pure 2D-nucleation process. The same conclusions can be drawn from the work of Rohrer et al.[18]. In fact, these authors calculate the Nucleation Energy Barrier (NEB) for the precipitation of atoms (not for the dissolution, occurring preferentially at the crystal edges) on an ideal facet. Simulations show that for perfect faceted crystals (without step-producing defects) coarsening comes to stop for a particle size of a few tens of nanometers because of the prohibitive value of the NEB for facets creation. At the opposite, for an initial distribution containing crystals with step-producing defects a bimodal population can develop: because nucleation on defects is favoured, defective crystals grow much faster than perfect crystals, and abnormal growth occurs. Considering that the number of abnormal grains depends on initial defects quantity, it would not

evolve during sintering. Additionally, the bimodal distribution is supposed to get back to a normal distribution as grains without defects are consumed.

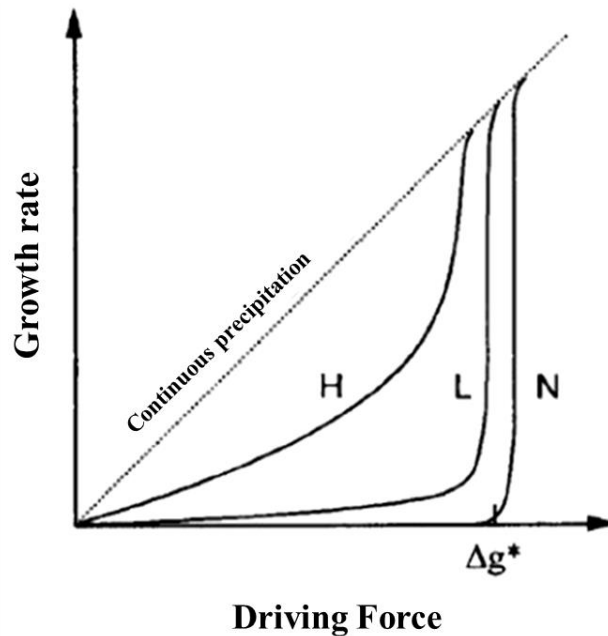


**Figure 7: Schematic variation of the growth rate of faceted particles with driving force at high (H), low (L) and zero (N) nucleation defect density [17].**

It should be noticed that after the step of 2D-nucleation, a new layer can develop, and two kinds of growth are to be distinguished: 2D or 3D (Figure 8). In the case where lateral growth by precipitation at the edges of a nucleus is much faster than kinetics of 2D-nucleation, a new layer finish to form well before a new nucleation occurs on this same layer, resulting in a 2D growth of the grain. In the case of 3D-growth, 2D-nucleation is faster than lateral growth and a new layer starts to form well before the preceding one is completed. The grain grows simultaneously parallel and orthogonal to the plane, presenting then facets, steps or terraces (Figure 12). According to Zhong and Shaw [19], a transition from 2D toward 3D growth would occur when increasing temperature. From their results, this transition seems to occur between 1300 °C and 1400 °C.

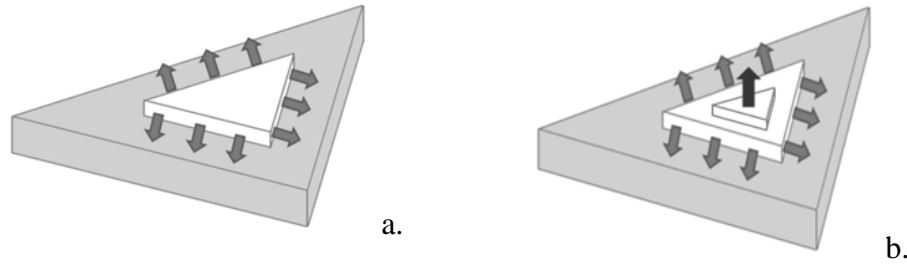


**Figure 8: Growth controlled by 2D-nucleation (2D growth) (a) or lateral growth (3D growth) (b)**

The previously described process (Ostwald ripening and 2D nucleation + lateral growth) results in the migration of phase boundaries with the liquid. But grain boundaries are also present, either coming from the powder or forming during sintering. The driving force for grain growth then results from a reduction of both the phase boundary energy and the grain boundary energy. Both phase boundaries and grain boundaries should migrate for grain growth to occur. Depending on their relative mobility, grain boundaries may either help or hinder phase boundary migration [15].

Another classical mechanism evoked in the literature is the coalescence of adjacent crystals by aligning their orientations through slight translations or rotations. Coalescence by orientation alignment is energetically favoured because it reduces the grain boundary energy of the system. It has often been observed or suspected at low temperatures, during the first stages of sintering, and with fine WC-Co powder ([17],[20]). This can be easily understood, considering the specificity of this mechanism: first it does not require long distance diffusion of atoms, and therefore can occur at low temperatures. Then, as particles need to align for merging, coalescence requires a low misorientation angle, a loose packing and/or a small grain boundary area.

Finally, coarsening/coalescence may also occur by the grain boundary migration between adjacent particles, as the specific evolution during sintering makes it possible for the grain boundary to move without increasing its area [21]. This mechanism may probably play a role in the elimination of fine particles at the beginning of sintering (Figure 9).

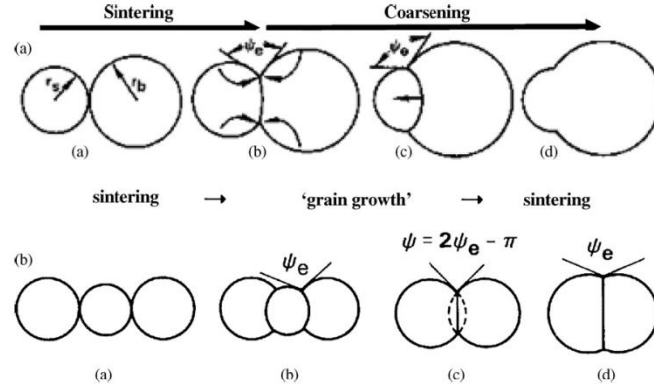


**Figure 9: Mechanism of coarsening/coalescence as described by Lange and Kellett [21].**

Mannesson et al. [22] proposed a numerical model of grain growth based on the multiple processes mentioned above: 2D-nucleation of new atomic layers is considered as the rate controlling step, but mass-transfer across the interface and long range diffusion are also taken into account. Results given by this simulation were consistent with experimental results. The calculated growth rate shows a rapid dissolution below a critical radius and a slow growth just above, characteristic of 2D nucleation becoming rate controlling (Figure 10). For larger grain sizes long-range diffusion and mass transfer across interfaces consumes a larger part of the driving force (see Figure 10b).

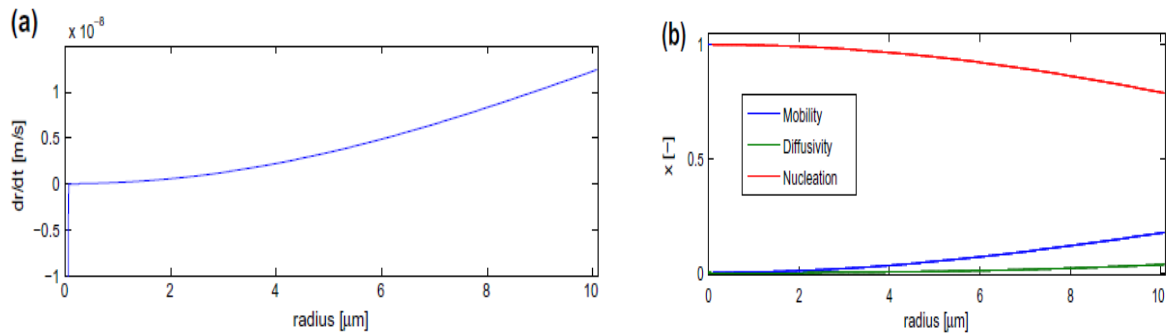


**Figure 10: a) The growth rate calculated from the shared processes model. B) The amount of total driving force consumed by each process [22].**

In their analysis of 3D structure of WC grains Borgh et al. [23] observed both rounded and faceted shapes (Figure 11 and Figure 12), supposing in turns that different growth mechanisms occur during sintering.

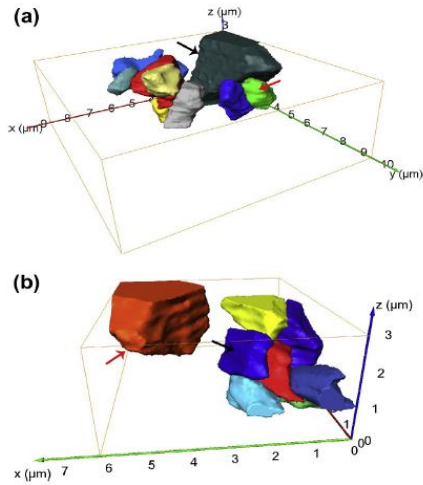


Figure 11: Individual 3D WC grains reconstruction for WC-6% Co alloy (a) and WC-20% Co alloy (b) (sintered 1h at 1430°C). The red arrows illustrate non-faceted grain surfaces and black arrows illustrate faceted grain surfaces. [23]

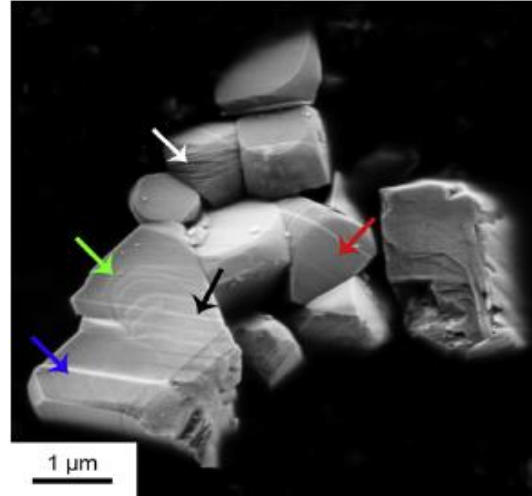


Figure 12: WC grains extracted from the Co matrix for the WC-20% Co alloy. The white arrow illustrates a non-faceted grain surface, the red arrow illustrates a faceted grain surface, the green arrow illustrates a stepped (terraced) surface structure, the blue arrow illustrates a terrace step and the black arrow illustrates a planar defect. [23]

### I.B.2 Influence of Carbon content

C/W ratio in cemented carbides is an important parameter influencing a lot the microstructure. At a given cobalt content, if this ratio increases, the system moves from a three-phase WC + Co +  $\eta$  domain to a WC + Co + graphite domain, across a two-phase WC + Co domain. But this ratio also seems to affect grain growth, as already reported in the literature.

First, it seems well accepted that C-rich binder favours rapid grain growth ([24],[25]). The hypothesis of a lower stability of the C-rich liquid phase was proposed to explain a faster nucleation, thus a faster growth in C-rich samples [24]. Another explanation would be a higher amount of surface defects which would facilitate precipitation at carbide surface in C-rich samples [25]. Last, high carbon content decreases the solidus temperature, thus liquid phase sintering is expected to start earlier.

At the opposite, the effect of C/W ratio on abnormal grain growth is not very clear. Abnormal grain growth can be evaluated in two different ways: by estimating the heterogeneity of the size distribution, or by detecting the presence of very large grains in the matrix.

According to results presented by Chabretou et al it appears that the size distributions around the mean diameter in both carbon rich and tungsten rich alloys is rather uniform [24]. Considering the second aspect of abnormal grain growth, the authors observed the presence of very large grains in either tungsten rich samples [24] or carbon rich samples [26].

Recently Borg et al. observed on samples sintered for 8h that the size distribution was more uniform in C-rich samples [25]. However, a further work of the same author [27] reported contradictory results where no difference is noticed in size distribution of C and W-rich binder. In fact, considering the evolution of the  $D_{90}/D_{10}$  ratio (which is more appropriate than  $D_{90} - D_{10}$  to characterize the abnormal character of grain growth) the effect of carbon content is not significant (Figure 13). In addition, this ratio is expected to be constant during normal grain growth and to be equal to 3 for reaction limited kinetics in the LSW theory [12]. Also, according to these results neither C-rich nor W-rich binder seems to particularly favour abnormal grain growth. However, samples were sintered for only one hour in this last work, what can explain the differences with their previous study.

Finally, C/W ratio effect on abnormal grain growth is yet unclear. Dedicated studies should be performed to isolate influence of this parameter from many other parameters which have a significant effect.

**Table 4: Parameters evaluated from 2D equivalent diameter measurements in EBSD analysis (samples sintered 1h at 1410°C) [27].**

	WC-Co- $\eta$	WC-Co- $\eta$ (lim)	WC-Co	WC-Co-g (lim)	WC-Co-g
$D_{10}$	0,769	0,808	0,913	0,951	0,989
$D_{50}$	1,507	1,553	1,733	1,726	1,796
$D_{90}$	2,634	2,732	3,13	3,049	3,284
$D_{90}-D_{10}$	1,865	1,924	2,217	2,098	2,295



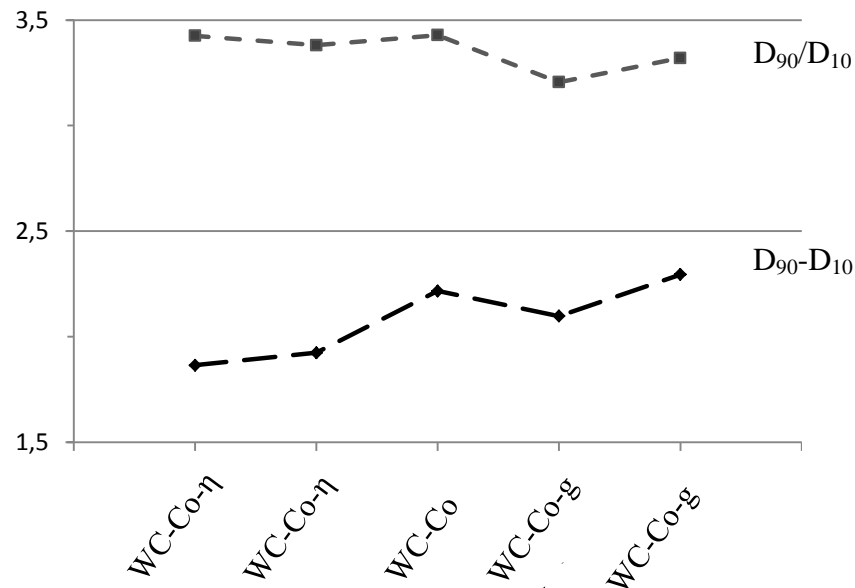


**Figure 13: Quantification of the variations of grain size distributions width with carbon content (samples sintered 1h at 1410°C), from Borg et al. measurements [27]. The authors considered the evolution of  $D_{90}-D_{10}$  but the evolution of  $D_{90}/D_{10}$  is more relevant to characterize abnormal growth.**

For their part, Gu et al. [28] studied the effect of carbon content on microstructure of a WC-Co alloy containing 20 vol% of cobalt, carbon varying from 4.45 wt% to 5.25 wt%. They observed a larger mean grain size when carbon content increases (see Table 5 and Figure 14). As proposed by Bock [29], they retain the earlier formation of the eutectic liquid due to high carbon content in the binder to explain this difference.

**Table 5 Evolution of the mean grain size with C content, measured by linear intercept method on SEM images [28].**

Composition of WC–20Co with various carbon contents.

Alloy	C (wt.%)	Phase composition after sintering	WC mean grains size ( $\mu\text{m}$ )
1	4.45	WC + Co + $\text{Co}_3\text{W}_3\text{C}$ ( $\eta$ phase)	2.5
2	4.68	WC + Co	2.6
3	4.81	WC + Co	2.8
4	5.01	WC + Co	3.0
5	5.25	WC + Co + graphite	3.1

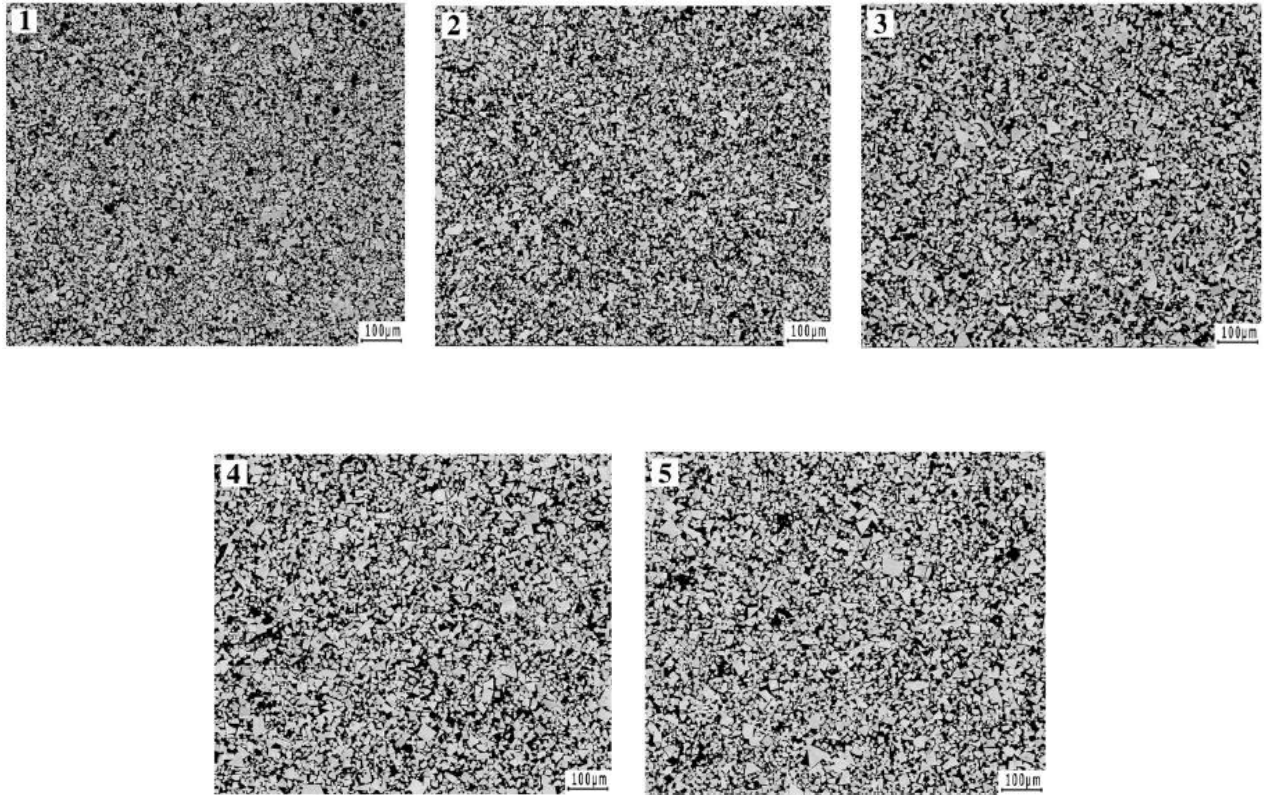


**Figure 14: Microstructures of the alloys with different C contents (increasing from 1 to 5), sintered 1h at 1450 °C. [28]**

### I.B.3 Influence of Cobalt content

The influence of cobalt content on grain growth is subject to discussion and results found in literature can be contradictory. Thus, in their study of grain growth during liquid phase sintering Shin and Matsubara [13] measured the influence of binder quantity on the growth rate constant, in the [2-60 vol%] range : they observed an influence, with a peak at a binder content around 30-40 vol% (see Figure 15). At the opposite, Coster et al. have not measured any influence of cobalt content on grain growth [14].

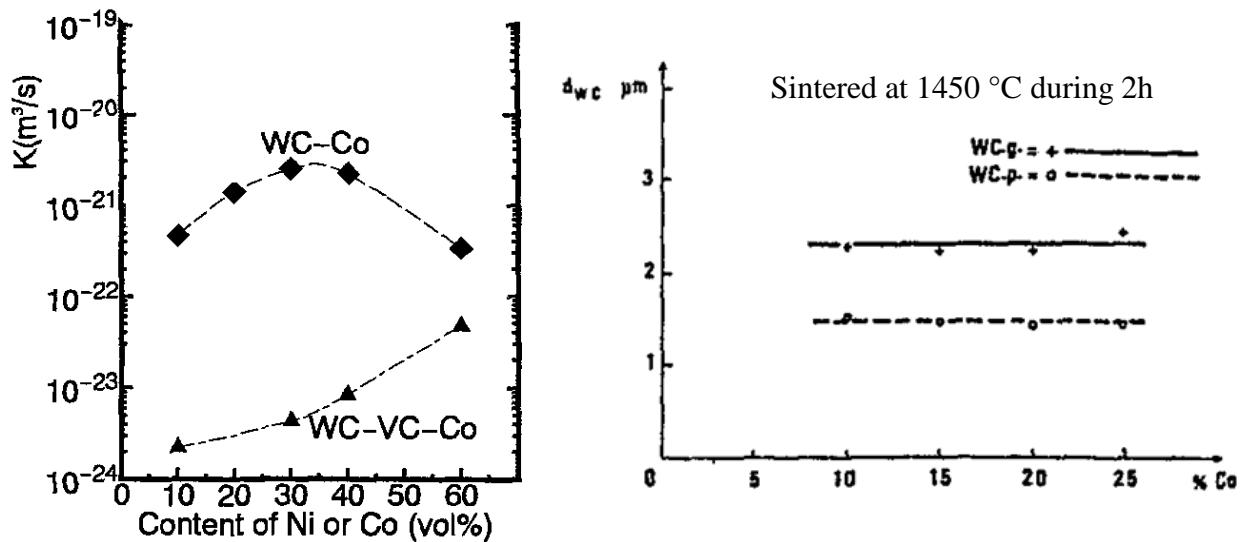
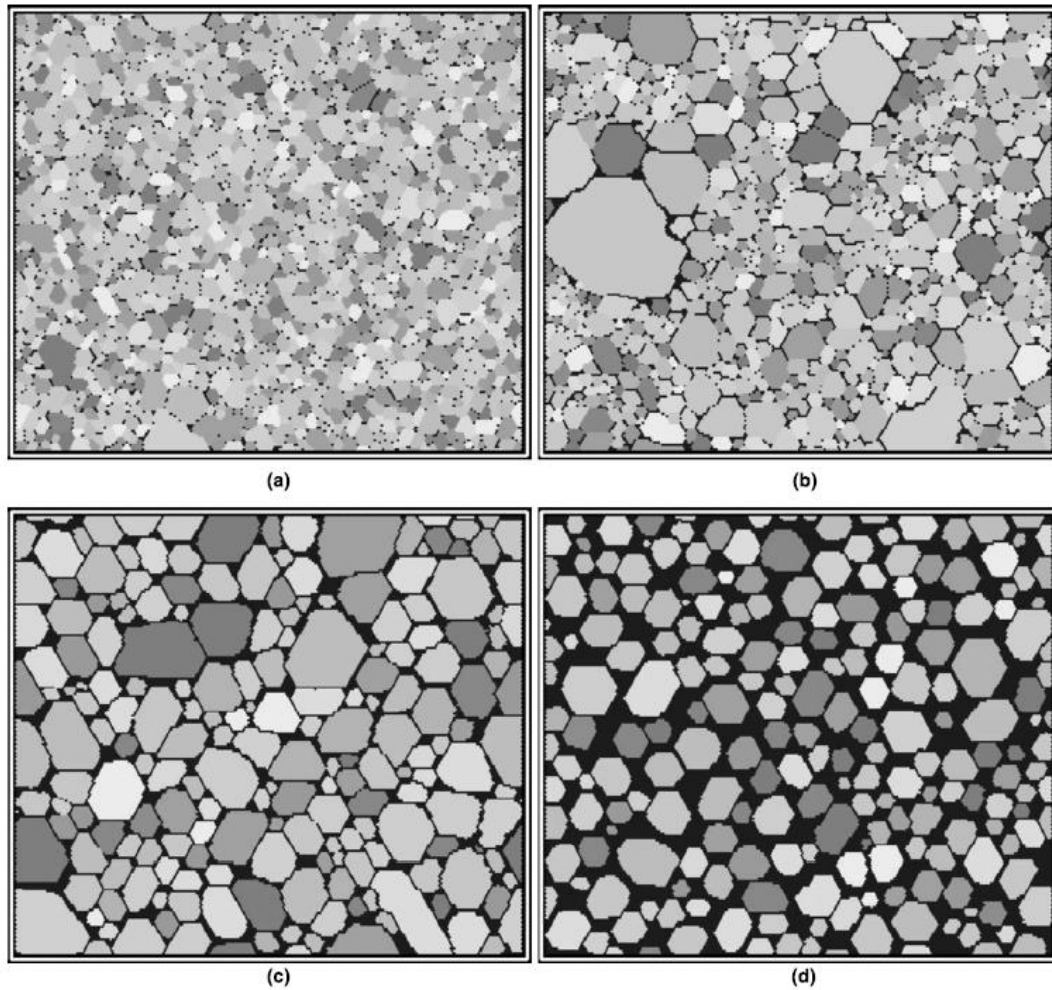


Figure 15: a) Experimental growth rate constant (evaluated from linear intercept) of various carbide cermets by Shin and Matsubara [13]. It passes by a maximum at around 30 vol% of Co. b) Evolution of the mean 3D diameter of WC grains with cobalt content, for two sizes of initial powder [14]: no effect of binder content is seen.

As already discussed grain boundaries could play an important role in grain growth mechanisms. Using Monte Carlo simulation techniques, Kishino et al. [30] have then established a 2D model for the evolution of the microstructure, assuming two kinds of mechanisms for grain growth: mass transfer through the grain boundary on one hand, and dissolution, mass transfer through the liquid phase and precipitation on the second hand. The results show the importance of liquid phase distribution. In microstructures presenting a mix of wetted and non-wetted boundaries, grain and phase boundary migration is non-uniform. In fact, wetted phase boundaries grow by solution/precipitation mechanism, but in the non-wetted boundary case, mass transfer across the

boundary is the limiting process. This microstructure would then evolve in a discontinuous distribution, giving an abnormal character to grain growth. They also remark the sensitivity of their simulations to the cobalt content (see Figure 16): the results would indicate that the grain growth at lower liquid phase content occurs through both mechanisms, whereas solid/liquid mass transfer or diffusion through the liquid plays a major role in grain growth at higher liquid phase content. Their microstructure model is probably too simplistic since contiguity reaches zero above 20 vol% of binder in their study, which is not true (see Figure 31). Nevertheless, this work qualitatively illustrates the effect of the liquid fraction and of heterogeneity in the liquid dispersion on grain growth.



**Figure 16: Simulated microstructures at 1000 Monte Carlo steps, as a function of liquid fraction: (a) 5 vol%, (b) 10 vol%, (c) 20 vol% and (d) 40 vol% [30].**

### I.B.4 Influence of initial grain size distribution

Another parameter to consider is the initial distribution of grain sizes. Observations by Borgh et al. [25] show that powder with an initial smaller average particle size may grow quicker and up to a larger average grain size than a powder with an initial larger average grain size (Figure 17 a-d). Mannesson et al. [31] investigate the grain growth behaviour in powders with a small amount of a very coarse grain powder added to a fine powder. The powder with coarse grains shows a faster growth (fast increase of the average grain size). In the powder containing fewer coarse grains (1%), these grains grow abnormally and up to larger sizes. In the powder containing a higher amount of coarse grains, the driving force is reduced below the critical value for 2D nucleation when the fine grains are consumed (see Fig. 8) and therefore the abnormal grain growth stops. Therefore powders with a bimodal initial distribution may become lognormal after long sintering times. On the contrary, when only a few coarse grains are present in the initial powder, those grains will act as seeds for abnormal grain growth. In their Monte Carlo simulation study Kishino et al. [30] also observed this discontinuous grain growth after having implanted a coarse grain in the system (see Figure 18): this grain acted as a seed for abnormal grain growth.

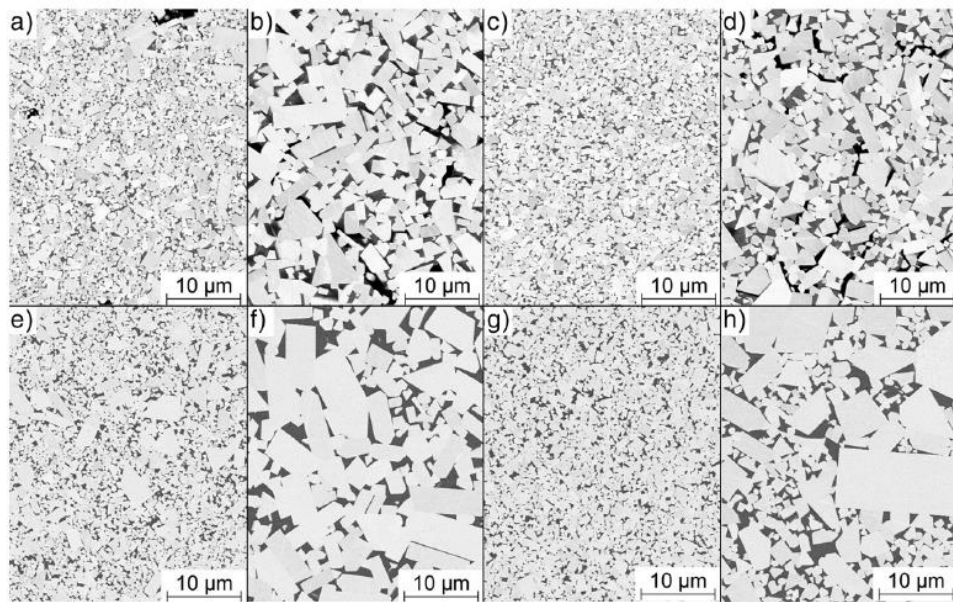
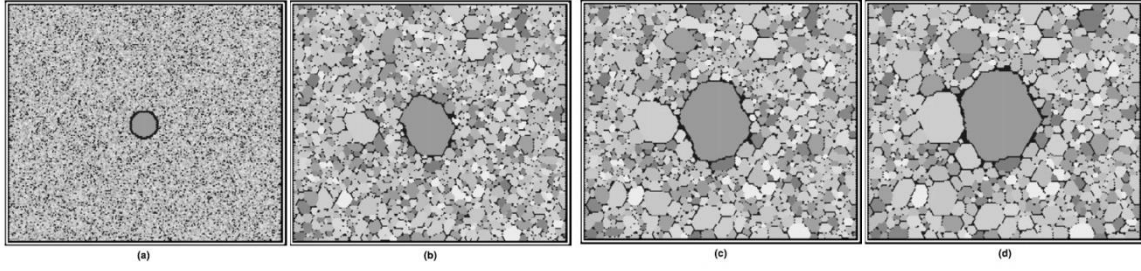
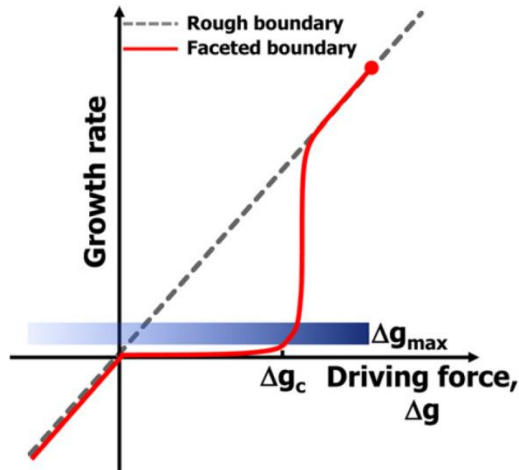


Figure 17: SEM micrographs showing microstructures with light WC grains in a darker binder phase. A  $0.25\ \mu\text{m}$  WC-Co-C<sub>g</sub> alloy after sintering time of a) 0.25 h and b) 8 h. A  $0.9\ \mu\text{m}$  WC-Co-C<sub>g</sub> alloy after sintering for c) 0.25h and d) 8h. A  $0.25\ \mu\text{m}$  WC two-phase alloy after sintering time of e) 0.25 h and f) 8 h. A  $0.9\ \mu\text{m}$  WC three-phase alloy after sintering for g) 0.25h and h) 8h. [25].



**Figure 18: Simulated microstructures with an implanted coarse grain as a function of Monte Carlo steps: (a) 0, (b) 200, (c) 500, (d) 1000 [30].**

Kang et al. also discussed the influence of faceted particles size distribution in the powder on abnormal grain growth [32]. According to them, abnormal grain growth requires the population to present a small fraction of large grains with a growth driving force  $\Delta g$  such as  $\Delta g_c < \Delta g < \Delta g_{\max}$  (where  $\Delta g_c$  is the critical driving force for a grain to grow, and  $\Delta g_{\max}$  the maximum driving force in the system). This condition also requires the presence of a significant fraction of smaller grains to insure  $\Delta g_c < \Delta g_{\max}$ . To summarize, if a particles population presents a significant fraction of grains too small to grow and a small fraction of grains large enough to grow, the growth is expected to be abnormal (Figure 19). If the population presents a main fraction of grains large enough to grow, the growth is normal.



**Figure 19: Graphic showing the mixed control of boundary migration and grain growth.  $\Delta g_{\max}$  is the maximum driving force for the largest grain.  $\Delta g_c$  is the critical driving force for appreciable migration of a faceted boundary, which is assumed to be constant.**

##### *Synthesis*

Several mechanisms have been proposed in the literature to explain grain growth in cemented carbides. Conventional Ostwald ripening by solution-precipitation is not sufficient to explain grain growth globally. Some authors proposed that precipitation would not be as rapid as assumed in LSW theory, but instead limited by a 2D-nucleation or defect-assisted process. Coalescence may also occur at the very beginning of sintering. The predominance of a mechanism over others would be depending on temperature. Influence of cobalt content is not clear. The high carbon activity in the binder has been shown to favor faster grain growth. Concerning abnormal grain growth, it is not clear if C/W ratio is expected to have influence. At the opposite, it is expected that the distribution of grain sizes influences it.





## I.C Grain boundary in WC-Co system

Because they are defaults in the crystalline arrangement, grain boundaries play a particular role in diffusion mechanisms, and influence electric/thermic conductivity and mechanical properties of a material. Thus, identifying grain boundary character and distribution in a material is of major interest in the perspective of understanding its properties.

### I.C.1 Grain boundary denomination and characterization

Transition from a grain lattice to another can be described with a rotation: applied to the lattice of the first grain, this rotation would bring lattice nodes of both crystals into coincidence. A rotation is described with the couple angle/ [rotation axis]. Owing to the symmetry of the crystal, several rotations can describe the same misorientation (12 in the case of hexagonal structure). The convention retains the rotation with the lowest rotation angle to characterize a grain boundary. In the following, a grain boundary may be referred to as a couple angle/[axis]. The particular cases when rotation axis is perpendicular or parallel to the boundary plane are referred to as twist or tilt configurations respectively (Figure 20). The last important parameter allowing to fully characterize grain boundaries is their habit planes, *i.e.* atomic planes of the two grains involved in the boundary.

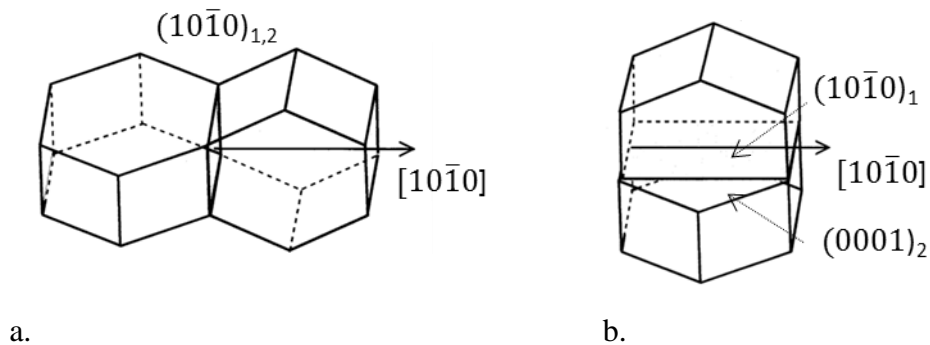


Figure 20: Illustration of  $90^\circ/[10\bar{1}0] \Sigma 2$  boundaries, twist (a) or tilt (b) characters [33].

### I.C.2 Technics for grain boundary study

Two methods are used for observation and identification of grain boundaries. The first one is based on observation of the grains by Transmission Electron Microscope: for some favorable situations it is possible to obtain the diffraction pattern of electrons that crossed through the material, and then determine the lattice orientation of grains involved in the boundary. Because of the sample preparation time and the small quantity of grains observable in one TEM sample, this is not a statistically representative method. The second method rose with the improvement of Electron BackScattered Diffraction equipment. This method, based on the interpretation of backscattered electron patterns, makes possible the mapping of grain orientation on larger areas and the automation of grain boundary identification. Figure 21 shows examples of observations made with both technics.

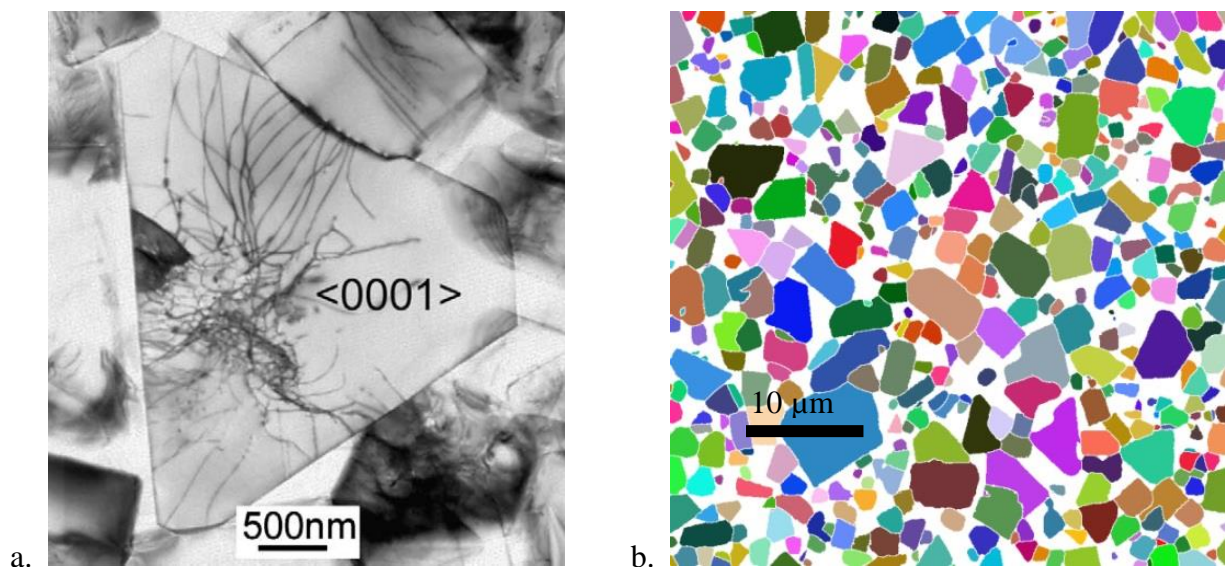
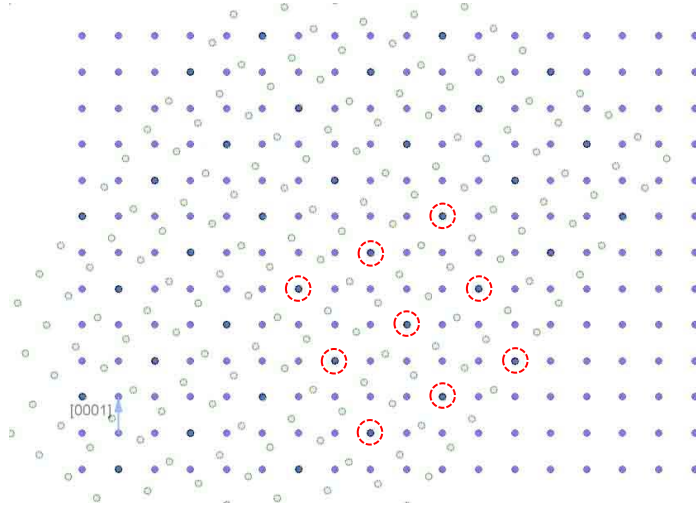


Figure 21: (a) Grain boundary observed with TEM technique. (b) Orientation mapping with EBSD technique (grains are colored according to their orientation).

### I.C.3 CSL approach for description of grain boundaries

For some specific misorientations, the interpenetrated lattices of both crystals exhibit common lattice nodes (Figure 22). Those coincidence nodes form the Coincidence Sites Lattice (CSL).



**Figure 22: Example of CSL configuration for a hexagonal crystal ( $c/a = 1$ ): a rotation of  $53.13^\circ$  around  $[10\bar{1}0]$  brings a fraction of node of both lattices into coincidence.**

This concept was first introduced by Bollmann [34]. From a physical point of view, coincidence sites can be seen as the best matching (or less strained) regions in a grain boundary. CSL configurations are identified with a coincidence index  $\Sigma$ , defined as the inverse of the coincidence sites fraction. Lower  $\Sigma$  values are often associated with stable and energetically favorable grain boundaries, the transition between adjacent crystals being expected to be more coherent. For hexagonal structures as WC, exact CSL configurations only exist for  $[0001]$  rotations. However, near CSLs configuration can also be defined, assuming the  $(c/a)^2$  ratio equal to a rational number [35]. The list of near CSLs for  $(c/a)^2=1$  was established by Hagege [36] and is presented in Table 6. It is interesting to note that a large number of coincidence configurations with low  $\Sigma$  values exist with the approximation  $(c/a)^2=1$ .

**Table 6:** List of the rotations leading to exact coincidence established for  $(c/a)^2 = 1$  in WC [36]. Rotations represented in the table are mentioned with the angle/[axis] pair with the smallest rotation angle and axis is expressed in the standard stereographic triangle. Only  $\Sigma \leq 19$  are presented.

$\Sigma$	angle	axis	$\Sigma$	angle	axis	$\Sigma$	angle	axis
<b>2</b>	90°	10 $\bar{1}$ 0	<b>10b</b>	69.51°	20 $\bar{2}$ 1	<b>16a</b>	57.91°	4 $\bar{2}$ 23
<b>4</b>	60°	2 $\bar{1}$ $\bar{1}$ 0	<b>11</b>	76.86°	8 $\bar{4}$ 43	<b>16b</b>	82.82°	3 $\bar{1}$ 20
<b>5</b>	53.13°	10 $\bar{1}$ 0	<b>13a</b>	27.80°	0001	<b>17a</b>	28.07°	10 $\bar{1}$ 0
<b>7a</b>	21.79°	0001	<b>13b</b>	32.20°	2 $\bar{1}$ $\bar{1}$ 0	<b>17b</b>	63.82°	40 $\bar{4}$ 3
<b>7b</b>	81.79°	2 $\bar{1}$ $\bar{1}$ 0	<b>13c</b>	67.38°	10 $\bar{1}$ 0	<b>19a</b>	13.17°	0001
<b>8</b>	46.57°	4 $\bar{2}$ 23	<b>14a</b>	41.41°	20 $\bar{2}$ 3	<b>19b</b>	46.83°	2 $\bar{1}$ $\bar{1}$ 0
<b>10a</b>	36.87°	10 $\bar{1}$ 0	<b>14b</b>	92.05°	10 $\bar{2}$ 83	<b>19c</b>	74.74°	5 $\bar{1}$ $\bar{4}$ 0

According to this table, grain boundaries in WC can be grouped in four main families:

- rotations around [10 $\bar{1}$ 0]:  $\Sigma$ 2, 5, 10a...
- rotations around [0001]:  $\Sigma$ 7a, 13a, 19a...
- rotations around [2 $\bar{1}$  $\bar{1}$ 0]:  $\Sigma$ 4, 7b, 10b...
- rotations around other axes.

The case of  $\Sigma = 2$  (the smallest value possible) is particularly interesting and does not appear in other systems. It can be described as a 90°/ [10 $\bar{1}$ 0] rotation.

$\Sigma$ 2 boundaries can be of two types: twist, so habit planes are (10 $\bar{1}$ 0) prismatic plane for the two grains, or tilt, in which case habit planes are the (0001) basal plane for one grain and the (2 $\bar{1}$  $\bar{1}$ 0) plane for the other one (Figure 20). In literature particular interest is shown to these interfaces which are thought to have low interfacial energy and high work of separation [37], as detailed later.

## **I.C.4 Grain boundary energy**

### **I.C.4.i Experimental results**

Grain boundaries regions are not energetically favorable because atomic arrangement is disrupted. The grain boundary energy represents the excess free energy per unit area due to the presence of the boundary, with reference to the perfect crystal. However grain boundary energy is rather difficult to estimate and few values are found in the literature. Warren calculated that grain boundaries in WC-Co would have an energy superior to 0,99J/m<sup>2</sup> [38]. This value was established combining contiguity, number of contacts and dihedral angle measurements on micrographs, made on a sample containing 50% of binder and sintered for 7h at a temperature of 1450°C. Therefore this value corresponds to a “mean” grain boundary in an equilibrium structure, where boundaries formed due to impingement are not taken into account. Considering also the preliminary assumptions for the calculation (spherical shape and uniform particle size) and the use of a carbide surface energy based on values for NbC and UC carbides, this result should be considered carefully.

### **I.C.4.ii DFT calculations**

If experimental determination of boundary energy is challenging, ab initio calculations are an alternative approach, with the limitation of being able to model the structure of the interface, thus to work on specific configurations. Studies by Christensen and Wahnström investigated the  $\Sigma 2$  boundaries, and established that, according to the work of separation values, tilt configuration is weaker than twist configuration, and even weaker than a random boundary with prismatic habit planes [39]. Especially they are expected to be less resistant to shear stress. For the  $\Sigma 2$  twist boundary, a mean energy value of the interface energy was evaluated to 1.9 J/m<sup>2</sup> (values in the range 0.03-7.41 J/m<sup>2</sup>) [37]. Recently published results by Johansson, Petism and Wahnström re-evaluate this value to 0.7 J/m<sup>2</sup> [40]. This is much lower than the grain boundary energies of more general boundaries calculated by the same authors, and found to lie between 2 and 3 J/m<sup>2</sup> [40].

**I.C.4.iii Infiltration and segregation in WC boundaries**

The main application of calculating phase and grain boundary energies for WC-Co alloys is to predict the tendency of the metal binder to infiltrate the boundary. The condition for the boundary to be infiltrated is:

$$\gamma_{WC/WC} - 2\gamma_{WC/Co} > 0 \quad (1.3)$$

According to Christensen and Wahnström DFT calculations of grain boundary and phase boundary energies, all pure grain boundaries (without segregants) but  $\Sigma 2$  twist boundaries should be infiltrated by cobalt, especially boundaries formed by random matching of prismatic planes [37]. In another publication [40] authors precise that substitution of cobalt in sub-monolayer proportion is favorable in most of grain boundaries excepted  $\Sigma 2$  twist. This segregation would even enhance the boundary cohesion and its resistance to further metal infiltration. These calculations confirm observations of segregation at carbide boundaries made by Henjered et al. [41]. Segregation of cobalt and dopants in  $\Sigma 2$  twist was also observed in  $Cr_3C_2$ -doped WC-Co with high resolution microscopy by Yamamoto et al.[42], who attributed this phenomena to the distortion of the lattice caused by the mismatch between a and c axis ( $c/a = 0.976$ ). For their part, Vicens et al. suggested that the amount of segregation would depend on the geometry of the grain boundary and the configuration of intergranular dislocations [33]. Finally, it seems to be well accepted that most of carbide boundaries in WC-Co present segregated cobalt in a sub-monolayer proportion ([41], [43], [44]) and that segregated cobalt atoms decrease the grain boundary energy and prevent infiltration by the liquid [39].

**I.C.5 The formation of WC grain boundaries in WC-Co**

Lay and Loubradou [45] noted the presence of dense clusters in submicron WC-Co powder doped with VC. Additionally, they observed grain boundaries in clusters (after sintering) by High Resolution TEM and showed they did not contain a cobalt film. As shown in a previous study [46], a thin layer of VC covers all surfaces of WC in contact with Co, and consequently traces of VC can be found in random WC/WC grain boundaries outside clusters. Authors concluded that the clusters observed in the sintered samples did not form during sintering, but are originally present in the powder and may be partially infiltrated by cobalt during sintering. Kumar et al took

interest in the origin of  $\Sigma 2$  boundaries in cemented carbides, and also came to the conclusion that they originated from the powder [47]. They suggested that they may form during the carburizing process, and because they are low energy boundaries, they may not break down during the milling process.

Additionally, WC grain undergo a large evolution of the shape during sintering, due to the preferential growth of some prismatic facets [48]. This change is likely accompanied with a partial destruction of  $\Sigma 2$  or  $\Sigma 4$  grain boundaries, and the separation of a fraction of clusters (Figure 23).

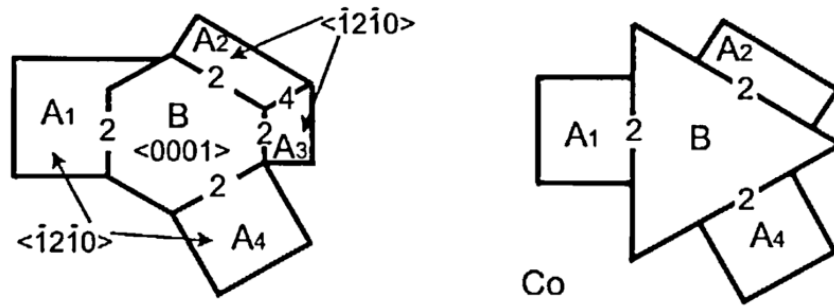


**Figure 23:** Evolution of the cluster from the powder (a) to the sintered state (b). Some of the grain boundaries are destroyed ([45]).

Kim and Kang also carried a study of the formation of grain boundaries and state that all grain boundaries present in liquid-phase sintered alloys originate from the grain boundaries present in the starting powder (Figure 24) [49]. However, one can oppose that if we assume the existence of a continuous carbide skeleton after sintering, some boundaries must obviously form during sintering and cannot only originate from grain boundaries in the powder.

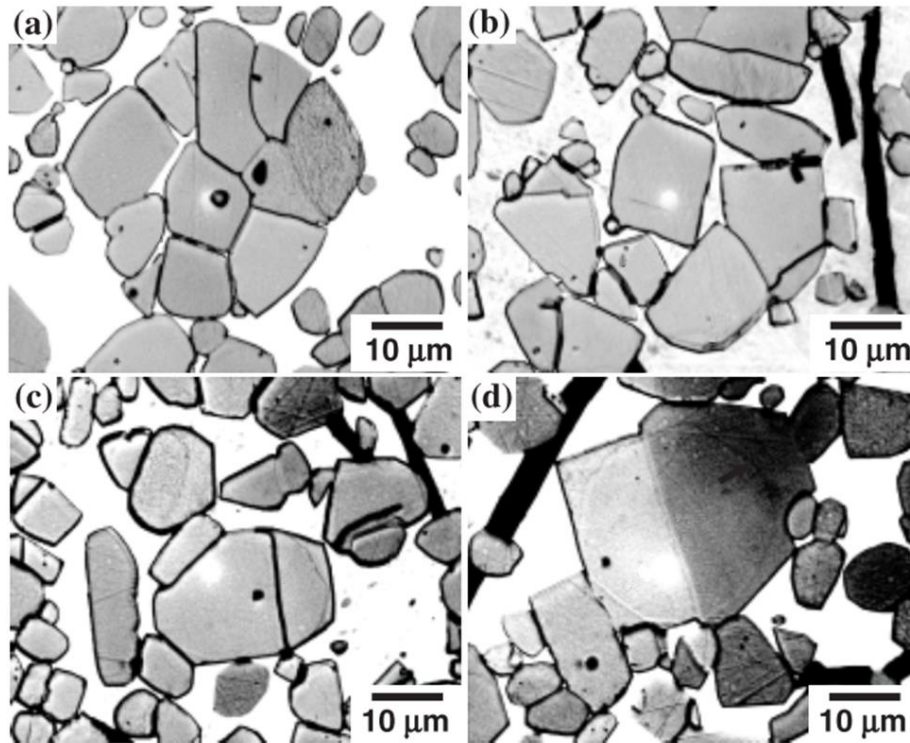


Figure 24: Microstructures of WC - 0.75wt% Mo<sub>2</sub>C - 25wt% Co - 0.2wt% C sample sintered at 1450°C for 1min (a), 1h (b), 3h (c) or 27h (d) [49]

### I.C.6 Distribution of WC grain boundary character in WC-Co

The study of grain boundary character distribution requires being able to observe and identify a large amount of grain boundaries. EBSD technique is then the most suitable method to collect data. The direct result is a distribution of misorientations between grains, in the form of a distribution of angle/rotation axis pairs. Because of stereology relationships, the grain boundary length fraction is an estimate of the surface area fraction in 3D.

Kim et al. [50] were among the first to apply misorientation imaging microscopy to the analysis of WC-Co and to publish results about grain boundary misorientation character distribution. They observed that three principal orientations were more represented (in a 10 vol% of cobalt WC-Co sample, sintered for 45 min at 1600°C):  $90^\circ/[10\bar{1}0]$  ( $\Sigma 2$ ), mainly twist, represents 11% of the total grain boundary surface,  $30^\circ/[0001]$  represents 3%, and  $90^\circ/[2\bar{1}\bar{1}0]$  in a smaller extent. The



profusion of those three particular boundary types is attributed to their resistance to infiltration by the liquid.

In a more recent study [51], the same authors measured grain boundary distribution on a set of samples with a cobalt content varying in the 12-31vol% range (grain size varying between 1.4 and 5.3  $\mu\text{m}$ ):  $90^\circ/[10\bar{1}0]$  ( $\Sigma 2$ ), mainly twist, represents 11-14% of the population,  $30^\circ/[0001]$  represents 2-3%, and  $90^\circ/[2\bar{1}\bar{1}0]$  represented a smaller fraction (Figure 25). Those results confirmed the previous measurements, but did not indicate any correlation of special boundary population with grain size or cobalt content. They suggested that the initial concentration of these boundaries is greater than the equilibrium value, and decrease in the early stage of sintering to rapidly reach a steady-state. Thus they suggested that special boundary population is largely determined by thermodynamics (relative energies of interfaces) and not kinetics processes. However, it is important to note that this work is based on the analysis of very different powders.

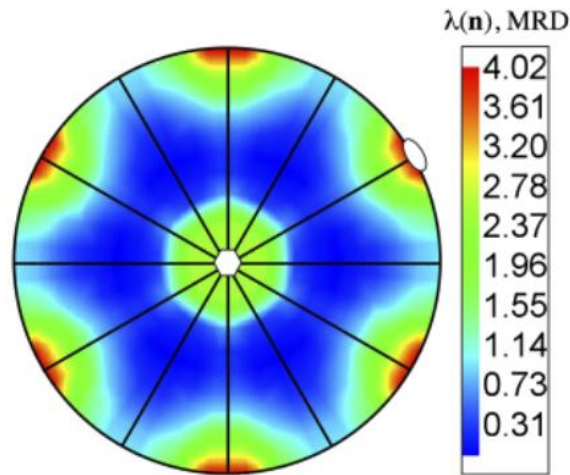
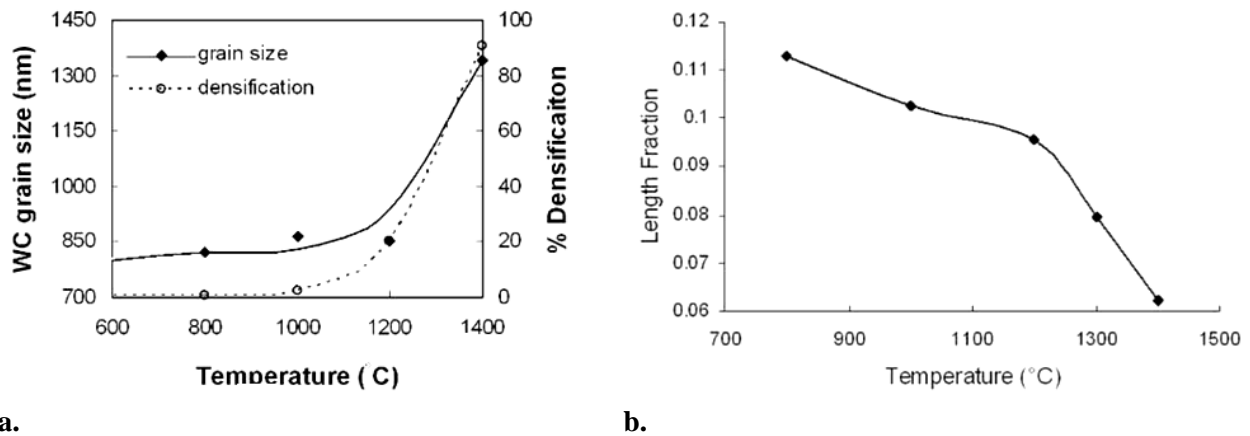


**Figure 25: Distribution of WC/WC grain boundary rotation axes in a 12 vol% of cobalt sample (mean grain size = 1.65  $\mu\text{m}$ ). Frequency of orientations is measured in Multiple of Random Distribution. Peaks are clearly visible for  $[10\bar{1}0]$  (oval) and  $[0001]$  (hexagon) rotation axis [51].**

Concerning the influence of cobalt content on the boundary population, contradictory results were recently published by Yuan [52] who measured a slight decrease in  $\Sigma 2$  population (around 10%) with increase of the cobalt content between 6 wt% and 10 wt%. In another work authors

proposed the values of 5.97% for  $90^\circ/[10\bar{1}0]$ , 1.88% for  $30^\circ/[0001]$  and 1.01% for  $90^\circ/[2\bar{1}\bar{1}0]$  (measurement in fraction of length, in a 6 wt% of cobalt sample) [53].

Kumar et al. [47] confirmed the existence of preferred grain boundary misorientations. They also showed a pronounced evolution of  $\Sigma 2$  boundary population during sintering. Their measurements show that  $\Sigma 2$  boundary length is high in the powder, and quickly decreases during sintering (Figure 26): authors concluded that  $\Sigma 2$  boundaries are eliminated in greater proportion than other boundaries. However, taking into account the formation of general grain boundaries during sintering, the length fraction of  $\Sigma 2$  boundaries is expected to decrease even if their amount does not change.



a. b.  
Figure 26: Evolution of grain size (a) and  $\Sigma 2$  length fraction (b) with sintering temperature (sintering time: 1 min, initial grain size: 1  $\mu\text{m}$ , 10 vol% of cobalt) [47].

Comparing this trend with grain size evolution during sintering (Figure 26a), authors concluded that grain growth is correlated to the elimination of  $\Sigma 2$  boundaries (Figure 27).

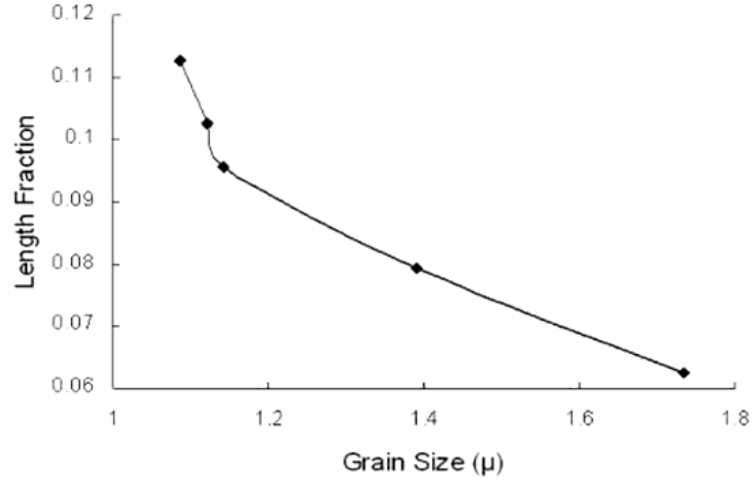


**Figure 27: Correlation between WC grain sizes and the length fraction of the 90°/[1010] boundaries during heat-up [47].**

The limitation of EBSD data set is that distribution of habit planes is not directly accessible. In this aim a method has been developed by Rohrer and Saylor ([50], [54]). In the observation plane, each line segment corresponds to a bounding plane. While the plane that generated the observed segment is not known, it is certain that it belongs to the set of planes whose normal  $n_{ijk}$  is perpendicular to the segment (in the hypothesis of faceted habit planes). Knowing the crystal orientation, all these possible planes can be expressed in the crystal reference frame  $n'_{ijk} = g.n_{ijk}$  (where  $g$  is the rotation matrix). Finally, in a stereographic projection all  $n'_{ijk}$  planes (planes whose normal is perpendicular to the segment, expressed in the crystal system) lie on a great circle perpendicular to the segment as illustrated in Figure 28.

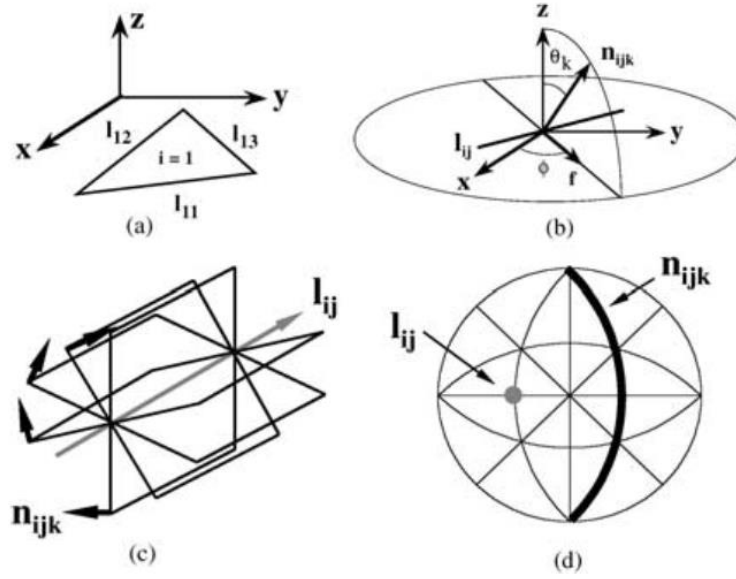


**Figure 28: Illustration of the stereological analysis of grain boundary or phase boundary planes developed by Saylor and Rohrer ([54], [50]).**

The principle of reconstruction relies on the fact that correct habit planes would be sampled with a higher probability compared to non-habit planes. Therefore, the great circles arising from the observation of line segment must intersect at the position of habit planes. The observations of line segments are used to calculate the probability  $p(\mathbf{n}')$  that a given length on the perimeter of a random section falls on a plane with the orientation  $\mathbf{n}'$ .  $p(\mathbf{n}')$  should exhibit a local maxima at the position of habit planes. Authors estimated the minimal number of grain boundary observations to be around  $5 \times 10^4$  for a good estimation of  $p(\mathbf{n}')$ .

Once the set of most probable habit planes has been identified, assumption is made that all habit planes belong to this set. The angle between each line segment and previously identified habit planes are computed. A predetermined tolerance angle is fixed between  $3^\circ$  and  $10^\circ$ . A line segment is associated to a habit plane if the angle is inferior to the tolerance. Finally, the method provides the total length per unit area representing, up to the  $4/\pi$  stereological factor, the total surface area per unit volume of remarkable habit planes. The method is used for grain boundaries or WC-Co interfaces.

Concerning grain boundary habit planes, EBSD data processing suggests that 60% (area fraction) of grain boundary planes are basal or prismatic for at least one grain (Figure 29 [50], [51]).

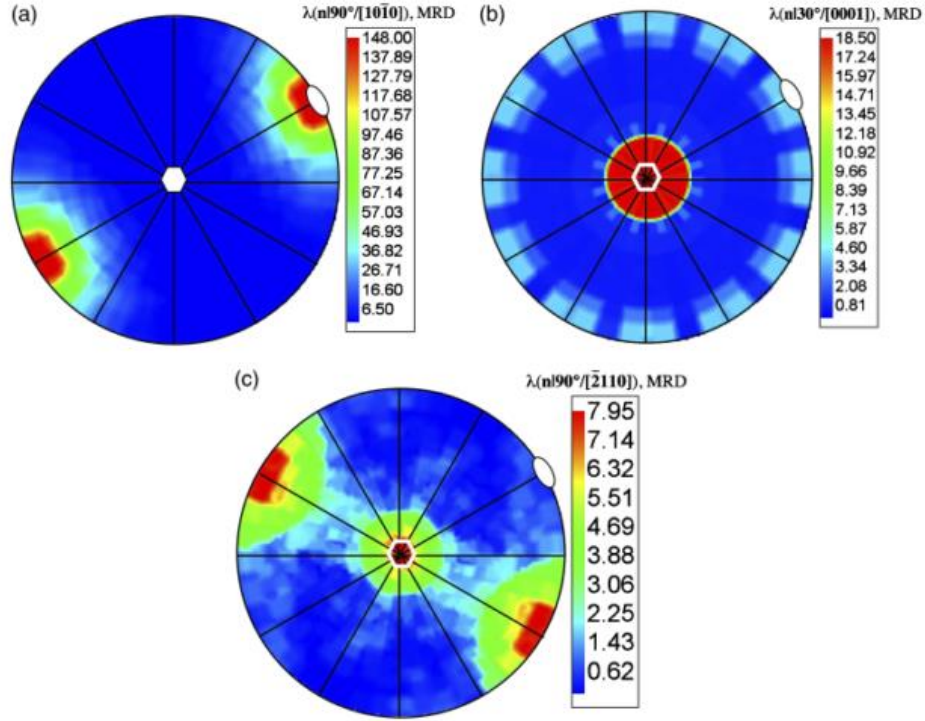


**Figure 29: Distributions of grain boundary planes in WC, for three types of grain boundary:  $90^\circ$  /  $[10\bar{1}0]$  (a),  $30^\circ$  /  $[0001]$  (b), and  $90^\circ$  /  $[-2110]$  (c). In the three cases prismatic and basal planes are the most occurring planes (represented with an oval and a hexagon respectively) [51].**

TEM observations qualitatively confirm this tendency [33]. Tilt  $[2\bar{1}\bar{1}0]$  boundaries are suitable for High Resolution TEM (it is possible to find an observation direction giving an atomic resolution in both crystals). Using this method Benjdir et al. observed that this type of boundary tends to facet so boundary habit planes get parallel to basal or prismatic planes (Figure 30) [55].

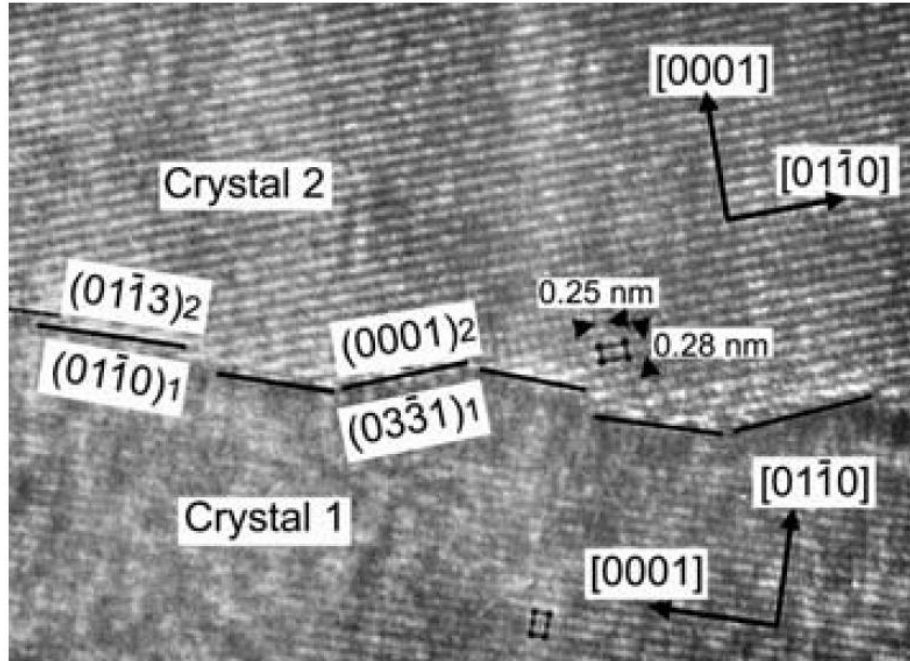


Figure 30: HRTEM micrograph of  $[2\bar{1}\bar{1}0]$  boundary, viewed along  $[2\bar{1}\bar{1}0]$  direction. Boundary plane presents facets corresponding to a basal or prismatic plane for one of the grains [55].

***Synthesis***

In conclusion, DFT calculations have shown that all pure WC/WC grain boundaries in WC-Co, excepted  $\Sigma 2$  twist, are expected to be infiltrated by liquid cobalt. This would explain the persistence of  $\Sigma 2$  boundaries coming from the powder in the sintered material, although part of them would be infiltrated in the very beginning of sintering.

Still, a large amount of grain boundaries are effectively observed experimentally. Cobalt segregation is expected to stabilize the grain boundaries and prevent their infiltration by the liquid.

Results on grain boundary distribution related the particular abundance of three type of special grain boundary:  $90^\circ/[10\bar{1}0]$  ( $\Sigma 2$ ), mainly twist,  $30^\circ/[0001]$  and  $90^\circ/[2\bar{1}\bar{1}0]$ .

The influence of cobalt content on these special boundaries is still an open question since contradictory results are reported. Eventually no results are found in the literature clarifying the influence of C/W ratio.





## I.D Contiguity

### I.D.1 Definition

Contiguity was first introduced by Gurland in 1958, who defined it as “the fraction of the total internal surface area that is shared by particles of the same phase” [56]. Thus it quantifies the degree of mutual contact between particles in a composite material. For a two-phase composite with constituents A and B, contiguity of phase A can be expressed as follow [56]:

$$C_A = \frac{S_{VAA}}{S_{Vtot}} = \frac{2S_{AA}}{2S_{AA}+S_{AB}} \quad (1.4)$$

where  $S_{VAA}$  is the internal surface area per unit volume of particles A in contact with particles A and  $S_{Vtot}$  is the total internal surface area per unit volume of particles A.  $S_{AA}$  and  $S_{AB}$  are classical interface areas between the corresponding phases. Factor 2 arises in the equation because A-A interfaces are shared by the two adjacent grains of A phase. According to this definition, contiguity varies between 0 (fully dispersed phase A) to 1 (fully agglomerated phase A).

### I.D.2 Equilibrium VS Geometry approach

Two approaches are usually presented to explain contiguity [57]: equilibrium approach ([15], [58]), in which minimizing the total surface energy of interfaces is considered as the driving force for contact development, and geometry approach ([59], [60]), which considers contacts as the result of geometrical impingement of carbide crystals. Equilibrium approach is convenient for sufficiently rounded crystals and high binder content. At the opposite, either an increase of carbide crystals faceting or a decrease of the binder content leads to take into account a geometry-driven constituent in contiguity value [57]. As an illustration, it is interesting to consider the evolution of VC-Co (well-rounded crystals) contiguity with cobalt content (Figure 31), where two domains can be distinguished. Contiguity drops rapidly from 1 to 0.17 when cobalt content increases from 0 to about 10 vol% but does not evolve much above this binder content. In this case, initial decrease of contiguity could be explained by a decrease of the

geometry-driven component, as far as being insignificant for binder content higher than 10 vol%. Contiguity would then only be driven by surface energy reducing, and reach an equilibrium value [57].

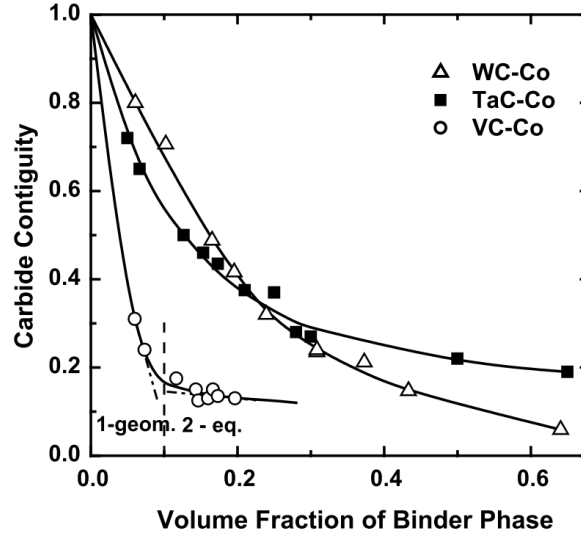


Figure 31: Effect of binder phase content on the contiguity of VC-Co, TaC-Co and WC-Co cemented carbides ([57]).

Yet, this transition between geometric and equilibrium contribution is not clear in well faceted WC-Co contiguity variation [57]. The high value of contiguity for high cobalt content could also be attributed to the particular stability of some special high coincidence boundaries [58].

### I.D.3 Influence of composition

It has been largely observed that contiguity decreases with binder content in cemented carbides ([13], [14], [58], [61]–[63], Figure 31). In 1978 Gurland and Lee established a stereological relationship between contiguity ( $C$ ), cobalt volume fraction ( $V_{Co}$ ), mean free path in WC grains ( $d$ ) and mean free path in the binder ( $\lambda$ ) [64]:

$$C = 1 - \frac{V_{Co}}{(1 - V_{Co}) \lambda / d} \quad (1.5)$$

Assuming homothetic microstructures whatever the grain size,  $\lambda/d$  and hence contiguity in sintered materials should only depend on the cobalt volume fraction  $V_{Co}$ . Using an empirical expression for  $\lambda/d = f(V_{Co})$ , Luyckx and Love [63] reduced Gurland and Lee equation (2) to a relation depending only on  $V_{Co}$ :

$$C \cong 1 - \frac{V_{Co}}{(1 - V_{Co})(5.975V_{Co}^2 - 0.691V_{Co} + 0.214)} \quad (1.6)$$

Roebuck and Almond [65] also determined, by fitting experimental data, a relationship between contiguity of WC phase in WC-Co and  $V_{Co}$  only:

$$C = \frac{D}{(1 - V_{Co})^n} \quad (1.7)$$

where parameters  $D$  and  $n$  were experimentally determined to be 0.2 and 0.45 respectively.

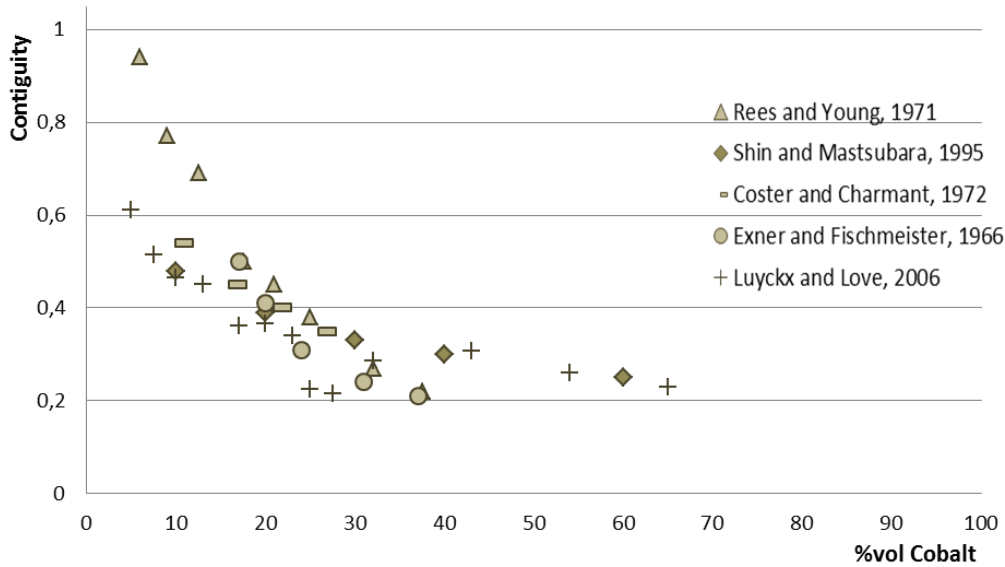


**Figure 32: Variation of WC contiguity with binder content according to several studies ([13], [14], [61]–[63]).**

Exner and Fischmeister [60] also suggested a relationship between  $C$  and  $V_{Co}$ , based on their contiguity values:

$$C = 1.03 e^{-5 V_{Co}} \quad (1.8)$$

More recently, Luycks and Love [63] fit their contiguity results with the following equation:

$$\left. \begin{aligned} C &\cong e^{-8.4V_{Co}} \text{ for } 0.05 \leq V_{Co} \leq 0.20 \\ C &\cong 0.25 \text{ for } 0.20 \leq V_{Co} \leq 0.64 \end{aligned} \right\} \quad (1.9)$$

According to Figure 32, a high dispersion of contiguity values for a fixed amount of binder content is observed in the studies cited above. It has been suspected that this variability would come from differences in processing conditions or changes in size distribution of WC grains ([63], [66]). In order to take into account this distribution effect Golovchan and Litoshenko [66] proposed a new relationship:

$$C \cong 1 - V_{Co}^{0.644} e^{0.391V} \quad \text{with } V = \frac{\sigma_{WC}}{d_{WC}} \quad (1.10)$$

where  $d_{WC}$  is the mean WC grain size and  $\sigma_{WC}$  the standard deviation.

Because sintering conditions (temperature, time) and grain size distribution are linked, it is expected from this expression that samples of same composition sintered in different conditions would present different values of contiguity.

#### **I.D.4 Modelling contiguity**

Based on a system made of an aggregate immersed in a liquid, Delannay developed a model expressing the dependence of the solid-liquid and solid-solid interfaces areas on the system parameters (dihedral angle, grain size, liquid fraction and particles coordination) during liquid phase sintering [67]. Each particle of the aggregate is considered enclosed into a Voronoï cell

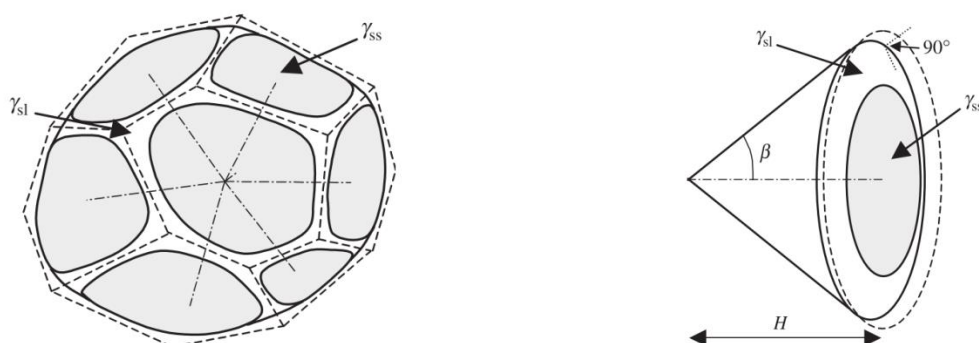
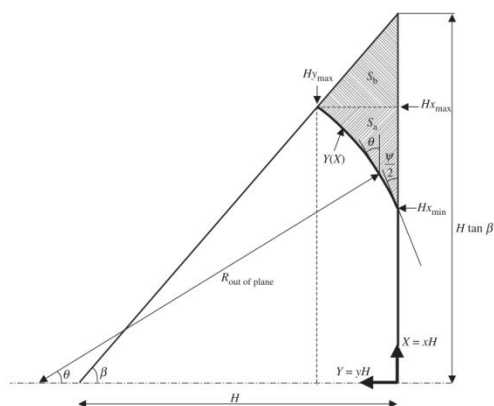


Figure 33: Each particle of the aggregate is considered enclosed into a Voronoï cell. Each cell is modelled as equivalent to  $n_c$  identical cones [67].



**Figure 34: Cone section along the revolution axis. The gray surface represents the liquid [67].**

This model can be used for the prediction of the influence of binder volume fraction and coordination number on contiguity (Figure 35).

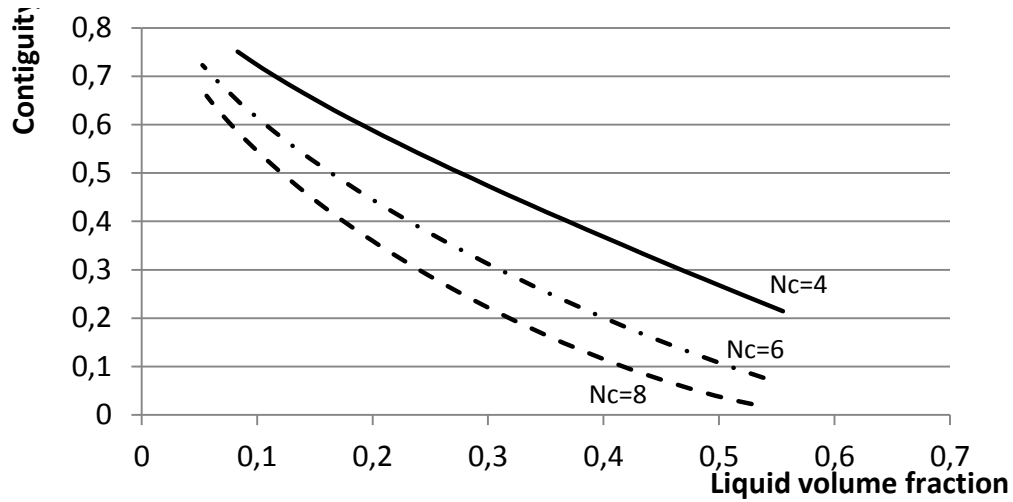


Figure 35: Modeling of the variation of contiguity with liquid volume fraction and coordination number (with a  $60^\circ$  dihedral angle), according Delannay's model [67].

Another model has been proposed by German, taking into account particle size distribution effects [68]. The model considers two contacting spherical grains with a partially penetrating liquid phase (Figure 36). Two angles  $\Phi_1$  and  $\Phi_2$ , which are related to the relative values of interface energies, are introduced to calculate the contiguity.

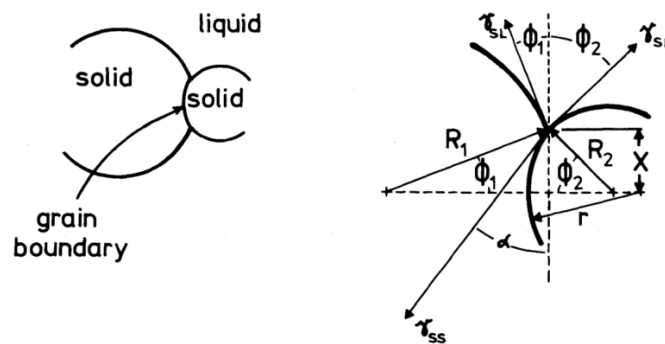


Figure 36: German model for contiguity calculation [68].

It confirmed the strong dependence of contiguity on volume fraction of binder and dihedral angle (Figure 37). It also indicates the need for grain shape accommodation at large volume fraction and low dihedral angle in order to reach a complete densification. At fixed binder content, large grain size distribution is expected to decrease contiguity, in agreement with Golovchan and Litoshenko expression (6).

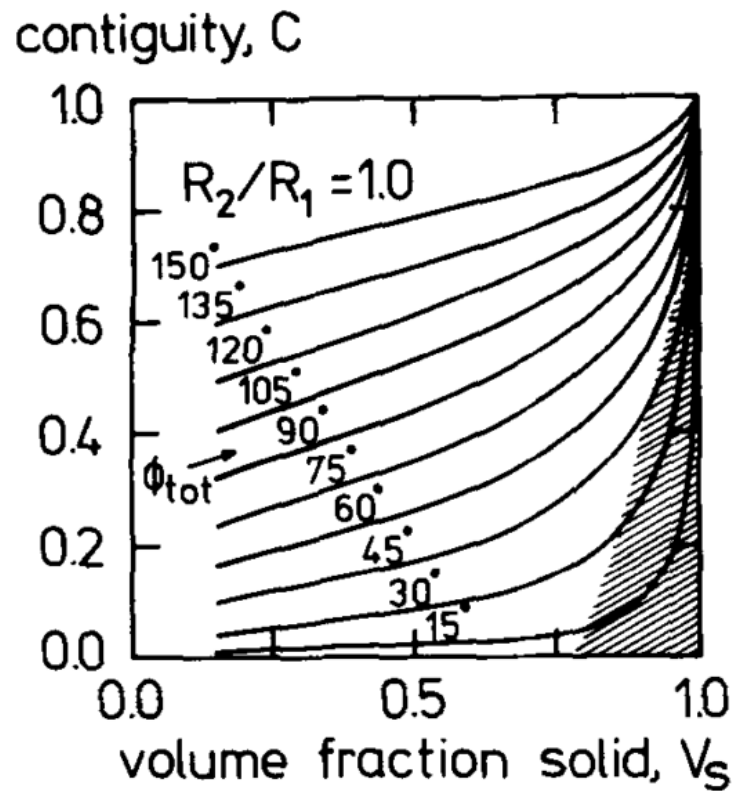


Figure 37: Evolution of contiguity with volume fraction of solid, for equal size spherical grains sintered in a liquid phase. Different dihedral angles are represented. The model is invalid in the shaded region because grain shape accommodation is necessary[68].

***Synthesis***

Contiguity in WC-Co sample is largely influenced by binder content. Values show a rapid decrease from 1 to  $\approx 0.3$  in the [0 – 30vol%] cobalt content range, and reach then a plateau around 0.3. This decrease has been fitted with either linear or exponential law with a good agreement. From experiments, contiguity is more or less insensitive to grain size and only depends on cobalt content. However, grain size distribution would have an effect, and at fixed binder content, a broader grain size distribution would decrease contiguity. Finally, contiguity has been shown to be very dependent on dihedral angle, *i.e.* on the relative values of grain boundary and phase boundary energies. An important dispersion of contiguity values is observed in the literature, and the variability of experimental conditions has been suspected. Yet, variations of carbon content have not been taken into account in the literature.



## I.E Grain shape

Hexagonal carbide crystals as WC sintered with cobalt or nickel binder develop a triangular prism shape formed by (0001) basal planes and (10 $\bar{1}$ 0) prismatic planes (Figure 38 a.). In both [0001] and [10 $\bar{1}$ 0] directions the structure of the crystal consists in stacking layers of carbon and tungsten. Then, the crystal is terminated by either carbon or tungsten at the WC/Co phase boundary. Contrary to a (0001) WC/Co phase boundary, the termination (carbon or tungsten) is not enough to specify the nature of a (10 $\bar{1}$ 0) WC/Co phase boundary, and two types of prismatic phase boundaries are differentiated. At a type I (type II) phase boundary the interplane distance between the first planes is 0.84 (1.7) Å, and the atoms in this layer have four (two) closest neighbors (Figure 38 b.).

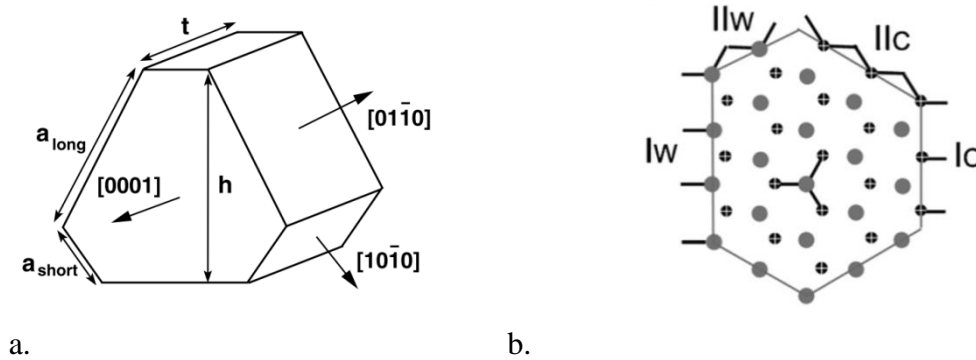


**Figure 38: a) Schematic representation of WC grain shape, with basal and prismatic planes. The shape can be characterized by truncation parameter ( $r = \sum a_{short} / \sum a_{long}$ ) and elongation parameter ( $k = t/h$ ) [69]. b) Projection of WC crystal atoms in the (0001) plane, with the illustration of type I or II [10 $\bar{1}$ 0] WC/Co phase boundaries, both carbon and tungsten terminated [70].**

A qualitative explanation of the carbide grain faceting is given by considering the interface anisotropy. Thus, an equilibrium shape can be determined by the relative energy of basal and prismatic planes. However, crystal shape is also dependent on growth mechanism during liquid phase sintering [71]. Impingement also has an influence, especially in low binder content alloys [27]. Thus, the actual shape of WC crystals in cemented carbide is a balance of the equilibrium shape modified by growth mechanisms and impingement.

If interface energy is of main importance in shape development, the only energy data available in literature are those calculated by Christensen et al ([69], [72]). For prismatic planes, their simulation work gave values in the range 0.7/2.9 J/m<sup>2</sup> (Figure 39 a.). It also showed that the most stable prismatic phase boundaries are W terminated, whatever the carbon content of the alloy, probably due to the formation of metal-metal bonding with cobalt atoms in the liquid. Moreover, type I facets have a lower energy so are expected to grow preferentially. An HRTEM observation of prismatic planes by Lay et al. confirmed the dominance of type I prismatic planes [73]. The energy of the basal facets was found in the same range as prismatic planes, between 0.7 and 2.3 J/m<sup>2</sup> (Figure 39 b.). The most stable basal phase boundary is tungsten terminated in W-rich alloys, but equivalently carbon or tungsten in C-rich alloys.

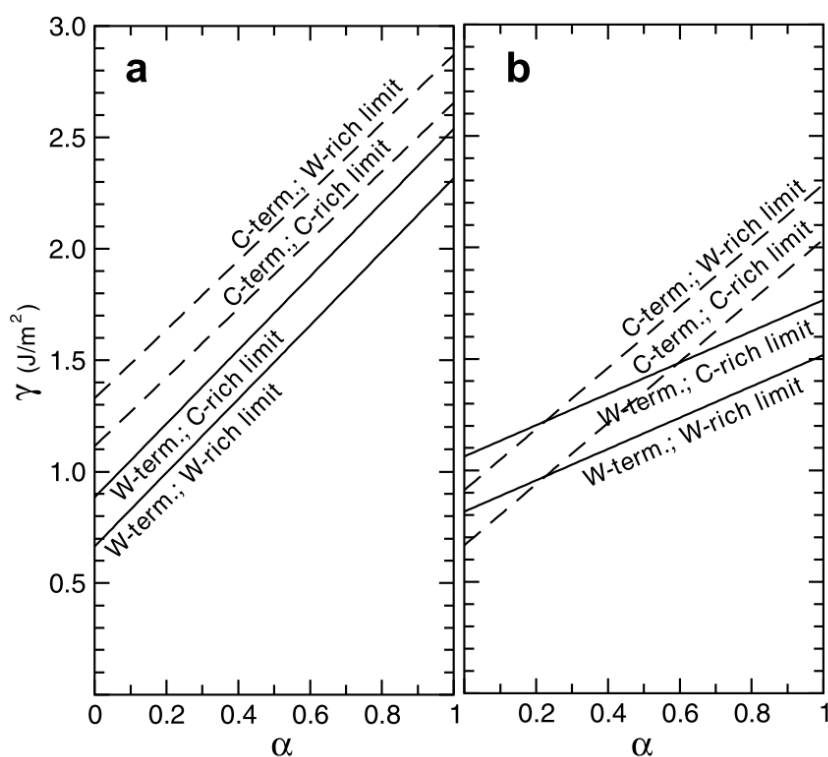
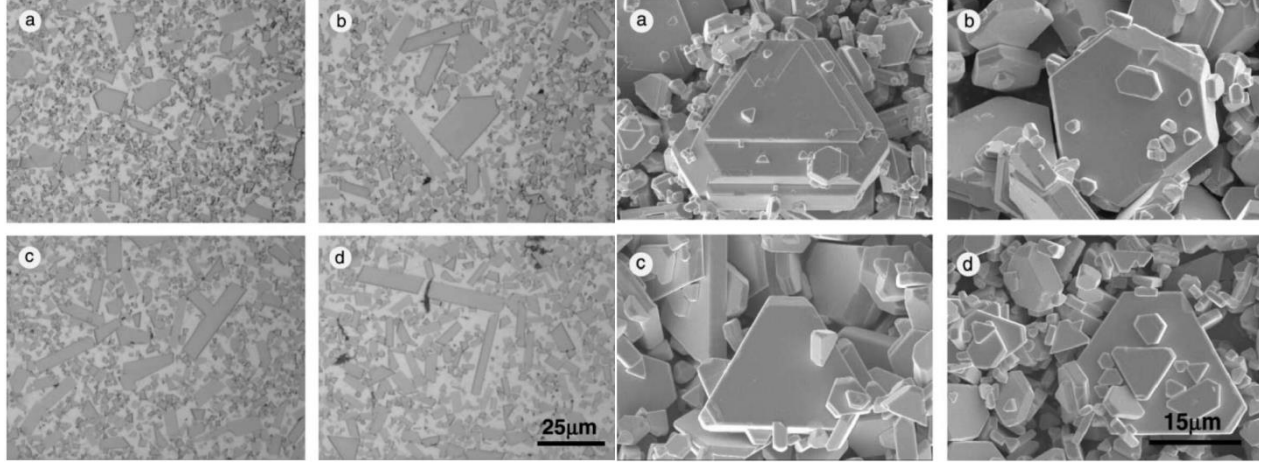


Figure 39: Evolution of interface energy as a function of  $\alpha$  (coherency of the interface: from coherent  $\alpha = 0$ , to incoherent  $\alpha = 1$ ), for prismatic (a) and basal (b) interface planes. For prismatic planes the mean value of type I and II is represented [69].

The carbon content in the binder has been shown to strongly influence WC crystals shape between three-phase C-rich and W-rich samples ([23], [27], [70], [74]). In carbon rich alloys large grains are less truncated and flatter than in W-rich alloys Figure 40.



**Figure 40:** SEM observation of the morphology of WC grains on cross sections (left) and extracted grains (right). WC-30%Co alloys with C content of 0.1% (a), 0.3% (b), 0.7% (c), and 1% (d) (sintered at 1450°C for 8h) [74].

In equilibrium conditions, the ratio  $\gamma_{PI}/\gamma_{PII}$  of interface energies of the prismatic facets determines the truncation  $r$ , whereas the ratio of energies  $\gamma_B/\gamma_{PI}$  of the basal and prismatic planes determines the elongation  $k$  (Figure 38 b.). It is possible to link those shape factors with energy ratio in the following equations:

$$r = \frac{(2\gamma_{PI}/\gamma_{PII}) - 1}{2 - (\gamma_{PI}/\gamma_{PII})} \quad (1.11)$$

$$k = \frac{2\gamma_B(2r + 1)}{3\gamma_{PI}(r + 1)} \quad (1.12)$$

The truncation and elongation values measured by Lay et al. [70] are in good agreement with the values deduced from the calculated interface energies.

It is to note that in three-phase W-rich alloys some large grains in contact with  $\eta$  phase present a shape similar to large grains in C-rich alloys. It is assumed to be due to the proximity of  $\eta$  phase that absorbs more W than C atoms from the binder, creating a locally C rich environment [70].

Most of the results gathered here were obtained thanks to 2D characterization of the microstructure (SEM or TEM). Recently Borgh et al. published direct 3D measurements, using focused ion beam serial sectioning coupled with EBSD imaging. Their results confirmed the shape change of WC grains comparing the three-phase compositions, with more planar surfaces and triangular shapes for the samples sintered at a higher C activity. They also highlight the significant effect of impingement on grain shape at low binder content.

It is also possible to obtain 3D information on grain shape from 2D EBSD analysis of habit planes, using the stereological method described in I.C.6. Kim and Rohrer deduced for this reconstruction method that the WC shape is an approximately equiaxed trigonal prism bound by three prismatic facets and two basal facets [50]. They also observed that the shape of the 20% largest grains and of the 20% smallest grains are indistinguishable from each other and from the whole set of data, concluding that the system is at the equilibrium or that growth and dissolution shapes are similar (samples sintered at 1400°C or 1600°C for 45min) [50].

### *Synthesis*

WC crystals in cemented carbide present a truncated triangular prism shape formed by (0001) and (10-10) planes. The C content in the binder significantly influences both elongation and truncation of the crystals. In three-phase C-rich samples, the grains are flatter and less truncated than in three-phase W-rich samples. Impingement also has a significant effect on the grain shape.

## Chapter II Experimental details

### II.A Sample preparation

#### II.A.1 Compositions

In order to cover a wide range of binder content, five compositions were chosen, varying from 10 to 50 vol% of binder.

The C/W ratio was calculated according to the phase diagram isothermal section at 1000°C, a temperature below which the composition is assumed not to change significantly due to slow diffusion. Two sets of samples were prepared, with decreasing C/W ratio:

- C-rich compositions, at the limit with WC-Co-graphite domain (2 phases).
- W-rich compositions, at the limit with WC-Co- $\eta$  phase domain (2 phases).

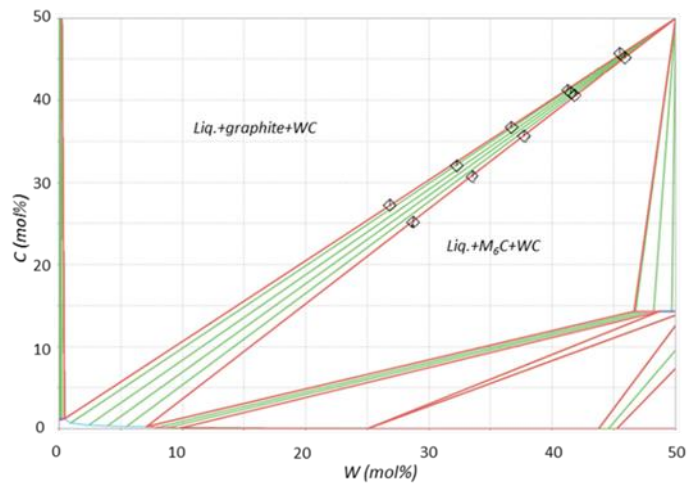
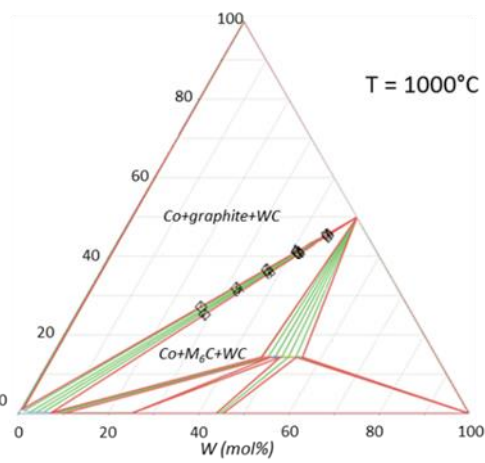
The samples were sintered at 1410°C with two holding times: 1h and 5h.

Figure 41 represents the different sets on isothermal sections at 1000°C and 1410°C (sintering temperature).

Table 7 and Table 8 summarize the compositions of the 22 samples prepared and analyzed for the study. The component volume fractions were obtained with chemical analysis and binder content was determined through image analysis on EBSD images.

A sample was prepared in order to observe the initial state of WC in the powder. WC powder was mixed with 40w% of copper powder. WC dissolution in copper is negligible and the low melting point of copper (around 1085°C) makes possible the sintering of a dense sample by liquid phase sintering without starting consolidation of WC skeleton [49].

a)



b)

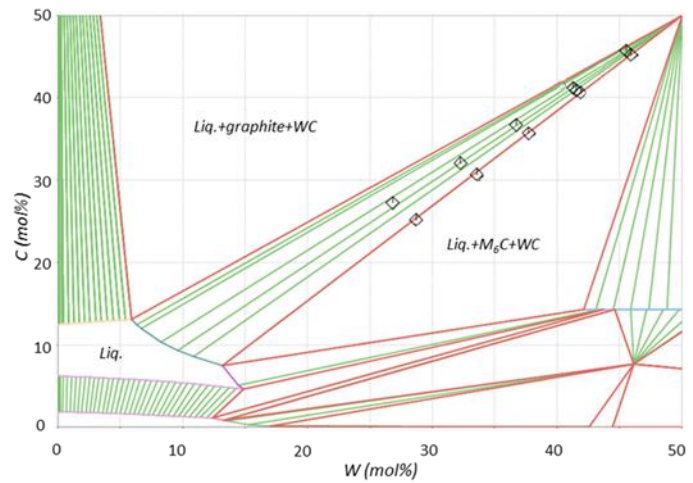
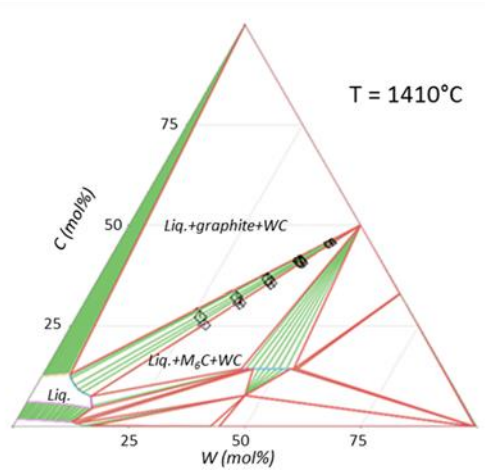


Figure 41: Compositions of the samples at equilibrium at  $1000^{\circ}\text{C}$  (a) and  $1410^{\circ}\text{C}$  (sintering temperature, b).

**Table 7: Composition of two-phase C-rich samples, theoretical and measured values.**

	binder (vol%)		Co (vol%)		W (vol%)		C (vol%)		C/W ratio	
	theo.	meas.	theo.	meas.	theo.	meas.	theo.	meas.	theo.	meas.
5h sintering	10	7.0	7.8	7.7	57.6	57.6	34.6	45.7	1.00	1.00
	15	11.0	12.8	11.6	54.2	55.4	32.9	33.1	1.00	1.00
	20	17.1	15.9	15.5	52.5	52.9	31.6	41.2	1.00	1.00
	30	28.0	24.5	23.9	47.1	47.7	28.4	36.6	1.01	0.99
	40	35.7	33.4	33.2	41.5	41.7	25.1	31.8	1.01	1.00
1h sintering	50	45.5	42.9	42.5	35.5	35.7	21.6	27.2	1.01	1.01
	10	7.4	7.8	7.8	57.6	57.7	34.6	45.5	1.00	1.00
	20	16.9	15.9	16.8	52.5	56.1	31.6	36.0	1.00	0.81
	30	24.0	24.5	24.5	47.1	47.3	28.4	36.3	1.01	0.99
	40	37.8	33.4	31.9	41.5	39.0	25.1	36.3	1.01	1.24
	50	44.1	42.9	42.9	35.5	35.6	21.6	27.0	1.01	1.01

**Table 8: Composition of two-phase W-rich samples, theoretical and measured values.**

	binder (vol%)		Co (vol%)		W (vol%)		C (vol%)		C/W ratio	
	theo.	meas.	theo.	meas.	theo.	meas.	theo.	meas.	theo.	meas.
5h sintering	10	8.7	7.8	7.8	57.9	57.9	34.3	34.2	0.99	0.98
	15	11.8	11.8	11.5	55.6	55.7	32.6	32.7	0.99	0.98
	20	19.0	15.9	15.5	53.2	53.5	30.9	31.0	0.97	0.97
	30	29.4	24.3	23.7	48.3	48.8	27.4	27.5	0.94	0.94
	40	42.5	33.1	33.2	43.2	43.1	23.7	23.7	0.91	0.91
1h sintering	50	45.0	42.4	42.3	37.8	37.8	19.8	19.9	0.87	0.88
	10	10.4	7.8	7.8	57.9	57.9	34.3	34.3	0.99	0.99
	20	21.8	15.9	15.8	53.2	53.1	30.9	31.0	0.97	0.97
	30	31.1	24.3	24.3	48.3	48.2	27.4	27.5	0.94	0.95
	40	42.8	33.1	33.0	43.2	43.0	23.7	23.9	0.91	0.93
	50	52.1	42.4	42.2	37.8	37.6	19.8	20.2	0.87	0.90



## II.A.2 Elaboration

### II.A.2.i WC-Co samples

Samples were all prepared in Sandvik facilities, with usual powder metallurgy methods. Samples dimensions are 10 x 10 x 5 mm (Figure 43).

WC and cobalt (plus graphite or tungsten to adapt C/W ratio) powders are mixed in proportions corresponding to the nominal composition and wet-milled. An organic binder is added to facilitate powder processing and help during the compaction process. Eventually samples are pressed by uniaxial compaction.

Sintering process can be split up in four steps as presented in Figure 42. First, during the so-called debinding step the organic binder used as pressing aid is removed at a relatively low temperature (350°C-450°C). Then the furnace temperature increases up to the sintering temperature. During this second stage, solid-state sintering occurs until the eutectic temperature is reached and liquid phase sintering starts. Most of the shrinkage takes place during solid-state sintering. In the third step (“sintering”), temperature is held constant in the range of 1300-1500°C usually (here at 1410°C). Finally the material is cooled down.

Samples are sintered under a mix of argon and carbon monoxide gas in order to avoid decarburation.

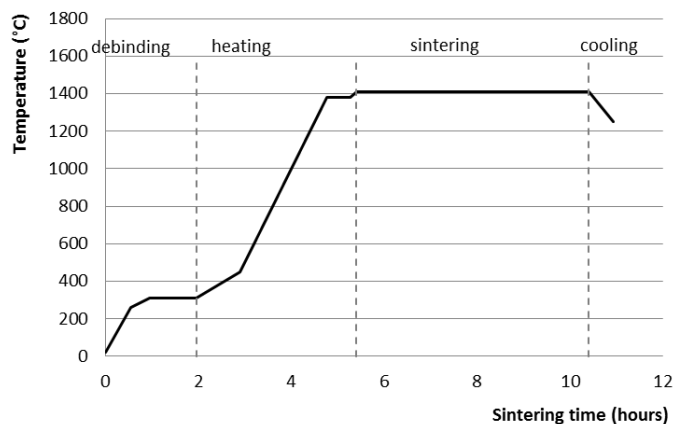


Figure 42: Sintering cycle for a 5h sintering.



Figure 43: A tray of samples after sintering.

### II.A.2.ii Powder sample

WC-Co powder (20 vol% cobalt) was picked up after the milling step. The organic binder was removed by dissolution in butanone (or methyl-ethyl-ketone) at 155°C, and cobalt dissolved with hydrochloric acid (HCl). A TURBULA® shaker-mixer was used to mix the resulting WC powder with copper powder for 1h.

A cylindrical sample ( $\phi$ : 8mm x h: 8mm) was pressed and sintered in a TGA device at 1120°C (the melting temperature of copper is around 1085°C) for 900s in reducing atmosphere (He- 4% H<sub>2</sub>).

### II.A.3 Cross-sections preparation

Samples were cut parallel to the compaction direction with diamond disk, a few millimetres from the edges in order to avoid influence of any surface effect on further measurements. Cross-sections were polished with diamond solution down to 1/10  $\mu\text{m}$ , followed with an ion polishing step (Gatan Precision Ion Polishing System (PIPS), for 2 hours, with a 2° incident angle and a 4 kV accelerating voltage). This last step aims at removing the strain-hardened layer created by mechanical polishing. This preparation method allows a good indexation of Kikuchi diffraction pattern in EBSD.

WC-Cu sample has only been polished mechanically.

## II.B EBSD method

Electron Back Scattered Diffraction is an electronic microscopy method for local analysis, based on the observation of backscattered electrons diffraction patterns. First implemented in the early 1970s, it developed dynamically in the 1990s, following improvements of the acquisition, digitalization and data treatment processes. Still, improvements of the EBSD method are strongly linked to the development of faster cameras. Thanks to its vast potential of use (crystalline orientation determination, texture characterization, phase identification, grain boundary identification...), and ever shorter acquisition time, EBSD is nowadays widely used in material science. Additional details about the EBSD technique can be found in Appendix 1.

### II.B.1 Experimental parameters

EBSD analyses were made with the equipment and parameters described below.

#### ***EBSD equipment:***

- SEM instrument: ZEISS Supra 55 VP
- EBSD detector: *HKL NordlysMax*
- software: Aztec (Channel 5 Suite)

#### ***Acquisition parameters***

- Step size: 40 nm
- Map dimensions: 30 x 30  $\mu\text{m}$  (750 x 750 pixels)
- Magnification: x 4000
- Acceleration voltage: 20 kV
- Aperture: 240  $\mu\text{m}$  (320  $\mu\text{m}$  when possible)
- Working distance: 8.5 mm
- Binning: 4x4
- Gain: 0

***Crystallographic references***

- WC: *Acta crystallographica* [ACCRA9], 1961, vol 14: 200-201 (59 reflexions)
- Co (cubic): *Z. Angew. Phys.* [ZAPHAX], 1967, vol 23: 245–249 (56 reflexions)
- Co (hexa.): *Fitz. Met. Mettalloved* [FMMTAK], 1968, vol 26: 140-143 (50 reflexions)

**II.B.2 Data cleaning and post processing**

Because of the poor quality of the signal some pixels of the map remain non-indexed. Experimentally, non-indexed points (NIPs) are more often observed at phase boundaries and in the cobalt phase.

Those points create irrelevant interfaces and influence automated measurements, so data cleaning is necessary. It is a very sensitive process. In the first hand NIPs disturb measurements, but on the other hand a too extensive extrapolation will modify the phase boundary position and often to the detriment of cobalt phase (NIPs that should have been indexed as cobalt are assimilated to tungsten carbide phase). Thus, it is important to keep in mind that only a part of NIPs can reasonably be extrapolated to preserve the original microstructure. Always in the aim of preventing extrapolation errors it is necessary to acquire maps with the best indexation rate as possible. In our case, obtaining a hit rate comprised in-between 90% and 95% is a realistic objective. As shown in Table 9, this empirical criterion is well respected for the studied samples

Data cleaning process consists in attributing a phase to a NIP considering its neighbours (Figure 44). A smooth cleaning step is performed thanks to specific operations of the Chanel 5 Suite.

Only sets of points containing more than 6px ( $0.01 \mu\text{m}^2$ ) are considered as grains, and smaller sets are deleted from the global data set. The minimum misorientation for grain boundary definition is set at  $2^\circ$ .

**Table 9: Mean hit rate (%) obtained for each sample.**

Binder (vol%)	C-rich		W-rich	
	1h	5h	1h	5h
10	92,8	94,1	93,3	94,6
20	90,5	94,1	92,6	94,3
30	92,3	92,6	94,2	94,9
40	87,1	93,5	94,5	95,7
50	83,0	89,2	95,9	94,8

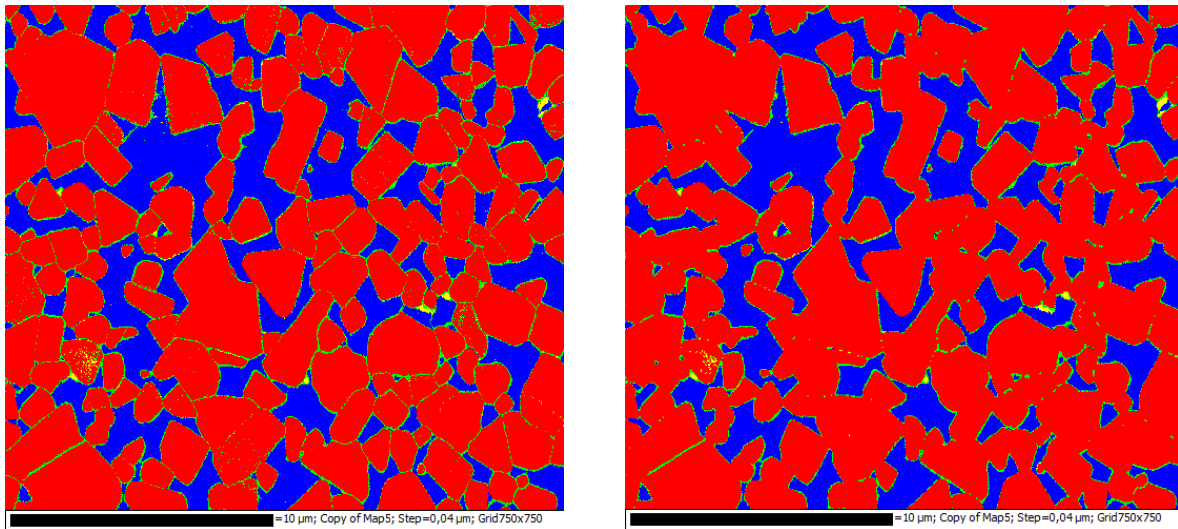


**Figure 44: EBSD map (phase representation: red WC, yellow hexagonal Co, blue cubic Co and green NIPs) of 30 vol% of binder, W-rich sample, before (left) and after (right) cleaning process. NIPs are concentrated at phase boundaries and in cobalt phase. After cleaning process WC grain are mostly free of NIPs.**

Figure 45 is an example of an EBSD map after cleaning. Grain boundaries are marked by a line of one pixel width. WC grains are coloured according to their crystal orientation, cobalt phase and WC/WC boundaries are represented in white.

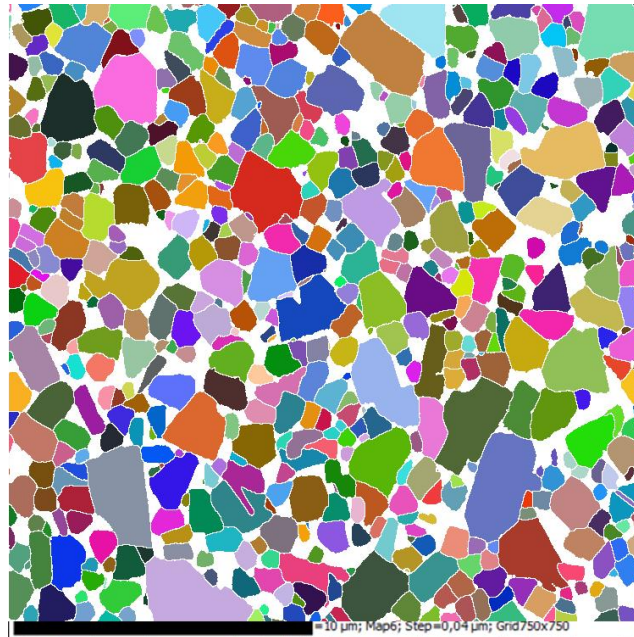


**Figure 45: Example of a map (20 vol% of binder, W-rich sample, sintered 5h at 1410°C) after cleaning.**

### II.B.3 Influence of resolution on measurements

EBSD acquisitions were realized with a 40 nm step size. This choice makes possible to realize representative maps of 30 µm side in a reasonable time considering the number of samples to analyze in the study. On the other hand it limits the precision of microstructure observation.

Resolution can influence the determination of phase boundary positions. In fact, because of the difference in WC and Co atomic numbers, the interaction volume is larger in cobalt. Thus, when analysing a point in cobalt at the phase boundary, this pixel may be mis-indexed as WC. For the same reason, small regions of binder enclosed between WC grains might be mis-indexed in the carbide phase (Figure 46).

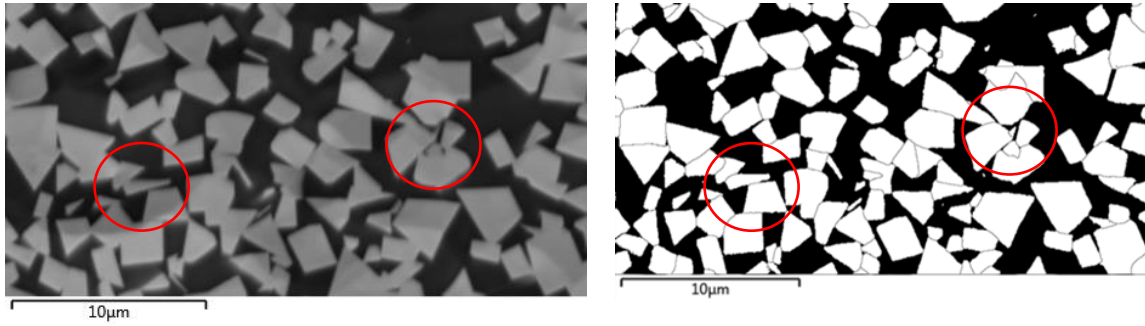


Figure 46: SEM and EBSD image of the same area, highlighting the difficulties to index small binder regions.

Therefore a discrepancy between the binder volume fraction measured on the EBSD maps and the theoretical value was detected in the samples. This discrepancy was compared to the specific phase boundary length  $L_A(WC/Co)$  (Figure 47).

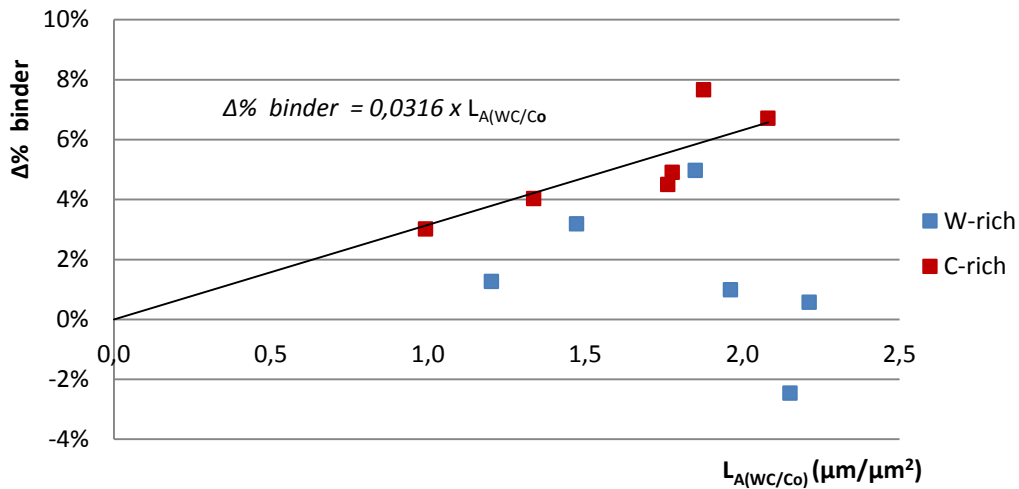


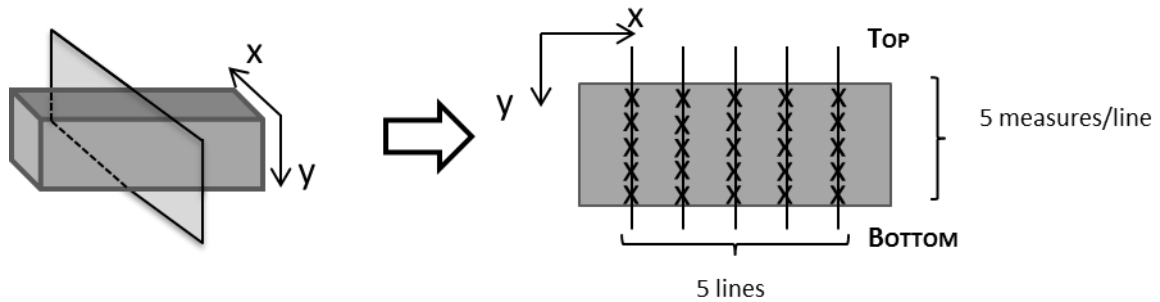
Figure 47: Evolution of the discrepancy between measured and theoretical values ( $\Delta\% \text{ binder}$ ) in relation with the phase boundary length.

Evolution of  $\Delta\% \text{ binder}$  and phase boundary length seems to be related, especially in carbon rich samples. The error  $\Delta A_A(Co)$  on the measured Co area fraction can then be related to a mis-indexed layer of average thickness  $\delta$ :

$$\Delta A_A(Co) = L_A(WC/Co) \delta \quad (2.1)$$

Linear regression gives a thickness  $\delta$  around 30 nm: it would mean that pixels that are less than 30 nm far from the phase boundary are indexed in the carbide phase rather than in the cobalt phase. The order of magnitude is coherent with the resolution.

In addition, heterogeneity of binder repartition in the sample was investigated since it is expected to participate in the discrepancy between measured and theoretical values. Binder content was measured on a cross section in 20 vol% and 40 vol % of binder, on W and C-rich samples. Inserts were cut by the middle and cross sections were mechanically polished with diamond suspension down to 1/10  $\mu\text{m}$ . 25 SEM images (60x40  $\mu\text{m}$ , Back Scattered electrons) were acquired (Figure 48) and binder area fraction was measured.



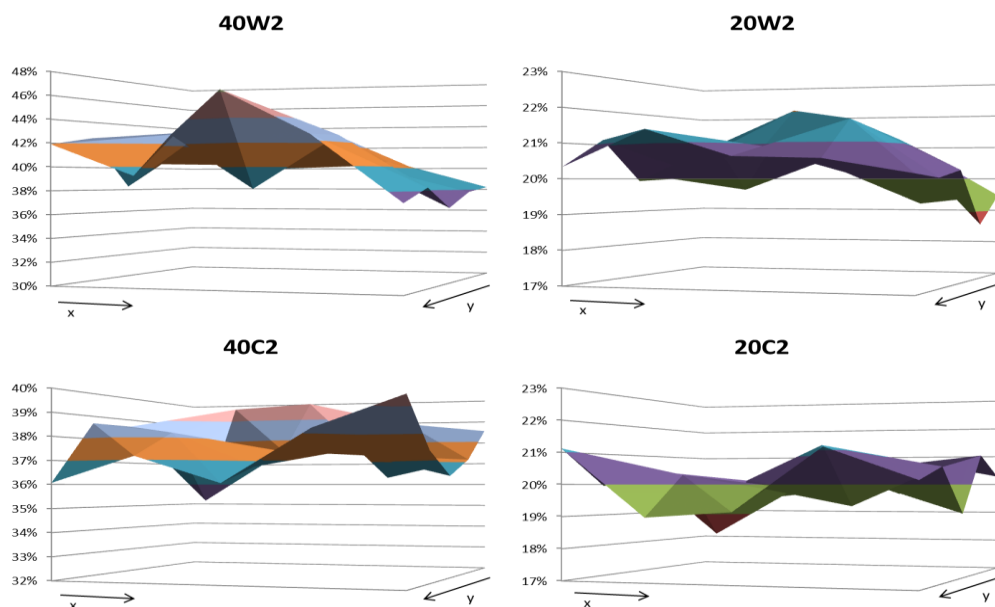
**Figure 48: Distribution of the 25 images on the cross section (y is the gravity direction).**

Figure 49 shows variations of cobalt content in a 2D cross section. Significant fluctuations of the binder content are observed but no systematic deviations with the vertical position y, which could indicate a sedimentation of WC grains. The measured standard deviation of the binder fraction falls in the range 1-2% on these 2400 $\mu\text{m}^2$  SEM images. Assuming that this corresponds to the natural dispersion of the Co-phase in our samples, it would induce a statistical error in the same range on our EBSD measurements on 4 x 30 x 30 = 3600  $\mu\text{m}^2$  image surface area.

In conclusion, EBSD technics can induce indexation errors that tend to favour indexation of carbide phase at the detriment of binder phase on a  $\approx 30\text{nm}$  layer thickness around carbide grains. This leads to a loss of precision in further measurements, which increases with the binder content. Hence, the binder fraction would be underestimated by roughly 10% of the nominal value. Also



this is expected to have an influence on the detection of the position of phase boundaries. In addition, natural fluctuations of the binder composition in our samples would be responsible of a 1-2% statistical error on the measured binder fraction.



**Figure 49: Variation of cobalt content along a 2D cross section. X and Y directions refer to direction specified on Figure 48.**

## II.C Focused Ion Beam microscopy

Focused Ion Beam (FIB) systems became commercially available in the late 1980s and are increasingly usual in the material science research field. The use of the FIB column as a precision sectioning tool, combined to a focused electron beam imaging, offered new possibilities for three-dimension imaging. A focused ion beam serial sectioning coupled with SEM imaging makes possible the characterization of substantial 3D volumes. It is an interesting alternative to tomography techniques, especially in the case of heavy materials as WC.

### II.C.1 Experimental parameters

Because the method is time consuming, only four samples were analyzed: 20/40 vol% of binder, W and C-rich, sintered for 5h. Acquisitions were made on the same system (*ZEISS Nvision 40* featured with a *Seyco SII* FIB column).

The volume of the boxes is 40x25x15  $\mu\text{m}$  approximately. It was chosen to set the step size at 40nm in order to have a resolution similar to EBSD acquisitions. FIB milling probe parameters were chosen in order to have an acceptable sectioning time (around 1min with 30kV and 1.5nA). Imaging was realized with backscattered electron mode at x2790 magnification, low tension (1.5kV) and tilt correction.

### II.C.2 Post-processing

Because of material re-deposition during the preparation of the volume and eventually non-homogeneous milling (especially at the deepest field of the slices), the first images of the acquisition are often not interpretable (Figure 50). Furthermore, because it is a long time process a slight drift of the image field can occur. Consequently a post-processing step is necessary to prepare measurement on the 3D volume. Post-processing was made with the open-source software Fiji (formerly ImageJ). Re-aligning of drifted images was made with the *StackReg* module. The volume was then cropped to keep the cleanest area and finally threshold. The final usable volume is approximately 40x20x10 $\mu\text{m}$ . An example is given with a small volume in Figure 51.

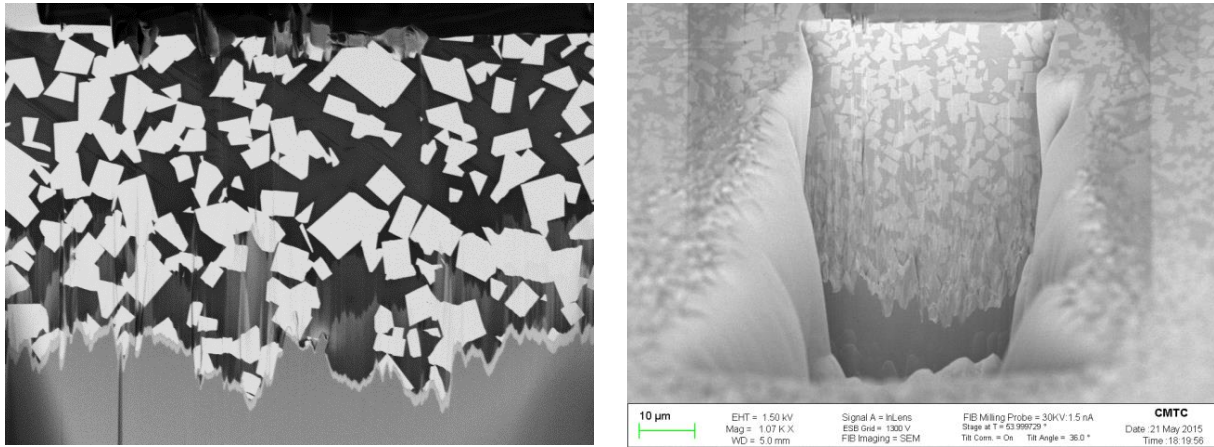


**Figure 50:** a) First slices of the acquisition are often polluted by material re-deposition (homogeneous gray layer) and are not usable (40vol% of cobalt C-rich sample). b) The difficulty to keep a focused beam with depth can cause non-homogeneous milling (vertical marks).

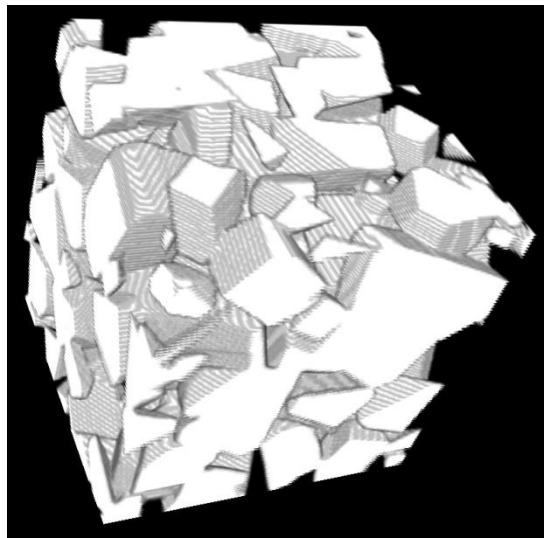


**Figure 51:** Illustration of 3D imaging on WC-Co with FIB serial sectioning (40vol% of cobalt C-rich sample, 8x8x8 $\mu\text{m}$ ).

## II.D Image Analysis and microstructure characterization

Considering the large number of samples to investigate and the numerous measurements to perform, it was necessary to develop measurement routines working on EBSD, SEM and FIB images. This part aims at presenting the measurement methods used in the study, in 2D and in 3D. The Appendix 2 gives additional details about image analysis principles and basic operations.

Dedicated image analysis measurements were made by using in-house routines developed for the study with software Aphelion™.

### II.D.1 Basics of stereological methods

Analysis of material requires accessing the 3D characteristic parameters of the microstructure. However, cross section observation methods are often more convenient and easier to implement than 3D imaging technics. Stereology provides practical techniques for extracting quantitative 3D information from measurements made on 2D planar sections.

Different stereological parameters can be considered to characterize the microstructure of a given set X, depending on the dimension of the sampling space ([75]–[77]):

- ❖  $R^3$ :
  - Volume fraction of the set ( $V_V$ )
  - Surface density, or surface area of the set per unit volume ( $S_V$ )
  - Integral mean curvature of the set per unit volume ( $M_V$ )
  - Number of connexity of the set per unit volume ( $N_V$ )
  
- ❖  $R^2$ :
  - Area fraction of the set ( $A_A$ )
  - Perimeter of the set per unit area ( $L_A$ )
  - Number of connexity of the set per unit area ( $N_A$ )
  
- ❖  $R^1$ :
  - Length fraction of the set ( $L_L$ )
  - Number of intercepts of the set per unit length ( $N_L$ )

❖  $R^0$  : - Fraction of points of the set ( $N_P$ )

As those parameters are attached to a space dimension they can only be measured in their proper space. Thus, the 3D parameters needed for microstructure analysis cannot be measured from observation of planar section. However, they can be estimated thanks to stereological relationships ([75]–[77]):

$$V_V(X) = A_A(X) = L_L(X) = N_P(X) \quad (2.2)$$

$$S_V(X) / 4 = L_A / \pi = N_L(X) \quad (2.3)$$

$$M_V(X) / 2\pi = N_A(X) \quad (2.4)$$

Hence  $N_L$  is an estimator of  $S_V$ . Considering the Euler-Poincaré construction [78], the number of intercepts of a phase  $X$  with a grid of straight lines can also be defined as the number of entry points of this phase following those straight lines (1 intercept = 1 entry point). Using the same construction, stereological relationships can be extended to the set boundaries. The surface area of internal interfaces of set  $X$ ,  $S_V(X/X)$  can be estimated from the number of entry points in set  $X$  coming from  $X$ :

$$N_L(X/X) = N_L^{entry}(X/X) \quad (2.5)$$

and  $S_V(X/X^c)$  can be estimated from the number of entry points per unit length in set  $X$  coming from  $X^c$ :

$$N_L(X/X^c) = N_L^{entry}(X/X^c) \quad (2.6)$$

Considering these relations and contiguity definition given in I.D.1 contiguity can be expressed as follows:

$$C = \frac{S_V(X/X)}{S_V(X/X) + S_V(X/X^c)} = \frac{N_L(X/X)}{N_L(X/X) + N_L(X/X^c)} = \frac{N_L^{entry}(X/X)}{N_L^{entry}(X/X) + N_L^{entry}(X/X^c)} \quad (2.7)$$

As a reminder, the factor 2 in contiguity definition results from the definition of contiguity as a fractional surface area per grain. Hence, the surface density of grain boundaries is half the internal surface density  $S_V(X/X)$  of grain boundaries since each boundary belongs to 2 grains;  $S_V(X/X^c)$  is equivalently the surface density of phase boundaries, or the internal surface density of phase boundaries.

Finally, specific notations used in the chapter IV are detailed here:

- $N_A(WC/WC)$  represents the number of grain boundaries per unit analyzed area A:

$$N_A(WC/WC) = \frac{N(WC/WC)}{A} \quad (2.8)$$

- $N_{AWC}(WC/WC)$  represents the number of grain boundaries per unit carbide area:

$$N_{AWC}(WC/WC) = \frac{N_A(WC/WC)}{A_A(WC)} \quad (2.9)$$

- $S_V(WC/WC)$  represents the surface area of grain boundaries per unit analyzed volume.

$$S_V(WC/WC) = \frac{S(WC/WC)}{V} \quad (2.10)$$

- $S_{V_{WC}}(WC/WC)$  represents the surface area of grain boundaries per unit carbide volume:

$$S_{V_{WC}}(WC/WC) = \frac{S_V(WC/WC)}{V_V(WC)} \quad (2.11)$$

- Partial contiguity  $C(\Sigma)$  is a restriction of the contiguity to a specific family  $\Sigma$  of boundaries. It represents the fraction of surface area occupied by a boundary of type  $\Sigma$  on the internal surface of a grain:

$$C(\Sigma) = \frac{S_V([WC/WC]_{\Sigma})}{S_V(WC/WC) + S_V(WC/Co)} \quad (2.12)$$

## II.D.2 Distribution of grain size and 3D reconstruction

### *Measuring grain size distribution*

The definition of the grain size, *i.e.* the parameters used to evaluate the size of a grain, depends on the dimension in which the measurement is carried out and on the dimension in which this grain size is expressed (Table 10). In this study two parameters are used to measure grain size:  $d_{2D}$  and  $d_{3D}$ .

**Table 10** Different sizes obtained by geometrical measurements, as a function of the dimension of the measurement space.

	Dimension of the measurement space		
	(1) Line	(2) Plane	(3) Space
Grain Size	l, length of intercepts through the grains	$d_{2D}$ , diameter of a disk of same area (2D equivalent diameter)	$d_{3D}$ , diameter of a sphere of same volume (equivalent diameter)

Once the distribution of size has been determined, it is necessary to normalize the population in every class by the total number of particles  $N$ , to obtain the frequency associated with the class  $i$  (density distribution):

$$f_i = \frac{n_i}{N} \quad (2.13)$$

Density distributions make possible to compare size distributions in various populations. Another way to represent a distribution is the cumulative distribution  $F_i$  which represents the fraction of grains with a size smaller than the maximum size of class  $i$ :

$$F_i = \sum_{j \leq i} f_j \quad (2.14)$$

In this work, only density distribution and cumulative distributions will be presented

#### ***Determination of $d_{2D}$ distribution***

The 2D equivalent diameters distribution can be established thanks to *individual analysis*. This method can only be applied if particles to analyze in the set  $X$  are separated. Also, it is easily implementable with EBSD images, where grain boundaries are well identified (Figure 52).

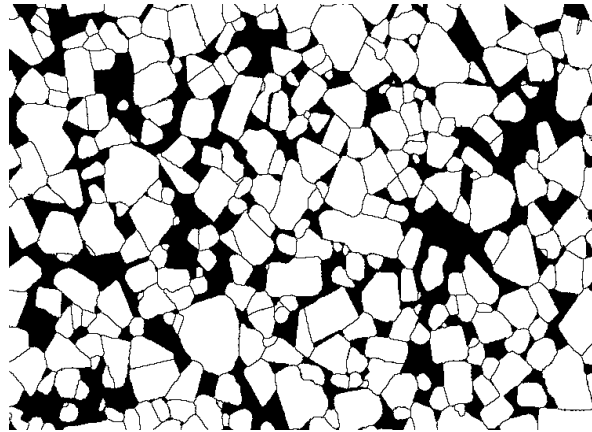


**Figure 52: EBSD Image of WC-Co microstructure (30 vol% Co, W-rich binder) after threshold: grains are separated.**



As grains are separated it is possible to isolate each grain one after the other to measure the area  $A$ , from which  $d_{2D}$  is easily calculated ( $d_{2D} = \sqrt{4A/\pi}$ ).

### II.D.2.i Reconstruction of 3D grain size distribution

The reconstruction of 3D grain size distribution from 2D or 1D distribution does not admit any general solution, and necessitates making a hypothesis on the particle shape.

The case of a distribution of spherical particles of varying sizes has been largely documented. The first methods were presented by Hagerman or Scheill, and improved by Saltykov [79]. The Saltykov method is based on a population of non-overlapping and randomly distributed spherical grains with discrete sizes  $R_1, \dots, R_n$ . The fundamental assumption is to consider the maximum observed size radius in the sizes histogram  $R_n$  as equal to the true radius of the largest grains (Figure 53). Knowing the probability  $p_{n,n}$  of cutting a sphere by its diameter (between  $2R_n$  and  $2R_{n-1}$ ), and the number of elements in the last class  $n_n$  the number  $N_n$  of grains of size  $R_n$  is known:

$$N_n = p_{n,n} n_n \quad (2.15)$$

As the elements in the penultimate class  $N$  only consists in diameter sections of the  $N_{n-1}$  grains with radius  $R_{n-1}$  and sections of the  $N_n$  grains, it is possible to determine  $N_{n-1}$ , if the probability  $p_{n,n-1}$  that a section of a grain of size  $R_n$  give a disk of radius between  $R_{n-1}$  and  $R_{n-2}$  is known:

$$N = p_{n,n} n_{n-1} + p_{n,n-1} N_n \quad (2.16)$$

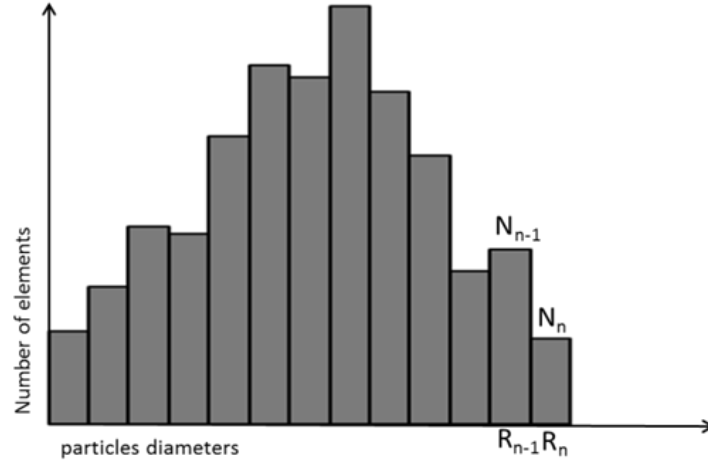


Figure 53: Sizes histogram. Because it is the maximum size observed,  $N_n$  comes from sections of grains with a radius  $R_n$ .

The probability that the section a grain of radius  $R_n$  gives a disk of radius between  $r$  and  $r+dr$  can be expressed as:

$$p(r)dr = \frac{rdr}{R\sqrt{(R^2 - r^2)}} \quad (2.17)$$

Finally, by successive iteration it is possible to relate the 3D size distribution to the 2D size distribution with a transformation matrix.

### II.D.3 Measuring contiguity

The method for contiguity measurement used in this study is based on the counting of entry points in the WC phase along the straight lines of the grid. Entry points in the WC phase are detected, differentiating the cases of interface with WC or Co. The contiguity is then determined using equation described in II.D.1.

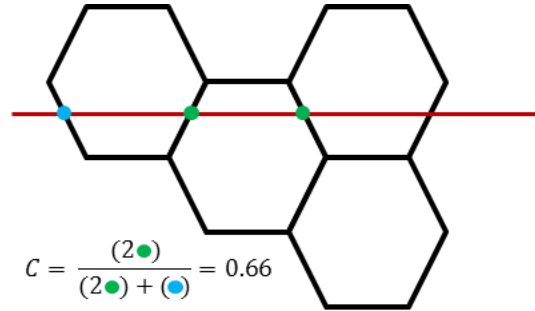


**Figure 54: Contiguity can be measured by counting entry points: entry in WC from Co (blue) or from another WC grain (green).**

The contiguity measurements are performed on Euler images issued from EBSD analysis. The main steps of the image analysis process are described in the algorithm presented in Figure 55. It mainly consists in detecting separately all points constituting WC/WC and WC/Co interfaces, in order to detect entry points of each type. Finally contiguity is calculated.

Performing this routine on a regular pattern whose contiguity value is known gave accurate results, confirming the reliability of the method (see Table 11). The small difference is mainly due to high proportion of perfectly horizontal separators that are interpreted as entry points when contiguity is measured in horizontal direction. Contiguity results presented in the literature (I.D) were obtained by manual measurements. Intercepts were drawn on SEM images and intersection with WC/WC and WC/Co interfaces are counted manually. Finally contiguity was calculated with expression (3.1). Thus EBSD and manual technics were compared on some samples of the present study in order to point out the differences. The manual measurement method was used to measure the contiguity on SEM and EBSD images made in the conditions of the experiment (Figure 56), and the values were compared to the value returned by the measurement routine.

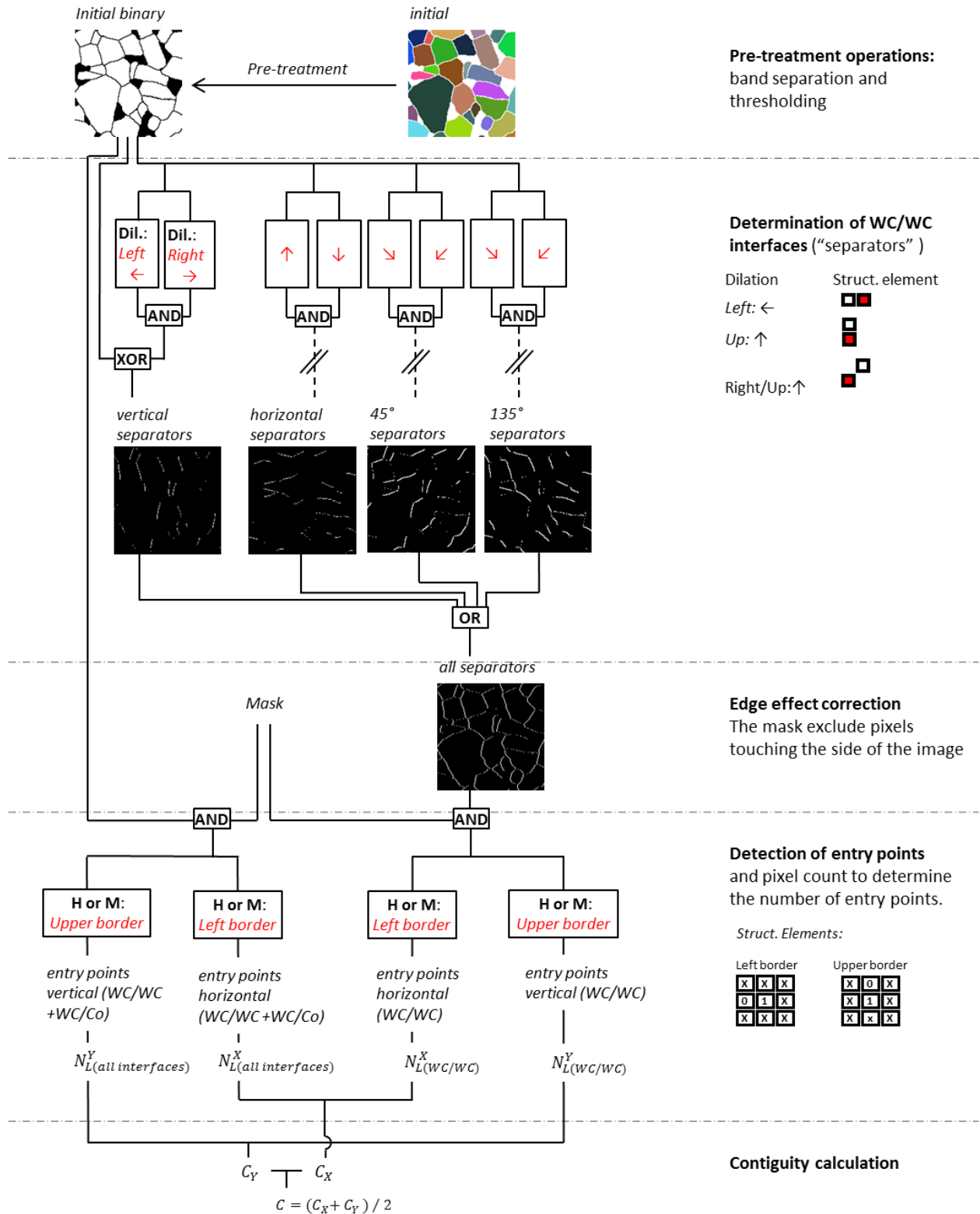
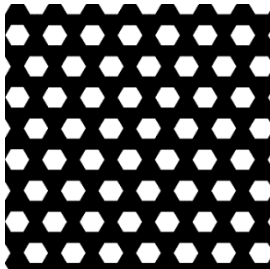
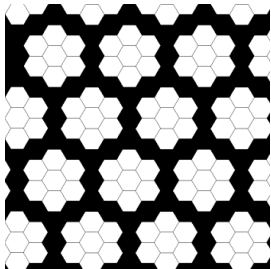
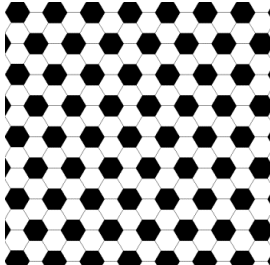
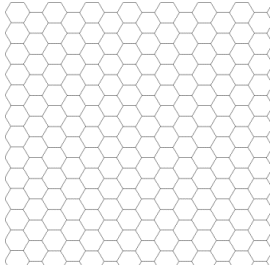
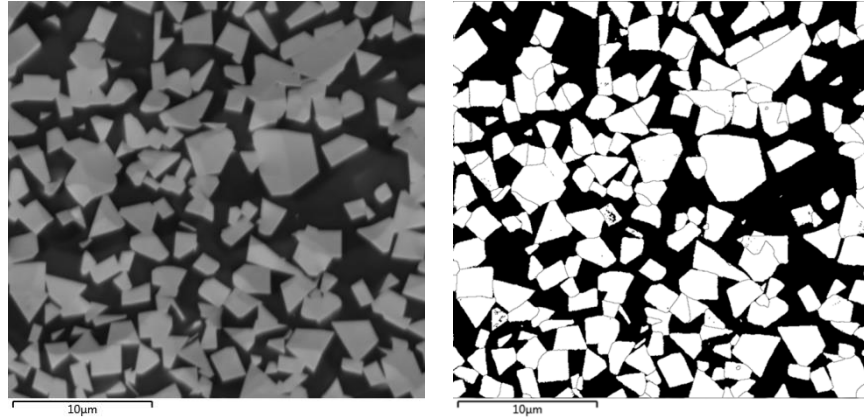


Figure 55: Bloc diagram of the algorithm used for contiguity measurement on EBSD images with image analysis

The manual method on the EBSD separated image and the routine gave the same contiguity ( $C = 0.32$ ), confirming the reliability of the automated measurement method. At the opposite the value obtained by manual measurement on the SEM image is significantly lower ( $C = 0.17$ ). It underlines the difficulty to determine the existence of a grain boundary without the orientation information provided by EBSD. But resolution issues presented in II.B.3 can also be a source of overestimation of the contiguity in EBSD, especially because the finest binder pockets are missing in these images. It is to note that the large discrepancy between both technics in this case can be partially explained by the small analysis area analyzed ( $30 \times 30 \mu\text{m}$ ) which decreases the number of intercepts and then gives more weight to errors.

**Table 11: The contiguity measurement method was tested on several regular patterns. The theoretical and measured contiguity values of the white phase are given in this table.**

Theoretical		Measured	Theoretical		Measured
	0.00	0.00		0.57	0.58
	0.50	0.51		1.00	0.99



**Figure 56: SEM and EBSD image of the same area, made in the condition of the experiment (30x30µm). Manual measurements of contiguity were made on both images.**

#### II.D.4 Grain boundary characterization

A program has been developed in order to establish the distribution of grain boundary misorientations and grain boundary habit planes from EBSD data. Two parts can be distinguished: the first one, performed with Aphelion™ extracts orientation information from the EBSD data, and the second, performed with MatLab®, calculates grain boundary misorientations and analyses grain boundary habit planes distribution. The following section aims at presenting the simplified algorithm of this program. Details about image analysis operation can be found in Appendix 2: Basics of image analysis.

##### II.D.4.i Part 1: collection of orientation data (Aphelion™)

###### *Euler angles*

The orientation of the lattice can be defined with 3 angles ( $\varphi_1$ ,  $\phi$ ,  $\varphi_2$ ) called Euler angles which describe the orientation of the crystal in relation to the sample orientation. They correspond to the 3 successive rotations that bring the sample system into coincidence with the crystal system.  $\varphi_1$  and  $\phi$  are in the  $[0-180^\circ]$  range, and  $\varphi_2$  in the  $[0-60^\circ]$  range.

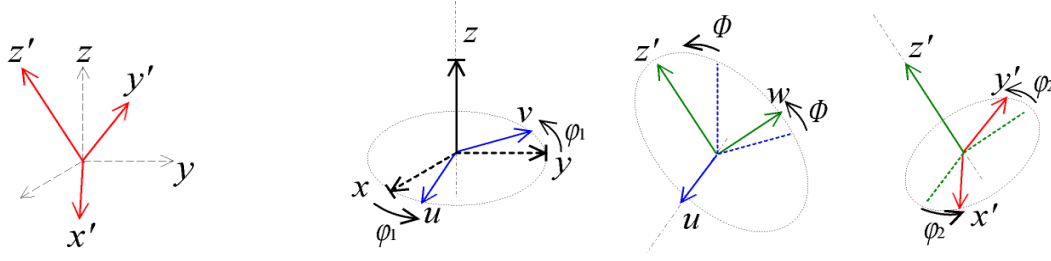


**Figure 57:** Sample (dashed line) and crystal (red line) systems. Rotation  $\phi_1$  around  $z$ , followed with rotation  $\Phi$  around the new axis  $u$  and finally rotation  $\phi_2$  around  $z'$  brings the sample system into coincidence with the crystal system.

The maps used as input represent the orientation of the grains (Figure 45): each grain is colored according to the 3 Euler angles. Each component of grain's color (in RGB system) is defined according to Euler angles as follow:

$$R = \frac{\phi_1}{180}$$

$$G = \frac{\phi}{180}$$

$$B = \frac{\phi_2}{60}$$

### *Global view of the algorithm*

The aim of this first part is to list all grain boundaries (so all grain/neighbour couples), with the coordinates of their constitutive pixels and with the orientations of adjacent grains, so that misorientation and boundary planes can be determined latter.

The different steps of this part are sketched in Figure 58 and will be developed in next sections. First, a grain is detected in the picture, and its RGB components (so Euler angles) are collected. Then all its neighbours (*i.e.* grains sharing a boundary with this grain) are reconstructed. Every neighbour is considered one after the other for collecting Euler angles and for the reconstruction and determination of the coordinates of the grain boundary trace associated to the grain/neighbour couple. Once every neighbour has been analysed, the system moves to the next grain and the process is repeated.

The final output of the process is a file gathering orientations and a file gathering the coordinates of the grain boundaries.

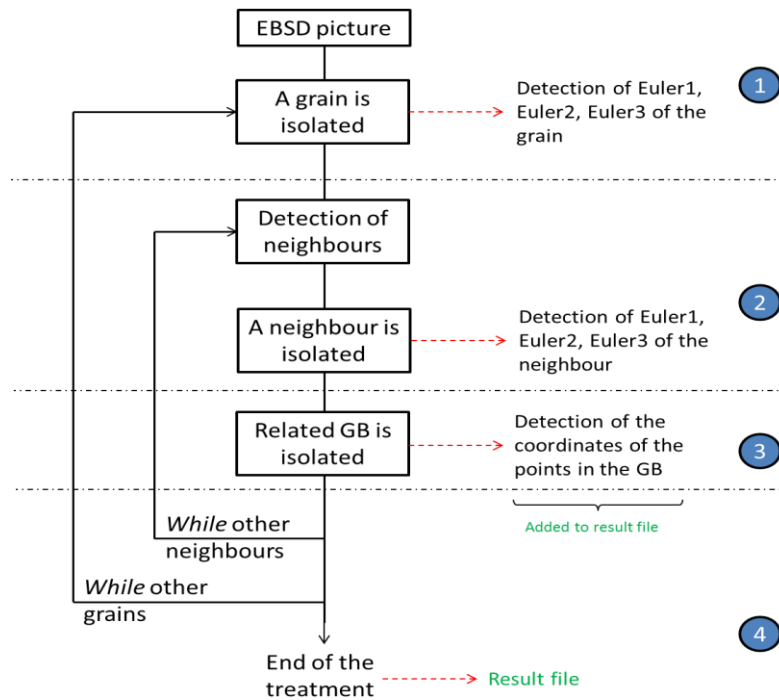


Figure 58: Global view of the different steps in the Aphelion process.

### Step 1: isolating the reference grain (Figure 59 and Figure 60)

- From the original EBSD image four different copies are created:
  - Black and White copy (*B&W*): with a *threshold* operation to select the WC phase (white)
  - *Red, Green, Blue* bands: the 3 colour band images are transformed in grey level images representing the 3 Euler angles of the grains.
- The further transformations are made on *B&W* :
  - A *mask* is applied to the image, in order to avoid edge effects.
  - The first point of *B&W* inside this mask is detected and used as a “seed”.
  - This seed is used for a *reconstruction operation* which provides an image (*Grain*) containing only the grain containing the seed. This grain is considered as the reference for the further operations.
- From *Grain* and *Red* (resp. *Green* or *Blue*) a *logical AND* operation isolate the red (resp. green or blue) band of *Grain*: finally it is possible to measure the red (resp. green or blue) level of the grain and calculate Euler1 (resp. Euler2 or Euler3).



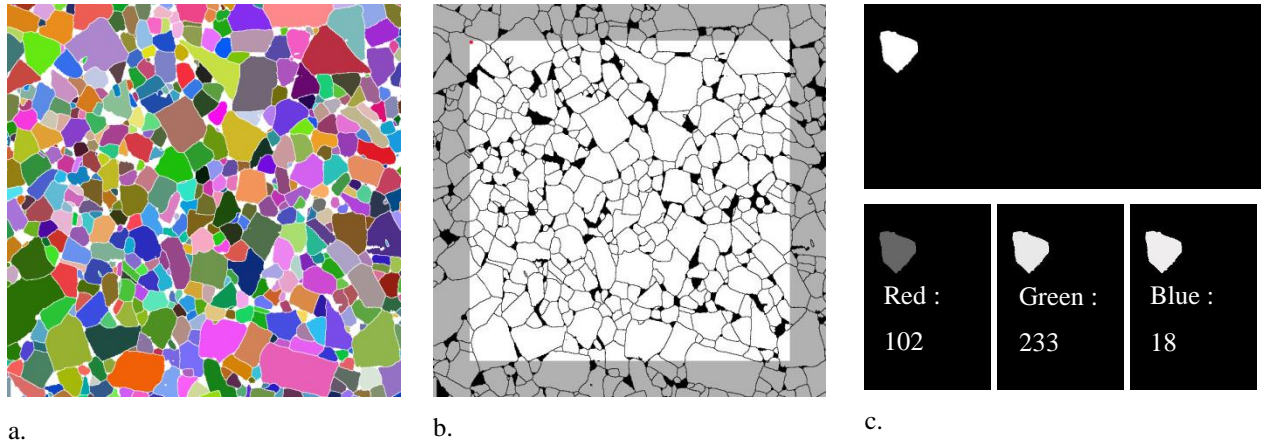


Figure 59: a) Original image. b) After threshold and application of the mask. The first seed has been marked in red. c) The grain corresponding to the red seed has been reconstructed in the binary image and color bands have been obtained: this combination of RGB levels corresponds to the green grain of the original image.

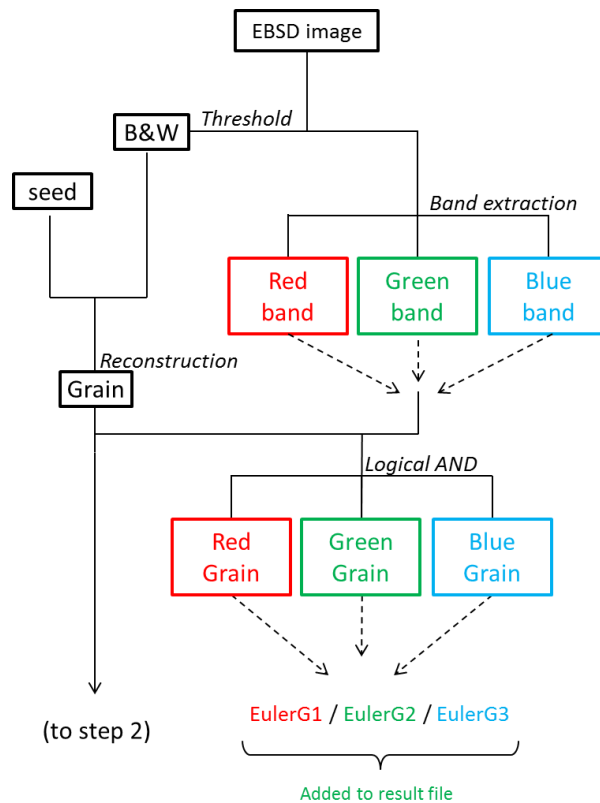


Figure 60: Detailed bloc diagram of step 1 algorithm.

**Step 2: detection of neighbours (Figure 61 and Figure 62)**

- Operations are made on *Grain*:
  - *Grain* is dilated
  - A reconstruction operation is made from dilated *Grain* and *B&W*: as the dilated grain overlaps the edges of its neighbours, the result gives the neighbours of the reference grain (Figure 61). Since reconstruction is performed in the global binary image, neighbours may extend beyond the mask and hit the edge of the image.
  - Neighbours only are selected: a logical XOr will remove the reference grain from the image. The final result contains only neighbours of the reference grain, well separated one from the other.
- Because neighbours are well identified and separated, it is now possible to consider them one after the other, and to determine their relative Euler angles.
- Before moving to the next neighbour, the program moves to step 3 to determine the boundary coordinates.

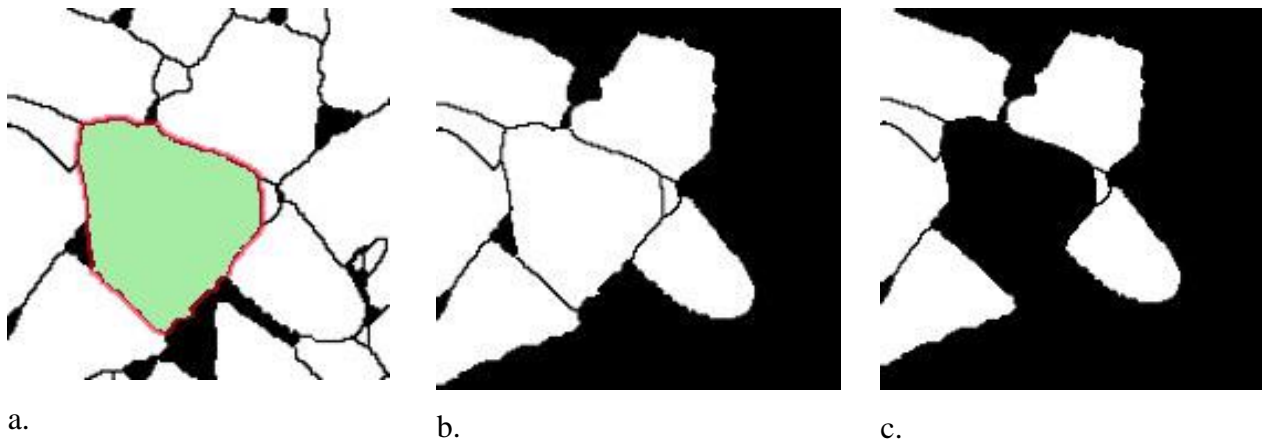


Figure 61: a) Original grain is colored in green, and the dilated part in red. One can see that it overlaps its neighbors which will be reconstructed (b). The reference grain is deleted: a new image containing only neighbors is obtained (c).

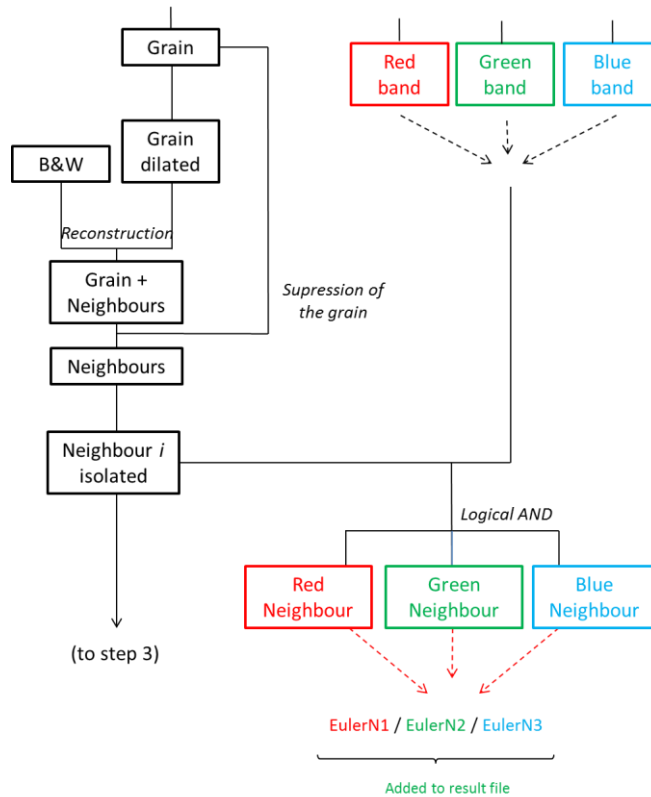


Figure 62: Detailed bloc diagram of step 2 algorithm.

**Step 3: determination of grain boundary coordinates (Figure 63 and Figure 64).**

Determining the boundary coordinates is necessary to determine the “trace” of the grain boundary and thus the distribution of boundary habit planes.

- Treatments are made on both the reference grain and the isolated neighbour:
  - The *intersection* between the dilated reference grain and the dilated neighbour give the grain boundary, *4-connected*.
  - *HitOrMiss* operation with a structuring element makes possible to detect pixels which are specific of 4-connected lines.
  - *XOr* operation removes those pixels in order to get an 8-connected grain boundary.
  - Finally coordinates of the pixels in this image are detected step by step: the ending points of the GB are isolated, their coordinates are saved and those pixels are removed from the GB. This process is repeated until all pixels have been treated. The inconvenient of this method is that pixels are not sorted in the “natural” order. Coordinates are saved in an individual file and will be sorted later.

- All the parameters we needed have been measured on the couple reference/neighbor, so the program loops to the next neighbour. If every neighbour has been treated, the reference grain is suppressed from the B&W image and the program loops to another grain that will become the new reference. When every grain has been treated the program stops (Figure 65).

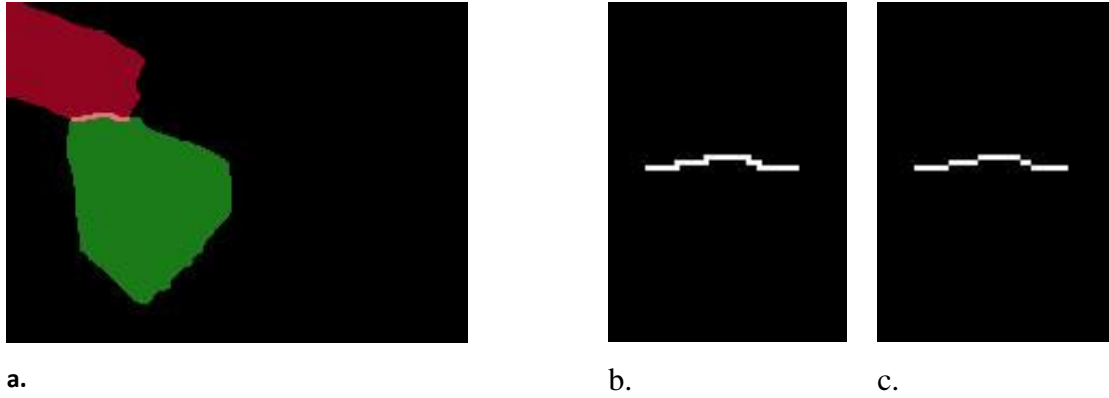


Figure 63: a) Dilated reference grain is colored in green, dilated neighbor in red. The intersection corresponds to the grain boundary. b) The isolated grain boundary in 4 connexity. The HitOrMiss operation detects pixels in 4 connexity to delete them. The grain boundary in 8 connexity is obtained (c).

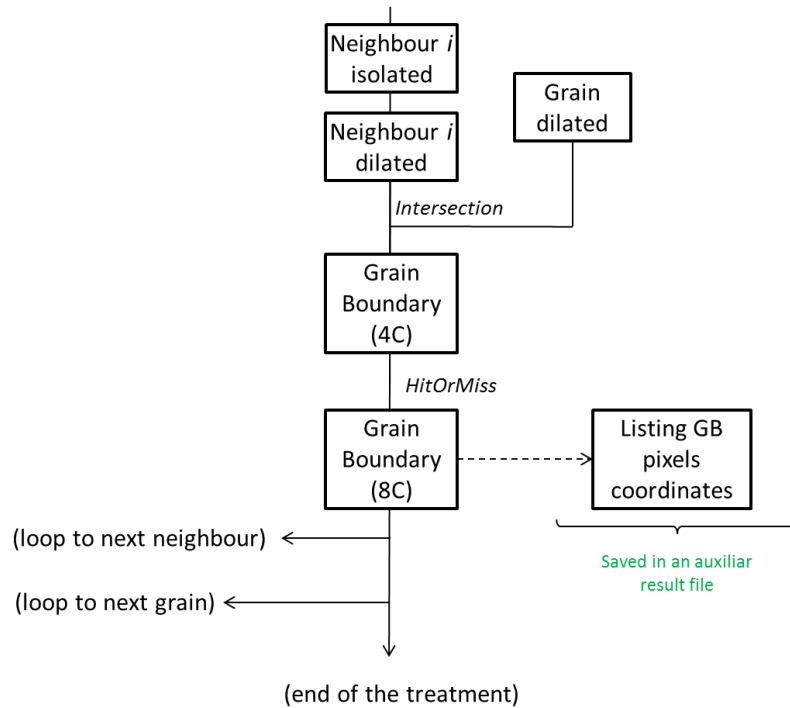
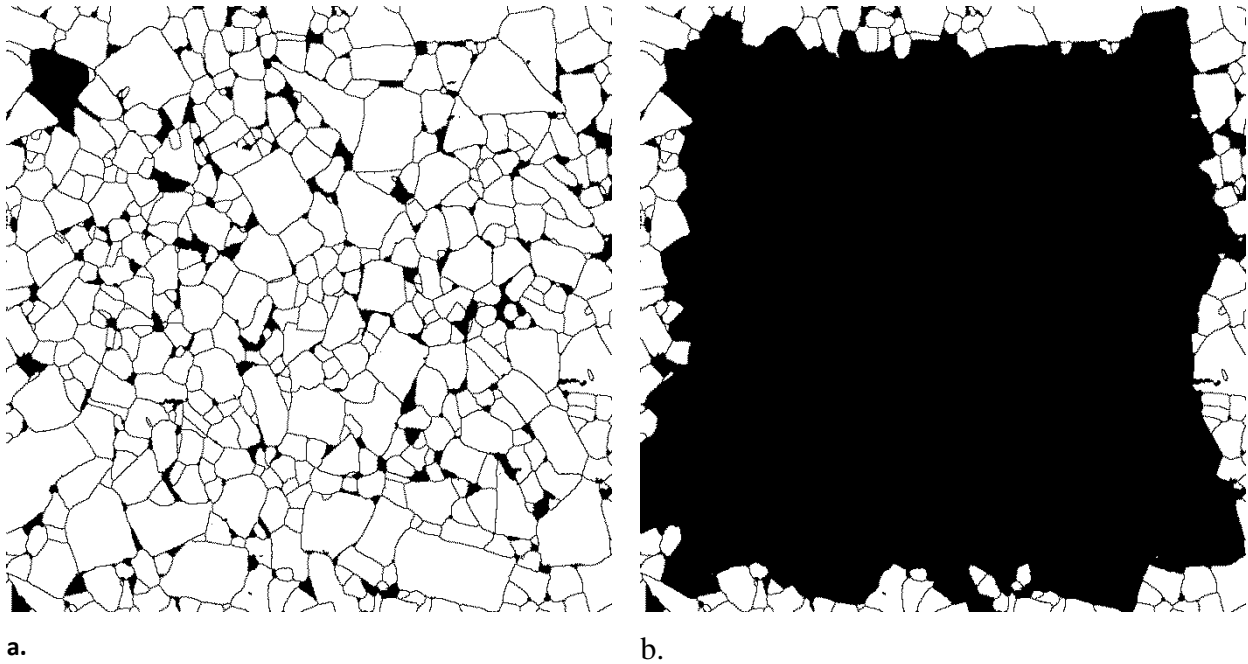


Figure 64: Detailed bloc diagram of step 3 algorithm.

***Focus on grain detection and optimization***

The process of detecting a grain and its relative neighbours, one grain after the other, would lead to detect twice each grain boundary, which is a waste of calculation time. Also, before analysing a neighbour the program check if it is still part of the *B&W* image. In fact, if the neighbour is not part of the *B&W* image, it means that it has already been analysed (as a reference grain), and the relative grain boundary has already been taken into consideration. In this case the program will step to the next neighbour.



**Figure 65:** a) Before looping to the next grain, the reference is deleted from the *B&W* image. At the end of the treatment, only grains not included in the mask remain in *B&W* (b).

### II.D.4.ii Part II: treatment of orientation data (MatLab®)

The previous part isolated grain boundaries and collected the orientation information. The next step consists in measuring the grain boundary length and identifying grain boundaries rotation [axis]/angle (from orientation data) and the fraction of remarkable (basal or prismatic) grain boundary planes. Those calculations are processed with MatLab® software.

The main steps of orientation calculations are summarized in Figure 66.

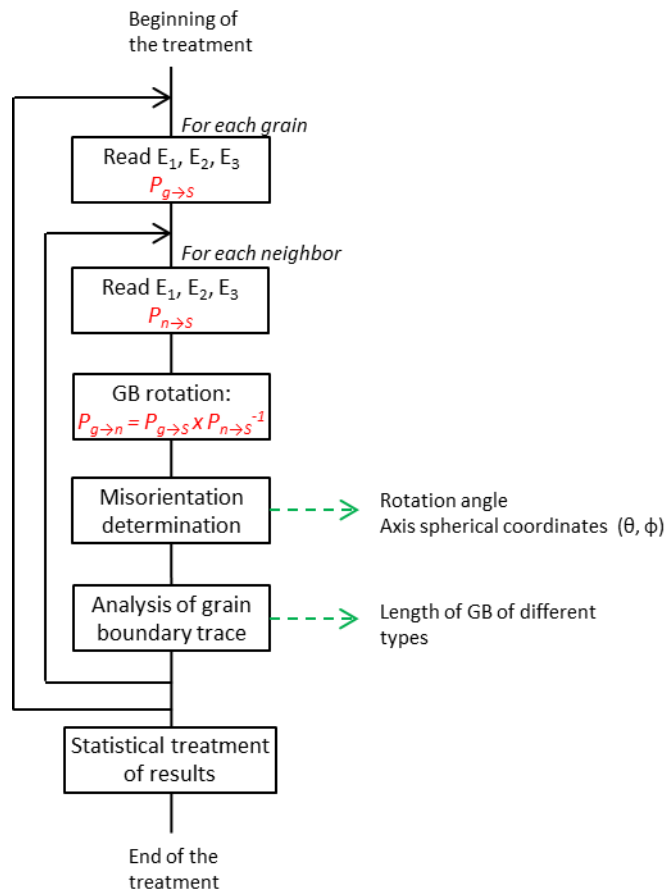


Figure 66: Bloc diagram resuming the main steps of orientation calculation.

#### *Analysis of grain boundary misorientation*

The first aim of the program is to determine the misorientation characterizing the grain boundary.

Euler angles are defined so they describe the orientation of the crystal in relation to the sample orientation. Thus the change-of-base matrix from the grain crystal basis to the sample basis

$(P_{g \rightarrow S})$  is determined by the product of the three successive Euler rotation matrices ( $R_{E_1^g}$ ,  $R_{E_2^g}$ ,  $R_{E_3^g}$ ):

$$P_{g \rightarrow S} = P_{S \rightarrow g}^{-1} = \left( R_{E_3^g} \times R_{E_2^g} \times R_{E_1^g} \right)^{-1} \quad (2.18)$$

Similarly the change-of-base matrix from the crystal basis of a neighbor to the sample basis ( $P_{n \rightarrow S}$ ) can be defined:

$$P_{n \rightarrow S} = \left( R_{E_3^n} \times R_{E_2^n} \times R_{E_1^n} \right)^{-1} \quad (2.19)$$

The characteristic rotation of the grain boundary is the rotation bringing lattices of both grain and neighbor into coincidence. This rotation can be seen as a combination of the two previous rotations. Therefore the rotation matrix characterizing the grain boundary can be defined:

$$P_{g \rightarrow n} = P_{n \rightarrow S}^{-1} \times P_{g \rightarrow S} \quad (2.20)$$

Finally,  $P_{g \rightarrow n}$  is a rotation matrix whose eigenvalues and eigenvector give respectively the rotation angle and the rotation axis characteristic of the grain boundary.

Because of symmetries in WC crystal, twenty four equivalent rotations can be used to describe the orientation of a crystal. Therefore, 24x24x2 equivalent rotations describe the misorientation between two crystals. By convention the equivalent rotation with the smallest angle associated with an axis in the fundamental trihedron (delimited by  $[10\bar{1}0]$ /  $[2\bar{1}\bar{1}0]$ /  $[0001]$ , see I.A.2.ii) is chosen to limit the result to a unique solution.

The program offers three levels in the boundary population analysis. The first one is a global analysis and aims at determining preferential rotation axes. The second is a detailed analysis focusing on a set of chosen axes for which frequency statistic and rotation angle distribution are determined, making possible to isolate preferential [axis]/angle couples. The last one calculates frequency statistics on a set of chosen [axis]/angle couples.

For the first step rotation axes are described with polar coordinates ( $\theta$   $[0^\circ-30^\circ]$ ) and  $\varphi$   $[0^\circ-90^\circ]$  in the fundamental trihedron). In order to display the distribution of rotation axes the fundamental

trihedron is discretized. Classes are defined to be  $5^\circ$  wide ( $\theta$  or  $\phi$  directions) and centered on multiples of  $2.5^\circ$  (Figure 67). This definition presents the advantage of placing axes that are likely to be interesting (rotation around  $[10\bar{1}0]$ ,  $[2\bar{1}\bar{1}0]$ ,  $[0001]$  especially) at the center of a class. At the opposite, an evident drawback is that the solid angle corresponding to the different classes is not uniform. Additionally, because of symmetries, classes centered on the limit values of the trihedron ( $0^\circ$  and  $90^\circ$ ) are  $2.5^\circ$  wide instead of  $5^\circ$ . This variation of the solid angle has a direct influence on the number of axes found in each class. Thus, in order to compare the population of different axes it was chosen to express the frequency in Multiple of Random Distribution. The Random Distribution is calculated by considering rotation axes isotropically oriented in the whole sphere of orientations, so it reveals the bias due to the construction of the distribution (Figure 67). The random fraction of boundaries in a class of the distribution is calculated as follow:

$$x_{RANDOM} = \frac{\Omega}{4\pi} \quad (\text{with } \Omega \text{ the solid angle attached to the class})$$

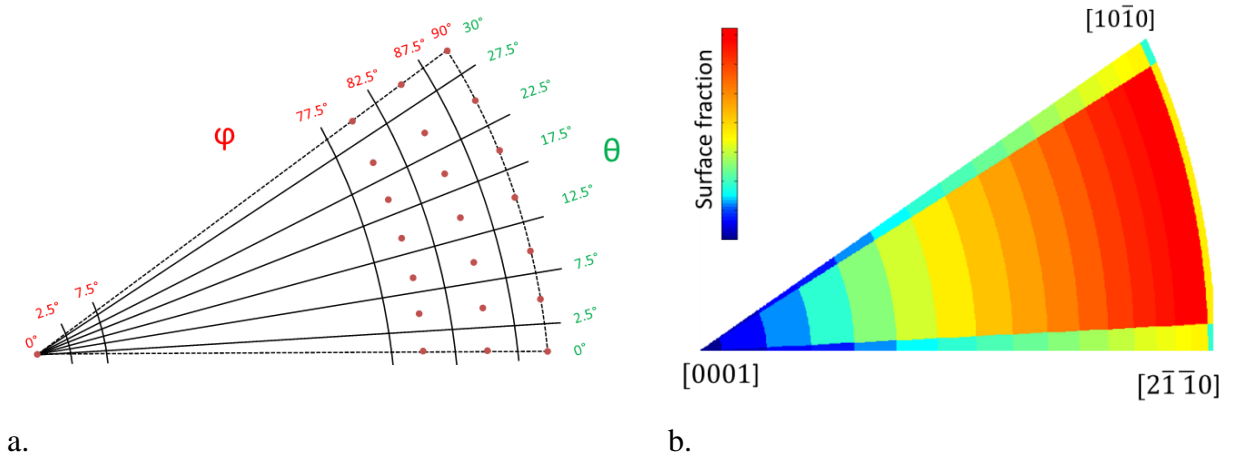


**Figure 67: a) Fundamental trihedron divided into classes in order to establish the distribution of rotation axes. Dots represent the centers of classes. b) Random Distribution of rotation axes.**

The fraction of boundaries in each class is divided by the random fraction in order to obtain a frequency distribution in Multiple of Random Distribution. The number fraction or the length fraction of boundary in each class can thus be obtained. The length fraction is an estimate of the



surface fraction of the corresponding boundaries, from stereological relationships (§ II.D.1). The following Figure 68 gives an example of representation of the rotation axis distribution, expressed as surface area fraction in MRD, in the fundamental trihedron. For example  $[10\bar{1}0]$  are 7 times more frequent compared to random distribution,  $[0001]$ , 1.7 times. Thus it would be interesting to focus on these axes for the second step.

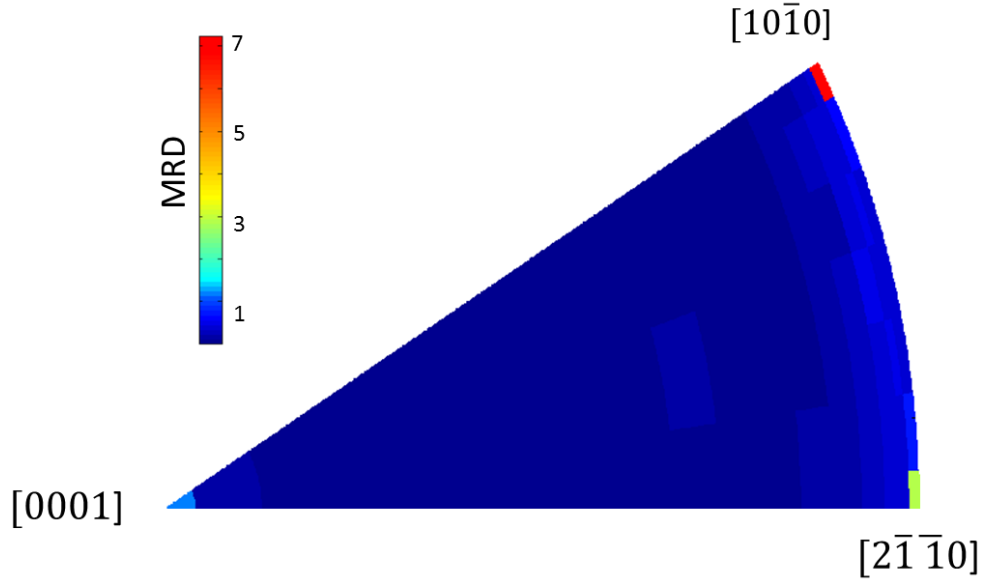


Figure 68: Representation of rotation axes distribution in MRD, in the fundamental trihedron (left). [W-rich, 10 vol% binder sintered 5h]

The second step is a detailed analysis: boundaries corresponding to chosen rotation axes (given a tolerance  $\alpha$ ) are detected by calculating a scalar product between the actual and exact orientations. So the precise frequency (in surface or number) of these boundaries and the distribution of rotation angles can be determined.

Last, once interesting [axis]/angle couples are isolated the precise frequency (in surface or number) of the corresponding boundaries is determined.

#### ***Identification of remarkable boundary planes***

As evoked in the description of the technique developed by Rohrer (I.C.6), grain boundary plane identification necessitates a huge amount of data. Thus, full characterization of grain boundary planes is not worth considering in this study because of the numerous samples that are to be

analyzed. However, limiting the process to the identification of a known set of planes significantly decreases the amount of needed data. As the equilibrium shape is expected to consist in basal and prismatic planes, and because of their particular stability, this study proposes to particularly focus on this set of remarkable planes. A method is proposed here for the estimation of remarkable (basal or prismatic) boundary planes surface fraction.

Grain boundaries were detected during the image analysis step (Aphelion) and the coordinates of the boundary trace were extracted. In order to determine the direction vector characterizing its orientation, the trace is segmented. For this purpose, the two end points  $E_1$  and  $E_2$  of the trace are considered, and the distance from each points of the trace to the segment  $E_1E_2$  is calculated (Figure 69). If the maximum distance does not exceed a limit distance  $d_{lim}$  the trace is assimilated to  $E_1E_2$ . At the opposite if the maximum distance exceeds  $d_{lim}$  the corresponding point is considered as a new end point  $E_3$  and two segments  $E_1E_3$  and  $E_3E_2$  are considered for the next iteration.

Because some boundaries are curved, this step can result in the creation of multiple segments with different orientations (Figure 69).

In a second step, the traces in the observation plane of the remarkable planes of the grains/neighbors are determined. In this aim, the normal to these planes ( $[0001]$ ,  $[10\bar{1}0]$ ,  $[0\bar{1}10]$ ,  $[\bar{1}100]$  in the crystal hexagonal system are expressed in the image system by a succession of conversions: first in an orthonormal system attached to the crystal, then in the sample system ( $P_{g \rightarrow s}$  matrix described before), and finally in the system of the image (sample and image systems are  $180^\circ$  rotated around x axis).

Last, the scalar product of boundary trace and remarkable plane trace direction vectors gives the angle between both. Finally the fraction of length of boundary traces which are collinear within  $\pm 5^\circ$  with traces of remarkable planes ( $p_{oriented}$ ) is established.

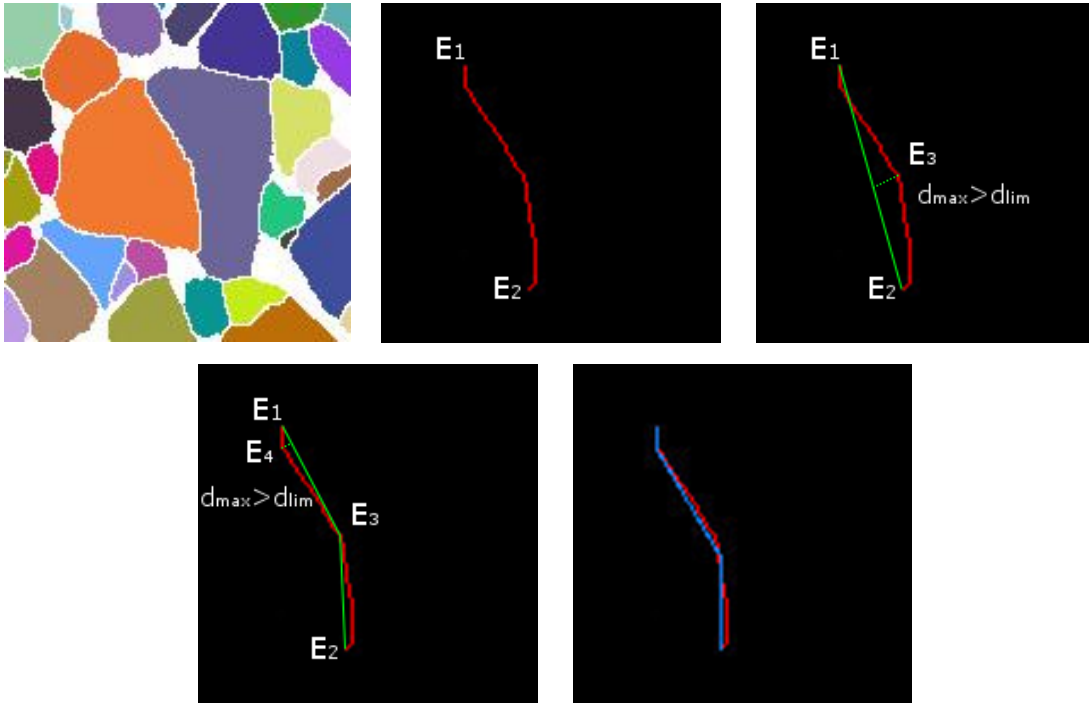


Figure 69: Detection of a curved boundary trace. After 2 iterations the segmentation results in three different segments, fitting the three successive directions of the trace.

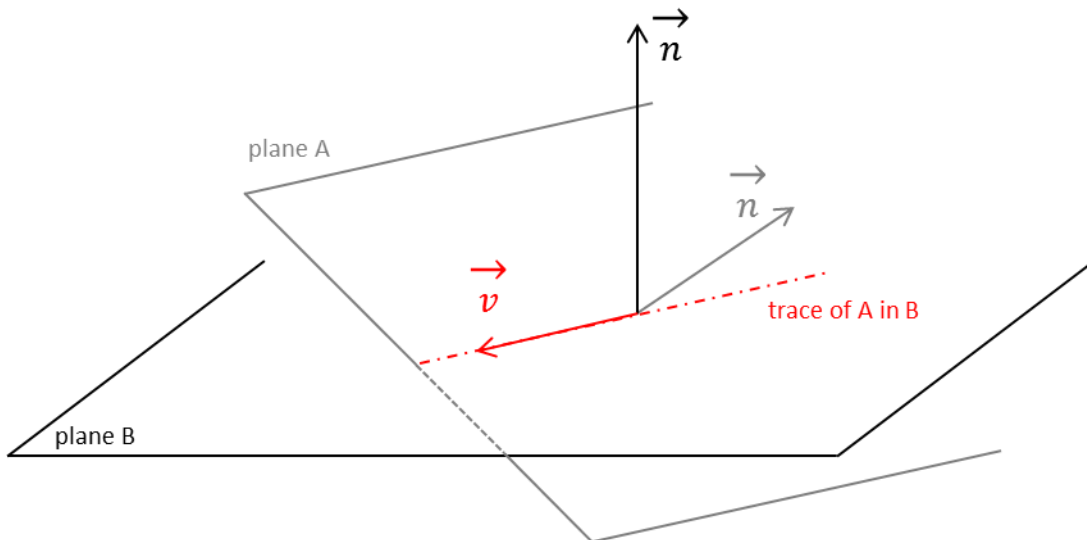


Figure 70: Cross product of the normals of two planes gives the direction vector of the intersection line.

### ***Stereological determination of the fraction of remarkable boundary planes***

The second aim of the program is to determine the fraction of boundary planes which are coplanar with remarkable crystallographic planes (basal or prismatic). The 2D analysis induces a loss of information: only the grain boundary trace can be determined. However, stereological considerations make it possible to estimate the fraction of boundary planes coplanar with remarkable planes from the fraction of boundary traces collinear with remarkable plane traces.

In order to do so, let's consider two borderline cases of grain boundary plane distribution.

In the first one, the distribution of grain boundary planes is isotropic. The probability for a boundary trace to fall within a certain angle  $\alpha$  from the trace of a remarkable plane in the observation plane is simply  $2 \times 2\alpha/2\pi$  (Figure 71). Then, the probability  $p_{oriented}$  for a grain boundary to present a trace in the observation plane which is collinear within  $\pm 5^\circ$  to the trace of a remarkable plane (among 1 basal and 3 prismatic planes) is:

$$p_{oriented} = 2 \times 4 \times \frac{10}{360} = \frac{2}{9} \quad (2.21)$$

And:

$$p_{non\ oriented} = 1 - p_{oriented} = \frac{7}{9} \quad (2.22)$$

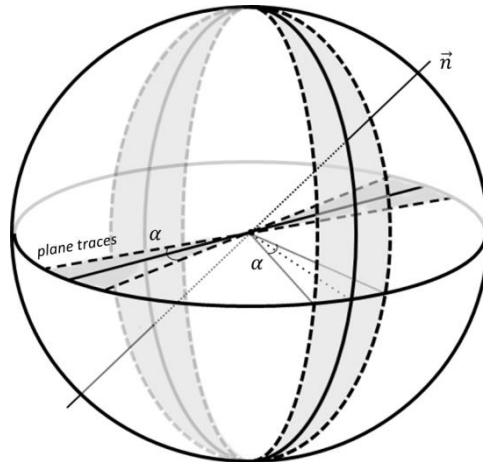


**Figure 71:** Considering planes with a trace within  $\pm\alpha$  of a given direction, in the equatorial section plane. Normal to those planes lies in the grey area. Hence the probability for a trace to fall within  $\alpha$  of the given direction is proportional to the fraction of grey area on the surface of the sphere, which is  $2 \times 2\alpha/2\pi$

In the other borderline case all boundary planes are coplanar with a remarkable plane. As a consequence:

$$p_{oriented} = 1$$

The case corresponding to the effective microstructure can be considered as intermediate to these two borderline cases: a fraction of boundary planes  $f_{rem}$  are remarkable, and  $(1 - f_{rem})$  are random. Also, the probability to measure an oriented boundary trace becomes:

$$p_{measured} = f_{rem} \times 1 + (1 - f_{rem}) \times \frac{2}{9} \quad (2.23)$$

Giving:

$$f_{rem} = \frac{9p_{measured} - 2}{7} \quad (2.24)$$

$p_{measured}$  corresponds to the fraction of length of boundary traces which are collinear with traces of remarkable planes, which is measured with the program. From the previous equation the effective fraction of remarkable boundary planes  $f_{rem}$  can be deduced from the measured value  $p_{measured}$ .

## II.D.5 WC/Co phase boundary identification

In order to characterize the shape of WC grains and the stability of habit planes, it has been necessary to adapt the program developed for the analysis of grain boundaries to the analysis of phase boundaries.

The detection of WC-Co phase boundaries is performed with the Aphelion™ software, and is an adaptation of the boundary detection algorithm presented above. Only a global view of the algorithm is given here, the main steps of this program being similar to the steps described previously.

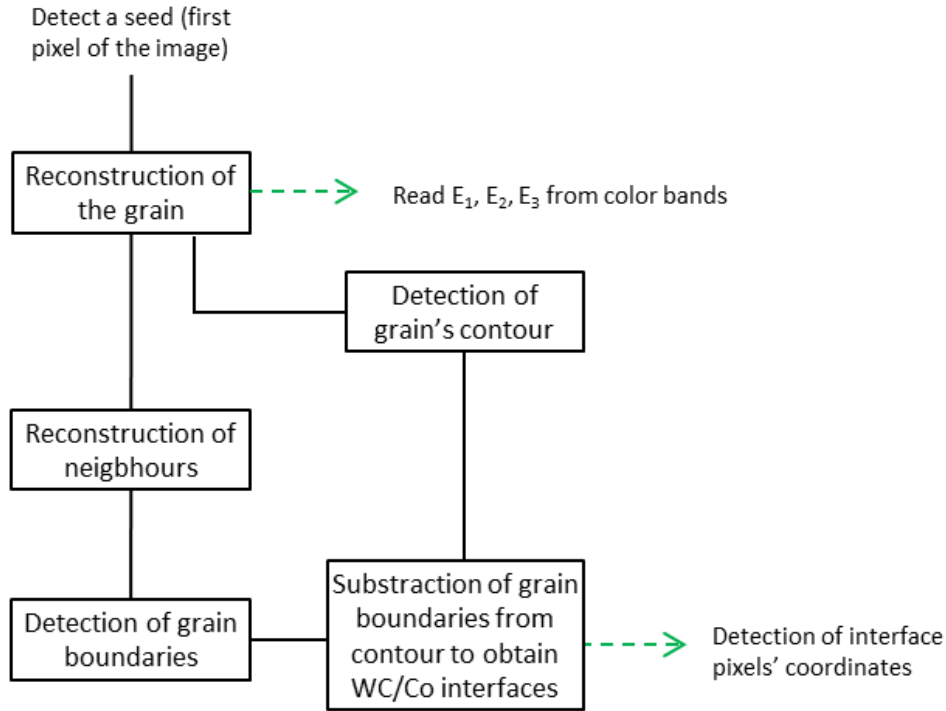


**Figure 72: Algorithm for WC-Co phase boundaries identification by image analysis.**

The identification of remarkable phase boundaries is similar to the identification of remarkable boundary planes. Figure 73 shows the result of phase boundary detection, drawn on the initial image. The good fitting of segments set with phase boundaries confirms the good working of the segmentation algorithm. However, it is important to keep in mind that the representation in Figure 73 b) show planes detected as possibly remarkable, but only a fraction  $\alpha$  determined with the previously described method actually correspond to remarkable planes.

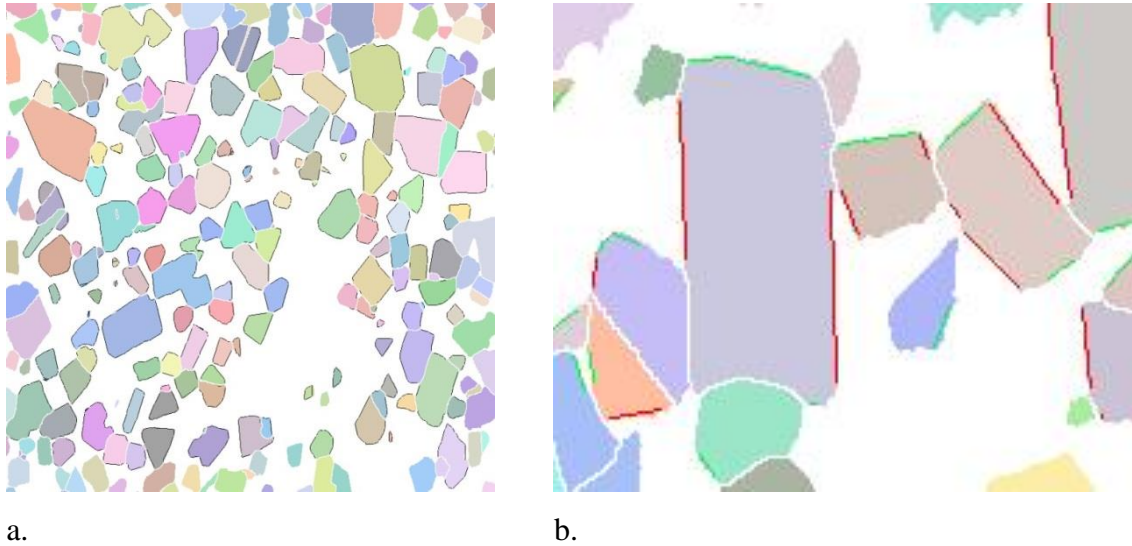


**Figure 73: (a) Phase boundaries detected by the program (black segments) are drawn on the initial image (W-rich, 50 vol% of binder sintered for 5h). (b) Identification of basal (red) and prismatic (green) planes (W-rich, 50 vol% of binder sintered for 5h).**

## II.D.6 3D image analysis

The interest of a 3D analysis in this study is to characterize the effective grain shape of WC grains from FIB/SEM images.

However, unlike EBSD images which give well separated grains, plane section images in SEM are made with backscattered electron mode and a segmentation step is necessary to separate the objects. Grains are separated thanks to an adaptation of the watershed algorithm. Because of the complex shape and imbrication of WC crystal, the result of automated grains separation is not precise and reliable enough to allow individual analysis shape measurement. Nevertheless, it is possible to isolate grains for a qualitative shape observation. In the case of 20 vol% of binder samples, impingement is so important that grain separation and shape observation are not very concluding. Thus, only 40 vol% of binder images are presented.

Last, in order to determine the rounded or faceted character of particles, measurements of local curvature distribution were made with the tool provided by Aviso software (FEI). This analysis was not made on the whole 3D set because of the important calculation resources it requires, but rather on smaller boxes extracted from the main set.





# Chapter III Influence of carbon and cobalt content on grain growth and carbide grain shape

## III.A Evolution of grain shape

### III.A.1 2D analysis of grain shape

Variations of the grain shape were investigated by the mean of 2D shape factors. Among the variety of possible factors, circularity and elongation were chosen.

Circularity characterizes shape irregularity and is defined as follow:

$$I_{circularity} = \frac{4\pi A}{P^2} \quad (2.25)$$

where A is the area and P is the perimeter of the particle section. Circularity of a circle is 1, and it decreases for more complex shapes. It is close to zero for star shaped objects, or for shapes with high surface rugosity for example. Evolution of circularity is presented in Figure 74.

Elongation characterizes shape isotropy and can be defined as the absolute value of the difference between the lengths of the major and the minor axes of the bounding ellipse, divided by the sum of these lengths.

$$I_{elongation} = \frac{|L - l|}{L + l} \quad (2.26)$$

This measure is zero for a circle and approaches 1 for a long and narrow ellipse for example. Evolution of circularity is presented in Figure 75.

No significant evolution of circularity or elongation is to notice between the different sintered samples. The grain shape does not appear to experience significant change neither with composition nor with sintering time, or the 2D shape analysis is not sensitive enough to reveal it.

On the other hand an evolution of shape factors is to notice between the powder and the sintered samples: the decrease of elongations can be attributed to the anisotropic growth of WC grains, while decrease of the circularity dispersion is probably due to faceting (elimination of objects with rounded shapes or rough surface).

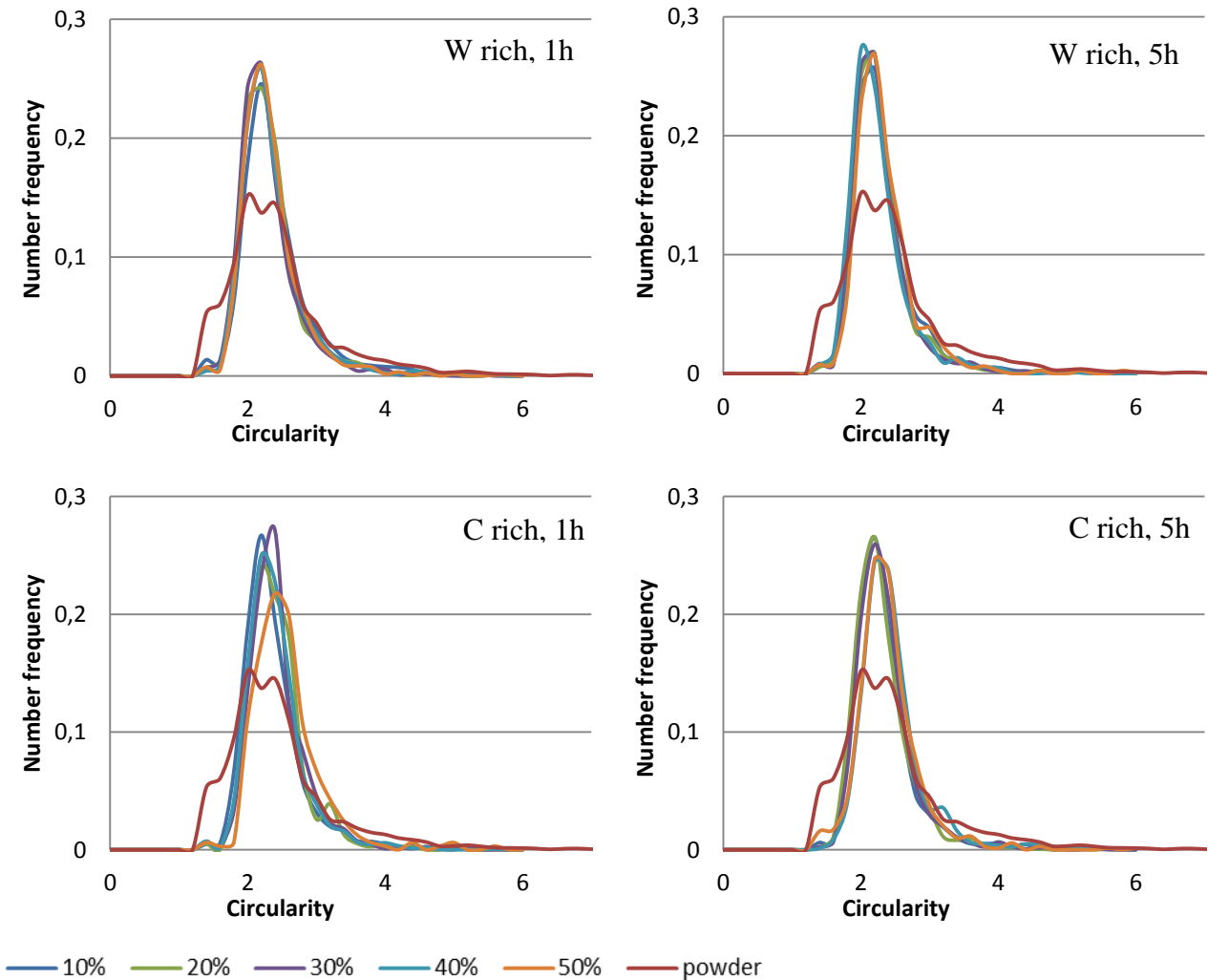


Figure 74: Evolution of the circularity of WC grains (measured in 2D) with composition and sintering time.

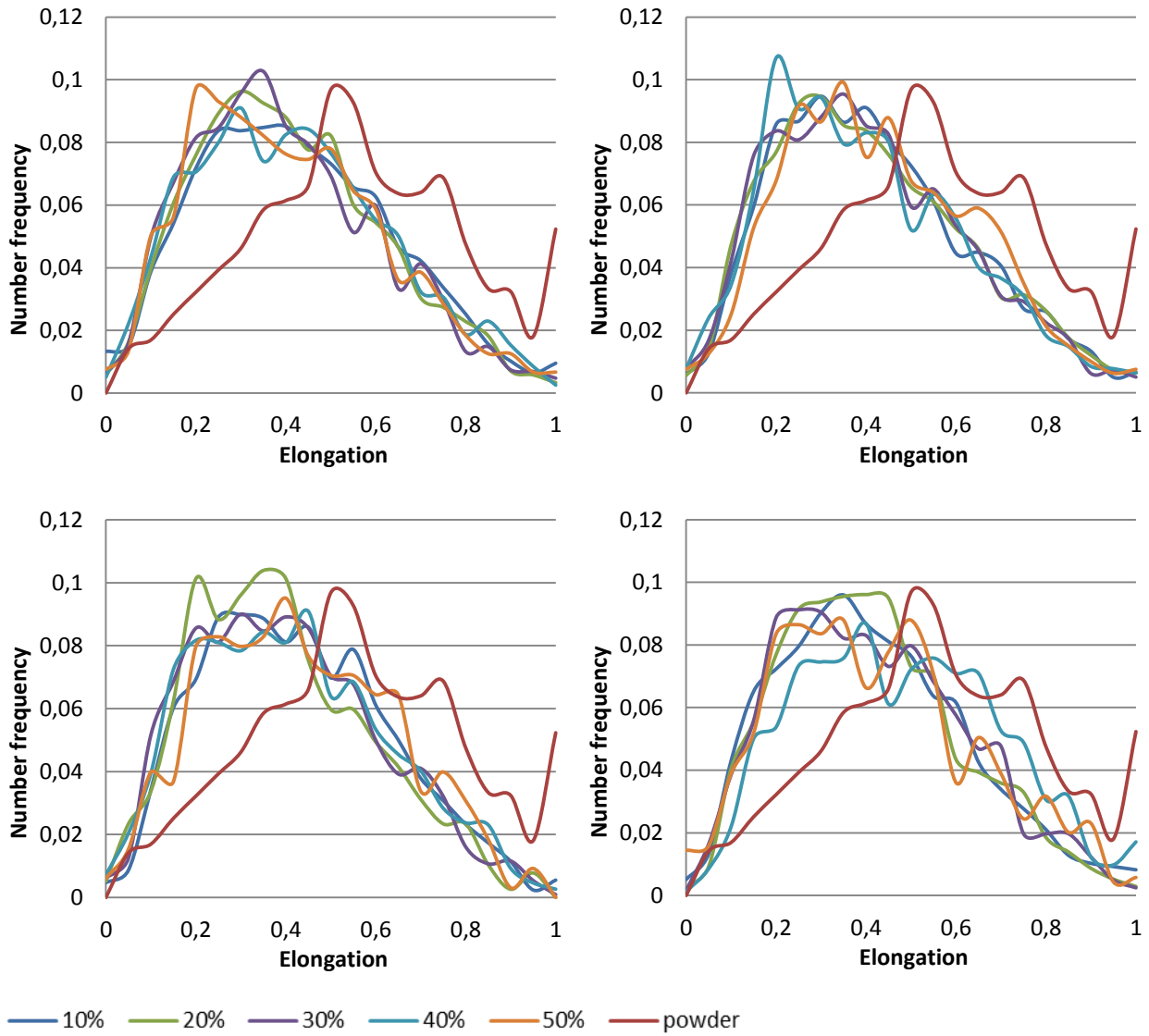


Figure 75: Evolution of the elongation of WC grains (measured in 2D) with composition and sintering time.

### III.A.2 FIB analysis

FIB analyses of the samples made possible a 3D reconstruction of the microstructure. A qualitative observation of the grain shape is proposed. Grain shape measurements, as local curvature for example, are in process but because of a lack of time no results can be presented.

The following Figure 76 show different grains extracted from the matrix.

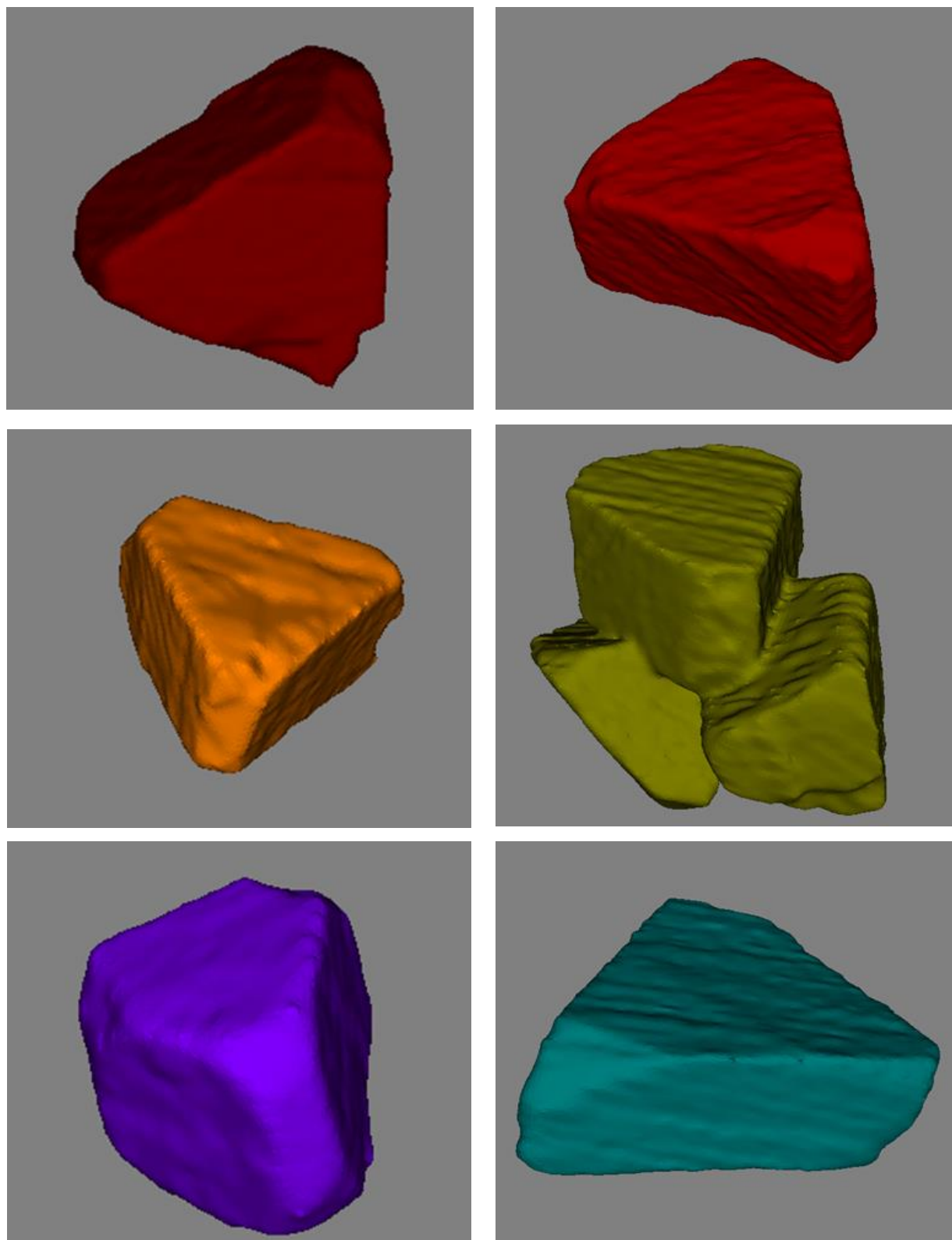


Figure 76: Examples of isolated grains extracted from 40 vol% of binder sample, sintered for 5h and C-rich (left) or W-rich (right). No particular shape difference is to notice. Magnification is different between images, grain sizes are 1-3  $\mu\text{m}$  roughly.

The first observation is that isolated grains actually present a triangular prism shape with an aspect ratio  $t/h$  (Figure 77) between 0.5 and 1 roughly, as it is mentioned in the literature [48], although it is not possible without EBSD analysis to confirm that all facets strictly correspond to a remarkable (basal or prismatic) plane. In addition, in the same sample different types of grains are found: small grains, with little facets, big grain with large basal planes, or big grains with large prismatic planes. In particular, no influence of the carbon content on the basal/prismatic ratio was to note. This is in opposition with some of the literature results mentioning flatter grains (with more developed basal planes) in C-rich binders ([23], [24], [70], [74]). The Figure 76 illustrates the previous points.

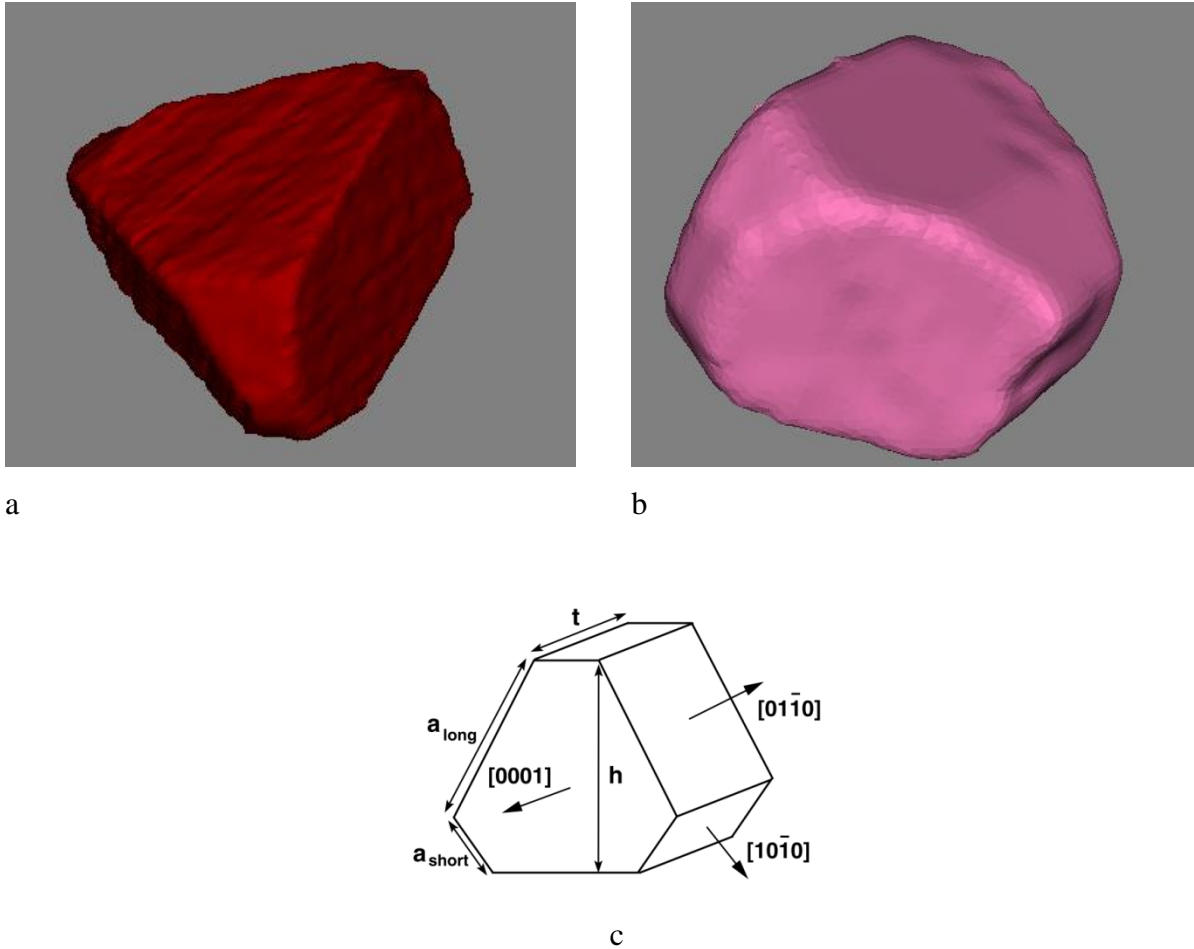
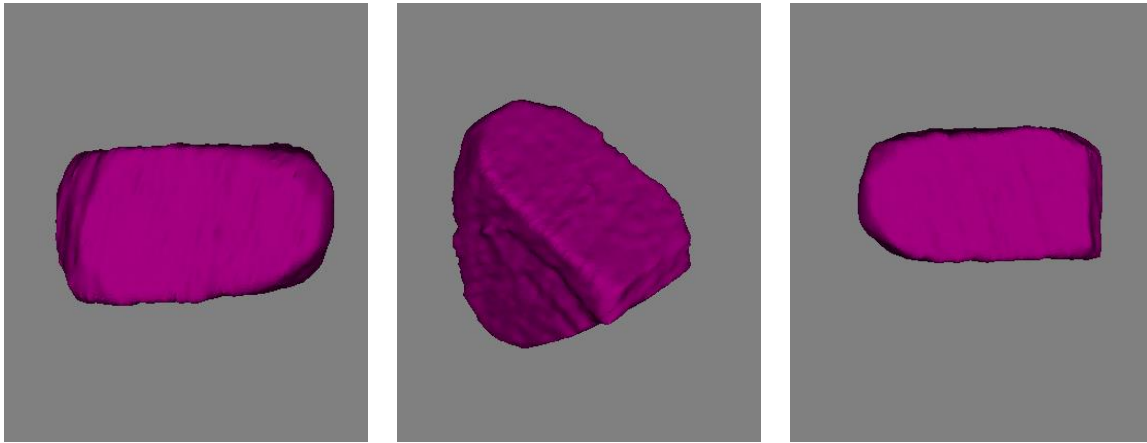


Figure 77: The grain shape truncation observed (a –C-rich- and b –W-rich) is different from the apparition of a type II prismatic plane as mentionned in the litterature (c).

The second principal observation is that in our material grains are truncated in a different way than what is presented in the literature. In fact, literature mentions a truncation of the shape by the development of type II prismatic plane. But in the analyzed samples this kind of truncation is not very developed compared to the truncation of the prism vertices that is mainly observed, and that does not correspond to a prismatic plane (Figure 77).

Often this truncation is not well established and the grain rather presents a rounded tip (Figure 78).



**Figure 78: Some grains present a rounded tip, where faceting is not well established.**

In conclusion, no significant change in grain shape is detected between C-rich and W-rich samples. However, literature results reported shape variations between crystals in the three-phase samples with different carbon content. The difference is then probably due to the larger change in carbon activity between C-rich and W-rich three phase samples. In addition, the equilibrium shape has been observed to be slightly different from what is usually reported in the literature. In particular a different truncation of the grains is observed.

## III.B 3D equivalent diameter distributions

Grain size evolution is presented through the 3D equivalent diameter variations, obtained from 2D measurements with the Saltykov reconstruction method. As evoked in the description of this method (II.D.2.i), the reconstruction is based on the hypothesis of a distribution of spherical particles. Thus, applying the method with a distribution of faceted grains may induce a significant error, even more if grain shape varies depending on the samples. Shape measurements made on 2D images (presented in III.A) did not reveal significant evolution of grain shape with composition or sintering time. It may be assumed that 3D equivalent diameter variations observed with sintering time or composition can be attributed to an effective variation of grain size, and 3D equivalent diameters of the different samples can be compared. These diameters are equivalent diameters of spheres which would give the same distribution of areas for the planar profiles.

The 3D equivalent diameter distributions are represented in Figure 79 (W-rich samples) and Figure 80 (C-rich samples) with frequency (a) and cumulative frequency (b) representations.

Two mechanisms can be involved in the process of increasing grain size: the dissolution of fine particles in the binder, for the system to reach the chemical equilibrium, and grain growth, namely a dissolution-precipitation process. As dissolution is a fast process occurring in the first moments of sintering, it can be considered as terminated after 1h sintering. Thus variations of grain size between 1h and 5h can be entirely assimilated to grain growth process. Unfortunately, between the powder and sintered samples it is not possible to distinguish the contribution of each mechanism in the light of the equivalent diameter distributions presented here. In addition, shape variations between the powder and 1h sintered samples make the analysis more complicated.

The first thing to note is the remarkable increase of grain size between the powder and sintered samples, traduced by a global shift toward higher equivalent diameter of frequency and cumulative frequency curves of sintered samples. This difference is too large to be attributed simply to shape variations. In addition, faceting and shape flattening tends to decrease the mean section area, thus the 3D equivalent diameter, so that the size variations between the powder and 1h sintered samples would rather be underestimated. The second difference between powder and

sintered samples distributions is the fraction of fine particles, present in the powder and that has been consumed in the sintered samples.

The evolution of sintered samples between 1h and 5h reveals a noticeable growth in either W-rich or C-rich samples. Evolution of the cumulative frequency (Figure 79 b) shows that the higher is the binder content, the more important the growth. However in C-rich samples the effect of binder content is not clear and would rather be responsible for the higher grain growth until 1h.

Considering the effect of the C/W ratio, it is particularly clear that C-rich samples present a higher grain size, as the distributions are shifted to the high equivalent diameters for all binder contents compared with W-rich samples.



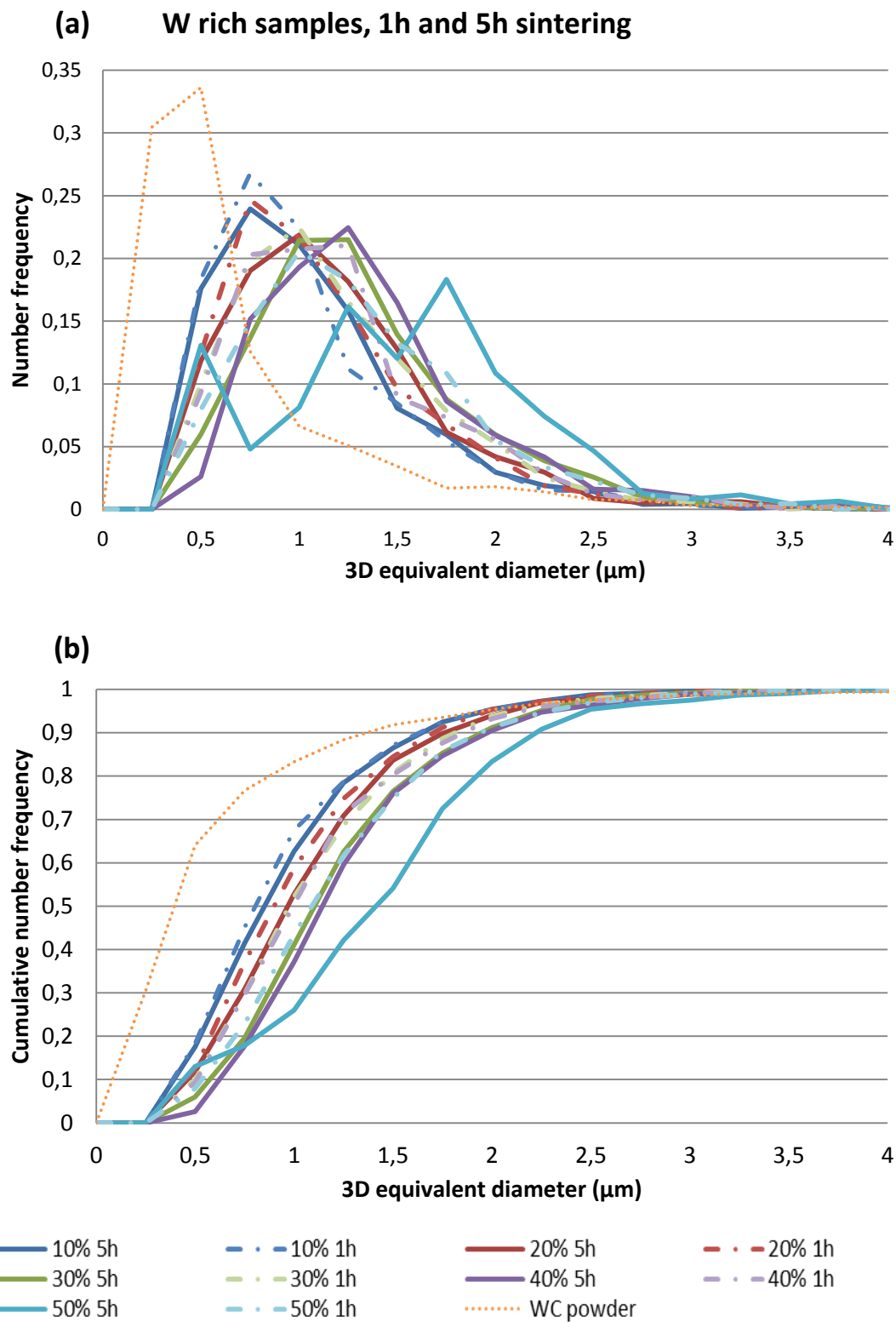


Figure 79: Frequency (a) and cumulative frequency (b) representation of 3D equivalent diameter distribution in W-rich samples with different binder contents, for 1h and 5h sintering time.

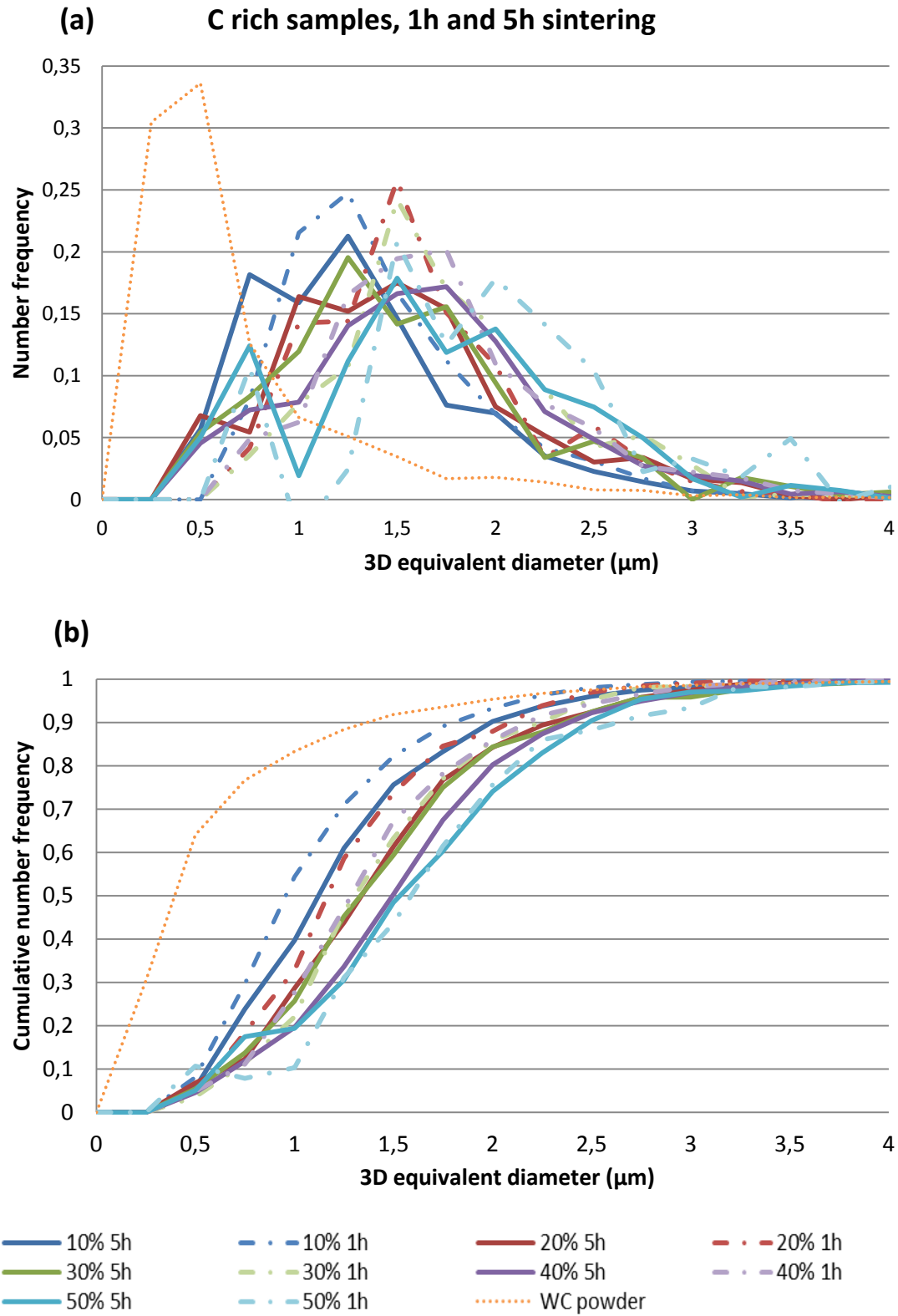


Figure 80: Frequency (a) and cumulative frequency (b) representation of 3D equivalent diameter distribution in C-rich samples with different binder contents, for 1h and 5h sintering time.

### III.C Evolution of mean grain size

Evolution of the mean grain size was investigated in order to study the growth of the microstructure.

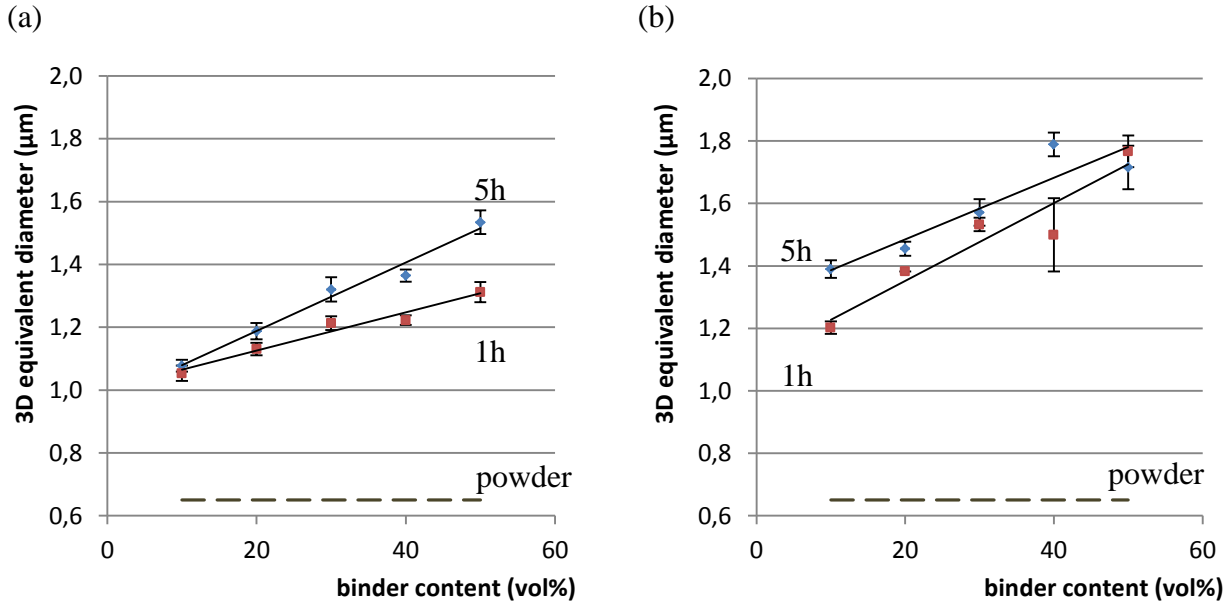


Figure 81: Evolution of mean 3D equivalent diameter in W-rich (a) and C-rich (b) samples.

As presented in Figure 81 the mean diameter increases significantly between the powder and the samples sintered for 1h at 1410°C, confirming observations made on equivalent diameter distributions. As proposed earlier, it can be attributed mainly to the dissolution of small carbide particles for the system to reach equilibrium with the liquid. It is illustrated by the micrographs in Figure 82. The effect of binder content on mean grain size after 1h can also be partially linked to the dissolution process. In fact high binder content implies to dissolve more WC to reach the equilibrium, but even less fine particles are available in the sample. Thus the range of particles size dissolved to reach equilibrium, consequently the mean grain size, increases with the binder content.

A contribution of grain growth (*i.e.* a dissolution-precipitation process) in the first hour of sintering is also very likely, but it is not possible to distinguish contributions of both mechanisms.

From the variations between 1h and 5h, it is possible to conclude that grain growth is increased by higher binder content in W-rich samples. The effect is maximal for the 50 vol% sample with a 17% increase of mean diameter between 1h and 5h. At the opposite, no significant growth is measured for the 10 vol% of binder sample, for which the system seems to be locked and not evolve anymore.

Evolution of the mean diameter in C-rich samples is different. First, after both 1h and 5h sintering time mean diameters in C-rich samples reach larger values than in W-rich samples, thus grain growth is significantly faster in C-rich samples. However, evolution between 1h and 5h is limited. In fact, the minimum growth is measured for 50 vol% sample and the maximum growth is measured for the 10 vol% sample. As it was observed in W-rich samples that high binder content increases grain growth, and that grain growth is faster in C-rich binder, it is reasonable to make the hypothesis that in the 50 vol% C-rich sample the system evolved fast enough to consume most of the driving force during the first hour of sintering. Thus no further evolution of the mean diameter is observed between 1h and 5h sintering. At the opposite, in the 10 vol% sample the growth is slowed down by the high amount of carbide, thus the system keeps growing between 1h and 5h sintering.

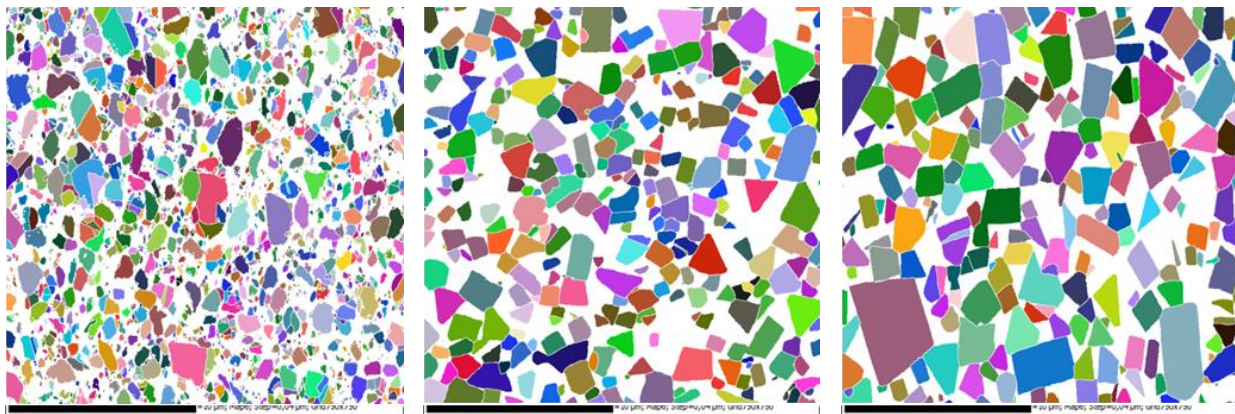


**Figure 82: Evolution of the microstructure with the sintering time. From left to right: powder, 1h sintering and 5h sintering (C-rich, 40 vol% of binder).**

### III.D Abnormal grain growth

The abnormal character of grain growth was analysed. As defined in the LSW theory (refer to p. 21) normal grain growth yields a self-similar evolution of the particle population. As a consequence, the grain size distribution becomes broader but the ratio of two characteristic sizes (average, minimum, maximum...) of the distribution remains constant. On the contrary, abnormal grain growth corresponds to a non-uniform evolution of the particle population. The abnormal character of grain growth was quantified by measuring the  $D_X$  particle size ( $X\%$  of the particles in the distribution have a diameter lower than  $D_X$ ). The  $D_{90}/D_{10}$  ratio should remain constant for normal grain growth, and is expected to be about 3 for reaction-limited kinetics. The evolution of this ratio is presented in Figure 83, for W-rich (a) and C-rich (b) samples.

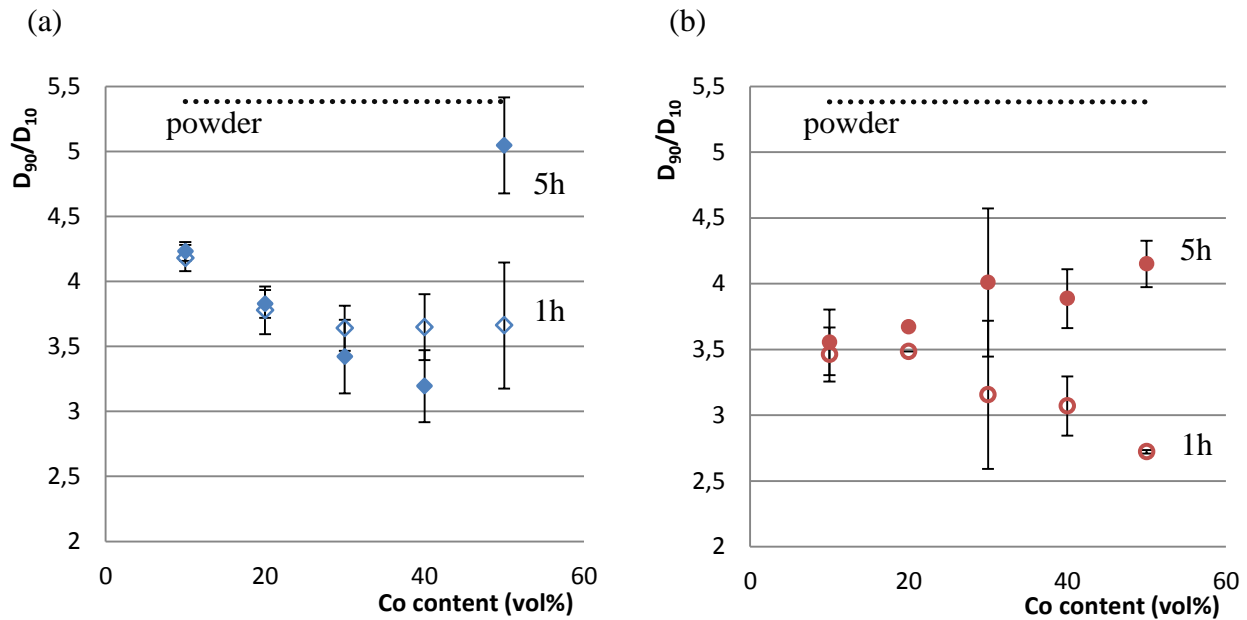


Figure 83: Evolution of  $D_{90}/D_{10}$  with cobalt content and sintering time for W-rich (a) and C-rich (b) alloys.

The  $D_{90}/D_{10}$  ratio tends to decrease until 1h sintering, likely due to dissolution of fine particles leading to the increase of  $D_{10}$  (Figure 83). The average value is not far from the value of the LSW theory for reaction limited kinetics. Between 1h and 5h this ratio hardly evolves for low binder contents. However a significant increase is noticed at large binder contents, which would be the sign of an abnormal character of grain growth. It can reach values as high as 5 for the 50 vol% of

binder, W-rich sample. The abnormal growth in this sample is also visible in the distribution of grain size presented earlier (Figure 79 a).

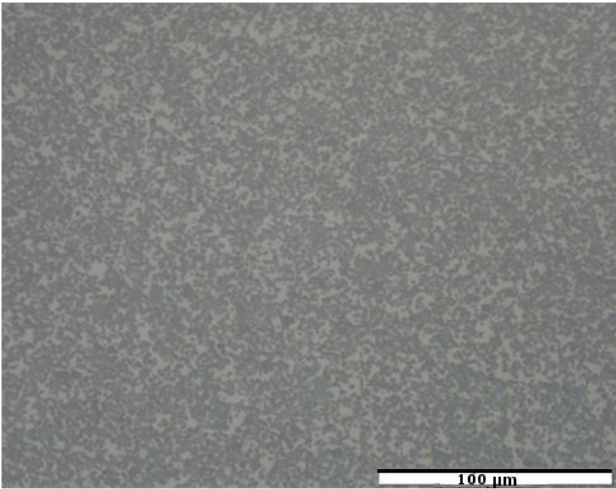
However, abnormal growth can lead to the development of very large grains. The observation field allowed by the EBSD study that led to the establishment of the measurements presented here can appear to be limited for the study of this phenomenon. Optical observation allows a wider field of observation and turns out to be complementary for the interpretation of  $D_{90}/D_{10}$  measurements.

In C-rich samples, optical observations confirm the occurrence of abnormal grain growth in high binder content samples, as shown with the example of 50 vol% of binder sample in Figure 84.

At the opposite, in the 50 vol% of binder W-rich sample the  $D_{90}/D_{10}$  ratio is higher, yet abnormal grain growth seems less marked (Figure 85). Other samples do not show abnormal growth evidences under optical observation.

Finally, it is shown here that the size distribution around the mean value tends to be less uniform with high binder content, with a higher amount of relatively larger grains. In carbon rich samples this tendency extends to abnormal grain growth at larger scale. This is consistent with results presented in Chabretou's thesis work [26] where high carbon content samples presented very large grains. At the opposite no evidence of abnormal growth is found at a large scale in tungsten rich samples. In the literature abnormal grain growth was observed in tungsten rich samples but at high sintering temperature or in the three-phase domain ([24], [25], [27] see I.B.2), whereas samples presented here were sintered in the two-phase domain and at lower temperature.

1h sintering



5h sintering

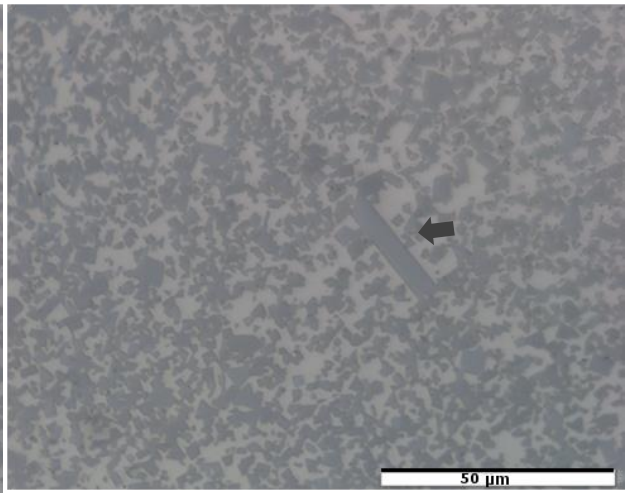
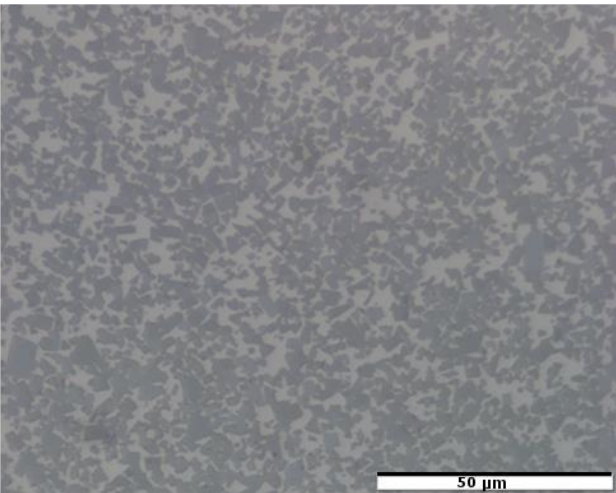
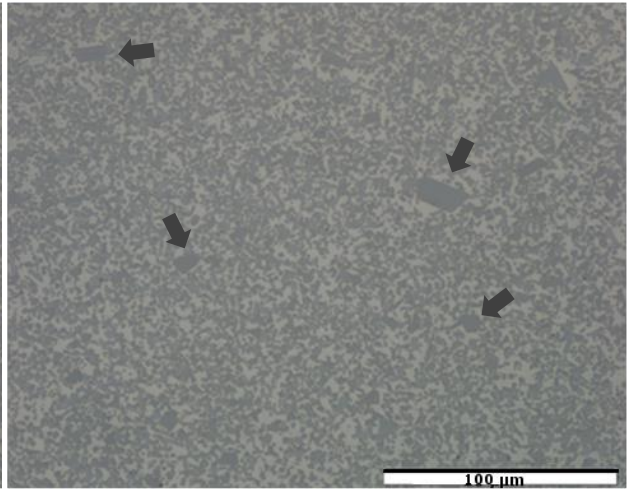
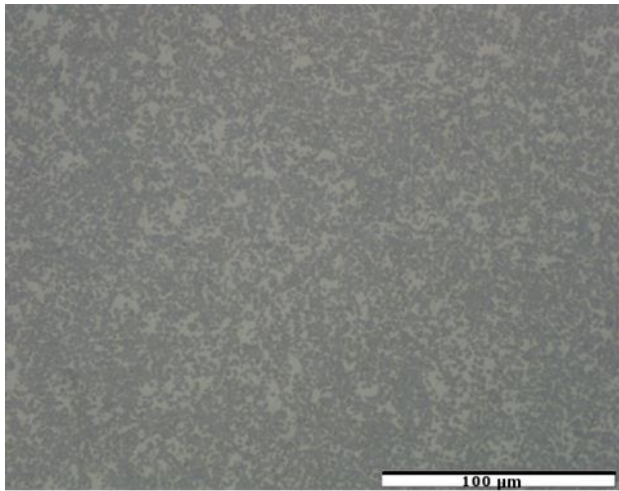


Figure 84: Optical observations of abnormal grain growth between 1h and 5h of sintering in 50 vol% of binder sample, C-rich. Large and very large grains are easily identifiable.



1h sintering



5h sintering

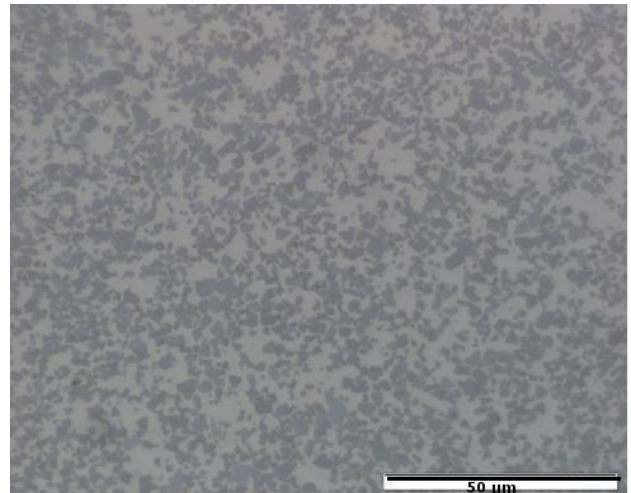
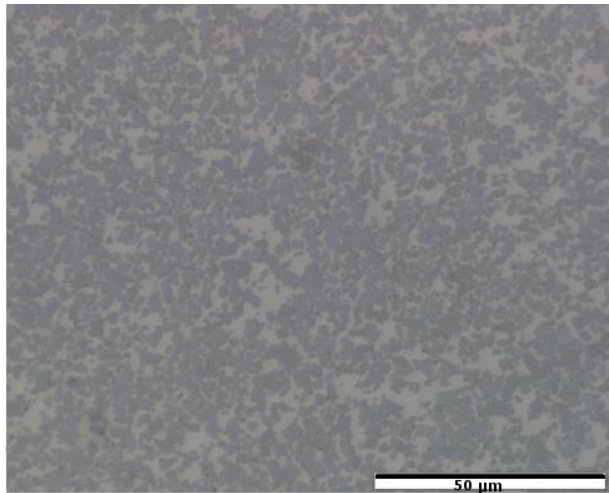
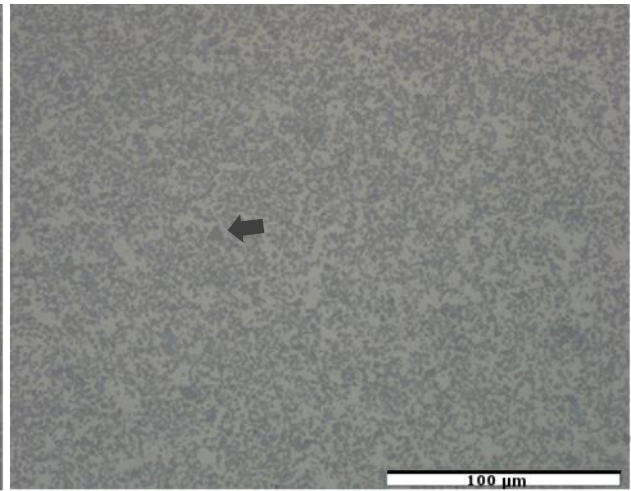


Figure 85: Optical observations of abnormal grain growth between 1h and 5h of sintering in 50 vol% of binder sample, W-rich. Some grains are large comparing with the matrix, but the difference is not as visible as in C-rich samples.



---

# Chapter IV Influence of C and Co on the interface development

## IV.A Evolution of contiguity

### IV.A.1 Measurements results

Contiguity was measured on the whole sample set in order to determine the influence of sintering time, carbon content in the binder, and binder content. Contiguity values are presented in Figure 86. Each value was measured on an EBSD image, and is represented with respect to the cobalt content measured on this image. In fact, because of the restrained field analyzed in each image, the statistical fluctuations of the composition at this scale have an influence on the apparent binder fraction (II.B.3).

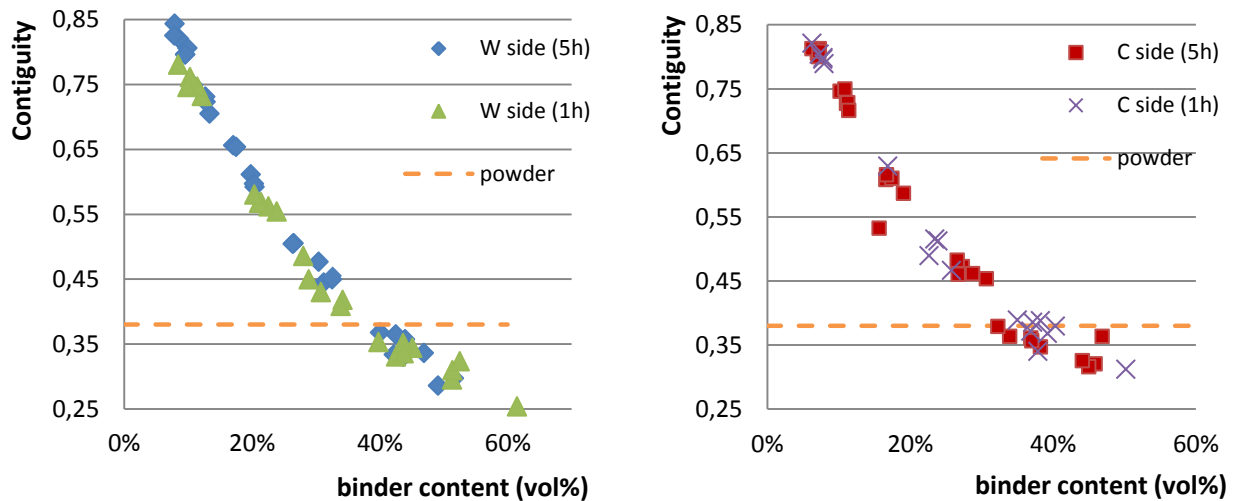


Figure 86: Contiguity values measured on W-rich (left) and C-rich (right) samples and on the powder.

### **IV.A.2 Influence of composition**

As shown in Figure 86, no significant evolution of the contiguity is to note between 1h and 5h of sintering. It indicates that equilibrium value of the contiguity has probably been reached after 1h. Also contiguity is constant despite the evolution of grain size with sintering time underlined for W-rich compositions in the precedent part, which indicates that phase boundaries and grain boundaries must develop at a similar rate during grain growth.

No significant difference is noticed between contiguity values of alloys with a C-rich or W-rich binder. However literature mentions a dependence of grain shape toward carbon content in the binder. Because of its influence on imbrication of particles, grain shape is expected to have an influence on contiguity. The independence of contiguity toward carbon content observed in this study indicates either that grain shape is a parameter of second order in the establishment of contiguity, or that grain shape is not significantly different in the two sets of samples analyzed. Shape factors measurements presented in the previous part and 3D shape observations are in favor of the second proposition.

Comparing the contiguity values measured in sintered samples and in the powder, it appears that contiguity in samples with binder content higher than 40 vol% is lower than in the powder. It would indicate either that more boundaries are destroyed than formed during sintering, or that phase boundaries significantly develop during sintering in the high binder content samples.

Finally, contiguity evolution shows a remarkable decrease when increasing the binder content. This important dependence of contiguity toward binder content is confirmed by a better fitting of the evolution of contiguity obtained when contiguity values are represented with respect to the binder content measured on the image rather than the mean binder content in the sample. Heterogeneity of binder distribution induces heterogeneity of contiguity. Thus, contiguity is very depending on impingement.

### **IV.A.3 Fitting of experimental values**

Because sintering time and carbon content do not significantly influence contiguity, all measurements were gathered to establish an empirical fitting. The best result is obtained with an

exponential fitting, with a correlation index of 0.957 (Figure 87). Examples of exponential fitting of contiguity are found in the literature as presented earlier. However at the opposite with results presented by Luycks, the evolution of contiguity does not seem to present a plateau for high binder contents.

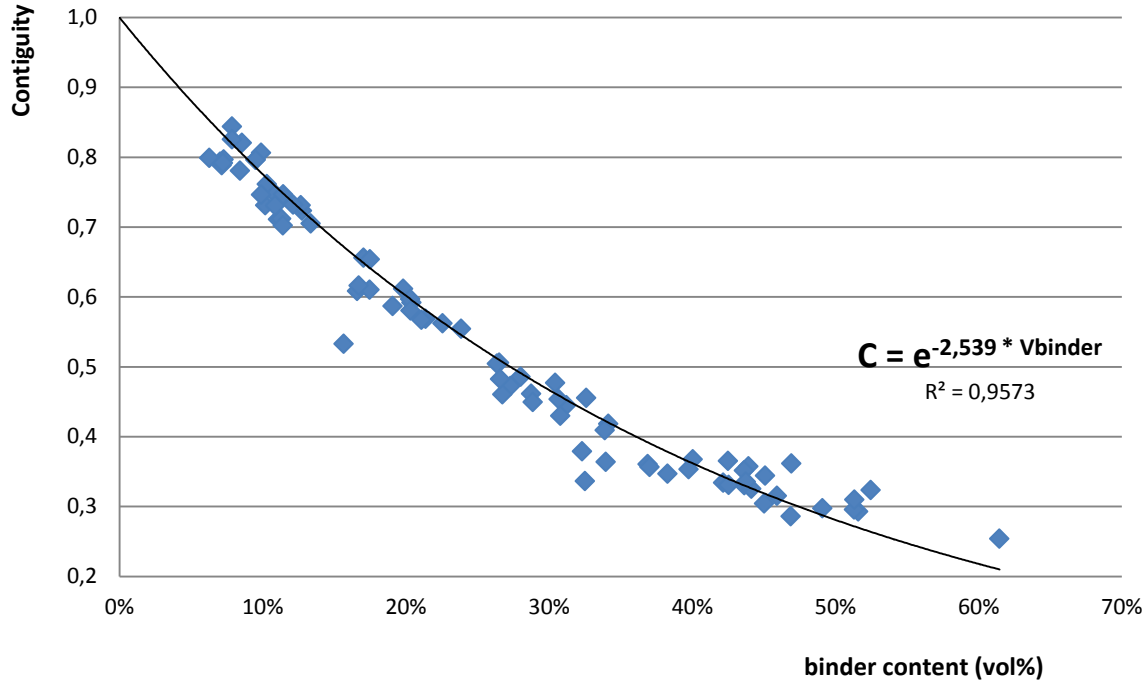


Figure 87: Experimental fitting of contiguity values.

#### IV.A.4 Comparison with literature value

Comparing with literature, contiguity values measured in this study are significantly higher, especially in the 20-40 vol% of binder range (Figure 88).

As already mentioned, literature values were obtained by manual measurement on SEM images. With this technic the segmentation of very coherent boundaries, as  $\Sigma 2$  boundaries for example, is difficult due to the feeble crystalline contrast. It is especially true at low binder fraction where the grain shape is of no help to deduce the presence of a boundary. In order to determine if the

population of  $\Sigma 2$  boundaries detected with EBSD could explain the discrepancy between literature and experimental values, contiguity was reappraised, excluding  $\Sigma 2$  type boundaries.

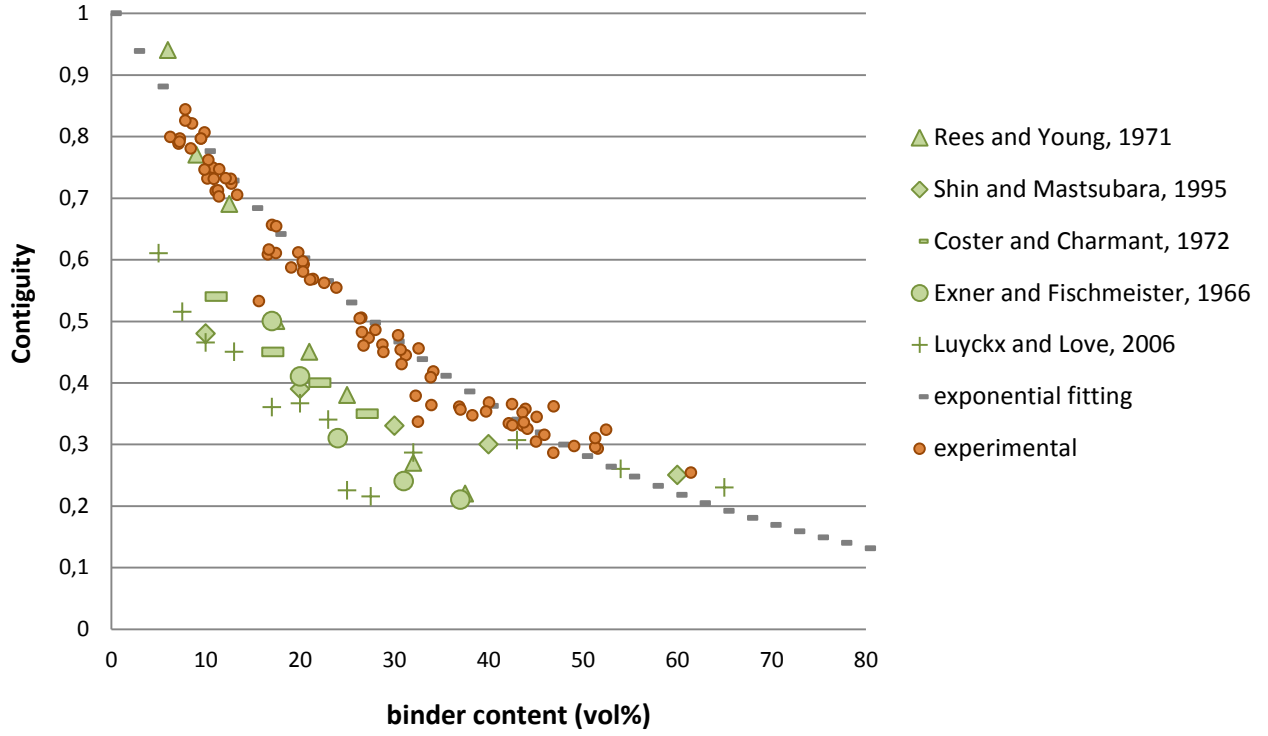


Figure 88: Comparison of experimental contiguity value with literature results.

To this end, the surface fraction of  $\Sigma 2$  boundaries was measured with the grain boundary characterization program, and used to calculate  $\Sigma 2$  partial contiguity. Partial contiguity represents the fraction of the grain surface occupied with  $\Sigma 2$  type boundary, and can be defined as follow:

$$C(\Sigma 2) = \frac{2 S_{\Sigma 2}}{2 S_{WC/WC} + S_{WC/Co}} \quad (4.1)$$

Contiguity value excluding  $\Sigma 2$  type boundaries is thus  $C - C(\Sigma 2)$ .

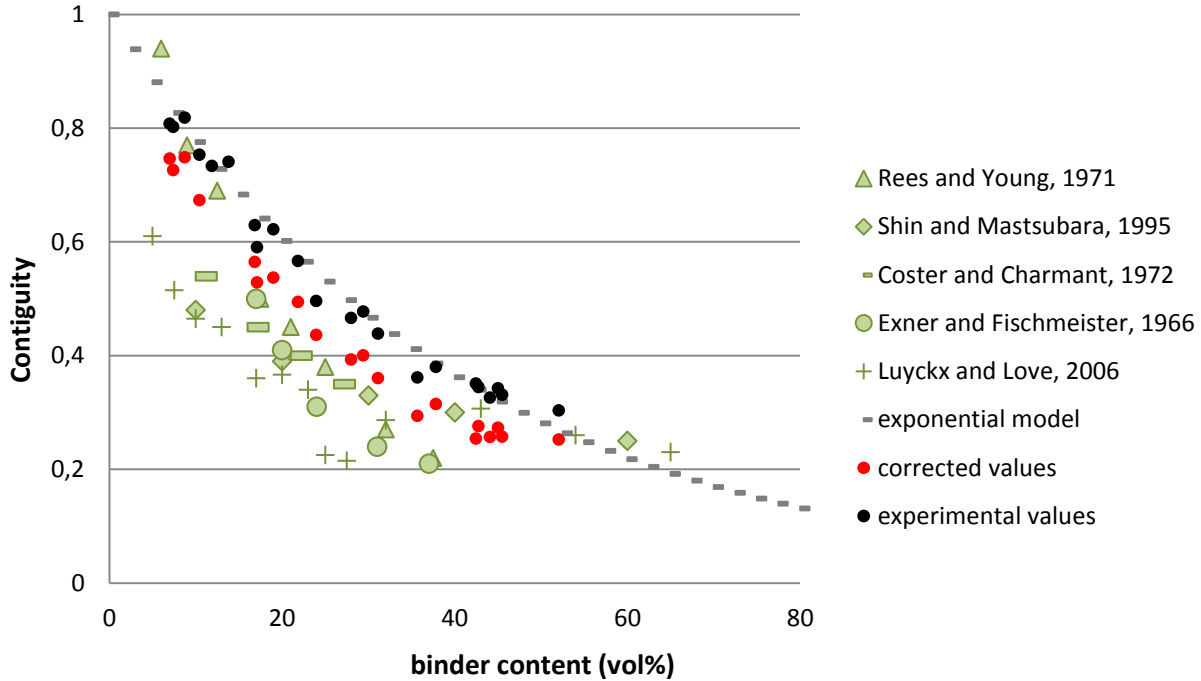


Figure 89: Calculated contiguity values without taking into account  $\Sigma 2$  type boundaries.

As seen in Figure 89, the decrease induced by the elimination of  $\Sigma 2$  boundaries partially compensates the discrepancy between literature and measured values. However, contiguity values measured between 20 vol% and 40 vol% of binder are still slightly higher than literature values.

Nonetheless, it is important to note that considering that  $\Sigma 2$  boundaries are systematically excluded of manual contiguity measurement is a rough correction, as some of them (as other boundaries) can be deduced from the global microstructure even without crystalline contrast. In addition, other effects can be expected to lead to overestimate contiguity either induced by the EBSD method (the non-detection of small binder regions for example, see II.B.3 or by the microstructure (curved boundaries).

Finally, actual contiguity values are probably in between values obtained from SEM observations in the literature, which underestimate the fraction of special boundaries, and our EBSD values, which overestimate the grain boundary fraction by missing thin binder areas.

## IV.B Phase boundaries distribution

The results presented in this part were all obtained from the analysis of EBSD images with the grain boundary analysis program described in II.D.4. Notations used in this part to express results are fully described in II.D.1.

### IV.B.1 Influence of composition on grain boundary development

#### IV.B.1.i Evolution of the number of grain boundaries

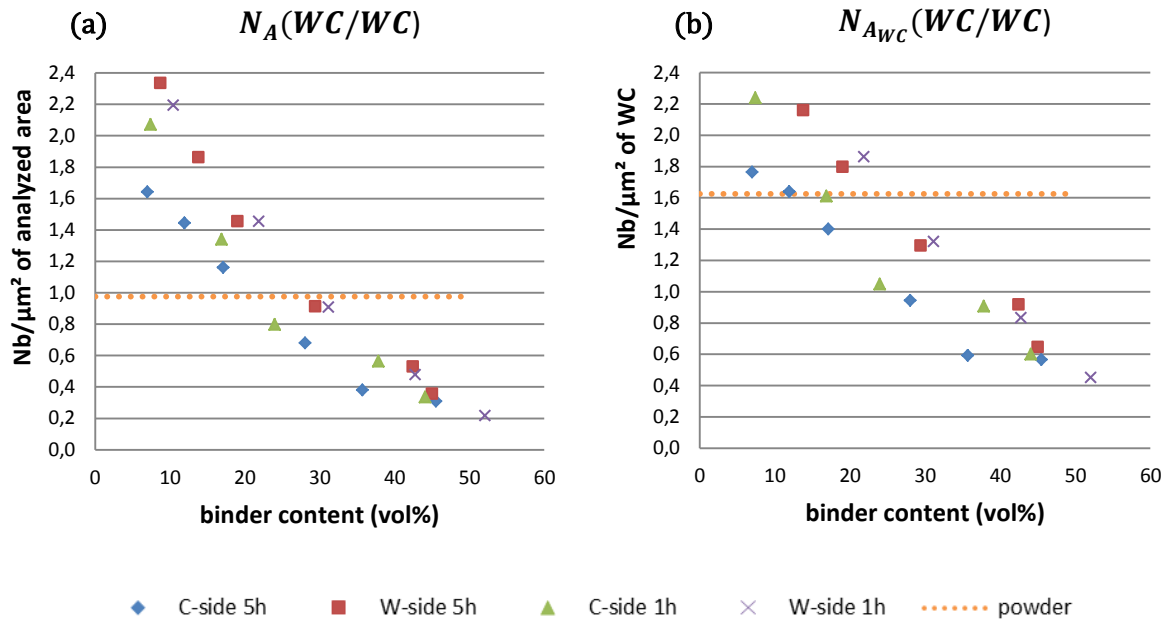


Figure 90: Evolution of the number of grain boundaries per unit of analyzed area  $N_A(WC/WC)$  (a) or per unit of carbide area  $N_{A_{WC}}(WC/WC)$ .

The evolution of  $N_A(WC/WC)$  and  $N_{A_{WC}}(WC/WC)$ , represented in Figure 90, shows a substantial decrease of the number of grain boundaries when the binder content increases. Considering  $N_A(WC/WC)$ , this evolution is expected as decreasing the carbide quantity leads to

a diminution of the number of grains. This effect is taken into account and corrected in  $N_{A_{WC}}(WC/WC)$ . Still an effect of the binder content is to note, which can be easily attributed to the diminution of impingement as the binder content increases. However, another parameter must be considered as participating to this large decrease: grain growth. As discussed in the previous chapter, grain growth is significantly different between low binder content and high binder content samples, and the bigger the grain size, the fewer the grains (so the boundaries) observed in the same area. This effect may also be one of the explanations for the consequent discrepancy between the number of grain boundaries in C-rich and W-rich samples, while contiguity is the same in both.

Likewise, no conclusion can be made from these results concerning the differences between the number of grain boundaries in sintered samples and in the powder.

#### IV.B.1.ii Evolution of the grain boundaries surface area

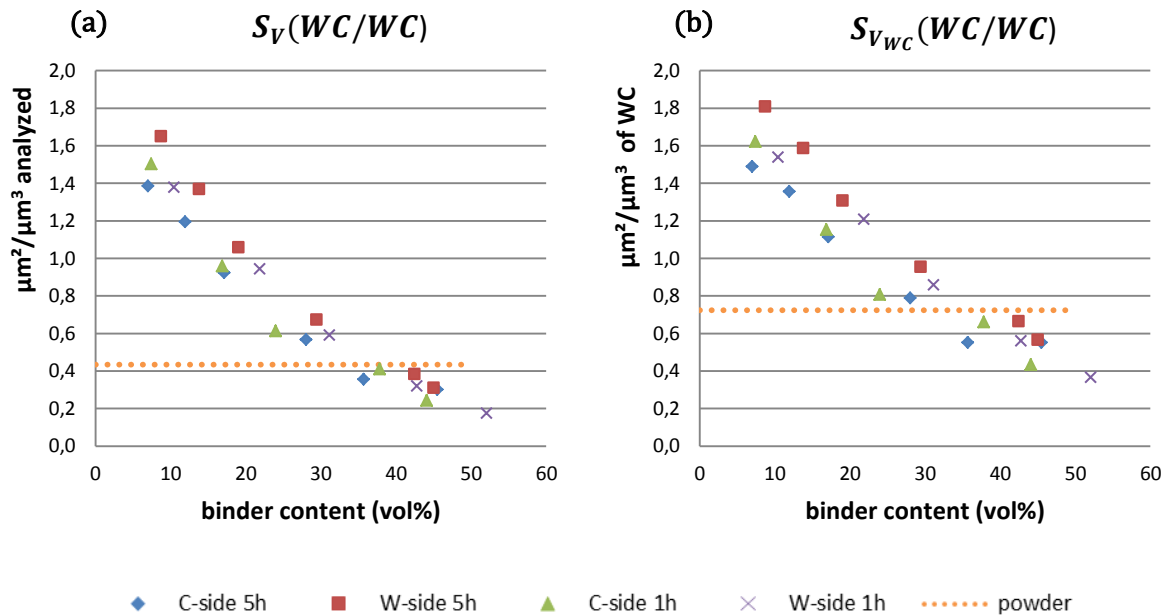
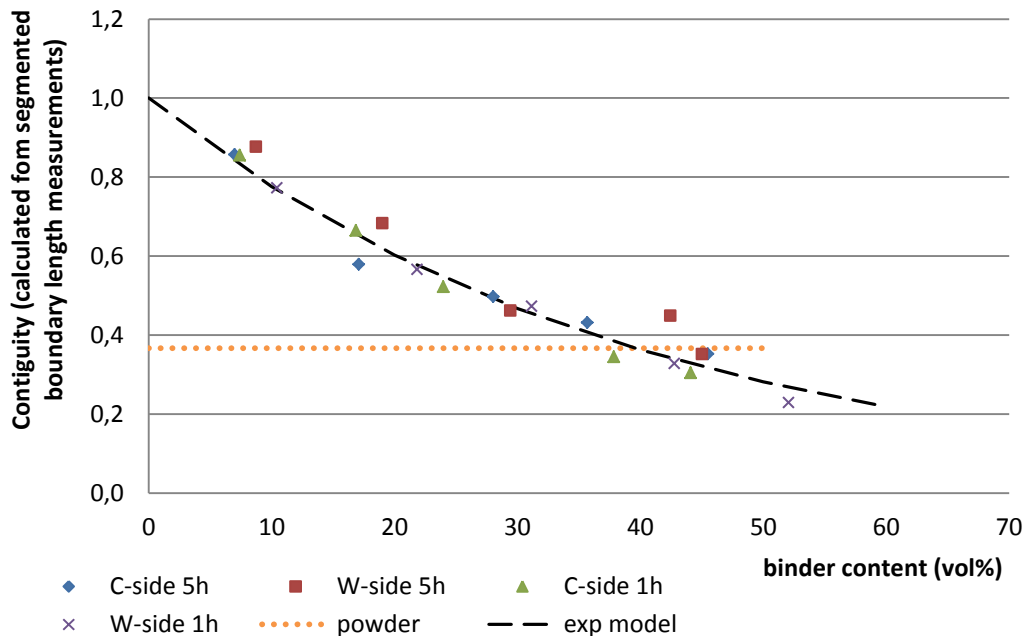


Figure 91: Evolution of the grain boundaries surface area per unit analyzed volume (a) or per unit carbide volume (b).

The variations of boundary surface area with binder content or C/W ratio (Figure 91) are similar to variations of the number of boundaries, yet the variation range is smaller. As for the evolution of the number of grain boundaries, the influence of grain growth limits the interpretation.

However, it is interesting to compare the surface area of grain boundaries (WC/WC) to the surface area of phase boundaries (WC/Co) of the grains. Thanks to the program, it has been possible to calculate the surface area of grain boundaries and phase boundaries, and then determine contiguity as for the global analysis of phase boundaries (IV.A). If the contiguity measurements presented here can appear as redundant, they are in fact measured with a fundamentally different method. Instead of working globally on all phase boundaries of the image, this method detects and segments each grain boundary and phase boundary.

Hence, the good agreement between contiguity values obtained from the segmented boundary length and the global measurements presented in IV.A125 tends to attest the validity of both methods, and especially of the phase boundary segmentation program.



**Figure 92:** Comparison of contiguity values obtained from measurement of the segmented boundary length, compared with the exponential modeling obtained by fitting global contiguity measurements (IV.A).



## IV.B.2 Evolution of grain boundary type population

### IV.B.2.i Distribution of rotation axes

The first step in the analysis of grain boundary population was to determine the distribution of rotation axes in order to identify preferential axes. These distributions were determined thanks to the program described in II.D.4 and results are expressed in the fundamental trihedron (II.D.4.ii). The surface area frequency is expressed in multiples of the random distribution (MRD). Axes presenting a frequency above 1 MRD can be considered as remarkable since it is particularly abundant compared to a random, isotropic distribution.

The following Figure 93 presents the distribution of rotation axes detected in the whole set of sintered samples, in comparison to the distribution in the powder.

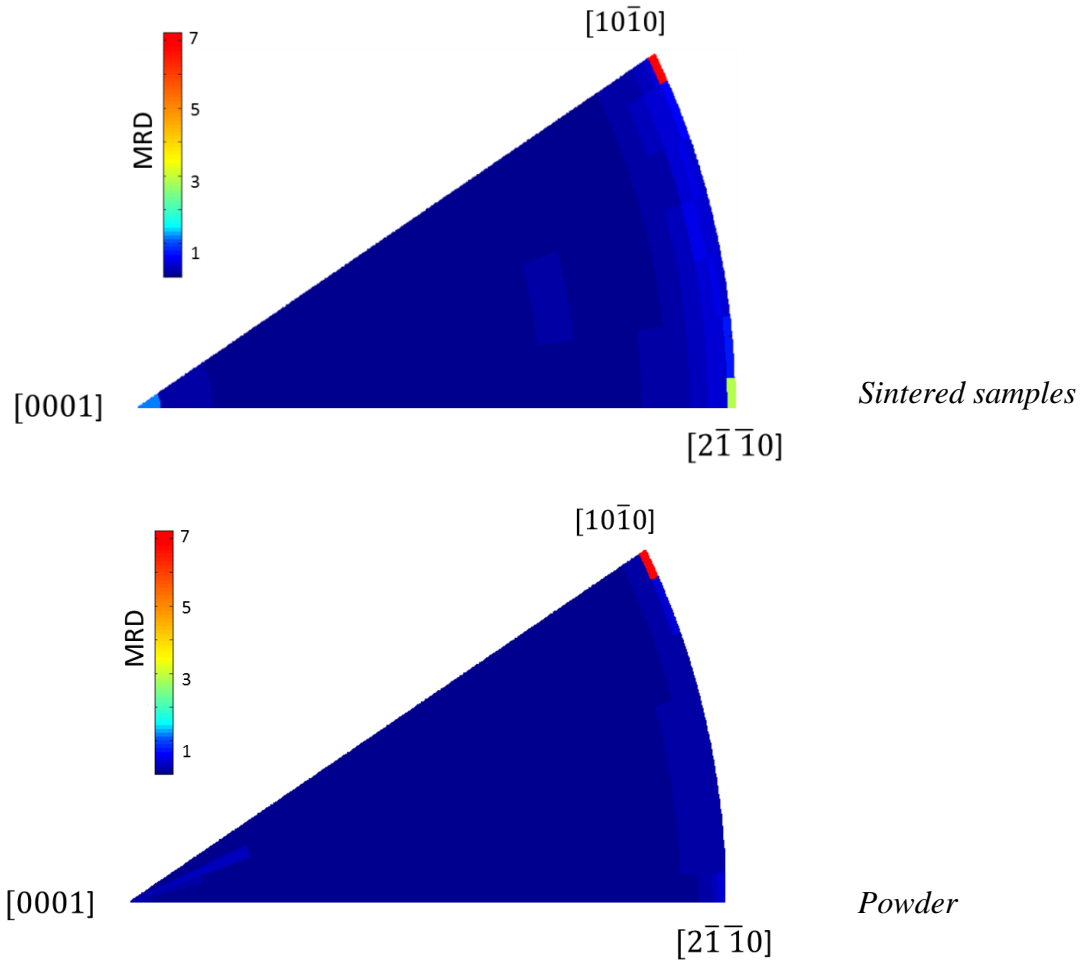


Figure 93: Comparison of rotation axes distribution in all sintered samples and in the powder (boundary area in MRD).

Three rotation axes stand out from global distribution. Rotations around  $[10\bar{1}0]$  are found to be very abundant in all samples, included in the powder. Rotations around  $[2\bar{1}\bar{1}0]$  are also found in large amount in every sintered sample, yet not particularly in the powder. Finally,  $[0001]$  rotations are significantly more represented than expected in a random distribution in sintered samples, but not in the powder. Observation of these rotation axes in large quantities in sintered samples is fully consistent with literature results (I.C.6), where  $90^\circ/[10\bar{1}0]$  ( $\Sigma 2$ ),  $30^\circ/[0001]$  and  $90^\circ/[2\bar{1}\bar{1}0]$  rotations are often mentioned. It also corresponds to the 3 main families of axes allowing good coincidence of lattices on both sides of the boundary.

Furthermore, a detailed analysis of distributions in the different samples reveals that the abundance of these axes depends on the composition. The frequency of the three particular rotations (measured within  $\pm 5^\circ$  of one axis of a given family) has been evaluated as a surface area in MRD and as a fraction of the total boundary area (Figure 94). The measure in MRD informs on the remarkable character of an axe, and the surface fraction informs on the proportion of such boundaries in the global boundary population.

***Rotations around  $[10\bar{1}0]$ : (a) and (b)***

No substantial influence of C/W ratio on the evolution of the surface area fraction (% or MRD) is observed. Then, C/W would have a limited influence on  $[10\bar{1}0]$  grain boundary stability. Likewise, no particular evolution of the population is noticed between 1h and 5h sintering, implying that  $[10\bar{1}0]$  grain boundaries grow at the same rate as the global boundary population.

Surface fraction of  $[10\bar{1}0]$  grain boundary remarkably increases with binder content, from 10% in the 10 vol% samples to more than 20% in the 50 vol% samples. Because the total surface area of grain boundaries decreases in the same range, the  $[10\bar{1}0]$  grain boundary area is more or less constant with binder content.

***Rotations around  $[2\bar{1}\bar{1}0]$ : (c) and (d)***

As for  $[10\bar{1}0]$  boundaries, C/W ratio and sintering time do not seem to have any significant influence on the population of  $[2\bar{1}\bar{1}0]$  boundaries.

Surface fraction of  $[2\bar{1}\bar{1}0]$  grain boundaries is half the  $[10\bar{1}0]$  boundaries surface fraction, but also remarkably increases with binder content, from 6% in the 10 vol% samples to more than

12% in the 50 vol% samples. Thus  $[2\bar{1}\bar{1}0]$  grain boundaries are more frequent in high binder content samples although their total area is about the same.

***Rotations around [0001]: (c) and (d)***

[0001] boundaries represent a low fraction of the total boundary surface in the samples: around 1%. They are none the less remarkable since they are up to five times more frequent than in a random distribution. Additionally it is expected to find less [0001] boundaries in the microstructure as it presents only two equivalent positions in the crystal, instead of six for  $[10\bar{1}0]$  or  $[2\bar{1}\bar{1}0]$  rotations.

Because of the low statistics, no influence of sintering time or C/W ratio can be detected.

Last, partial contiguity (Figure 95) was also calculated from the measurements, to overcome the influence of grain size, thus grain growth. At the opposite with the surface area fraction, partial contiguity pictures the amount of a boundary type in the actual microstructure, compared to other types of interfaces (other grain boundaries, phase boundaries...).

For the three remarkable axes the partial contiguity does not vary with C/W ratio or sintering time, in agreement with previous conclusions, and is slightly sensitive if not insensitive to binder content. It means that the surface area fraction of a grain occupied by these types of boundaries does not vary. Considering that global contiguity decreases in the same time, it can be concluded that those grain boundaries are particularly stable and resist to infiltration or are preferentially formed compared to random boundaries.

$[10\bar{1}0]$  partial contiguity is slightly lower in sintered samples than in the powder. At the opposite  $[2\bar{1}\bar{1}0]$  and [0001] partial contiguities is very low in the powder (around 0.1), suggesting that these types of boundaries are essentially formed during sintering.

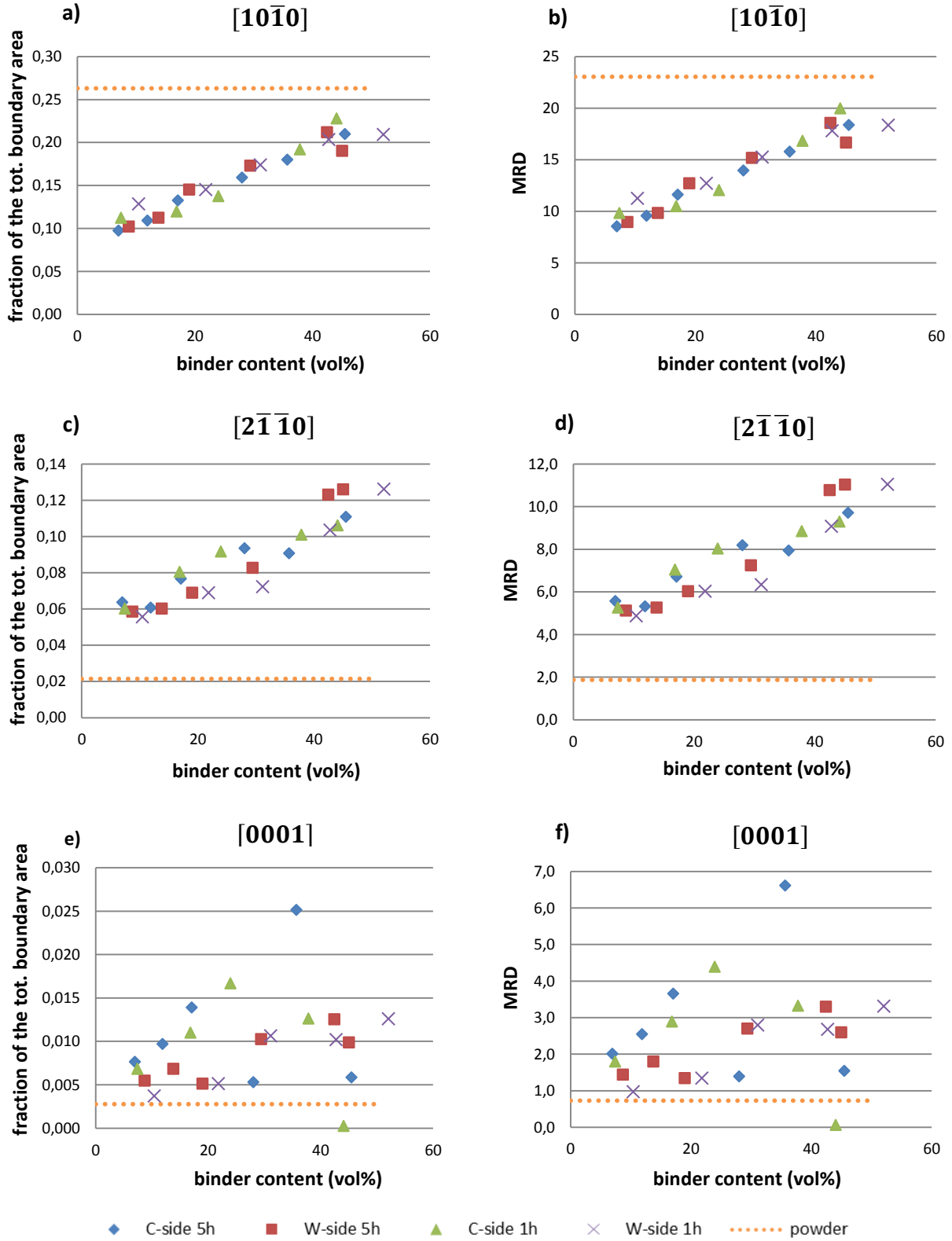


Figure 94: Evolution with composition of rotations axes population for the three remarkable axes. The frequency is evaluated as a fraction of total boundary area (a, c and e) and MRD (b, d and f).

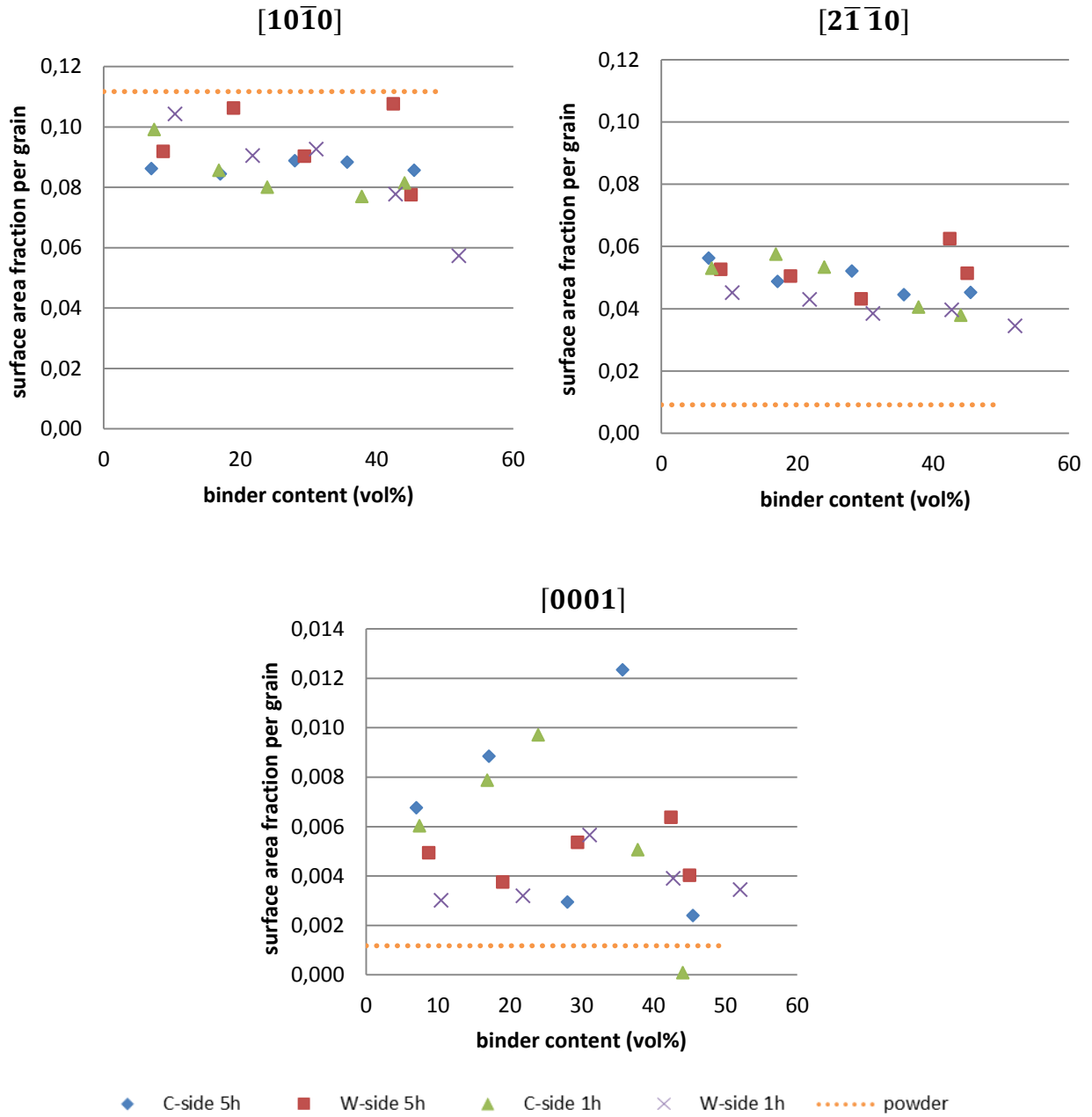
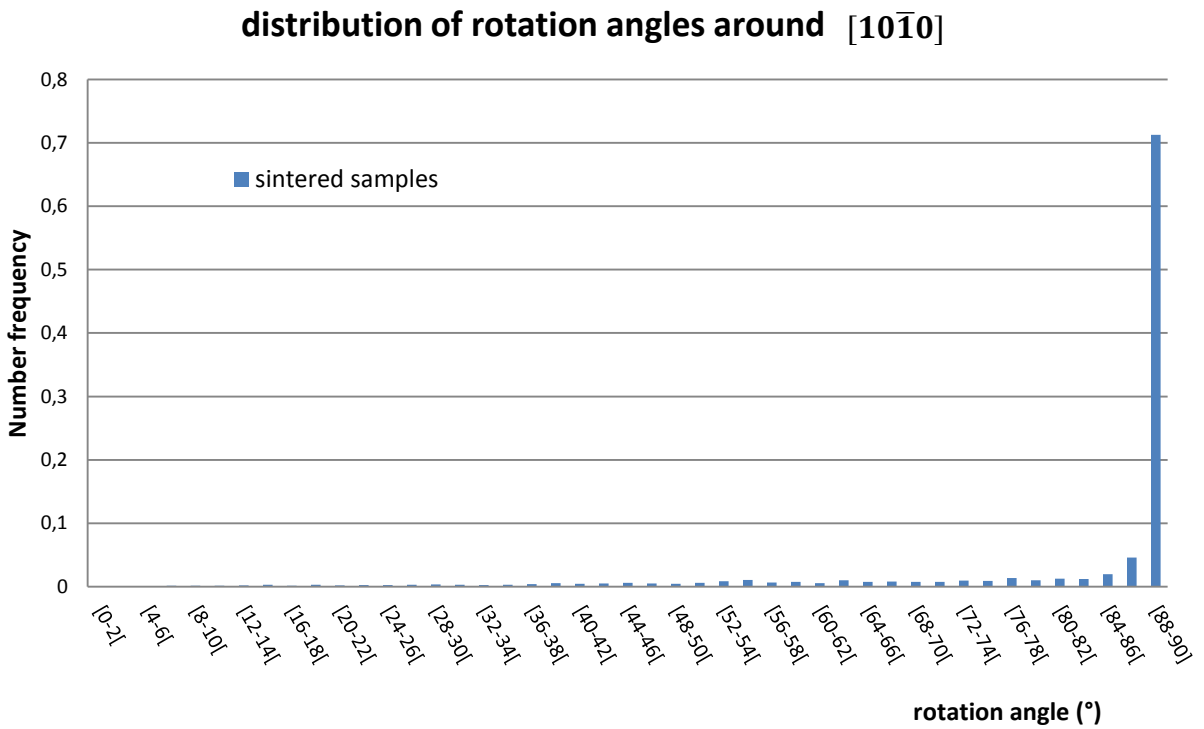


Figure 95: Partial contiguity measured for each remarkable axis.

IV.B.2.ii **Rotation angles**

The previous analysis of rotation axis distribution highlights three particular rotation axes. The purpose of this part is to focus on the rotation angles associated with these axes, in order to identify preferential [axis/rotation] couples.

Rotation angles of boundaries identified as rotations around  $[0001]$ ,  $[2\bar{1}\bar{1}0]$  or  $[10\bar{1}0]$  were extracted in order to establish the rotation angle distributions around these axes. Because angle distributions obtained for each sample are very similar (even after 1h or 5h sintering), it was chosen to gather all angle data in a global angle distribution for each axis, in order to increase the statistical representability of observations.

***Rotations around  $[10\bar{1}0]$ :***

**Figure 96: Distribution of rotation angles around  $[10\bar{1}0]$  in sintered samples. Misorientation data of all samples (1h and 5h sintering, and C-rich and W-rich composition).**

As the distribution in Figure 96 puts in evidence, the most part of rotations around  $[10\bar{1}0]$  can be associated to a  $90^{\circ}$  rotation angle, as the  $[88^{\circ}-90^{\circ}]$  range represents approximately 71% (number

fraction) of the  $[10\bar{1}0]$  population. This  $[10\bar{1}0]/90^\circ$  rotation corresponds to the  $\Sigma 2$  configuration in the CSL description (Table 6). As illustrated in Figure 97, the  $90^\circ$  misorientation is not always rigorously respected, and grain boundaries with a small deviation are often encountered.

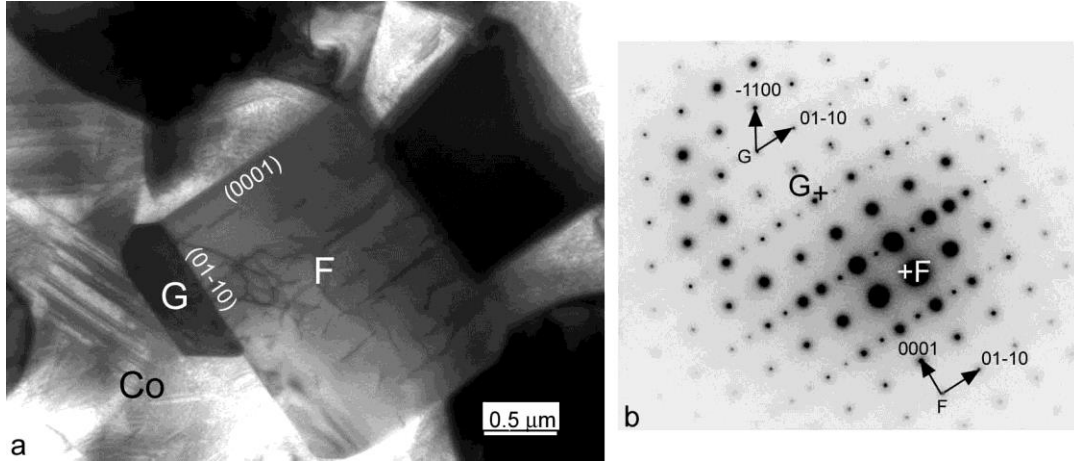


Figure 97: Grains F and G are observed along their  $[2\bar{1}10]$  and  $[0001]$  axis respectively. Diffraction diagram reveals a  $1.3^\circ$  misorientation around  $[01\bar{1}0]$  between zone axes of the two grains, thus a  $88.7^\circ$  misorientation around  $[01\bar{1}0]$ . Observation made in a 5h sintered, W-rich and 50 vol% of binder sample.

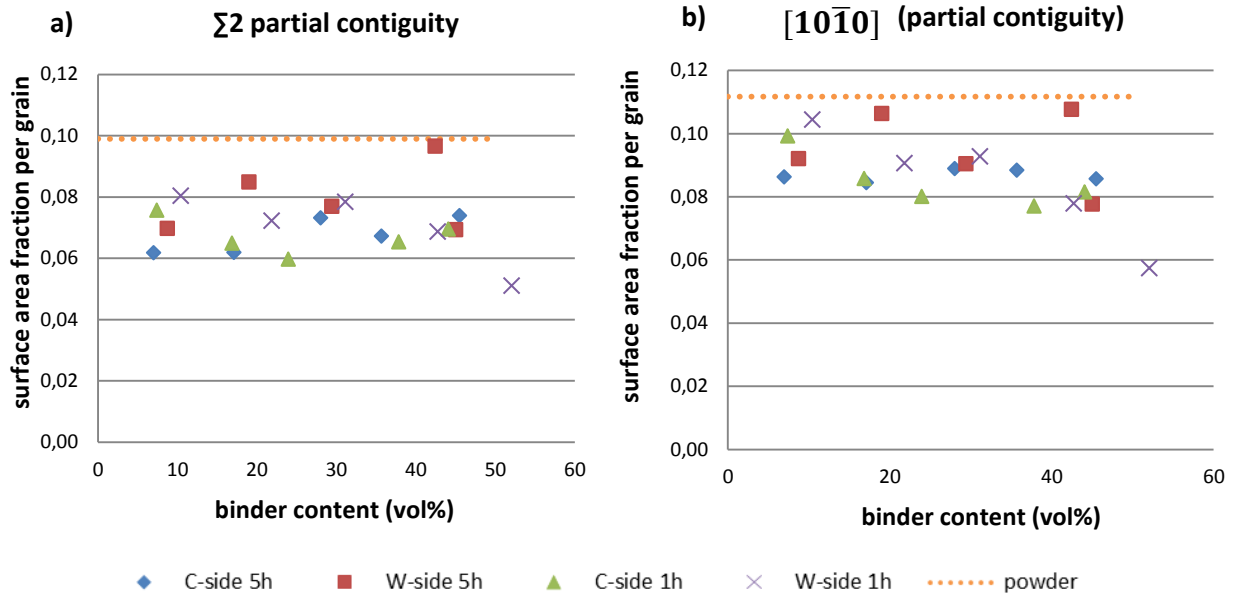


Figure 98: Partial contiguity of  $\Sigma 2$  grain boundaries (a) compared to the partial contiguity of  $[10\bar{1}0]$  grain boundaries (b).

In order to quantify the  $\Sigma 2$  boundary abundance and in addition to number frequency values, the  $\Sigma 2$  partial contiguity was measured in parallel with partial contiguity of  $[10\bar{1}0]$  boundaries (Figure 98).

Comparing the partial contiguity of  $[10\bar{1}0]$  rotations and  $\Sigma 2$  confirms that boundaries described with rotations around this axis are mainly  $\Sigma 2$  boundaries whatever the composition (between 75% and 80% of the surface area, depending on the sample).  $\Sigma 2$  partial contiguity does not seem to be influenced by composition, and after sintering keeps close from the value measured in the powder.

The hypothesis that  $\Sigma 2$  boundaries could originate from the powder is sometimes found in the literature (I.C.5). It has been shown in the previous part that the amount of  $[10\bar{1}0]$  boundaries in the powder and sintered samples are similar. The distribution of rotation angles around  $[10\bar{1}0]$  in the powder (Figure 99) shows that 65% (number fraction) of the rotations around  $[10\bar{1}0]$  are  $\Sigma 2$  boundaries, *i.e.* close to the fraction in sintered samples (70%, number fraction).

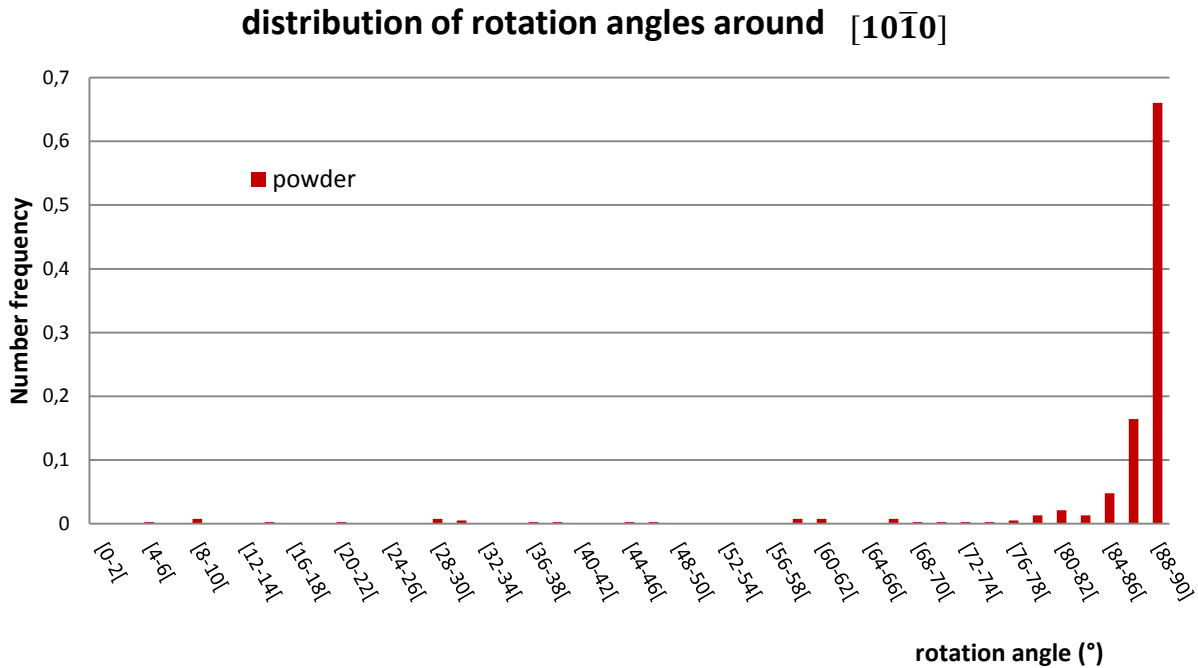
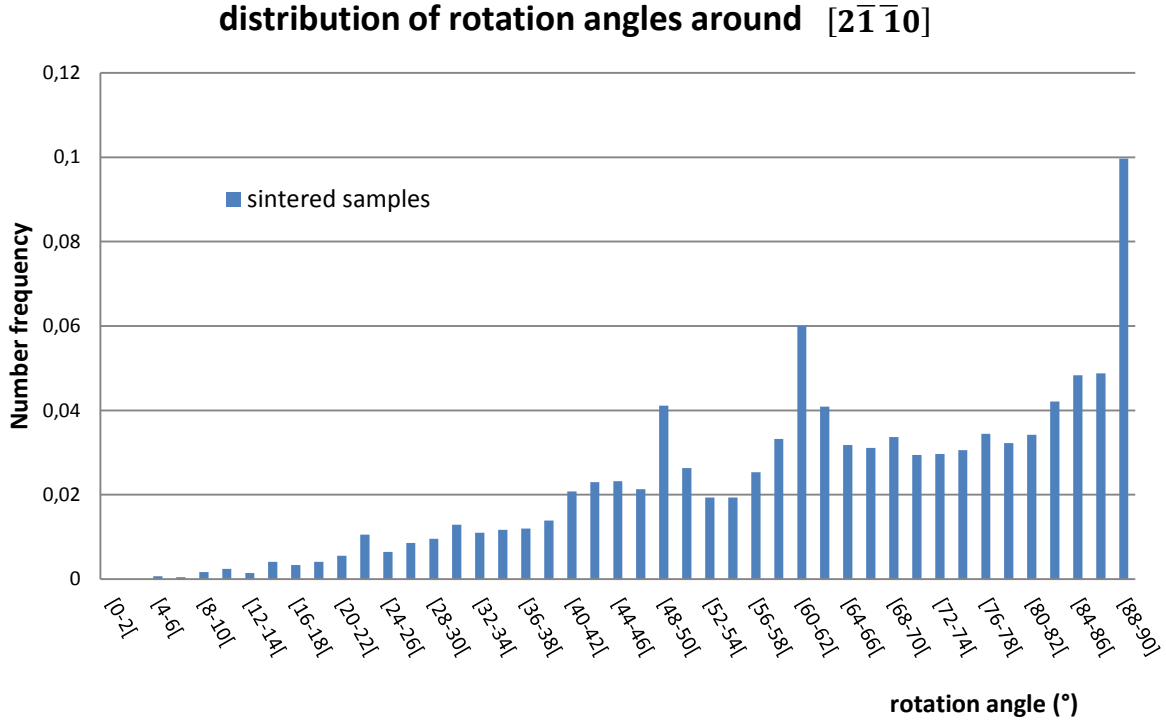


Figure 99: Distribution of rotation angles around  $[10\bar{1}0]$  in the powder.



**Rotations around  $[2\bar{1}\bar{1}0]$ :**

**Figure 100: Distribution of rotation angles around  $[2\bar{1}\bar{1}0]$ . Misorientation data of all samples (1h and 5h sintering, and C-rich and W-rich composition).**

The distribution is more contrasting concerning rotations around  $[2\bar{1}\bar{1}0]$ . Three main peaks are rising from the random distribution. The  $c/a=1$  CSL theory could explain the position of the main peak in the  $[60-62]^\circ$  range, which is consistent with  $\Sigma 4$  boundaries, described as  $[2\bar{1}\bar{1}0]/60^\circ$ . At the opposite the two other peaks do not fit with a CSL. The  $c/a=1$  approximation is assumed to be the main reason for not identifying all the peaks with a CSL configuration.

Therefore, the most coherent interfaces resulting from a rotation around  $[2\bar{1}\bar{1}0]$ , considering the real  $c/a$  ratio attached to WC crystal system, were determined. In order to simplify the different possible configurations, the grain boundary plane was assumed lying in a remarkable plane (basal or prismatic) for one of the two grains, and one of the densest planes ( $h0k\bar{l}i$ ) for the other. In fact densest planes are more likely to generate a high coherency interface. Thus, a list of the densest planes, with the respective rotation angle, was determined (Figure 101). It appears that three

rotations could explain the peaks in the distribution:  $[2\bar{1}\bar{1}0]/48.42^\circ$  with a basal/ $(10\bar{1}1)$  interface,  $[2\bar{1}\bar{1}0]/60.59^\circ$  with a prismatic/ $(10\bar{1}2)$  interface, and  $[2\bar{1}\bar{1}0]/90^\circ$  with a prismatic/basal interface. Two of those boundaries are illustrated in Figure 102.

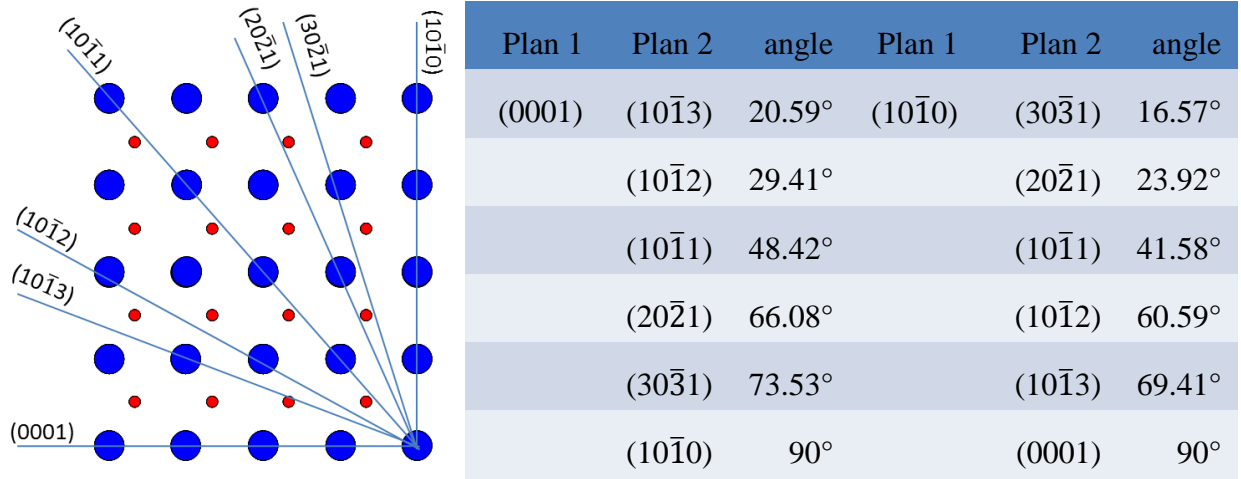


Figure 101: Representation of the densest planes (with a maximum index of 3) which are parallel to  $[2\bar{1}\bar{1}0]$  in WC crystal (left), and the list of angles between these planes and remarkable planes (right).

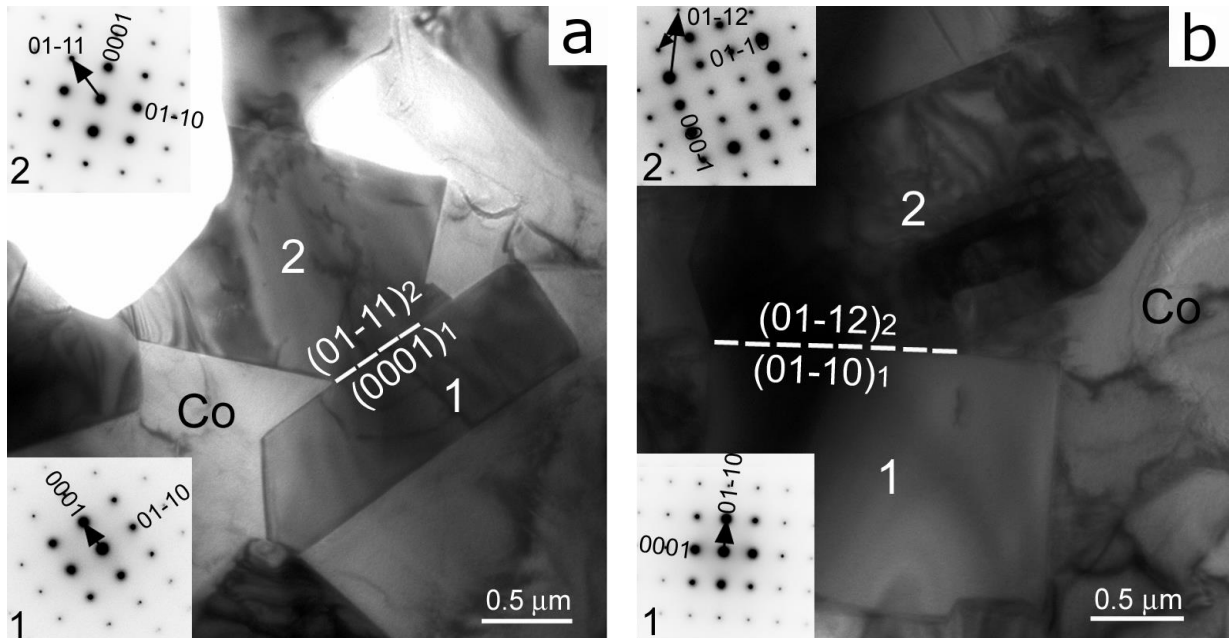
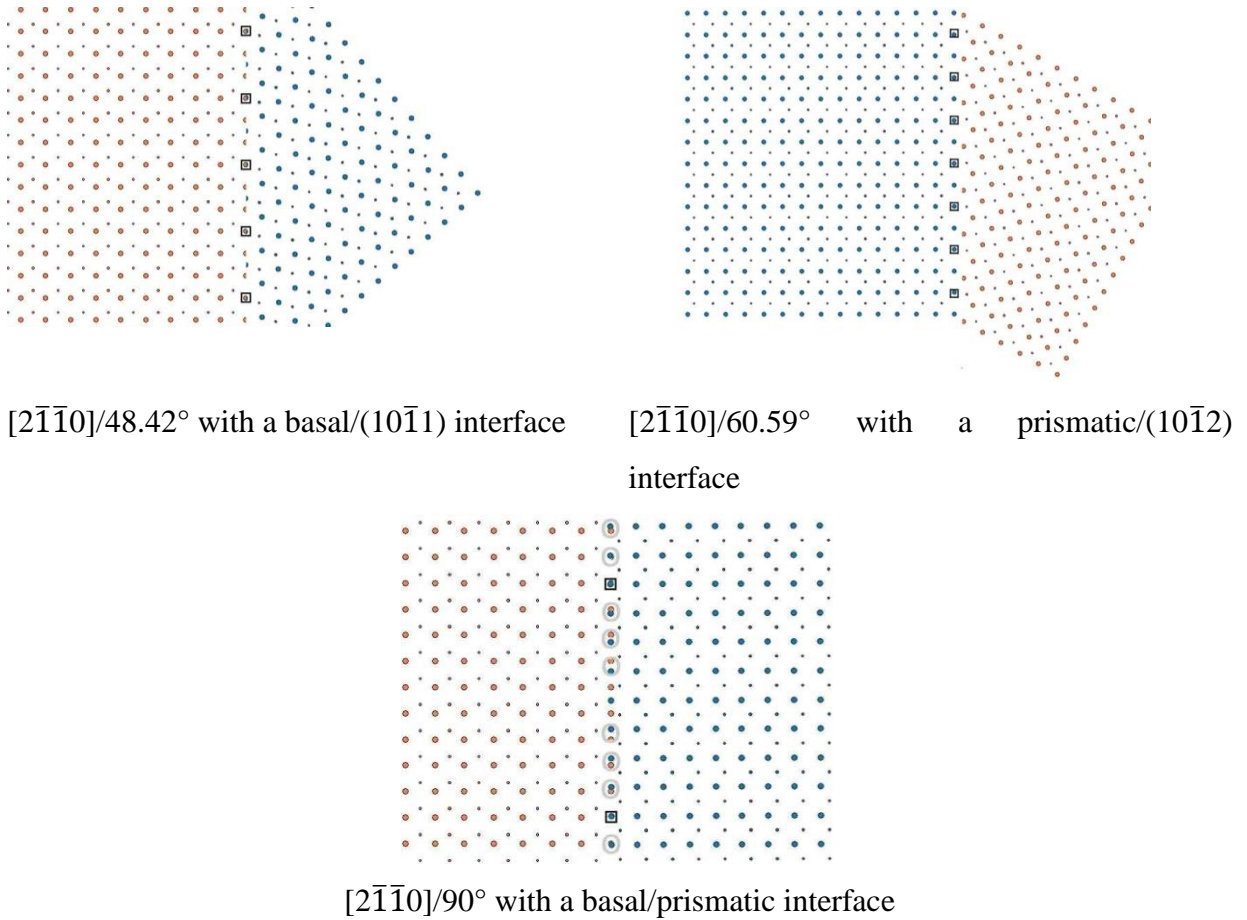


Figure 102 :TEM observation of  $[2\bar{1}\bar{1}0]$  rotation of  $48^\circ$  (a) and  $64^\circ$  (b). The boundary planes observed corresponds to the predictions obtained by considering densest planes. Observations made in a 5h sintered, W-rich, 50 vol% of binder sample.

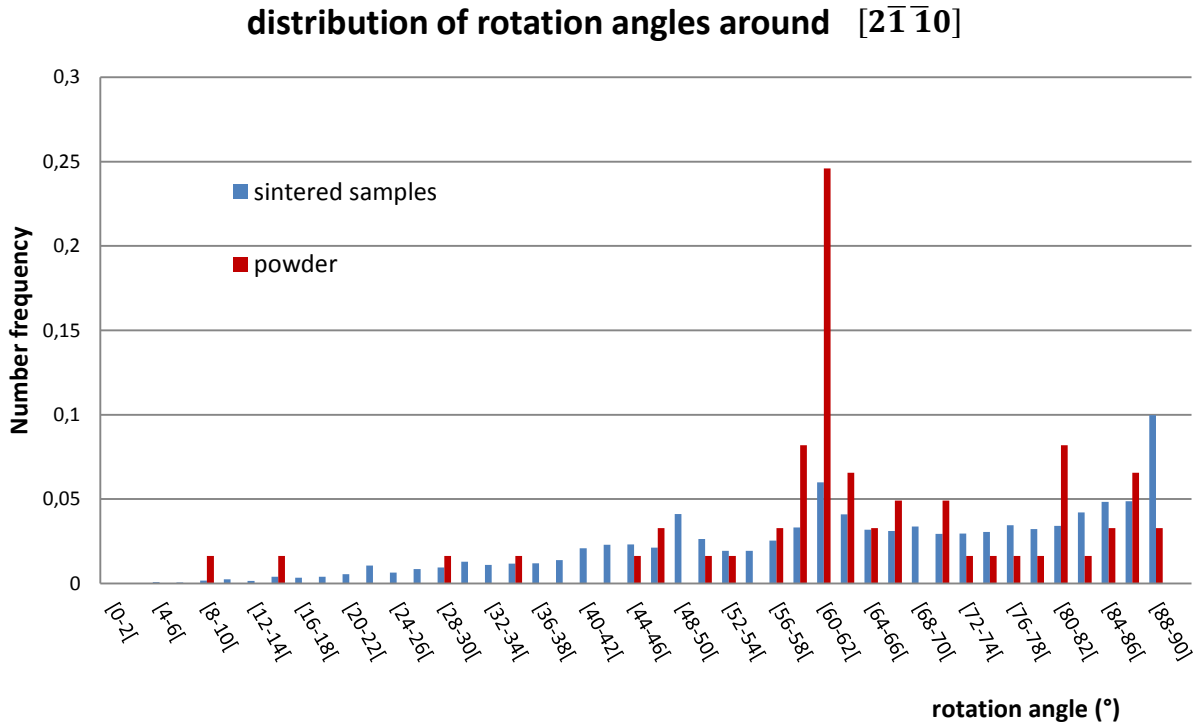
Figure 103 represents the lattice configurations at the boundary plane corresponding to these three particular rotations. It appears that they present a high density of coincidence sites in the boundary plane. The boundary planes corresponding to the other configurations presented in Figure 101 were also determined, but they present a lower density of coincidence sites.

High coincidence sites density implies a good continuity between the lattices of both grains, so likely a lower energy than for a random interface. Thus, the particular abundance of rotation angles in the  $[48^\circ-50^\circ]$  ,  $[60^\circ-62^\circ]$  and  $[88^\circ-90^\circ]$  ranges can be expected to result from the particular stability of grain boundaries defined by  $[2\bar{1}\bar{1}0]/48.42^\circ$  rotation with a basal/ $(10\bar{1}1)$  interface,  $[2\bar{1}\bar{1}0]/60.59^\circ$  rotation with a prismatic/ $(10\bar{1}2)$  interface and  $[2\bar{1}\bar{1}0]/90^\circ$  rotation with a basal/prismatic interface.

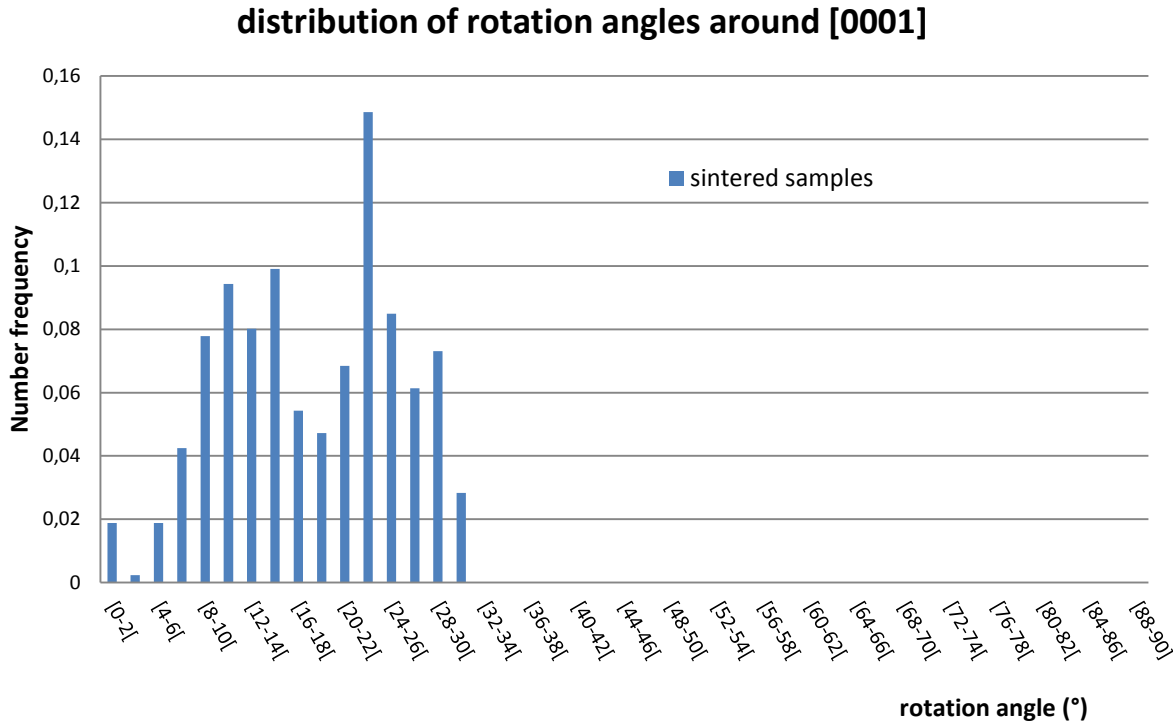


**Figure 103: Representation of the coherency at the boundary for particular rotations around  $[2\bar{1}\bar{1}0]$ . Coincidence sites are marked with a square symbol.**

The comparison of rotation angle distributions around  $[2\bar{1}\bar{1}0]$  reveals that the peak around the  $[60^\circ-62^\circ]$  is also present in the powder (Figure 104). At the opposite, the two other peaks are not clearly present. However, it is important to keep in mind that the number of analyzed boundaries is two orders of magnitude lower in the case of the powder (61, and 4185 for sintered samples), thus this distribution must be considered with precaution.



**Figure 104:** Comparison of the distributions of rotation angles around  $[2\bar{1}\bar{1}0]$  in the powder and the sintered samples.

**Rotations around [0001]:**

**Figure 105: Distribution of rotation angles around [0001]. Misorientation data of all samples (1h and 5h sintering, and C-rich and W-rich composition).**

The lower statistic (426 boundaries, compared to 6618 and 4185 for the two other types of rotations) implies a significant noise in the distribution. Additionally, the distribution stops for angles superior to 30°: this is expected and due to the crystal symmetries (I.A.2.ii).

A peak is noticeable for rotation angles in the [22°-24°] range. In the particular case of [0001] rotations it is possible to refer to the CLS theory for peaks interpretation. In fact the  $c/a$  ratio is of no importance since  $c$  axes of both grains engaged in the boundary are collinear. CSL theory describes the special boundary  $\Sigma 7a$  as a [0001]/21.79° rotation. In the other hand no particular abundance of [0001]/30° boundaries was measured, despite this boundary type is cited in literature.

In the case of rotation around [0001] it is not possible to compare with the distribution of rotation angles in the powder as very few rotations of this type were detected in the powder.

Finally, five remarkable boundaries (special boundaries) with specific angle/[rotation axis] couple emerge from the global distributions because they present a higher frequency than it would be expected in the case of an isotropic distribution. Additionally, in all these configurations, the possibility of a remarkable boundary habit plane (basal or prismatic) with a high coincidence site density at the boundary (not necessarily in all the volume), seems to be a key factor for the particular stability of a grain boundary. The remarkable boundaries found in sintered samples are often present in the powder, but not always in the same proportions.

#### IV.B.2.iii Discussion about the origin of the special boundaries

The  $[10\bar{1}0]/90^\circ$  specific rotation represents the main part of the  $[10\bar{1}0]$  rotations. The case of this special boundary was often discussed in the literature. This rotation leads to the creation of two types of boundaries, twist and tilt. According to DFT calculation by Christensen and Wahnström, who investigated the stability of this rotation, tilt configuration is expected to be similar to a random rotation, whereas twist boundaries are expected to be more stable than any other type of boundary and particularly resistant to binder infiltration. As the partial contiguity of  $[10\bar{1}0]/90^\circ$  boundaries is only slightly lower in sintered samples than in the powder and does not vary with binder content, it can be supposed that  $[10\bar{1}0]/90^\circ$  boundaries found in sintered samples are mainly originated in the powder and develop during sintering to follow grain growth. Only the twist boundaries would remain after infiltration by the binder, explaining the small difference between partial contiguity before and after sintering (respectively 0.10 and 0.07).

At the opposite, partial contiguity of  $[2\bar{1}\bar{1}0]$  and  $[0001]$  is low in the powder (respectively 0.01 and 0.001) and significantly increases in sintered samples (respectively 0.05 and 0.004-0.006). Thus, those boundaries cannot be considered as originated in the powder but must mainly be formed during sintering.

Concerning the random boundaries (all other boundaries than those specified previously) that are initially present in the powder, they are expected to be destroyed during sintering, probably due to infiltration by the binder. In fact, DFT calculations tend to show that those boundaries are not stable toward infiltration by the liquid. It would be consistent with the fact that no trace of the

large clusters constituted of many large boundaries present in the powder is found in sintered samples (Figure 106).

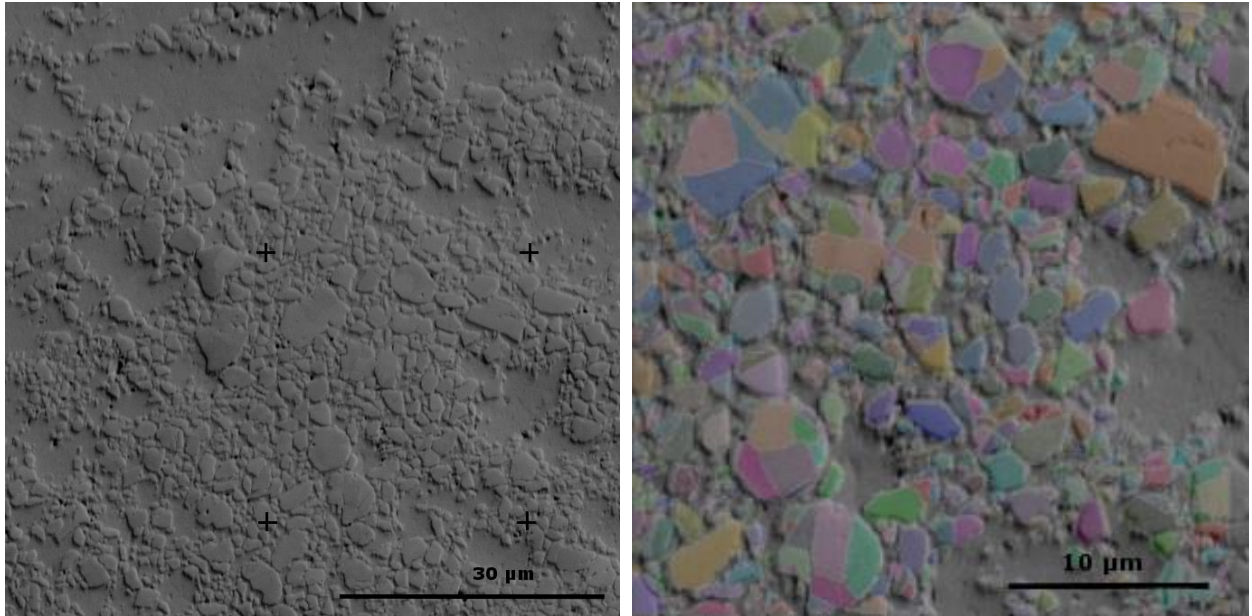


**Figure 106: SEM and EBSD comparison of the same area (identify between black crosses on right image) observed in the WC-Cu sample. Large clusters that are seen in the powder are actually constituted of multiple grains. No trace of these clusters is found in sintered samples.**

In conclusion, the major part of boundaries in the microstructure are formed during sintering, excepted a constant fraction of  $[10\bar{1}0]/90^\circ$  rotations, probably mostly twist, that would be originated in the powder. Thus, in agreement with Luyckx's conclusions, a plateau should be reached in the evolution of contiguity around the value of the  $[10\bar{1}0]/90^\circ$  partial contiguity, *i.e.* around 0.08. However, boundaries created during sintering are not completely random as a specific population develops, characterized by the particular abundance of  $[2\bar{1}\bar{1}0]/48.4^\circ$ -  $60.59^\circ$ -  $90^\circ$  and  $[0001]/21.79^\circ$  rotations.

#### IV.B.2.iv Grain boundary planes

Rotation axis and angle are not enough to fully describe a grain boundary, so grain boundary plane identification was further investigated. Remarkable planes (basal and prismatic) present particularly low surface energy, and were expected in the previous part to stabilize several boundary configurations. Hence, boundaries presenting such habit planes are expected to be more

stable and more represented in the microstructure, even without a specific angle/[rotation axis] couple.

As explain in II.D.4.ii the program measures the area fraction of grain boundary potentially presenting a remarkable plane for at least one of the two grains engaged in the boundary (potentially remarkable boundary plane). This value is corrected afterward to estimate the effective area fraction of remarkable boundary planes.

The following Figure 107 and Figure 108 represent the area fraction obtained before and after correction, respectively.

As seen in Figure 108 (a) (b) and (c) no significant evolution of the area fraction of remarkable boundary planes (either basal or prismatic) is detected with binder content. However, remarkable boundary planes represent approximatively 60% of the total boundary surface. This value is also approximately the fraction measured in the powder. Among those 60%, one third corresponds to basal boundary planes, the 2 others to prismatic planes. No significant influence of C/W ratio is noticed.

In a work mentioned in the bibliography, Rohrer [51] also measured a remarkable boundary plane fraction of 60% of the total boundary surface, with another boundary plane identification technique (also based on EBSD measurements). In particular no correction is applied after detection of traces of planes potentially remarkable.



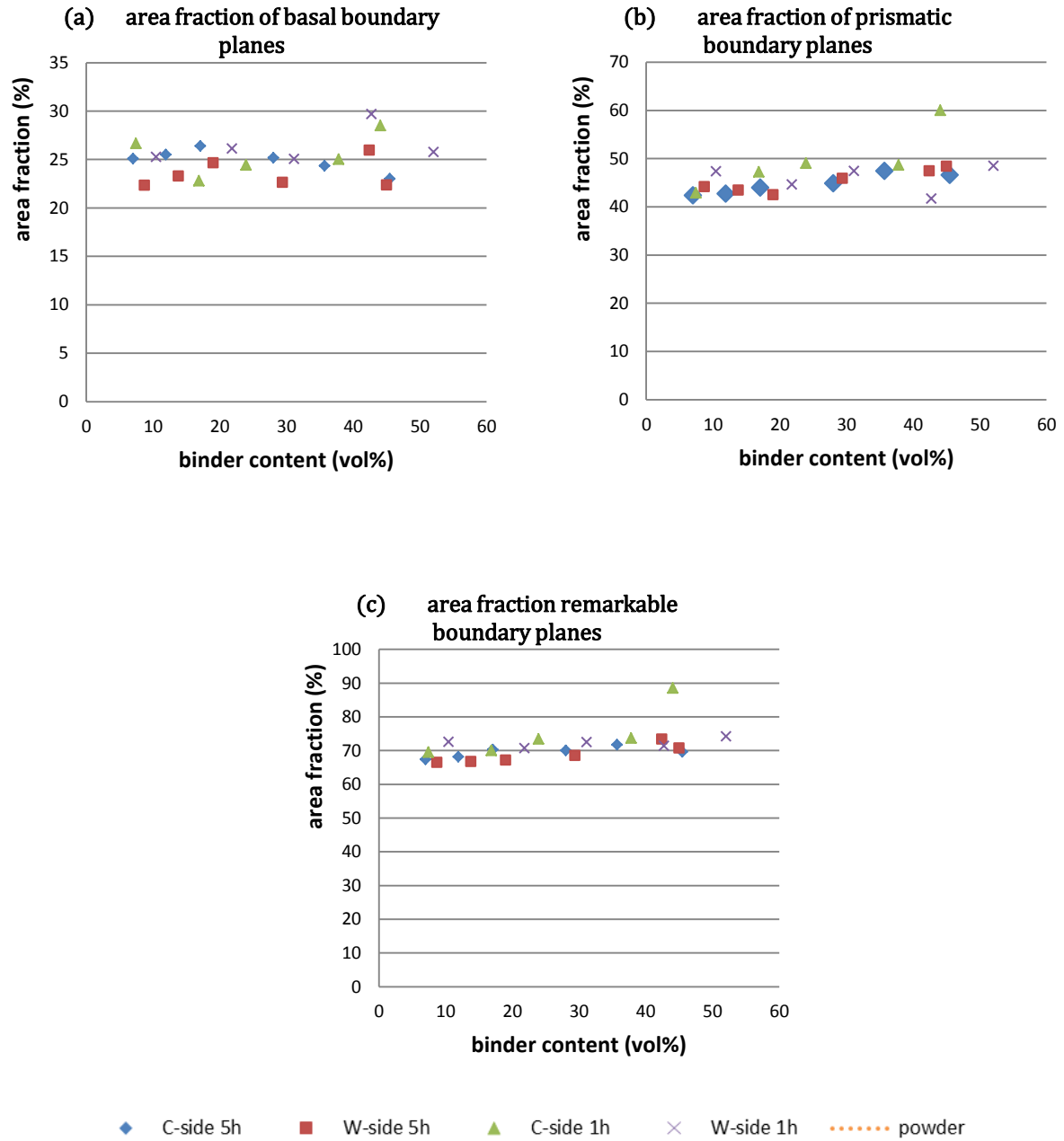


Figure 107: Evolution of remarkable boundary planes area (non-corrected) with sintering time, binder content and C/W ratio.

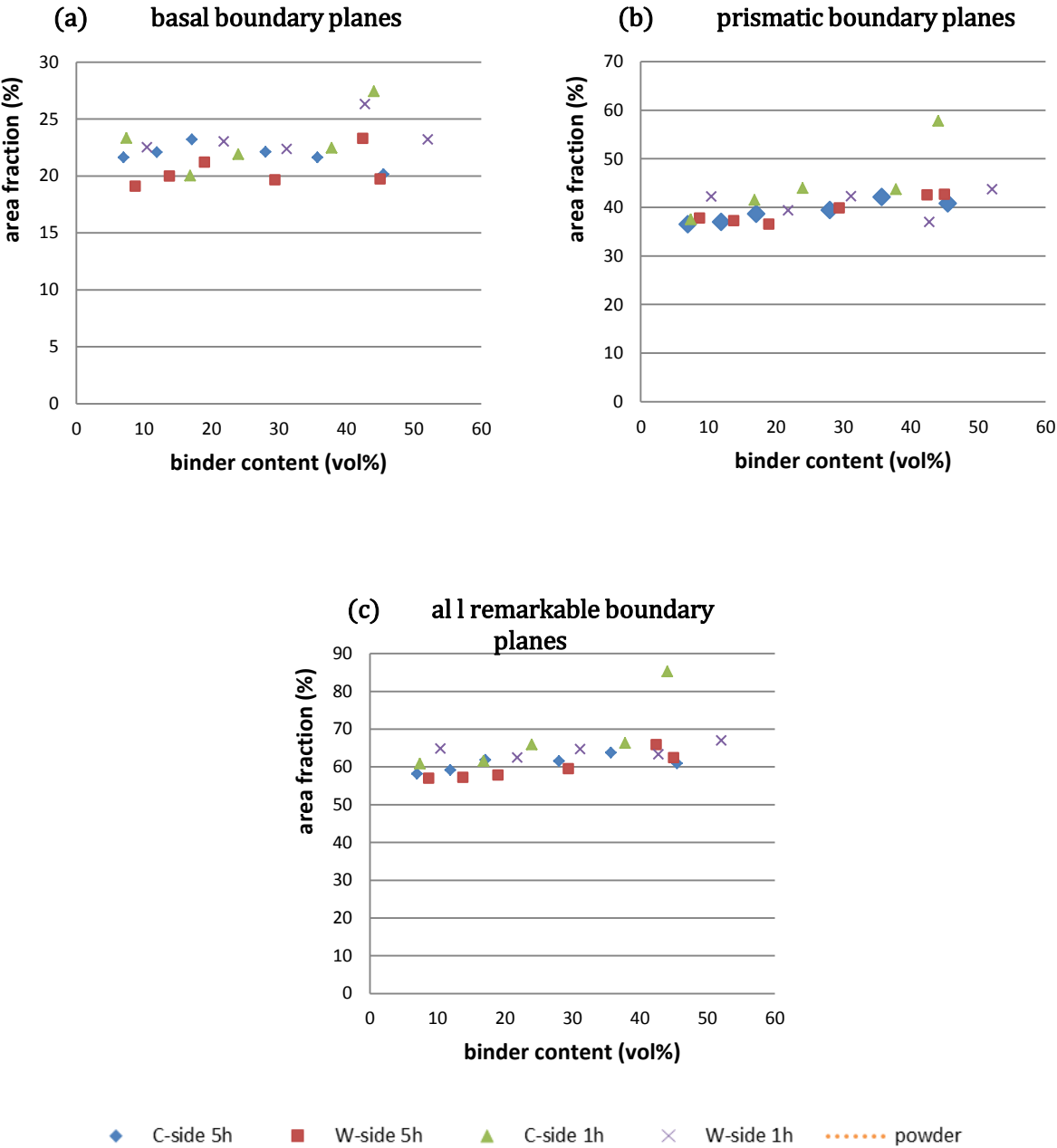
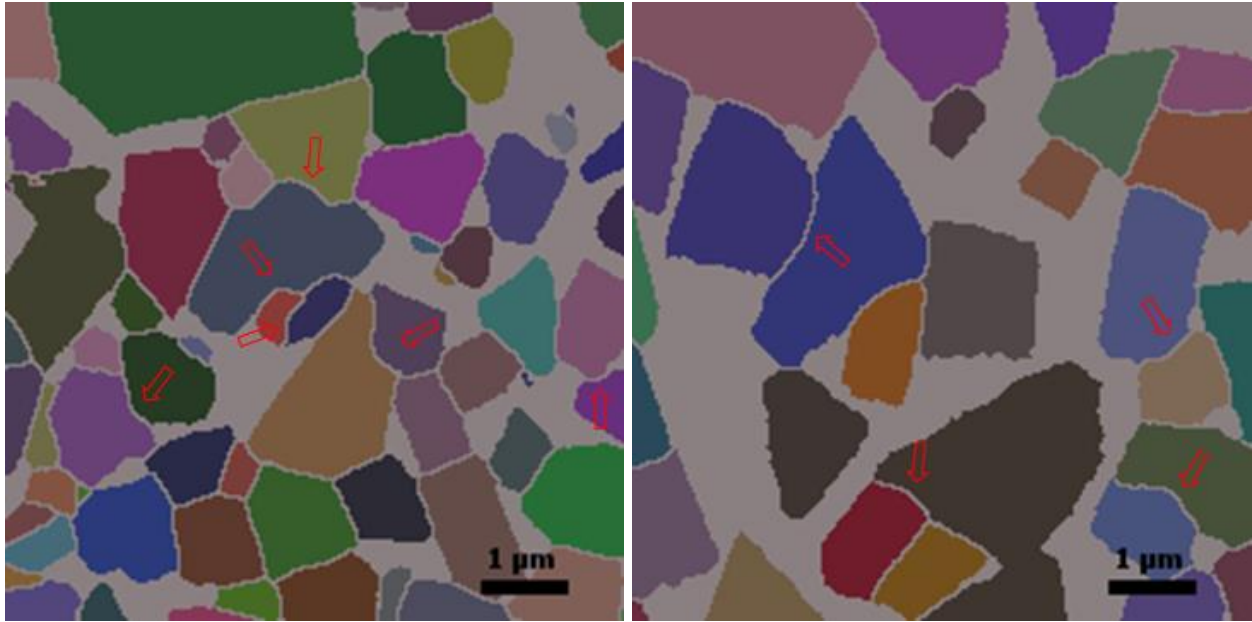
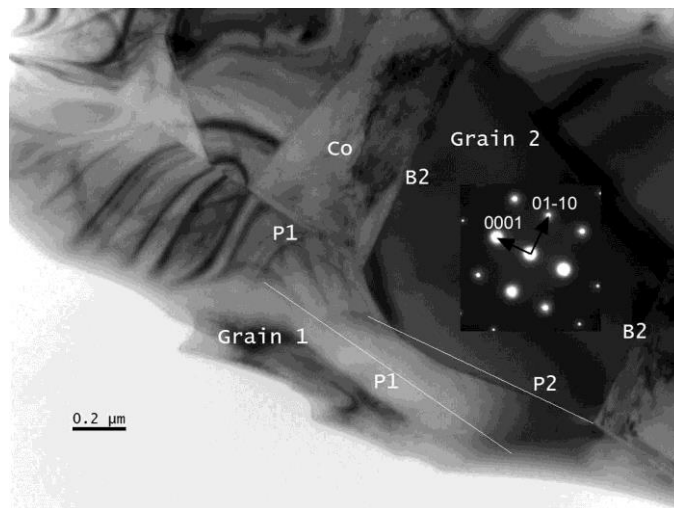


Figure 108: Evolution of remarkable boundary planes area (corrected) with sintering time, binder content and C/W ratio.

When the microstructure is observed in details, a significant number of curved grain boundaries are observed (Figure 109), raising the question of their stability. In fact, the principle of energy minimization implies to minimize the area, thus curved boundary should be energetically non-favorable and expected to straighten up (by moving the boundary), or to be infiltrated by the binder. This kind of grain boundary is also observed with TEM (Figure 110).



**Figure 109:** Example of curved boundaries observed in the sintered samples. EBSD observation in W-rich samples sintered for 5h, 20 vol% (left) and 50 vol% (right) of binder. Curved boundaries are frequently observed, either in low or high binder content samples.



**Figure 110:** The existence of curved boundaries has also been noted with TEM observations (C-rich sample sintered for 1h, 20 vol% of binder).

However, when visualizing remarkable boundary planes (Figure 111) it appears that those curved boundary partially exhibit a remarkable plane, for at least one of the two grains. This kind of “partial faceting” allows the boundary to change direction while staying energetically favorable enough. An even more favorable case of a combination of several remarkable planes (for one or the other grain) can also be observed.

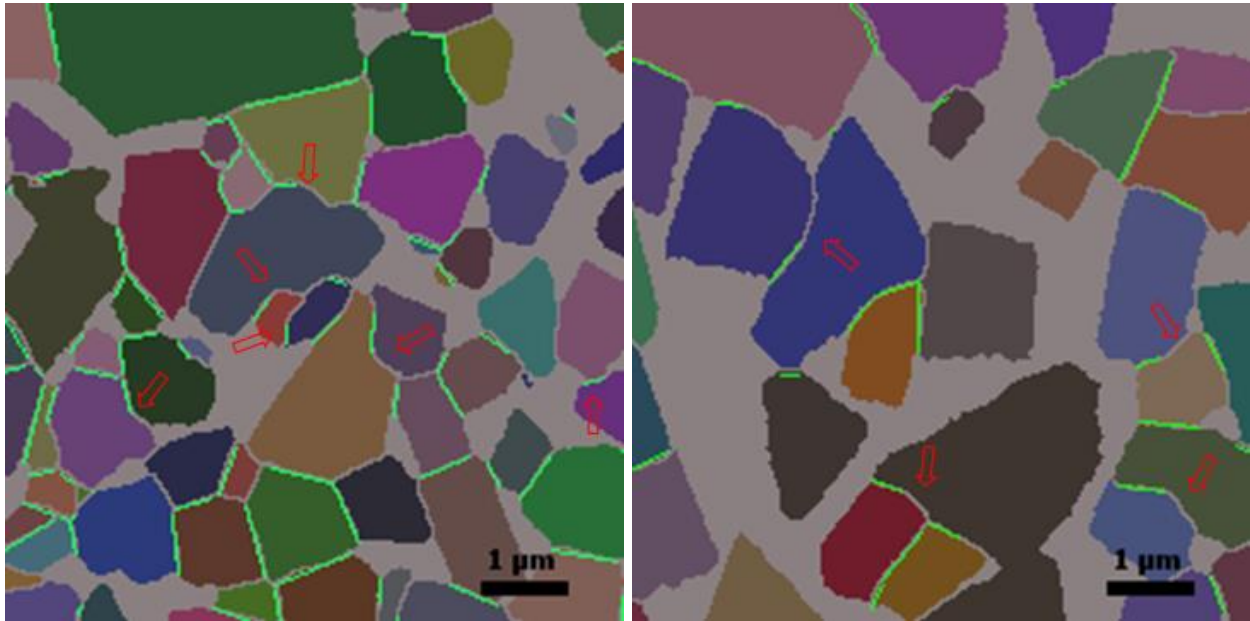


Figure 111: The same zones presented in Figure 109 are represented here with remarkable boundaries in overlay. Curved boundaries always partially correspond to a remarkable plane for at least one of the two grains. Green segments represent remarkable boundaries.

### IV.B.3 WC/Co phase boundaries

WC/Co Phase boundaries planes have also been characterized. As for grain boundary planes, non-corrected and corrected values are given in Figure 112 and Figure 113 respectively.

Focusing on the fraction of each type of remarkable phase boundary, it appears that both basal and prismatic types can be found in the same proportion approximately, around 20-25% of the total phase boundary area.

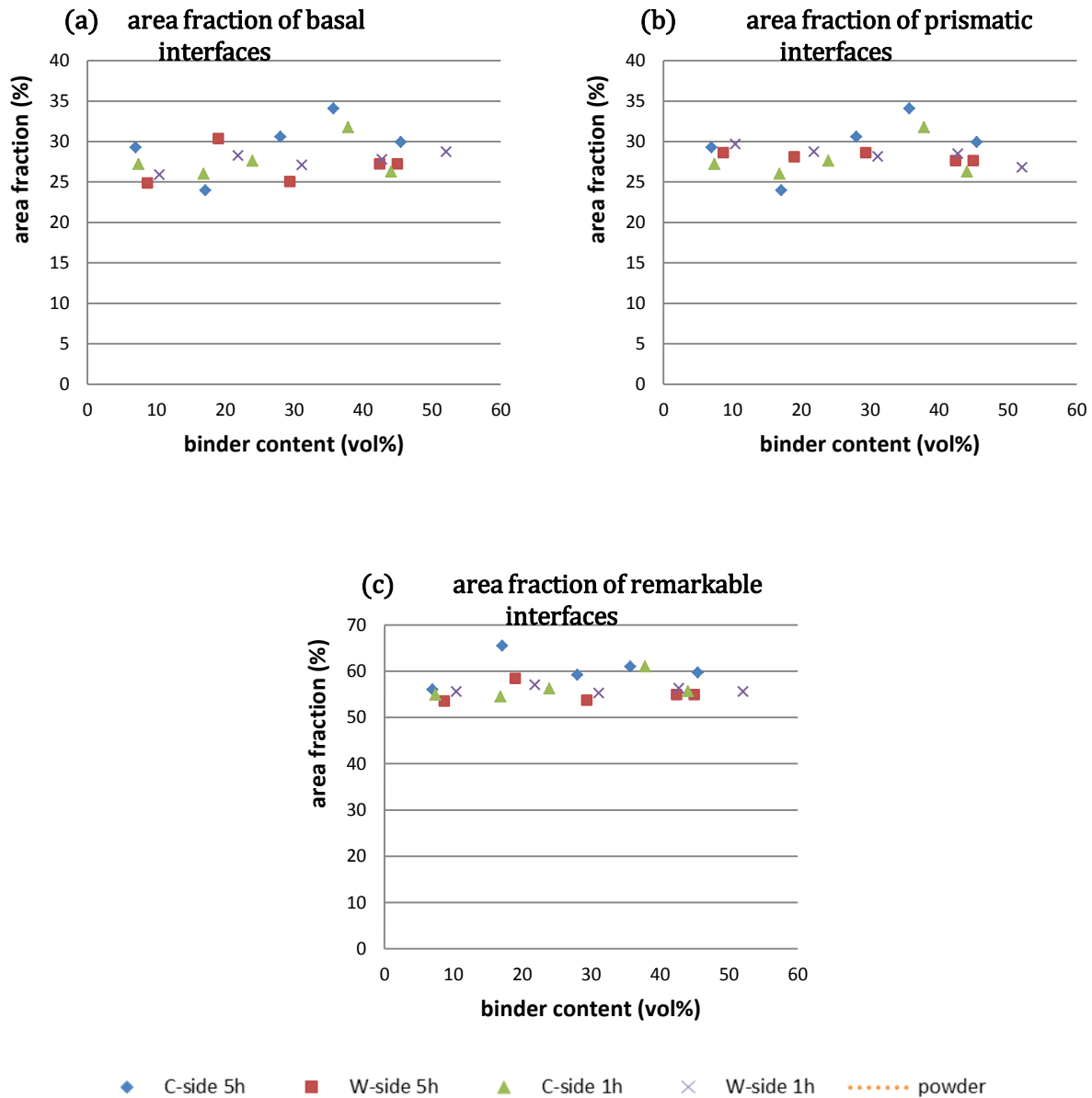
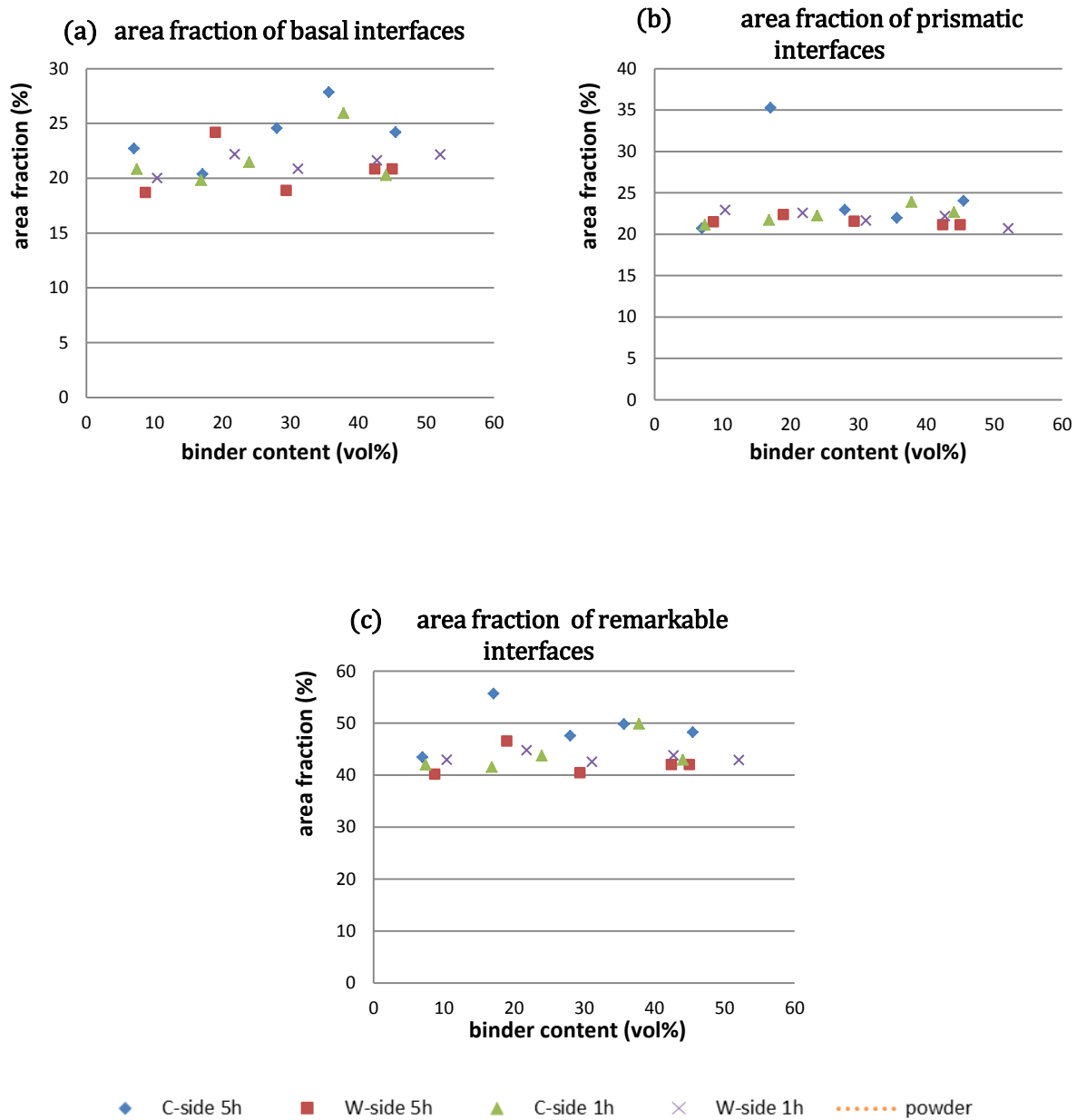


Figure 112: Evolution of remarkable WC/Co phase boundaries area (non-corrected) with sintering time, binder content and C/W ratio.



**Figure 113: Evolution of remarkable WC/Co phase boundaries area with sintering time, binder content and C/W ratio.**

Concerning the total fraction of remarkable phase boundary planes, the corrected value (45% approximately) can appear lower than expected. In fact, referring to TEM observations for example, grains appear to be mainly faceted according to remarkable planes. Besides, Rohrer

presented in his work a value of 60% of remarkable planes (without correction). A possible explanation for underestimating the fraction of remarkable phase boundary planes is the loss of resolution at the interface, mentioned in the II.B.3 . In fact, imprecision on the determination of the interface can be very influent on the segmentation by the program, thus on the identification of the boundary plane. In addition, non-corrected value appears to be closer to an expected value, what possibly reveal that the correction may be too rough.

Observing the microstructure it appears that many phase boundaries present a partial faceting aspect: only a fraction of the phase boundary has a remarkable habit plane (Figure 114). The rest of the phase boundary is oriented to accommodate the constraints of pinning to the different phase boundaries in the surrounding. Some phase boundaries are faceted in such a way that steps appear. It can be seen as a way to maximize the faceted surface while composing with impingement.

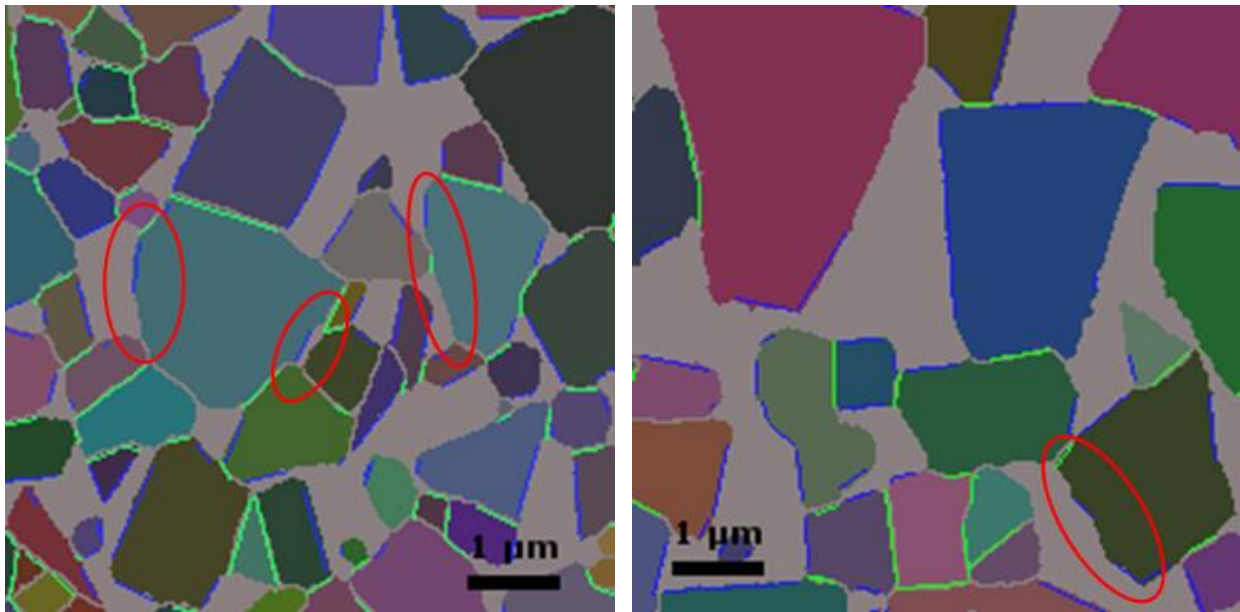


**Figure 114:** Example of partially faceted phase boundaries in sintered samples (W-rich samples sintered for 5h, 20 vol % -left- and 50 vol% -right- of binder). Green and blue segments represent respectively remarkable grain boundaries and phase boundaries.



It is important to remark that a lot of phase boundaries are planar and regular but reveal to not correspond to a remarkable plane. Often, grains only partially adopt the ideal shape (three prismatic and two basal planes), as illustrated in Figure 115.

Last, it was shown in the study that some grain boundaries or phase boundaries are not remarkable, that is they are established according a non-remarkable plane. More precisely, it should be mentioned that these interfaces are non-remarkable at the micronic scale. In fact, apparently random interface can actually be constituted of a succession of facets oriented according to remarkable planes, allowing the interface to reach an orientation not allowed with a unique and continuous remarkable facet. This “local” faceting was observed with High Resolution TEM, as presented in the following Figure 116.

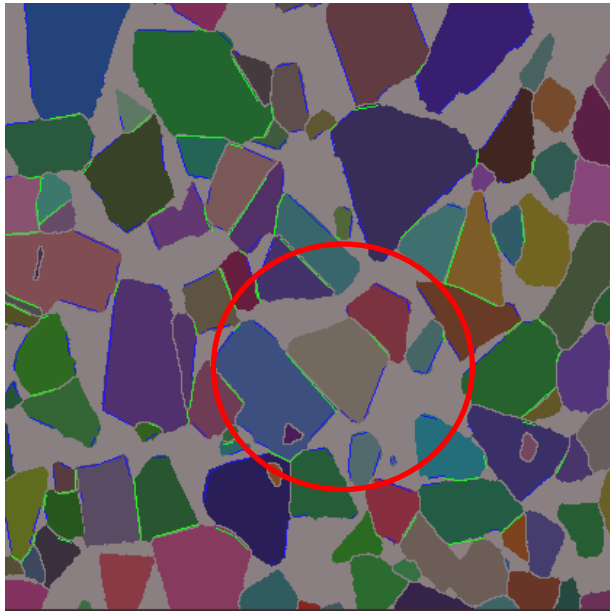


**Figure 115:** Illustration of a phase boundary that could have been expected to be prismatic: it may be due to a perspective distortion, but also many grains develop only partially the ideal shape.

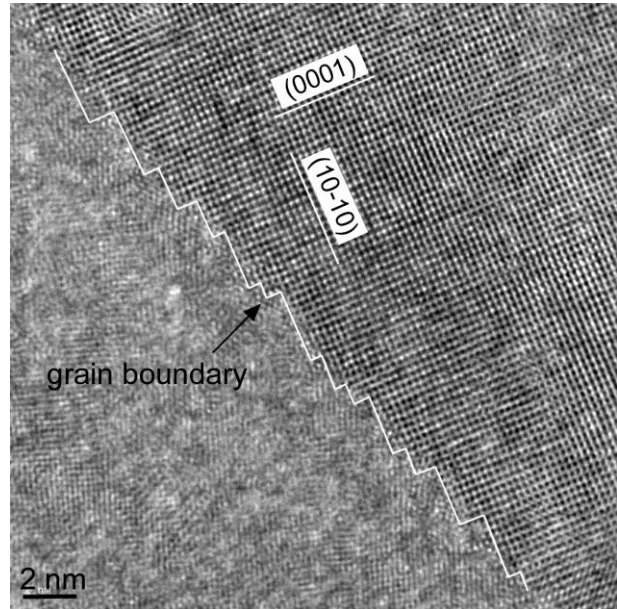


**Figure 116:** Example of a random grain boundary. The main orientation of the boundary plane does not correspond to a particular plane; however it locally adopts a remarkable orientation.



## Chapter V Discussion: development of grain and phase boundaries in cemented carbides

Microstructure in the material results from re-arranging of the matter during sintering, in order to reduce the interfacial energy of the system. The final interest in material engineering is to control matter re-distribution processes in order to obtain a designed microstructure, fitting with the required properties. Thus, identifying and understanding those processes is the keystone step, and is the final aim of microstructure study.

The aim of this last chapter is to consider each result obtained in this study with the perspective of matter distribution processes, in order to draw an overall coherence to this work.

### V.A Grain boundary formation

Contiguity results have shown that a high amount of boundaries are present in the microstructure, even at high binder content. Boundaries cover 30 % of a grain surface at 50 vol% of binder, up to 80 % at 10 vol% of binder. Thus, it raises the question of the formation of these boundaries.

A description of the grain boundary formation scenario is proposed in this part, based on the analysis of the grain boundary population presented in the study. The results supporting this description are summarized here:

- A particular population of special boundaries, constituted of rotations around  $[10\bar{1}0]$ ,  $[2\bar{1}\bar{1}0]$  and  $[0001]$  is more abundant in the microstructure than expected in the case of an isotropic, random distribution. It is particularly constituted of five specific rotations that are  $[10\bar{1}0]/90^\circ$ ,  $[2\bar{1}\bar{1}0]/48.4^\circ$ -  $60.59^\circ$ -  $90^\circ$  and  $[0001]/21.79^\circ$ , which also present a remarkable boundary plane (basal or prismatic) with a high density of coincidence sites. The partial contiguity of these boundaries does not change with binder content (Figure 117).

- A population of remarkable boundaries (basal or prismatic for at least one grain), possibly including the previous population. Its surface fraction does not evolve with binder content, thus its partial contiguity decreases with binder content (Figure 117).
- The rest of the boundaries can be considered as random since they present neither particular misorientation nor remarkable boundary plane (Figure 117).
- An important fraction of phase boundaries is remarkable (basal or prismatic), and this surface fraction does not change with binder content.
- DFT calculations reported in the literature predict that all types of grain boundaries, excepted  $\Sigma 2$  twist are supposed to be infiltrated by liquid binder. However, in the presence of cobalt, segregation of half a monolayer is expected to stabilize most grain boundaries. From the calculations, the grain boundary energy is comprised between  $0.7 \text{ J.m}^{-2}$  (special  $\Sigma 2$  twist) and  $2\text{-}3 \text{ J.m}^{-2}$  (random grain boundaries). In addition, stable phase boundaries are with a basal or prismatic plane and their minimum energy is around  $0.7 \text{ J/m}^2$ .
- According to DFT calculations the equilibrium shape is thus expected to be a triangular based prism, constituted of two basal planes and prismatic planes.

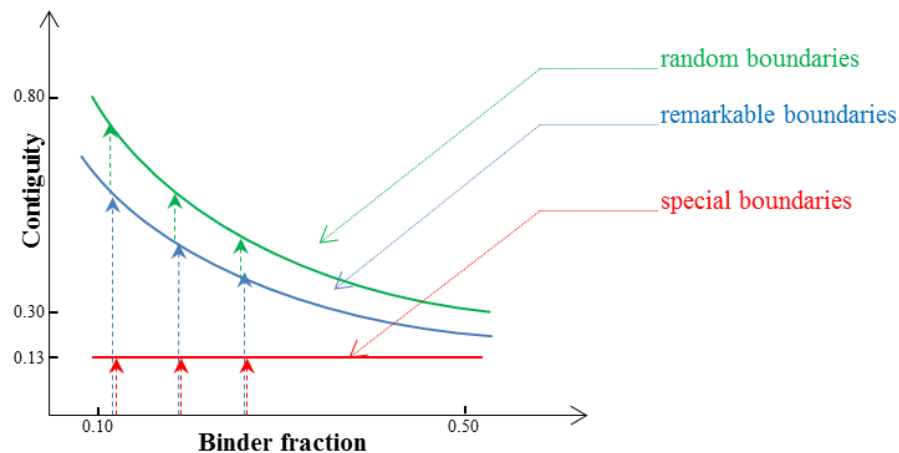


**Figure 117: Sketch of the contiguity variations with the contribution of the different grain boundaries population.**

**V.A.1 Scenario for grain boundary formation**

Considering these results, the following scenario can be proposed to explain grain boundary formation.

First, during the heating phase, whilst the system is still in solid phase, sintering and faceting start. As predicted by DFT calculations, the planes that preferentially develop during faceting are basal or prismatic, since they present a lower energy than any other planes.

When eutectic temperature is reached, the system is not dense (porosity 3-5%) and liquid phase appears in high quantity in the system. Thus a significant amount of tungsten carbide is dissolved in the binder, increasing the liquid phase fraction. Since they are free from cobalt segregation, grain boundaries initially present in the powder or formed during solid phase sintering are mainly infiltrated by the liquid. In addition, faceting of the grains becomes very fast thanks to the contribution of diffusion in the liquid phase. Henceforth the system consists in a loose particle packing in which essentially  $\Sigma 2$  twist boundaries subsist from the powder (as they are supposed to resist liquid infiltration) and grains are faceted with basal or prismatic planes.

Because of shrinkage due to particle rearrangement and sintering, grains are brought into contact with each other. When bringing two randomly oriented faceted grains closer, only two contact configurations are likely to occur: edge to edge or vertex to facet. These configurations are mechanically not stable, and the system will rotate toward a most stable position (edge to facet) and finally reach the most stable position (facet to facet). The rotation may stop and a grain boundary may develop as soon as the orientation is favorable for the replacement of a phase boundary by a grain boundary.

Results presented in the study revealed a high fraction of grain boundaries corresponding to rotations around  $[10\bar{1}0]$ ,  $[2\bar{1}\bar{1}0]$  and  $[0001]$ . In fact they correspond to configurations easy to encounter during the rotation of faceted prismatic particles in the initial stage of rearrangement/sintering: prismatic against prismatic ( $[10\bar{1}0]$ ), basal against basal ( $[0001]$ ) or edge against facet ( $[2\bar{1}\bar{1}0]$ ). In addition they present remarkable boundary planes. They can be expected to be more stable than random boundaries, and thus formed in the first place.

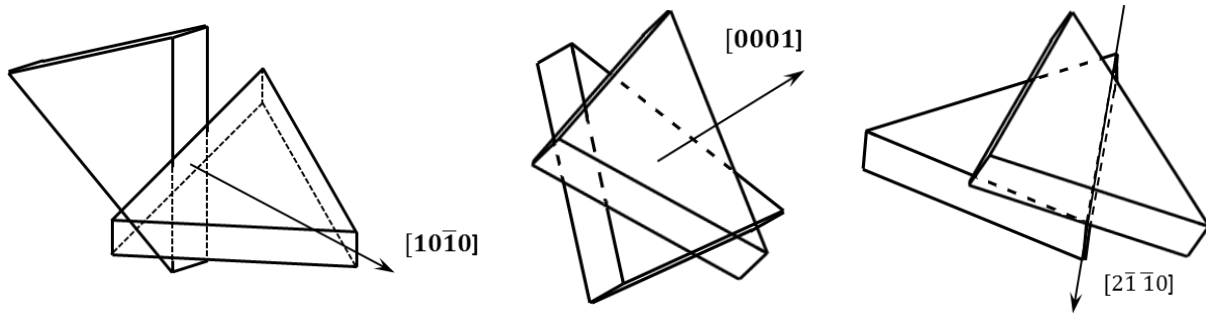


**Figure 118:** Grain boundary configuration described by  $[10\bar{1}0]$ ,  $[2\bar{1}\bar{1}0]$  and  $[0001]$  rotations.

These boundaries need the system to be loose enough to allow rotation of the grains in order to find the proper configuration. In consequence they are expected to develop in the beginning of sintering.

In a second stage, a more or less rigid particle skeleton has been formed due to the creation and growth of a significant amount of particle necks (grain boundaries) and rotations become less favorable. However, since grains are faceted, grain boundaries which form during further shrinkage are very likely to have a remarkable boundary plane (Figure 119). As a consequence, boundaries formed in the second stage of sintering also correspond to remarkable boundaries, but not necessarily to special boundaries (with a specific misorientation between the two crystals). In a few situations where it is not possible to create boundaries with a remarkable plane, random grain boundaries can be created, if it is still energetically favorable. According to this scenario, development of remarkable and random boundaries is directly linked to impingement: the higher the impingement the more likely the creation of random boundaries. This is consistent with the observed evolution with binder content of partial contiguity of remarkable boundaries (Figure 117). In addition, the relative proportion of remarkable and random grain boundary would be linked to the relative proportion of remarkable and random phase boundary. This is consistent with the observation of a constant fraction of remarkable phase boundary planes and remarkable grain boundary planes with binder content.

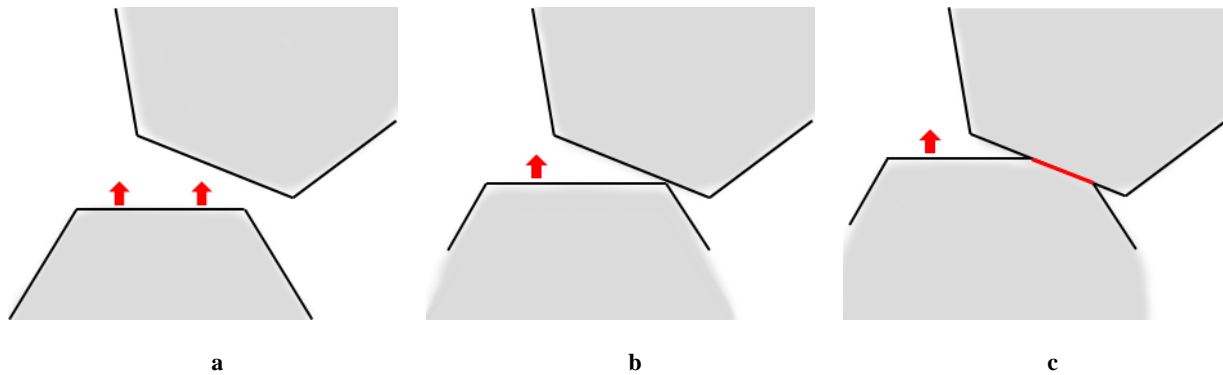


Figure 119: Grain boundaries that form during the second stage are likely to present a remarkable boundary plane

### V.A.2 Particular analysis of special boundary formation

The previous scenario explains why special rotations are found in a larger extend than in the case of a random distribution, and why the fraction of remarkable boundaries is constant. However, it does not explain why partial contiguity of the different special rotations is not influenced by binder content. Thus, two hypotheses are formulated below, the first one based on a mechanical approach, the second on an energetic approach.

#### *Mechanical approach*

As boundaries are created and grow, the system consolidates and soon grain rotation (then the development of  $[10\bar{1}0]$ ,  $[2\bar{1}\bar{1}0]$  and  $[0001]$  boundaries) is no longer possible. It is reasonable to assume that the system become too rigid for particles to rotate above a critical value for the contiguity, whatever the binder content. Assuming that boundaries which form first are the special boundaries, our results suggest that this limit would be around 0.10-0.15 (the sum of  $[10\bar{1}0]$ ,  $[2\bar{1}\bar{1}0]$  and  $[0001]$  boundary partial contiguities) and does not change with binder content.

It must be specified that this value of “limit” contiguity includes the partial contiguity of  $\Sigma 2$  boundaries (0.07) that are expected to subsite from the powder. The amount of  $[10\bar{1}0]$  and  $[2\bar{1}\bar{1}0]$  boundaries that are formed during this initial stage of sintering would rather be around 0.02 and 0.04 respectively (and a fewer quantity of  $[0001]$ ).

In summary,  $[10\bar{1}0]$ ,  $[2\bar{1}\bar{1}0]$  and  $[0001]$  boundaries are preferentially formed during the initial stage of sintering, as particle rotation is still possible. This would be possible until the system

reaches a critical value for the contiguity between 0.10 and 0.15. This value is the sum of the partial contiguities of grain boundaries which were already present in the powder and of the special boundaries which were created in the first stage of particle rearrangement/sintering.

### ***Energetic approach***

In the energetic approach, it is considered that special boundaries (formed when a favorable contact is made) will develop as long as it is energetically favorable. The energy variation due to corresponding contiguity increase can be decomposed into the energy gain due to the increase of the solid-solid contact, and the energy loss due to the redistribution of matter eliminated at the contact on the particle surface.

The values used in this part are summarized here:

$E$ : energy of the grain	$V$ : volume of the grain	$S$ : surface of the grain
$C$ : contiguity	$\gamma_{SL}, \gamma_{SS}$ : interfacial energy per unit area of phase/grain boundary	$\alpha_i, \beta_i$ : geometrical constant of the order of 1
$r$ : grain boundary radius		

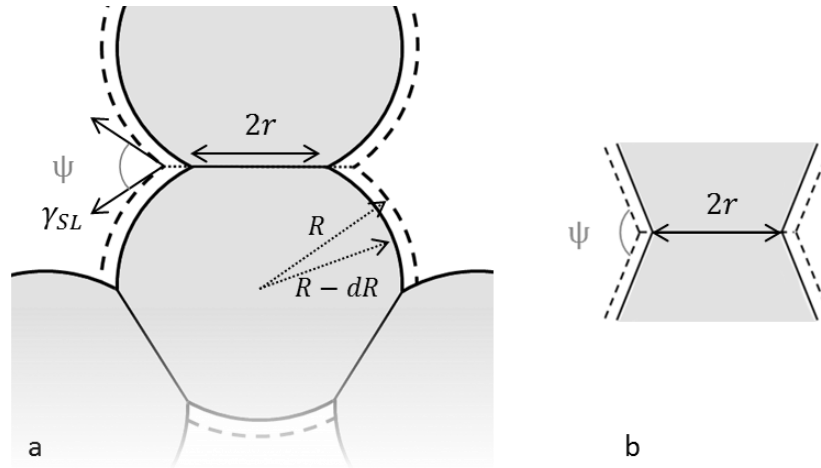


**Figure 120: Evolution of the grain surface with the development of a boundary (a). The dihedral angle  $\psi$  is constant as it is set by the ratio of surface energies. In the case of faceted phase boundaries, the dihedral angle is also a constant value (b).**

The energy variation per unit surface area of grain can be written as follows:

$$dE = dC_i(\gamma_{SS} - (1 + \alpha_i)\gamma_{SL}) + C_i\beta_i dr\left(\frac{S}{V}\right)(C_i\gamma_{SS} + (1 - C_i)\gamma_{SL}) \quad (5.1)$$

Assuming contiguity  $C_i$  is proportional to  $r^2$ :

$$dE = dC_i(\gamma_{SS} - (1 + \alpha_i)\gamma_{SL}) + \frac{1}{2}\beta_i r dC_i\left(\frac{S}{V}\right)(C_i\gamma_{SS} + (1 - C_i)\gamma_{SL}) \quad (5.2)$$

The initial development of the boundaries is favorable only if the first term in equation (5.1) is negative, *i.e.* if the grain boundary energy is similar or only slightly larger than the phase boundary energy:

$$\gamma_{SS} < (1 + \alpha_i)\gamma_{SL} \quad (5.3)$$

This corresponds to the case of special boundaries such as  $\Sigma 2$  twist boundaries. In this condition, an equilibrium configuration is found for:

$$\frac{dE}{dC_i} = 0 \quad (5.4)$$

$$r = -\frac{2(\gamma_{SS} - (1 + \alpha_i)\gamma_{SL})}{\beta_i\left(\frac{S}{V}\right)(C_i\gamma_{SS} + (1 - C_i)\gamma_{SL})} \quad (5.5)$$

This would explain why special boundaries grow until a critical size and then reach the same contiguity whatever the binder volume fraction. This energetic calculation only takes into account one special grain boundary type. However, taking into account the three types of special grains simultaneously, the value of the limit partial contiguities may change but it is expected not to change the global behavior.

Finally, a limit is observed in the formation and growth of special grain boundaries at the end of the first stage of boundary formation. Mechanical and energetic approaches can be used to justify this limit. The first one considers that the system tends to become mechanically rigid, implying that grains are not able to rotate anymore to form special boundaries. The second one considers that over a limit value of partial contiguity, the growth of special grain boundaries would increase the interfacial energy of the system and the development of the special boundaries would stop.

## V.B Grain boundary and phase boundary migration

In order to reduce the internal energy of the material, overall coarsening of the microstructure is expected. Grain growth implies that grain boundary and phase boundary migration occur simultaneously. The driving force for grain growth, *i.e.* the equivalent capillary pressure  $P_C$  exerted on the grain/phase boundaries of a grain of size  $R$  can be expressed in a mean field approach in a matrix of grains with an average size  $\bar{R}$  (Appendix 3: Migration pressure for grain growth in systems containing phase boundaries and grain boundaries), thus generalizing the LSW approach of grain growth of isolated particles in a liquid phase:

$$P_C = 2 \tilde{\gamma} \left( \frac{1}{R^*} - \frac{1}{R} \right) \quad (5.6)$$

where  $R^*$  represents the critical radius in the distribution (particles larger than  $R^*$  tend to grow whereas particles smaller than  $R^*$  tend to shrink) and is related to  $\bar{R}$ .  $\tilde{\gamma}$  is an equivalent interfacial energy of the system, which is an average interfacial energy obtained by weighting the phase boundary and grain boundary energies with their respective surface fraction. The aim of this part is to discuss the mechanisms of phase/grain boundary migration in our material and to isolate factors limiting the grain growth.



The discussion presented in this part is based on several results summarized here:

- High binder content favors grain growth: mean grain size after 5h sintering was measured larger in 50 vol% of binder samples than in 10 vol%.
- High binder content also favors abnormal grain growth.
- It is reported in literature that grain growth in submicronic powder show no limit until mean grain size reaches micronic average size.
- Carbon rich binder was observed to favor rapid grain growth, as it is reported in literature

Although grain boundaries and phase boundaries should move in a cooperative way, the slowest boundaries will limit the kinetic. If grain and phase boundary mobilities are very different, a drag force appears which pins the boundary with the highest mobility. Microstructural observations presented in chapter IV and discussed in the next section tend to attest the lower mobility of grain boundaries.

### **V.B.1 Phase boundary and grain boundary migration**

Two general observations made during study of remarkable boundary planes on EBSD images are reminded below.

First, many curved grain boundaries are observed in the microstructure, whereas they are not energetically favorable thus expected to disappear, or at least not form (Figure 121).

Secondly, remarkable grain boundaries are often observed to line up with a remarkable phase boundary of the same type for one of the adjacent grains. The alignment presents sometime a slight shift (Figure 121). This shift is also noticed in TEM observations.

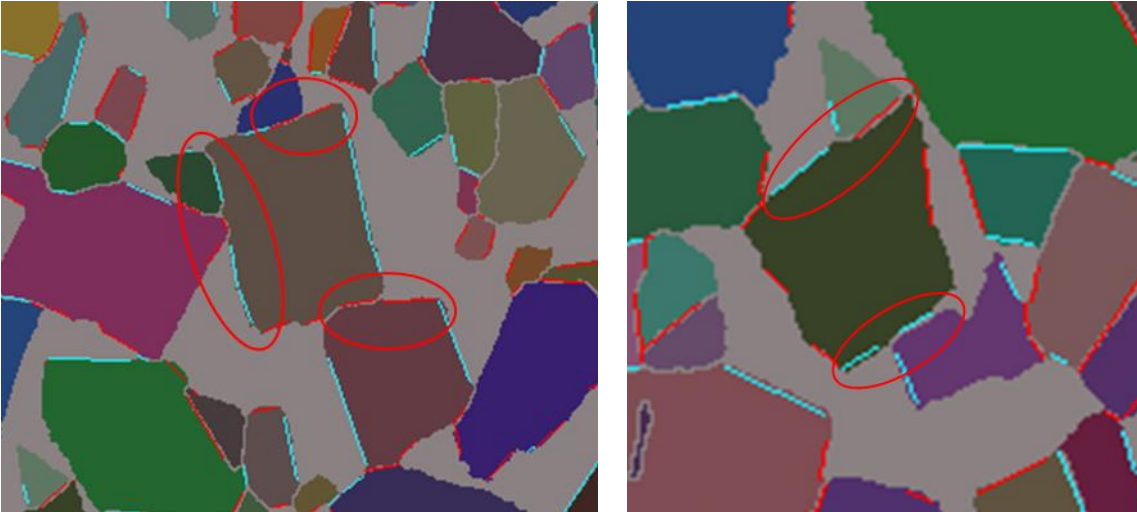


**Figure 121: Remarkable boundaries often line up with a remarkable phase boundary of the same kind for one of the adjacent grains. Prismatic (resp. basal) phase boundaries and grain boundaries are represented in red (resp. blue).**

A simple scenario is proposed, suggesting that those situations can result from an initial cooperative migration of phase and grain boundaries, which ends as phase boundaries are locally pinned by adjacent grain boundaries (Figure 122):

- Due to grain growth, phase boundaries are moving (a).
- Because of impingement, the migration of the boundary eventually comes across another grain. If the situation is favorable, *i.e.* if the grain boundary can be established according to a remarkable boundary plane, the phase boundary keeps moving, accompanied by cooperative migration or development of the recently created grain boundaries (b,c).
- At a point, the grain boundary cannot follow the migration of the phase boundary anymore. If the situation is energetically favorable enough, the phase boundary could keep moving. The boundary starts to curve and follow a non-remarkable boundary plane (d).
- As the situation is not energetically favorable anymore, the grain boundary stops developing and the phase boundary stops migrating.

- When all phase boundaries of the grain are pinned, phase boundaries cannot move anymore and the grain stops growing.

Finally, this displacement leads to the creation of a curved grain boundary, partially faceted and partially corresponding to a close remarkable phase boundary.

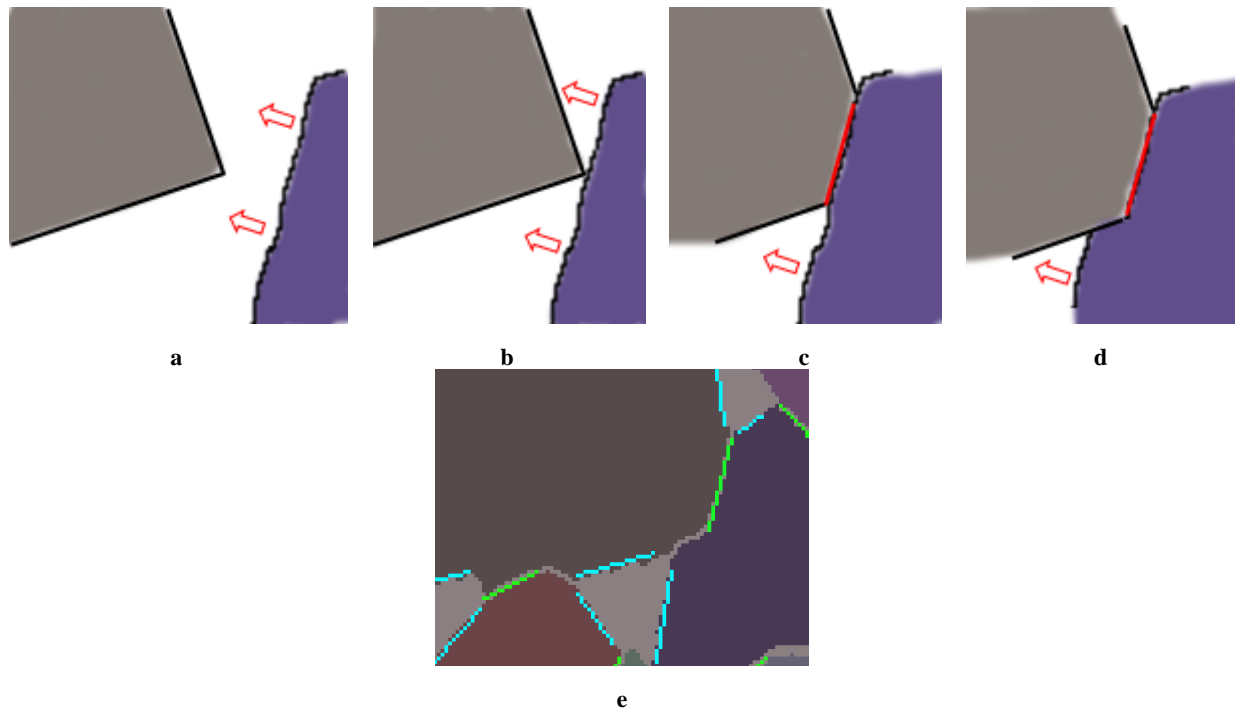


**Figure 122: Illustration of growth mechanism, based on an actual observation in 50 vol% of binder sample, C-rich. Blue (respectively green) segments represent remarkable phase boundaries (respectively grain boundaries).**

In the particular case presented in Figure 123, the rapid displacement of the phase boundary relatively to grain boundary explains how the small grain gets included in the large one, and why phase boundary parts on both sides keeps lined up. Finally, every facet is blocked by adjacent grains, and the boundaries cannot develop anymore without increasing the global interface energy. Thus, this grain is not expected to grow anymore.

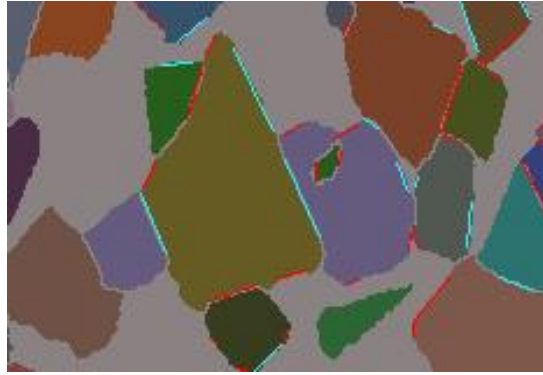


**Figure 123:** Example of curved boundaries observed in 50 vol% of binder sample. Blue (respectively red) segments represent remarkable phase boundaries (respectively grain boundaries).

These observations tend to indicate an easier migration of phase boundaries compared to grain boundaries. A more difficult migration of grain boundaries is not necessarily surprising. In fact, considering the consequent interlocking of carbides grains, grain boundary migration is likely to be at the cost of a remarkable (thus stable) phase boundary.

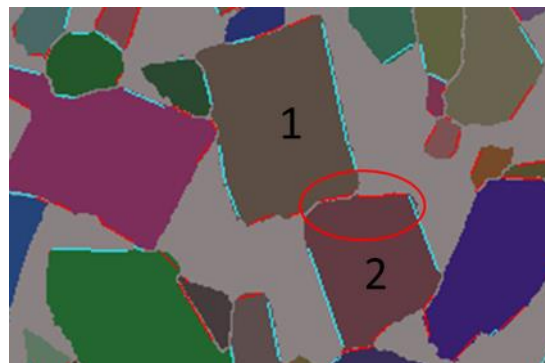


**Figure 124:** Example of microstructure observed in 50 vol% of binder sample. Blue (respectively red) segments represent remarkable phase boundaries (respectively grain boundaries).

As illustrated in Figure 124, supposing that grain 1 is growing, the migration of the boundary in the lower grain 2 would have been at the cost of the remarkable phase boundary (red) of grain 2. It may be more favorable for the grain boundary to grow.

## V.B.2 Modelling the role of grain boundaries and phase boundaries on grain growth

The previous observations suggest a difficult migration of grain boundaries. Considering the coupling between grain boundary and phase boundary migration evoked in the introduction of this part, the low mobility of grain boundaries can be expected to have a significant influence of grain growth. With a modelling approach, this part investigates the role that grain boundary pinning could play in grain growth.

The values used in calculation presented in this section are summarized here:

$P_C$ : capillary pressure	$C$ : contiguity	$v_{PB}, v_{GB}$ : rate of phase/grain boundary displacement
$P_D$ : drag pressure	$r$ : grain boundary radius	$M_{PB}, M_{GB}$ : phase/grain boundary mobility
$V_V, S_V$ : carbide volume/surface area per unit volume	$R$ : grain size	$\gamma_{SL}, \gamma_{GB}$ : interface energy per unit area of phase boundary, and grain boundary
$\bar{R}$ : average grain size	$\bar{R}_{max}$ : maximum average grain size	$\tilde{\gamma}$ : average interfacial energy per unit area

### V.B.2.i Kinetic approach

Phase boundaries and grain boundaries have to move in a cooperative way for a growing grain in a solid-liquid system with grain boundaries. From the previous observations, it is reasonable to assume that grain boundary mobility is much smaller than phase boundary mobility. Grain boundaries will then curve and exert a drag force  $P_D = 2C/r \gamma_{GB}$  on the moving phase

boundaries,  $r$  being the grain boundary radius (see Appendix 4). The rate of displacement  $v_{PB}$  and  $v_{GB}$  of both interfaces can be expressed:

$$v_{PB} = M_{PB} \left( P_C - \frac{2C}{r} \gamma_{GB} \right) \quad (5.7)$$

$$v_{GB} = M_{GB} \left( P_C + \frac{2}{r} \gamma_{GB} \right) \quad (5.8)$$

where  $M_{PB}$  and  $M_{GB}$  are the phase boundary and grain boundary mobilities.

In stationary conditions,  $v_{PB} = v_{GB}$ , and the rate of phase boundary displacement, or grain growth rate, can be deduced:

$$\frac{dR}{dt} = v_{PB} = \frac{(1-C)M_{GB}}{M_{GB} + CM_{PB}} M_{PB} P_C \quad (5.9)$$

An equivalent mobility  $M_{eq}$  can then be deduced:

$$M_{eq} = \frac{(1-C)M_{GB}}{M_{GB} + CM_{PB}} M_{PB} \quad (5.10)$$

which may be approximated by  $(1-C)M_{PB}$  as  $M_{GB} \gg CM_{PB}$  and by  $\frac{(1-C)}{C}M_{GB}$  as  $M_{GB} \ll CM_{PB}$ .

The equivalent mobility then varies as  $(1-C)/C$  as the grain boundary mobility is slow compared to the phase boundary mobility. Hence, grain growth rate may be expressed in a grain boundary controlled regime:

$$\frac{dR}{dt} = \frac{1-C}{C} M_{GB} P_C = \frac{1-C}{C} M_{GB} \left( \frac{3}{\bar{R}} (V_V + (1-C)) - \frac{2}{\bar{R}} \right) \tilde{\gamma} \quad (5.11)$$

$$\frac{dR}{dt} = (1 - C) M_{GB} \left( \frac{3}{\bar{R}} (V_V + (1 - C)) - \frac{2}{R} \right) \left[ \frac{(1 - C)}{C} \gamma_{SL} + \gamma_{GB} \right] \quad (5.12)$$

An increase of contiguity will then significantly decrease the grain growth rate. Assuming  $\gamma_{SL} \approx 0.7 \text{ J/m}^2$  and  $\gamma_{GB} \approx 1.5 - 2 \text{ J/m}^2$  in our WC-Co system, for a mixture of remarkable and random grain boundaries,  $dR/dt$  would increase by a factor  $\sim 6$  between 10 and 50 vol% of binder ( $C$  decreasing from 0.8 to 0.3). This factor may be overestimated. In fact, as the model assumes isolated grain boundaries at the particles surface, prediction at high contiguity values should be considered as qualitative. Especially, the grain boundary radius  $r$  would rather correspond to the equivalent radius of the contact surface, which may gather several contiguous grain boundaries. It is expected to increase with contiguity. For submicronic particles, the driving force brought by the fine particles (term in  $1/\bar{R}$ ) may be large enough for grain growth to be significant, whatever the contiguity. For particles larger than  $1 \text{ }\mu\text{m}$ , the low grain boundary mobility may explain the quasi-stagnant growth observed, especially in the low binder content alloys. Eventually, pinning of phase boundaries by grain boundaries may occur and completely stop grain growth (see next part).

In conclusion the kinetic approach described the decrease of the final grain size with contiguity observed in this work, and difference of growth reported in the literature between micronic or submicronic powder. However, it does not explicit the maximum average grain size the microstructure can reach.

#### V.B.2.ii Energetic approach: influence of grain boundary pinning

As suggested in the qualitative description, grain boundary pinning may play a major role in limiting grain growth.

The maximum drag pressure exerted on the surface area of a grain is:

$$P_D = \frac{2C}{r} \gamma_{GB} \quad (5.13)$$

Grain growth will stop as soon as this pressure is larger than the capillary pressure for any grain (Appendix 3: Migration pressure for grain growth in systems containing phase boundaries and grain boundaries), *i.e.* in practice for a grain of infinite grain size:

$$\frac{2C}{r} \gamma_{GB} > \frac{3}{\bar{R}} (V_V + (1 - C)) \tilde{\gamma} \quad (5.14)$$

or

$$\frac{2C}{r} \gamma_{GB} > \frac{3}{\bar{R}} (V_V + (1 - C)) [(1 - C) \gamma_{SL} + C \gamma_{GB}] \quad (5.15)$$

*i.e.*

$$\frac{\bar{R}}{r} > \frac{3}{2} (V_V + (1 - C)) \left( 1 + \frac{(1 - C)}{C} \frac{\gamma_{SL}}{\gamma_{GB}} \right) \quad (5.16)$$

An increase of contiguity will then significantly reduce the maximum average size which can be reached by grain growth. Assuming  $\gamma_{SL} \approx 0.7 \text{ J/m}^2$  and  $\gamma_{GB} \approx 1.5\text{-}2 \text{ J/m}^2$  in our WC-Co system, for a mixture of remarkable and random grain boundaries, the ratio  $\bar{R}/r$  would increase from 1.8 to  $\approx 3.5$  between 10 and 50 vol% of binder (C decreasing from 0.8 to 0.3).

### **Conclusion**

A scenario is proposed to describe the formation of the grain boundaries population during sintering. It is expected that special boundaries form during the first moments of sintering, when the system is loose enough to allow re-arrangement. From energetic considerations, it is expected that the equilibrium partial contiguity of these special boundaries does not depend on the binder fraction. In a second stage remarkable and random boundaries would form. As the probability to form a random boundary may be proportional to the fraction of random phase boundaries it is not



expected to depend on binder content. Those different predictions are consistent with the measurements.

Microstructural observations, as the presence of curved grain boundaries or interpenetrated grain lead to consider a limitation of grain growth kinetics by the mobility of grain boundaries. Hence, a microstructural model is proposed, based on the effect of the pinning force induced by the grain boundaries, assumed to have a lower mobility than phase boundaries. This model is consistent with the results presented in the previous chapter. As expected grain growth should be more rapid with a submicronic powder than with a micronic powder. But the model especially predicts that grain growth should be faster in high binder content samples. In addition, energetic considerations showed that grain size is expected to reach a limit value which increases when increasing the binder content (decreasing the contiguity). . Abnormal grain growth is then expected to be more likely at high binder content, as it was observed experimentally. Effect of diffusion in the liquid has not been discussed. It cannot be excluded that diffusion may have an effect at very high binder content, however the increase of grain size with binder content measured in this work confirm that it is not influent in the range of compositions considered. Last, this approach cannot explain the effect of carbon content on grain growth. Different explanations have been proposed in the literature, like the influence of carbon on the stability of the liquid phase (thus on the nucleation), or a higher amount of surface defect in carbon rich binder are the most probable explanations. Formation of liquid at a lower temperature (thus earlier in the sintering process) in carbon rich samples is also a plausible explanation.

Finally, the microstructural model proposed in this part is a complement to the classical models presented in the literature for grain growth in cemented carbides. These models only consider the phase boundary mobility, assuming that precipitation from the liquid, with a 2D-nucleation or defect-assisted nucleation step, is the limiting factor. By taking into account the competition between phase boundary and grain boundary migration, our approach is able to predict the effect of binder content on grain growth.

Finally, the model proposed in this part is a complement to the model presented in the literature, as it does not consider nucleation as the only limiting factor but also take into account an effect of grain boundaries. The advantage of this model is to predict an influence of binder content, at the opposite with the nucleation model.



---



---

## Conclusion

This thesis work was dedicated to the understanding of the influence of composition (in particular binder content and carbon content) on the microstructure of WC-Co cemented carbide. In this aim, two focal areas were investigated: grain growth and interface development.

A large place was given to Electron Backscattered Diffraction for sample characterization. With this technique, a large set of samples could be analyzed, thus covering a large composition range. Automation of measurements of microstructural parameters necessitated to set up image analysis routines.

Besides, EBSD makes possible to access orientations relationships in the microstructure, and hence it is an essential tool for the study of grain boundaries. Based on orientation data given by EBSD, a program was developed on purpose for grain boundary character identification and measurement of remarkable boundary plane fraction. This tool enabled systematic analysis of the grain boundary population.

Other characterization techniques were deployed in complement, as SEM observations, TEM observations or Focused Ion Beam 3D reconstruction.

To investigate evolution of grain size, the 3D equivalent diameter distributions were determined. The variation of mean grain size with composition indicates a faster grain growth in carbon rich binder, in agreement with literature. Besides, the role of binder content is clarified, and high binder content is shown to facilitate grain growth and favor abnormal evolution of the grain size distribution.

Grain shape was examined by two methods: evaluation of shape factor from 2D measurement and qualitative observation of 3D images obtained by FIB analysis. The grain shape of isolated

grains is a triangular prism as mentioned in the literature, but with truncation of the vertices rather than by formation of type II prismatic facets. No significant variation of grain shape with the carbon content was detected. This is likely due to the restriction of our analyses to the two-phase domain, where carbon activity varies little, whereas literature results reports shape variations between the three-phase C-rich and W-rich domain.

The examination of grain boundary population reveals the existence of boundary types more frequent than expected in the case of a random distribution, characterized by rotations around  $[10\bar{1}0]$ ,  $[2\bar{1}\bar{1}0]$  and  $[0001]$ . Among these, five boundary types are particularly abundant and are defined by the following [axis/rotation] couples:  $[10\bar{1}0]/90^\circ$ ,  $[2\bar{1}\bar{1}0]/48.42^\circ$ ,  $[2\bar{1}\bar{1}0]/60.59^\circ$ ,  $[2\bar{1}\bar{1}0]/90^\circ$  and  $[0001]/21.79^\circ$ . These rotations allow the possibility of a boundary habit plane with a good coherency between crystalline lattices of both grains engaged in the boundary. This good coherency is expected to decrease the energy of these special grain boundaries.  $[10\bar{1}0]/90^\circ$  rotations, also referred to as  $\Sigma 2$ , are present in significant quantity in the powder. It is likely that  $\Sigma 2$  boundaries found in sintered sample originate mainly from the powder. At the opposite  $[2\bar{1}\bar{1}0]$  and  $[0001]$  rotations are not present in the powder, thus they must form during sintering.

Habit planes of grain boundaries and phase boundaries were also investigated. It appears that a majority of boundaries correspond to the particular dense planes that are basal and prismatic planes. The fraction of remarkable grain boundary plane was measured around 65% of the total grain boundary surface, and the fraction of remarkable phase boundary plane was measured around 55 % of the total phase boundaries surface.

All the experimental results and microstructure observation were put into perspective. A scenario is proposed to describe the formation of grain boundaries during sintering. It is expected that special boundaries form during the first moments of sintering, when the system is loose enough to allow re-arrangement. In a second stage remarkable and random boundaries would form. According to energetic considerations, and in agreement with experimental results, the partial contiguity of special boundaries on one hand and the fraction of remarkable and random grain boundaries on the other hand do not depend on binder fraction.

From microstructural observations, the grain boundary mobility appears to be rather low, as compared to the phase boundary mobility. As a consequence a microstructural model is proposed

to take into account the pinning effect of the low mobility grain boundaries on grain growth. This model predicts a growth rate which scales inversely with the contiguity. In addition, grain size is expected to reach a limit value, which increases as contiguity decreases. This limit value would be in the order of one  $\mu\text{m}$  in our conditions. The model is consistent with our experimental results concerning the effect of binder content on grain growth. In addition, since grain boundary pinning is reduced at high binder content, abnormal grain growth is expected to be more likely, as observed experimentally. It cannot be excluded that diffusion may have an effect at very high binder content, however the increase of grain size with binder content measured in this work confirm that it is not influent in the range of compositions considered.

Finally, the model proposed here completes the classical literature analysis of a limitation of grain growth by precipitation from the liquid, with a 2D-nucleation or defect-assisted nucleation step at the particle surface. The classical approach deals with the phase boundary mobility but does not take into account the effect of the grain boundary mobility. A transition from a phase boundary to a grain boundary controlled mobility is expected at low binder content and this would explain the observed influence of binder content on grain growth.

The model proposed in this work to analyze grain growth kinetics made the simplification that phase boundaries are highly mobile while isolated grain boundaries act as pins for the migration. In the future, a more continuous description should be developed for contiguity variation between 0 and 1, by taking into account the local coupling between the different kinds of boundaries and also the role of triple lines. Further microstructural characterization should be performed in 3D to support the model, such as monitoring the evolution of the number of contacts between grains for a more thorough understanding of pinning effects.

As regards the characterization technique, improvements should be brought to the EBSD analysis, especially in order to overtake actual resolution limits. The constant improvement of acquisition devices could offer the opportunity to improve resolution without sacrificing too much acquisition time. In addition, it could be profitable to apply our systematic method of analysis to other issues dealing with WC-Co microstructure. For example, influence of carbon content on grain shape is still an open question and it could be interesting to enlarge the

investigation to the three-phase domain where carbon activity variations are more important. Considering the role of boundaries in grain growth pointed out in this work, the study of the effects of growth inhibitors on boundary population would be interesting. Another application could be the influence of the binder type on boundary stability, as alternative binders to cobalt know a renewed interest.

Last, classical 2D EBSD analysis is a powerful tool for grain boundary misorientation analysis but it reaches its limit for the analysis of the population of grain boundary habit planes where stereological methods only provide estimations of the corresponding fractions, with a limited precision. Despite of its prohibitive acquisition time, FIB/EBSD could be done on well-chosen compositions to confirm the results obtained in this study and give a more reliable description of the grain morphology. A qualitative 3D analysis of grain shape was performed by FIB/SEM in this study. The full potential of data collected will be exploited after improving the grain separation method. This will already bring interesting information on grain shape. Gathering all these results could yield to establish an equivalent model grain depending on the composition, taking into account the shape as well as the phase and grain boundary character. Implementation of an ideal grain in a discrete element model could also enable to predict evolution of microstructural parameters, such as grain morphology or contiguity, as a function of binder content. This would address the needs of a predictive tool for the evolution of microstructure with composition.



---

---

## References

- [1] L. Akesson, "An experimental study of the Co-W-C system in the temperature range 1473-1698 K," Royal Institut of Technology, Stockholm, 1982.
- [2] O. Kruse, B. Jansson, and K. Frisk, "Experimental Study of invariant equilibra in the Co-W-C and the Co-W-C-Me (Me = Ri,Ta,Nb) systems," *J. phase equilibria*, vol. 22, no. 5, pp. 552–555, 2001.
- [3] V. Bounhoure, "Frittage en phase solide des alliages WC-Co: influence du rapport C/W et de l'ajout de Cr," Institut Polytechnique de Grenoble, 2008.
- [4] P. Rautala and J. T. Norton, "No Title," *Tans. AIME*, vol. 194, pp. 1045–1050, 1952.
- [5] A. Guillermet, "PhD dissertation," Royal Institute of Technology, Stockholm, 1989.
- [6] R. G. Barrows and J. B. Newkirk, "No Title," *Metallography*, vol. 5, pp. 515–541, 1972.
- [7] J. Weidow, S. Johansson, H. O. Andrén, and G. Wahnström, "Transition metal solubilities in WC in cemented carbide materials," *J. Am. Ceram. Soc.*, vol. 94, pp. 605–610, 2011.
- [8] T. Johansson and B. Uhrenius, "Phase equilibria, isothermal reactions, and a thermodynamic study in the Co-W-C system at 1150°C," *Met. Sci.*, vol. 12, no. 2, pp. 83–94, 1978.
- [9] J. Freytag, "PhD dissertation," Stuttgart Universität, 1977.
- [10] J. Gurland and P. Bardzil, "Relation of strength, composition and grain size of sintered WC-Co alloys," *J. Met.*, vol. February, pp. 311–315, 1955.
- [11] I. M. Lifshitz and V. V. Slyozov, "The kinetics of precipitation from supersaturated solid solutions," *J. Phys. Chem. Solids*, vol. 19, no. 1, pp. 35–50, 1961.
- [12] C. Wagner, "Theory of the aging of precipitates by dissolution/reprecipitation (Ostwald ripening)," *Zeitschrift für Elektrochemie*, vol. 65, no. 7, pp. 581–591, 1961.
- [13] S. G. Shin and H. Matsubara, "Grain growth of carbide based cermets during liquid phased sintering," *Sinter. Technol.*, pp. 157–164, 1995.

- 
- [14] M. Coster, J. L. Chermant, and A. Deschanvres, "Cinétique de croissance des cristaux de WC dans le cobalt," *Mem. Sci. la Rev. Metall.*, vol. LXIX, pp. 465–478.
- [15] R. Warren and M. Waldron, "Microstructural development during the liquid-phase sintering of cemented carbides," *Powder Met.*, vol. 15, pp. 166–201, 1972.
- [16] S. Lay and J.-M. Missiaen, "Microstructure and morphology of hard metals," *Compr. hard Mater.*, vol. 1, no. section 1.03, pp. 91–122, 2014.
- [17] Y. J. Park, N. M. Hwang, and D. Y. Yoon, "Abnormal Growth of Faceted Grains in Liquid Matrix," *Metallurgical and Materials Transactions A*, vol. 27A, pp. 2809–2819, 1996.
- [18] G. S. Rohrer, C. L. Rohrer, and W. W. Mullins, "Coarsening of Faceted Crystals," *J. Am. Ceram. Soc.*, vol. 85, pp. 675–682, 2002.
- [19] Y. Zhong and L. L. Shaw, "Growth mechanisms of WC in WC–5.75wt% Co," *Ceram. Int.*, vol. 37, pp. 3591–3597, 2011.
- [20] X. Wang, Z. Z. Fang, and H. Y. Sohn, "Grain growth during the early stage of sintering of nanosized WC-Co powder," *Int. J. Refract. Met. Hard Mater.*, vol. 26, pp. 232–241, 2008.
- [21] F. F. Lange and B. J. Kellett, "Thermodynamics of densification: II, grain growth in porous compacts and relation to densification," *J. Am. Ceram. Soc.*, vol. 72, no. 199677, pp. 735–741, 1989.
- [22] K. Mannesson, J. Jeppsson, A. Borgenstam, and J. Gren, "Carbide grain growth in cemented carbides," *Acta Mater.*, vol. 59, pp. 1912–1923, 2011.
- [23] I. Borgh, P. Hedström, J. Odqvist, A. Borgenstam, J. Ågren, A. Gholinia, B. Winiarski, P. J. Withers, G. E. Thompson, K. Mingard, and M. G. Gee, "On the three-dimensional structure of WC grains in cemented carbides," *Acta Mater.*, vol. 61, pp. 4726–4733, 2013.
- [24] V. Chabretou, C. H. Allibert, and J. M. Missiaen, "Quantitative analysis of the effect of the binder phase composition on grain growth in WC-Co sintered materials," *J. Mater. Sci.*, vol. 38, pp. 2581–2590, 2003.
- [25] I. Borgh, P. Hedström, A. Borgenstam, J. Ågren, and J. Odqvist, "Effect of carbon activity and powder particle size on WC grain coarsening during sintering of cemented carbides," *Int. J. Refract. Met. Hard Mater.*, vol. 42, pp. 30–35, 2014.
- [26] V. Chabretou, "Croissance de cristaux facettés: cas de WC-Co," Grenoble INP, 2000.
- [27] I. Borgh, P. Hedström, T. Persson, S. Norgren, A. Borgenstam, J. Ågren, and J. Odqvist, "Microstructure, grain size distribution and grain shape in WC-Co alloys sintered at different carbon activities," *Int. J. Refract. Met. Hard Mater.*, vol. 43, pp. 205–211, 2014.

- 
- [28] L. Gu, J. Huang, and C. Xie, "Effects of carbon content on microstructure and properties of WC-20Co cemented carbides," *Int. J. Refract. Met. Hard Mater.*, vol. 42, pp. 228–232, 2014.
- [29] A. BOCK, W. D. SCHUBERT, and B. LUX, "Inhibition of grain growth on submicron cemented carbides," *Powder Metall. Int.*, vol. 24, no. 1, pp. 20–26, 1992.
- [30] J. Kishino, H. Nomura, S.-G. Shin, H. Matsubara, and T. Tanase, "Computational study on grain growth in cemented carbides," *Int. J. Refract. Met. Hard Mater.*, vol. 20, pp. 31–40, 2002.
- [31] K. Mannesson, I. Borgh, A. Borgenstam, and J. Ågren, "Abnormal grain growth in cemented carbides - Experiments and simulations," *Int. J. Refract. Met. Hard Mater.*, vol. 29, no. 4, pp. 488–494, 2011.
- [32] S.-J. L. Kang, J.-H. Park, S.-Y. Ko, and H.-Y. Lee, "Solid-State Conversion of Single Crystals: The Principle and the State-of-the-Art," *J. Am. Ceram. Soc.*, vol. 98, no. 35773, pp. 347–360, 2015.
- [33] J. Vicens, M. Benjdir, G. Nouet, a. Dubon, and J. Y. Laval, "Cobalt intergranular segregation in WC-Co composites," *Journal of Materials Science*, vol. 29, pp. 987–994, 1994.
- [34] W. Bollmann, "Crystal Defects and Crystalline Interfaces," *Springler-Verlag: Berlin*. 1970.
- [35] H. Grimmer, "Coincidence orientations of grains in rhombohedral materials," *Acta Crystallogr. Sect. A*, vol. 33, pp. 509–520, 1989.
- [36] S. Hagège, G. Nouet, and P. Delavignette, "Grain boundary analysis in TEM. IV. Coincidence and the associated defect structure in tungsten carbide," *Phys. Status Solidi*, vol. 62, no. Iv, pp. 97–107, 1980.
- [37] M. Christensen and G. Wahnström, "Co-phase penetration of WC(101 $\bar{0}$ )/WC(101 $\bar{0}$ ) grain boundaries from first principles," *Phys. Rev. B*, vol. 67, pp. 1–11, 2003.
- [38] R. Warren, "Determination of the interfacial energy ratio in two-phase systems by measurement of interphase contact," *Metallography*, vol. 9, no. 3, pp. 183–191, 1976.
- [39] M. Christensen and G. Wahnström, "Effects of cobalt intergranular segregation on interface energetics in WC-Co," *Acta Mater.*, vol. 52, pp. 2199–2207, 2004.
- [40] S. A. E. Johansson, M. V. G. Petisme, and G. Wahnström, "A computational study of special grain boundaries in WC-Co cemented carbides," *Comput. Mater. Sci.*, vol. 98, pp. 345–353, Feb. 2015.

- 
- [41] A. Henjered, M. Hellsing, H. O. Andrén, and H. Norden, "Quantitative microanalysis of carbide/carbide interfaces in tungsten carbide-cobalt base cemented carbides," *Mater. Sci. Technol.*, vol. 2, pp. 847–855, 1986.
- [42] T. Yamamoto, Y. Ikuhara, T. Watanabe, T. Sakuma, Y. Taniuchi, K. Okada, and T. Tanase, "High resolution microscopy study in Cr<sub>3</sub>C<sub>2</sub>-doped WC-Co," *J. Mater. Sci.*, vol. 36, pp. 3885–3890, 2001.
- [43] J. Weidow and H. O. Andrén, "Grain and phase boundary segregation in WC-Co with TiC, ZrC, NbC or TaC additions," *Int. J. Refract. Met. Hard Mater.*, vol. 29, no. 1, pp. 38–43, 2011.
- [44] J. Weidow and H.-O. Andrén, "Grain and phase boundary segregation in WC-Co with small V, Cr or Mn additions," *Acta Mater.*, vol. 58, no. 11, pp. 3888–3894, Jun. 2010.
- [45] S. Lay and M. Loubradou, "Characteristics and origin of clusters in submicron WC-Co cermets," *Philos. Mag.*, vol. 83, no. February 2015, pp. 2669–2679, 2003.
- [46] S. Lay, S. Hamar-Thibault, and a. Lackner, "Location of VC in VC, Cr<sub>3</sub>C<sub>2</sub> codoped WC-Co cermets by HREM and EELS," *Int. J. Refract. Met. Hard Mater.*, vol. 20, pp. 61–69, 2002.
- [47] V. Kumar, Z. Z. Fang, S. I. Wright, and M. M. Nowell, "An analysis of grain boundaries and grain growth in cemented tungsten carbide using orientation imaging microscopy," *Metall. Mater. Trans. A*, vol. 37, no. March, pp. 599–607, 2006.
- [48] A. Delanoë and S. Lay, "Evolution of the WC grain shape in WC – Co alloys during sintering : Effect of C content," *Int. J. Refract. Met. Hard Mater.*, vol. 27, no. 1, pp. 140–148, 2009.
- [49] J. D. Kim, S. J. L. Kang, and J. W. Lee, "Formation of grain boundaries in liquid-phase-sintered WC-Co alloys," *J. Am. Ceram. Soc.*, vol. 88, pp. 500–503, 2005.
- [50] C. S. Kim and G. S. Rohrer, "Geometric and Crystallographic Characterization of WC Surfaces and Grain Boundaries in WC-Co Composites," *Interface Sci.*, vol. 12, pp. 19–27, 2004.
- [51] C. S. Kim, T. R. Massa, and G. S. Rohrer, "Interface character distributions in WC-Co composites," *J. Am. Ceram. Soc.*, vol. 91, pp. 996–1001, 2008.
- [52] X. Yuan, "Grain boundary character distributions of sigma<sub>2</sub> boundaries in WC-Co composites with different cobalt volume fractions," *Ceram. Int.*, vol. 40, no. 1, pp. 1873–1878, 2014.

- 
- [53] X. Yuan, C. Wei, D. Zhang, J. Zhu, and X. Gao, "Characterization and comparison of grain boundary character distributions in cemented carbides with different binder phases," *Comput. Mater. Sci.*, vol. 93, pp. 144–150, 2014.
- [54] D. M. Saylor and G. S. Rohrer, "Determining Crystal Habits from Observations of Planar Sections," *J. Am. Ceram. Soc.*, vol. 85, pp. 2799–2804, 2002.
- [55] M. Benjdir, "Analyses cristallographiques et chimiques des joints de grain du carbure de tungstène dans le composite WC-Co. Etudes en microscopie électronique en transmission," *Thesis. Univ. Caen*.
- [56] J. Gurland, "The measurement of grain contiguity in two phase alloy," *Trans. AIME*, vol. 212, pp. 452–455, 1958.
- [57] A. V. Shatov, S. S. Ponomarev, S. A. Firstov, and R. Warren, "The contiguity of carbide crystals of different shapes in cemented carbides," *Int. J. Refract. Met. Hard Mater.*, vol. 24, pp. 61–74, 2006.
- [58] R. Deshmukh and J. Gurland, "A study of microstructural development during the liquid phase sintering of WC-Co alloys," *Proc. 2d Conf. Sci. Hard Mater.*, pp. 347–358, 1986.
- [59] H. Exner, "Physical and chemical nature of cemented carbides," *Inter. Met. Rev.*, vol. 4, pp. 149–173, 1979.
- [60] H. Exner, "Qualitative and quantitative interpretation of microstructures in cemented carbides," *Proc. 1st Int. Conf. Sci. Hard Mater.*, no. 233–262, 1983.
- [61] G. J. Rees and B. Young, "A study of the factors controlling grain size in sintered hard-metal," *Powder Metall.*, vol. 14, pp. 185–198.
- [62] H. Exner and H. Fischmeister, "Gefüge aufbildung von gesinterten Wolframkarbid-Kobalt-Hartlegierungen," *Arch. für das Eisenhüttenwes.*, vol. 37, pp. 417–426, 1966.
- [63] S. Luyckx and a. Love, "The dependence of the contiguity of WC on Co content and its independence from WC grain size in WC-Co alloys," *Int. J. Refract. Met. Hard Mater.*, vol. 24, pp. 75–79, 2006.
- [64] H. C. Lee and J. Gurland, "Hardness and deformation of cemented tungsten carbide," *Mater. Sci. Eng.*, vol. 33, pp. 125–133, 1978.
- [65] B. Roebuck and E. Almond, "Deformation and fracture processes and the physical metallurgy of WC-Co hardmetals," *Int. Mater. Rev.*, vol. 33, pp. 90–100, 1988.
- [66] V. T. Golovchan and N. V. Litoshenko, "On the contiguity of carbide phase in WC-Co hardmetals," *Int. J. Refract. Met. Hard Mater.*, vol. 21, pp. 241–244, 2003.

- 
- [67] F. Delannay, "Modelling of the influence of dihedral angle, volume fractions, particle size and coordination on the driving forces for sintering of dual phase systems," *Philos. Mag.*, vol. 85, no. December 2012, pp. 3719–3733, 2005.
- [68] R. M. German, "The contiguity of liquid phase sintered microstructures," *Metall. Trans. A*, vol. 16, no. July, pp. 1247–1252, 1985.
- [69] M. Christensen, G. Wahnström, S. Lay, and C. H. Allibert, "Morphology of WC grains in WC-Co alloys: theoretical determination of grain shape," *Acta Mater.*, vol. 55, pp. 1515–1521, 2007.
- [70] S. Lay, C. H. Allibert, M. Christensen, and G. Wahnström, "Morphology of WC grains in WC-Co alloys," *Mater. Sci. Eng. A*, vol. 486, pp. 253–261, 2008.
- [71] a. V. Shatov, S. a. Firstov, and I. V. Shatova, "The shape of WC crystals in cemented carbides," *Mater. Sci. Eng. A*, vol. 242, pp. 7–14, 1998.
- [72] M. Christensen, "Quantitative Analysis of WC Grain Shape in Sintered WC-Co Cemented Carbides," *Phys. Rev. Lett.*, vol. 94, p. 066105, 2005.
- [73] S. Lay, P. Donnadieu, and M. Loubradou, "Polarity of prismatic facets delimiting WC grains in WC-Co alloys," *Micron*, vol. 41, pp. 472–477, 2010.
- [74] S. Kim, S. H. Han, J. K. Park, and H. E. Kim, "Variation of WC grain shape with carbon content in the WC-Co alloys during liquid-phase sintering," *Scr. Mater.*, vol. 48, pp. 635–639, 2003.
- [75] J. C. Russ, *Practical Stereology*. New York: Plenum Press, 1986.
- [76] R. T. DeHoff and F. N. Rhines, *Quantitative Microscopy*, McGraw-Hil. 1961.
- [77] E. E. Underwood, *Quantitative stereology*. Addison-Wesley Pub. Co., 1970.
- [78] M. Coster and J. L. Chermant, *Précis d'analyse d'images*. Paris: Editions du CNRS, 1985.
- [79] S. A. Saltykov, "Stereometric metallography," *Metallurgizdat*, 1958.
- [80] J.-L. Pouchou, Ed., *L'analyse EBSD, principes et applications*. Groupement National de Microscopie électronique à balayage et de microanalyses, 2002.



---

# Appendix

---

---

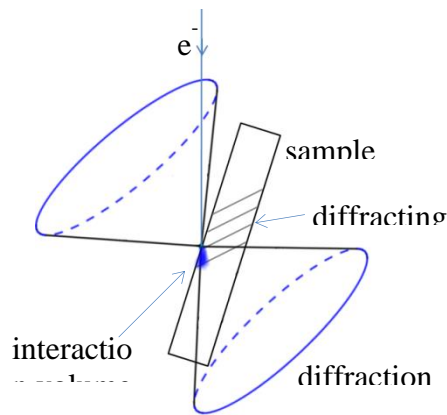
## Appendix 1: Principles of EBSD method

### *Kikuchi lines and formation of EBSD diagrams*

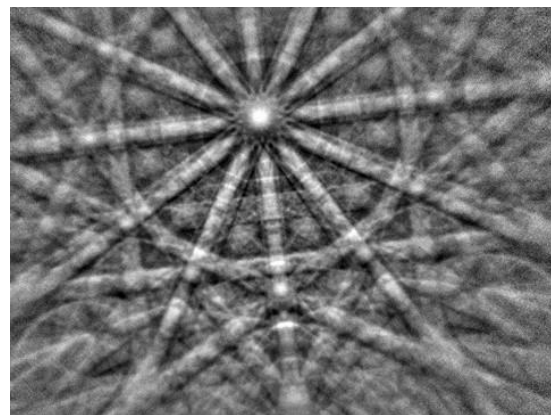
Due to interaction with atoms of the target, incident electrons are slowed and scattered in the crystalline structure. A fraction of them is backscattered. The higher the atomic number of the material, the higher is the fraction of backscattered electrons. Some of those backscattered electrons respect conditions to be diffracted by certain families of atomic planes. Conditions for diffraction are given by Bragg's law:

$$n \cdot \lambda = 2 \cdot d \cdot \sin \theta \quad [1]$$

where  $\lambda$  is electrons wave length,  $n$  a whole number,  $d$  the distance between planes of the family, and  $\theta$  the incidence angle of electrons on the planes.  $\lambda$  being fixed ( $\lambda \approx 0.09 \text{ \AA}$  for 20 kV electrons), electrons are diffracted along two cone whose opening depends on the family of planes (Figure 125a). The intersection of diffraction cones with a plan (basically the observation plane) forms Kikuchi lines. Because diffraction cones are rather open ( $\theta$  is in the order of  $1^\circ$ ) Kikuchi lines are approximately parallel. The ensemble of Kikuchi lines forms an EBSD pattern (Figure 125b) proper to the crystalline structure of the analyzed material.



a.



b.

**Figure 125** Diffraction of backscattered electron by atom planes of the sample (a) generates EBSD patterns (b).

As diffraction angle depends on electron wave length [1], a narrow distribution of backscattered electrons energy is necessary to guaranty a good sharpness of Kikuchi lines. Monte Carlo simulation showed that decreasing the incidence angle of electron beam relatively to the surface to analyze makes possible to obtain a quasi monoenergetic backscattered electron cloud, thus a sharp contrast between EBSD pattern and the background signal (Figure 126). The optimum has been found to be for a 30° incident beam, *i.e.* a 70° tilt of the sample.

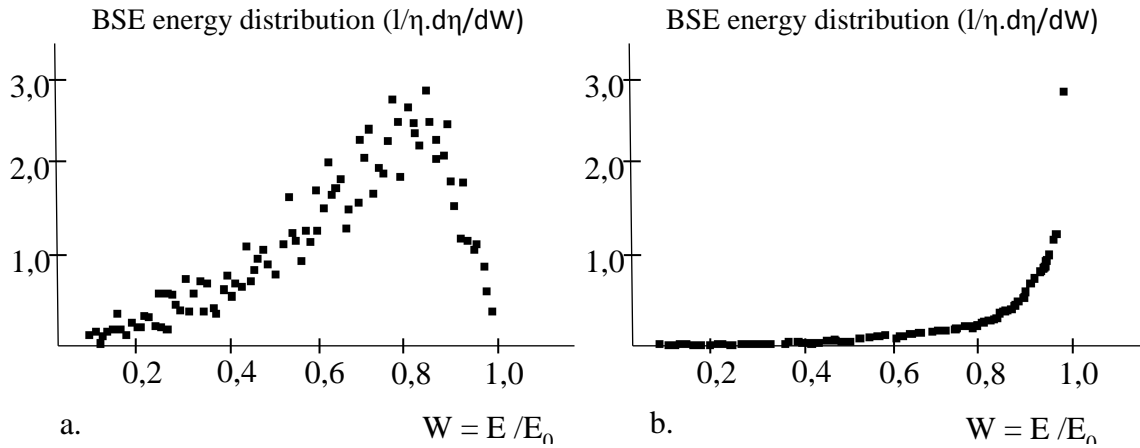


**Figure 126 Monte Carlo simulation of BSE energy distribution: comparison between normal incidence (a) and 70° tilt of the sample (b) (Ni sample, 20keV, 10<sup>6</sup> electrons) [80].**

The escape depth also decreases with incidence of the electron beam. As showed by Monte Carlo simulation, the most probable escape depth of 20keV electrons in a nickel target is around 15 mg/cm<sup>2</sup> for normal incidence and is significantly decreased when the sample is 70° tilted.

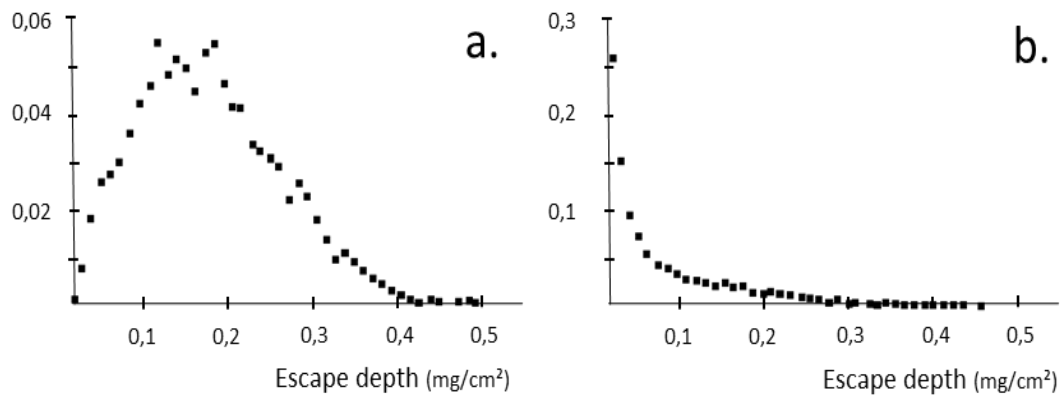


**Figure 127 Monte Carlo simulation of BSE escape depth distribution: normal incidence (a), 70° tilted sample (b) (Ni sample, 20keV, 10<sup>6</sup> electrons) [80].**

---

### ***Indexation of EBSD diagrams***

Kikuchi diagrams depend on nature and orientation of the crystal. Extraction of this information is taken over by an algorithm which roughly consists in:

- Conversion of EBSD diagram into Hough space thanks to Hough transformation. It consists in associating every pixel (i) in the image space (x, y) to a pixel (j) in Hough space ( $\rho$ ,  $\theta$ ) with the relation:

$$\rho = x_i \cos \theta_j + y_i \sin \theta_j$$

Thus this transformation associate each pixel of the image space to a sinusoidal curve in the Hough space, and a line in image space become a point of high intensity in Hough space (Figure 128).

- In Hough space N bright points (*i.e.* Kikuchi lines in the EBSD diagram) are detected.

- Every combination of n point among N is successively considered. The objective is to compare these n points to simulated diagrams (for any phase, any orientation) and determine which phase/orientation they are most likely to correspond to.

- Finally, the solution occurring most often is kept as final solution.

Three parameters must be given by the user to the system: the crystallographic parameters of present phases, the number of bands to consider (N) and the number of bands to use for orientation determination (n).

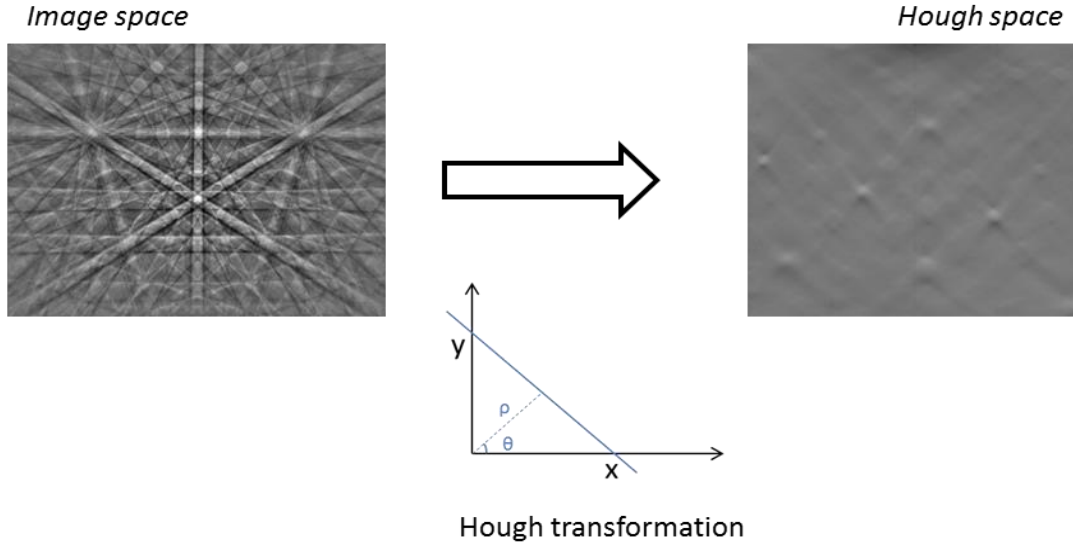


**Figure 128 Conversion of EBSD diagram in the Hough space.**

In order to quantify the quality of the acquisition a quality index (QI) is defined, depending on sharpness and contrast of EBSD diagrams. A confidence index (CI) is defined from probabilities  $p_1$  and  $p_2$  of the two first solutions:

$$CI = \frac{p_1 - p_2}{p_1 + p_2}$$

Sometime EBSD pattern quality is not sufficient to allow identification of the phase. It often occurs at grain boundary or in deformed regions (because of the high concentration of crystal defects). In this case the pixel is considered as NIP (Non Indexes Pixel). Thus quality of an acquisition can be estimated thanks to the Hit Rate, defined as the fraction of NIP.

### ***EBSD mapping***

The big advantage of EBSD is the possibility to map orientations in the sample. This is done by sweeping the electron beam on the surface of the sample, according to a rectangular or hexagonal grid, and reading EBSD diagram and orientation at each position (corresponding to a pixel of the final image).

---

## Appendix 2: Basics of image analysis

### *Image types and thresholding*

A numerical image can be seen as a two dimensions table whose cells (*i.e.* pixel) contain information.

The simplest type of image is binary type: the information can take only two values, 0 or 1 (black or white), and then can be stored with a single bit.

In the case of a grey level image, the information is an intensity that can take any value inbetween 0 (black) and 255 (white). Those 256 values correspond to the quantity of information that can be stored on eight bits (*i.e.* one byte, or octet).

In the case of a color image, the color associated to a pixel is interpreted as a combination of the three primary colors: red, blue, and green. The intensity of each color is stored in a single byte (*i.e.* 256 possible values). Thus, each pixel is associated with 3 bytes (or bands), which represent  $256 \times 256 \times 256 \approx 16.7$  millions of possible colors: if it is definitely too much for human eye perception, such a precise resolution is useful for image processing.

In order to extract and isolate a phase from the background it can be interesting to transform a grey level image into a binary image thanks to an operation called thresholding. The simplest thresholding method consists in attributing the value 1 to every pixel presenting an intensity value contained in a specified interval, and 0 to others. In the case of a color image it would be necessary to preliminary extract one of the three bands, on which the threshold operation can be performed.

### *Basic operations on binary images*

#### *Logical combinations*

Among the basic tools for image analysis are the logical operators (Figure 129):

- AND: selects points which are present in both original sets.

- OR: combines two sets of points.
- Exclusive-OR (X-OR): selects points which are present in one original set or the other, but not both.
- Not: selects points which are outside the original set.

All of these operators can be combined in any sequence, but some of them are not commutative (the order they are written in and parentheses are important: NOT(A OR B) and NOT(A) OR B are different).

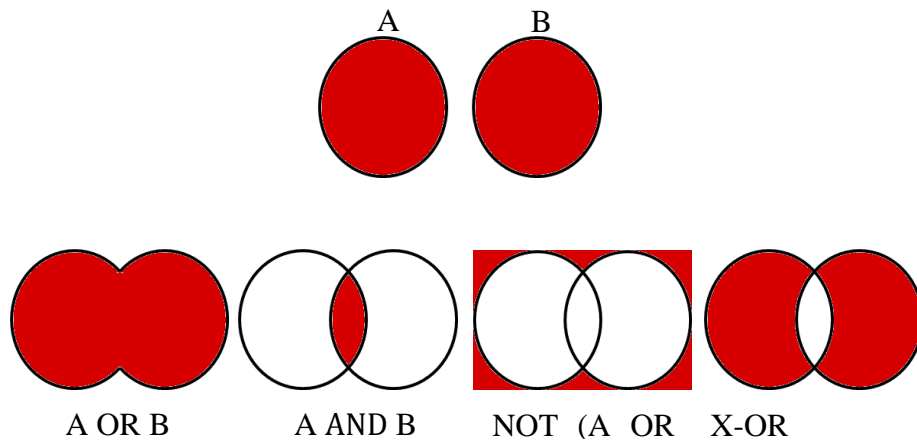


**Figure 129 Examples of logical combinations with original sets A and B.**

### *Morphology operations*

Morphology operations are based on the logical combination of the binary input image with a simple pre-defined shape called structuring element (B). B is shifted in each position  $x$  of the input image, and union, intersection or inclusion of  $B_x$  with input set is tested. The set of positions returning a true value form the transformed image.

### ***Erosion***

Erosion of a set of point  $X$  is the set of points  $x$  in input image such as  $B$  centered in  $x$  is completely included in  $X$ :

$$E^B(X) = \{x / B_x \text{ AND } X = B\}$$



---

### ***Dilation***

Dilation of a set of point X is the set of points x in input image such as B centered in x is partially included in X:

$$E^B(X) = \{x / B_x \text{ AND } X \neq \emptyset\}$$

### ***Opening***

Opening is the combination of the erosion of X by B, followed with dilation of the resulting image with B. This operation results in the suppression of any parts of X that cannot contain B.

### ***Closing***

Closing is the combination of the dilation of X by B, followed with erosion of the resulting image with B. This operation closes any parts of the image smaller than B.

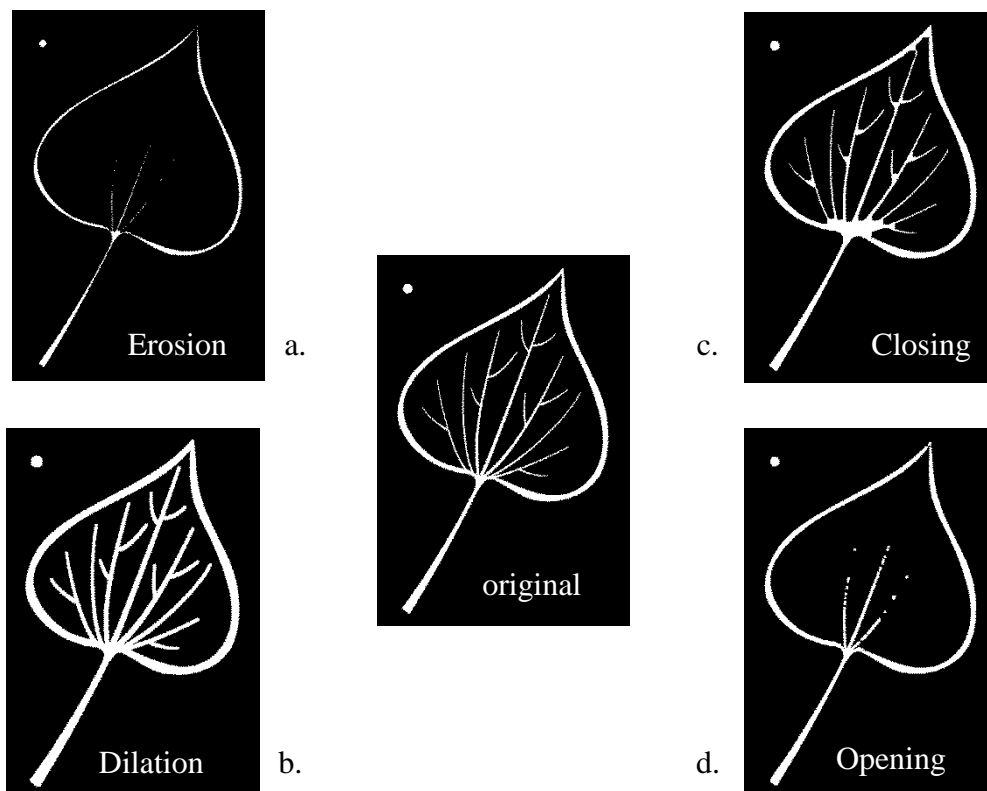
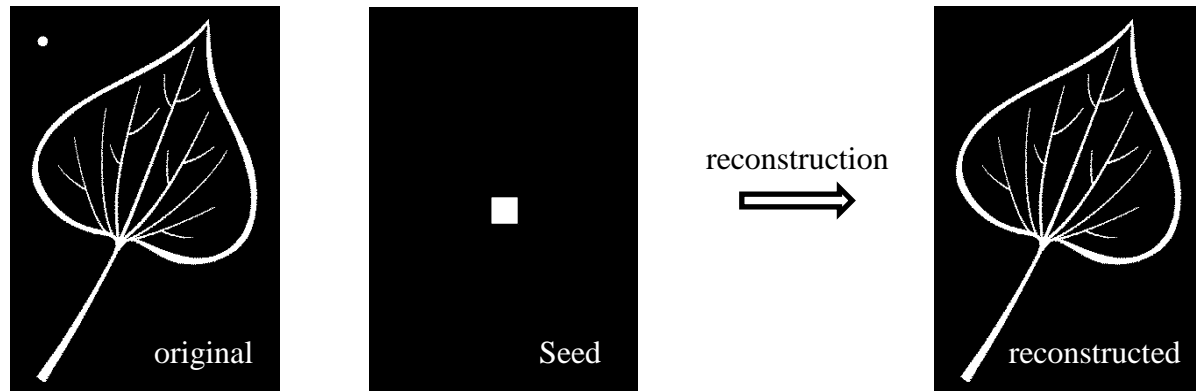


Figure 130 Examples of classic morphological operations, with a square 3x3 px structuring element.

---

### ***Reconstruction***

Reconstruction is an iterative operation leading to the partial reconstruction of a set X, from a “seed” M: only parts of X in contact with M are reconstructed.



**Figure 131** Example of reconstruction from a "seed" image.

### ***Side effects correction***

Some of the particles situated on the side of the image are not completely included in the analyzed field. Then, those particles will bias measurements. The solution could consist in not taking into account those particles, but it would bias the observed distribution (as it is more likely to suppress big particles rather than the little ones).

The method used in this work is the associated point method: only particles whose center is included into a mask are considered. This mask has to be chosen small enough to exclude all particles partially in the image. This way, the probability to select an object only depends on the position of its center and not on its size.

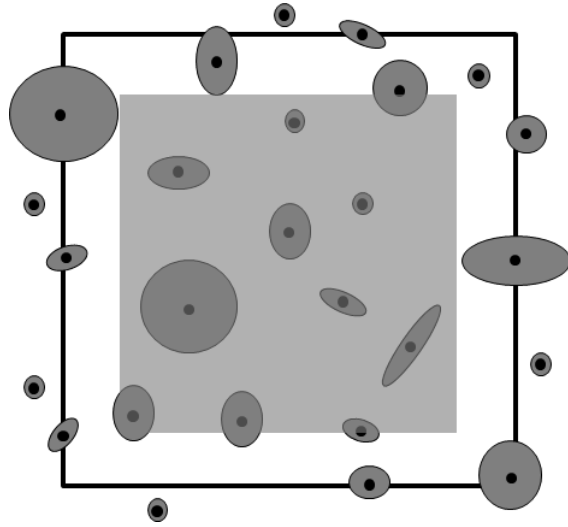
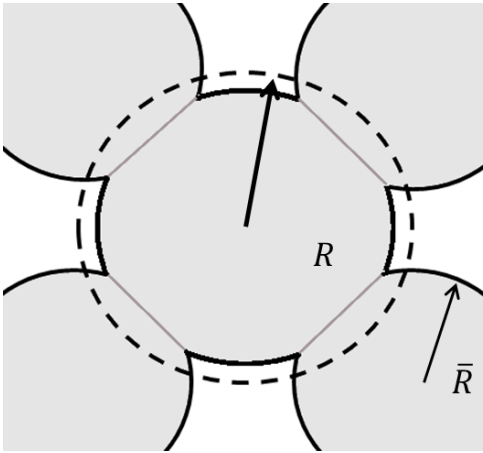


**Figure 132** Correction of side effect with the associated point method: only grains whose center is included in the mask (grey) are considered.

---

## Appendix 3: Migration pressure for grain growth in systems containing phase boundaries and grain boundaries



The average pressure exerted on phase boundaries and grain boundaries of a growing grain can be approached assuming a growing grain of size  $R$  surrounded by average grains of size  $\bar{R}$  (Figure). A cooperative migration of phase boundaries and grain boundaries is assumed. As the grain grows of  $dR$ , the interface energy variation  $dE$  has a positive contribution, due to the increase of the grain area, and two negative contributions: one is due to the elimination of interfaces in the neighboring volume, the other to decrease of interface area associated to the dissolution of particles in the matrix:

$$dE = 8\pi R dR \tilde{\gamma} - 4\pi R^2 dR S_V \tilde{\gamma} - 4\pi R^2 (1 - C) dR \frac{S_V}{V_V} \tilde{\gamma}$$

where  $\tilde{\gamma}$  is the average interfacial energy per unit area of the grains and is related to the interface energies  $\gamma_{SL}$  of solid-liquid phase boundaries,  $\gamma_{GB}$  of the grain boundaries, and to the contiguity  $C$ :

$$\tilde{\gamma} = (1 - C) \gamma_{SL} + C \gamma_{GB}$$

$S_V$  is the specific surface area of the solid phase in the microstructure and can be related to the solid volume fraction  $V_V$  and to the average grain size :

$$S_V = \frac{3}{\bar{R}} V_V$$

---

Reporting in the expression for the energy variation:

$$dE = \left( 8\pi R dR - 4\pi R^2 dR \frac{3}{\bar{R}} V_V - 4\pi R^2 (1 - C) dR \frac{3}{\bar{R}} \right) \tilde{\gamma}$$

The capillary pressure exerted to move phase boundaries and grain boundaries outside the growing grain is obtained from the relation:

$$P_C = - \frac{1}{4\pi R^2} \frac{dE}{dR}$$

which yields:

$$P_C = \left( \frac{3}{\bar{R}} (V_V + (1 - C)) - \frac{2}{R} \right) \tilde{\gamma}$$

or equivalently:

$$P_C = \left( \frac{2\tilde{\gamma}}{R^*} - \frac{2\tilde{\gamma}}{R} \right)$$

where  $R^*$  is the critical radius in the mean field approach, *i.e.* the size above which particle grow and below which particle shrink:

$$R^* = \frac{2}{3} \frac{1}{V_V + (1 - C)} \bar{R}$$

The driving force for grain boundary migration is then as larger as the average particle size is smaller and the growing grain is comparatively larger and as the phase and grain boundary energies are higher.

---

## Appendix 4: Calculation of the dragging force

Phase boundaries and grain boundaries have to move in a cooperative way for a growing grain in a solid-liquid system with grain boundaries. It is reasonable to assume that grain boundary mobility is much smaller than phase boundary mobility, since the latter only involves mass transport in the liquid phase (if atomic attachment from the liquid to the particle surface is not too slow).

Grain boundaries of radius  $r$  will then curve and exert a drag force  $F_D$  on the moving phase boundaries. The drag force may be expressed:

$$F_D = 2\pi r \gamma_{GB} \cos \theta$$

where  $\gamma_{GB}$  is the average grain boundary energy. This force is maximum and equal to  $2\pi r \gamma_{GB}$  as  $\theta$  tends to 0. Since the number of grain boundaries per unit area of a grain is  $C/\pi r^2$ , the maximum drag pressure exerted on the surface area of a grain is:

$$P_D = \frac{2C}{r} \gamma_{GB}$$

